

**STUDY OF VOLUME VARIATIONS IN ALPHA STIRLING ENGINE
DESIGN VIA A DISCRETE CONTROL VOLUME APPROACH**

by

JEAN C. ALICEA ROMÁN

A thesis submitted in partial fulfillment of the requirements for the degree of

MASTER OF SCIENCE

in

MECHANICAL ENGINEERING

UNIVERSITY OF PUERTO RICO

MAYAGÜEZ CAMPUS

2014

Approved by:

Ivan J. Baiges, Ph.D.

Member, Graduate Committee

Date

David B. Dooner, Ph.D.

Member, Graduate Committee

Date

Orlando E. Ruiz, Ph.D.

Chair, Graduate Committee

Date

Hector J. Carlo, Ph.D.

Representative of Graduate Studies

Date

Ricky Valentín, Ph.D.

Chairperson of the Department

Date

ABSTRACT

New demand for cleaner and low cost energy production are factors that have increased interest in the Stirling engine as a plausible alternative to internal combustion engines. The Stirling engine is based on the principles of having a machine work within a temperature differential and internal thermal regeneration. The regenerator is a waste heat recovery device that improves the thermal efficiency of the cycle. Theory shows that the Ideal Stirling cycle efficiency is the same found for the Carnot cycle efficiency. However, the use of Ideal cycle and First Order analysis methods tend to grossly over predict performance parameters. This often comes as a result of inadequate assumptions and ignoring loss terms in the system to make simplifications in the analysis. In practice, the design of Stirling engines is difficult because of the complex thermal and mechanical processes that are involved.

The Second Order method is found to be useful in engine design optimization, since the analysis assumes that all of the energy losses are decoupled. The individual loss mechanisms can be conveniently identified and quantified. This analysis allows the engine performance to be estimated in a more realistic manner by subtracting the losses to the idealized performance parameters in a simple and efficient approach. Such analysis model, if implemented with enough accuracy, could properly evaluate design changes required for developing technology to make the Stirling engine more reliable, sustainable and efficient. More efficient heat transfer and adequate kinematic mechanisms for performing cycle work are two major areas that can be improved. This research project considers the potential for improving the thermodynamic efficiency of the Stirling engine by evaluating alternative piston motions that substantially deviate from sinusoidal. The present study further expands on previous work in this area by incorporating the Second Order losses. Following in this effort, the studies are based on arbitrary functions that describe the piston motion and parametric studies of the cylinder compartments. Unfavorable results were obtained in the motion studies for the new arbitrary functions. The lower performance was related to larger gas velocities that significantly increased the power losses. However, an optimal configuration was found for cylinder compartment while maintaining the sinusoidal motion.

ABSTRACTO

Nueva demanda de producción de energía limpia y a bajo costo, son factores que han aumentado el interés en el motor Stirling como una alternativa a los motores de combustión interna. El motor Stirling se basa en los principios de operar un ciclo dentro de un diferencial de temperatura y regeneración termal interna. La teoría demuestra que para el ciclo Stirling Ideal la eficiencia es igual a la eficiencia del ciclo de Carnot. Sin embargo, el uso de los análisis basados en el ciclo Ideal y métodos de primer orden tienden a sobreestimar substancialmente los parámetros de rendimiento. A menudo, esto se debe a que las asunciones son inadecuadas y se ignoran términos que se atribuyen a pérdidas en el sistema para simplificar el análisis. En la práctica, diseñar motores Stirling es difícil debido a la complejidad de los procesos térmicos y mecánicos que están involucrados.

El método de Segundo Orden es útil para la optimización del diseño del motor, ya que el análisis supone que todas las pérdidas de energía se desacoplan. Los mecanismos de las pérdidas individuales pueden ser convenientemente identificados y cuantificados. Este análisis permite que el rendimiento del motor se estime de una manera más realista restando las pérdidas a los parámetros de rendimiento idealizados, usando un enfoque sencillo y eficiente. Si el modelo de análisis se aplica con suficiente exactitud, podrían evaluarse adecuadamente los cambios de diseño necesarios para desarrollar tecnología que impulsen al motor Stirling a una mayor fiabilidad, sostenibilidad y eficiencia. Transferencia de calor más eficiente y diseños cinemáticos más adecuados para llevar a cabo el trabajo del ciclo son áreas que se pueden mejorar. Este proyecto investiga el potencial de mejorar la eficiencia termodinámica del motor Stirling al evaluar movimientos alternativos para el pistón que se desvían del tipo senoidal. Este estudio amplía el trabajo previo en esta área mediante la incorporación de pérdidas de Segundo Orden. A raíz de este esfuerzo, se realizaron estudios que se basan en funciones arbitrarias que describen el movimiento del pistón y otros estudios paramétricos del compartimiento de los cilindros. Resultados desfavorables fueron obtenidos en los estudios de movimiento para las funciones arbitrarias. El bajo rendimiento obtenido se debió a altas velocidades del gas, aumentando significativamente las pérdidas de potencia. Sin embargo, se encontró una configuración óptima para el compartimiento en el cilindro manteniendo el movimiento senoidal.

ACKNOWLEDGMENTS

First and foremost I give thanks to God and Jesus Christ for giving me the strength and courage to continue to follow my dreams.

I am especially grateful to my advisor, Dr. Orlando Ruiz, for allowing me to partake in this project. His time spent over the thesis work, his willingness to meet with me even on weekends and nights is highly appreciated. His interest and dedication were the keys for working through all the problems encountered during the research work.

I would also like to thank Dr. David Dooner and Dr. Ivan Baiges for assisting me in my graduate committee, and been patient enough to see the end of this work. I'm indebted to Dr. David Dooner who has been kind to share his brilliant ideas of designing the piston motion by using a Fourier series approximation and decoupling the piston motion from the mechanism. I believe that the development of his ideas will significantly contribute to the field of Stirling engines through this work and in the future.

In addition I would like to give thanks to Dr. Pedro Vazquez for taking the time to discuss issues concerning optimization modeling and techniques. To all the professors, staff, graduate and undergraduate students of the Mechanical Engineering Dept. who have become a part of my life during this journey, thank you all and keep up the good work.

Finally, I want to dedicate this thesis to my family for their understanding, encouragement and unconditional love.

TABLE OF CONTENTS

ABSTRACT.....	ii
ABSTRACTO.....	iii
ACKNOWLEDGMENTS	iv
LIST OF FIGURES	vii
LIST OF TABLES	xi
NOMENCLATURE.....	xii
Letter Symbols.....	xii
Greek Symbols.....	xiii
Subscripts.....	xiv
Acronyms.....	xv
CHAPTER 1: INTRODUCTION.....	1
1.1 Introduction to Thesis Scope	1
1.2 Stirling Engine Description	3
1.3 Stirling Engine Applications.....	5
1.3.1 Concentrated Solar Power.....	5
1.3.2 Cryocoolers	8
1.3.3 Submarines and Underwater Vehicles.....	8
1.3.4 Cars and Motor Transport	9
1.3.5 Micro Combined Heat and Power.....	10
1.4 Thesis Objective.....	11
CHAPTER 2: LITERATURE REVIEW	14
2.1 Stirling Ideal Limit.....	14
2.2 Stirling Engine Configurations	16
2.3 Stirling Engine Analysis Methods	20
2.4 Case Study: The Ford-Philips 4-215 Stirling Engine	25
2.4.1 Piston and Cylinders	26
2.4.2 Heating System	27
2.4.3 Regenerator and Cooler	29
2.5 Previous Work.....	31
CHAPTER 3: Stirling Cycle Analysis & Studies	34
3.1 Ideal Cycle Analysis	34
3.1.1 Ideal Stirling Cycle Example Problem.....	34
3.1.2 Preliminary Parametric Studies.....	38
3.1.2 Working Gas Selection.....	43
3.1.3 Imperfect Regeneration.....	44
3.2 First Order Methods.....	48

3.2.1 Isothermal Analysis.....	49
3.2.2 Further Parametric Studies.....	56
3.2.3 Adiabatic Analysis	59
3.2.4 Finite Heat Transfer Analysis.....	68
3.3 Second Order Methods	79
3.3.1 Pressure Losses	80
3.3.2 Mechanical Losses	84
3.3.3 Heat Losses	87
3.3.4 Net Performance Prediction.....	90
3.4 Proposed Studies.....	93
3.4.1 Motion Studies.....	93
3.4.2 Parametric Studies	95
CHAPTER 4: Discussion and Results	98
4.1 Preview of Analysis Studies	98
4.2 Ideal Motion from a 2 nd Order Method Perspective	99
4.3 Motion Studies.....	101
4.4 Parametric Studies for the Cylinder Compartments	105
4.4.1 Individual Parametric Analysis	105
4.4.2 Simultaneous Parametric Analysis.....	108
CHAPTER 5: Conclusion and Future Work.....	112
5.1 Conclusion	112
5.2 Future Work	114
APPENDIX A	116
Appendix A.1	116
Appendix A.2	118
APPENDIX B	119
APPENDIX C	127
Appendix C.1	127
Appendix C.2	137
APPENDIX D.....	139
Appendix D.1	139
Appendix D.2.....	141
Appendix D.3.....	145
Appendix D.4.....	147
REFERENCES	148

LIST OF FIGURES

Figure 1– 1: Drawing of the Original Patented Stirling Engine.....	5
Figure 1– 2: Common Concentrated Solar Power Systems	6
Figure 1– 3: Concentrating Solar Factor for Common CSP Systems	6
Figure 1– 4: World CSP Energy Production by System Technology	7
Figure 1– 5: Solar Dish-Stirling unit.....	7
Figure 1– 6: Stirling Cryocooler Design and Schematic	8
Figure 1– 7: Kockums Submarine with Stirling AIP Unit	9
Figure 1– 8: Residential Home Schematic for mCHP unit	11
Figure 2–1: (a) Ideal P- \forall Diagram (b) Ideal T-s Diagram.....	16
Figure 2–2: Alpha-Stirling.....	17
Figure 2–3: Beta-Stirling	18
Figure 2–4: Gamma-Stirling.....	19
Figure 2–5: Rinia-Siemens engine configuration	19
Figure 2–6: Beale free-piston engine configuration	20
Figure 2–7: Double acting Bingham engine configuration.....	20
Figure 2–8: Design Block Diagram.....	21
Figure 2–9: (a) Ford-Philips 4-215 Engine (b) Ford-Philips 4-215 Engine Cross-Section	25
Figure 2–10: Piston-Swashplate Drive System	27
Figure 2–11: (a) Ford-Philips 4-215 Heater Head Design (b) General View of Heater Tubes mounted in Cylinder (c) General Heater Cross-Section.....	28
Figure 2–12: (a) Ford-Philips 4-215 Regenerator-Cooler Unit (b) General Regenerator Gauze Stack (c) General Single Wire Gauz (d) General Cooler Shell & Tube Arrangement	30
Figure 2–13: (a) Four Bar Dwell Mechanism (b) Resulting Piston Dwell Displacement	32
Figure 2–14: (a) Sinusoidal, Elliptical Drive, and Ideal Motions (b) Elliptical Drive General Design	33
Figure 3–1: Ideal Cycle P- \forall Diagram for Gases at the Same Starting Pressure.....	35
Figure 3–2: Ideal Cycle T- Δ S Diagram.....	36
Figure 3–3: Ideal Cycle P- \forall Diagram for Gases with the Same Cycle Mass.....	37
Figure 3–4: Ideal Cycle T- Δ S Diagram for Gases with the Same Mass	38
Figure 3–5: Regenerator Specific Heat Transfer as a Function of Temperature Ratio	39
Figure 3–6: Specific Net Work as a Function of Compression Volume Ratio.....	40
Figure 3–7: Specific Engine Work as a Function of Temperature Ratio	41
Figure 3–8: Specific Net Work as a Function of Compression Volume and Temperature Ratios	42

Figure 3–9: Thermal Efficiency as a function of Temperature Ratio	42
Figure 3–10: Computer Simulated Effect of Working Fluid on the Thermal Efficiency.....	43
Figure 3–11: Cycle Efficiency vs Regenerator Effectiveness.....	45
Figure 3–12: Cycle Efficiency as a Function of Regenerator Effectiveness and Temperature Ratio	46
Figure 3–13: Cycle Efficiency as a Function of Regenerator Effectiveness and Compression Ratio	47
Figure 3–14: Cycle Efficiency vs Regenerator Effectiveness Surface Contours.....	48
Figure 3–15: Five Component Model for Isothermal Analysis	50
Figure 3–16: Sinusoidal Volume Variation	53
Figure 3–17: Sinusoidal Pressure Variation over the Cycle for Isothermal Analysis	54
Figure 3–18: P- \forall Diagram for Sinusoidal Volume Variation for Isothermal Analysis	54
Figure 3–19: Ideal and Sinusoidal motion.....	55
Figure 3–20: Ideal Cycle and Sinusoidal P- \forall Diagram.....	55
Figure 3–21: Net Cycle Work for Phase Angle Variation	57
Figure 3–22: Dead Space Volume Effect on Cycle Net Work	58
Figure 3–23: Dead Space Volume Effect on P- \forall Diagram.....	59
Figure 3–24: Five Component Model for Adiabatic Analysis (Urieli, [2011]).....	60
Figure 3–25: Gas Temperature Diagram for Adiabatic Analysis.....	63
Figure 3–26: Adiabatic Analysis Interface Temperatures	64
Figure 3–27: Normalized Pressure and Compression Space Mass for Adiabatic Analysis	65
Figure 3–28: Cycle Mass Variation for Adiabatic Analysis.....	66
Figure 3–29: Cycle Mass Flow Rate Variation for Adiabatic Analysis	67
Figure 3–30: Cycle Work and Heat Diagram for Adiabatic Analysis.....	68
Figure 3–31: Internal Heat Transfer Characterization of the Ford-Phillips 4-215 engine	70
Figure 3–32: Five Component Model for Finite Heat Transfer Analysis	71
Figure 3–33: Cycle Temperature Diagram for Finite heat Transfer Analysis.....	75
Figure 3–34: Control Volume Interface Temperature Variation for Finite Heat Transfer Analysis	76
Figure 3–35: Cycle Work and Heat Comparison between Finite Heat Transfer & Adiabatic Analysis	77
Figure 3–36: Ideal Cycle, Isothermal, Adiabatic, and Finite Heat Transfer P- \forall Diagrams.....	79
Figure 3–37: (a) Cooler Diagram Depicting Major & Minor Losses (b) Heater Diagram Depicting Major & Minor Losses.....	81
Figure 3–38: Flow through a Woven-Screen Matrix	82
Figure 3–39: (a) Pressure Drop in Heat Exchangers (b) Pumping Power Loss in Heat Exchangers	83
Figure 3–40: Mechanical Power Loss Estimation	84

Figure 3–41: (a) 4-215 DA Brake Power (b) 4-215 DA Mechanical Loss from Costea.....	86
Figure 3–42: Regenerator Temperature Profile for Imperfect Regeneration	88
Figure 3–43: (a) Regenerator NTU for First Blow at 4500 RPM (b) Regenerator Effectiveness for First Blow at 4500 RPM.....	89
Figure 3–44: Power Output & Power Loss Mechanisms as Function of RPM	91
Figure 3–45: Power Loss Percentile from Adiabatic Power as Function of RPM.....	92
Figure 3–46: (a) Compression Space Volume Variation (b) Expansion Space Volume Variation (c) Net Volume Displaced.....	94
Figure 4– 1: Swept Volumes for an Arbitrary Ideal Function	100
Figure 4– 2: Cycle P- v diagram for Ideal, Sinusoidal and Arbitrary motion in Figure 4-1	101
Figure 4– 3: (a) Volume Variation in V_c and V_e (b) Volume Rate of Change (c) Difference in Volume Variation (d) Difference in Volume Rate of Change	104
Figure 4– 4: (a) Heater Volumetric Flow Rate Comparison (b) Heater Gas Velocity Comparison	105
Figure 4– 5: 2 nd Order Cycle Efficiency and Power Output vs. Swept Volume Ratio.....	106
Figure 4– 6: 2 nd Order Cycle Efficiency and Power Output vs. Clearance Length Ratio.....	107
Figure 4– 7: 2 nd Order Cycle Efficiency and Power Output vs. Phase Angle.....	107
Figure 4– 8: Cycle Efficiency Contours vs CLR and SVR for 60°, 90°, 77°, and 105° phase angles.....	109
Figure 4– 9: Power Output Contours vs CLR and SVR for 60°, 90°, 77°, and 120° phase angles.	110
Figure 4– 10: Cycle Efficiency and Power Output for Baseline and Optimize Ford-Phillips Engine.....	111
Figure B–1: Flow Chart for Adiabatic Analysis Program.....	121
Figure B–2: Flow Chart for 4 TH Order Runge-Kutta Integration Loop in Adiabatic Analysis Program ..	122
Figure B–3: Energy Conservation for Adiabatic Analysis.....	123
Figure B–4: Normalized Error (using max error) for Adiabatic Analysis	126
Figure B–5: Error in Expansion and Compression Space Temperature for Adiabatic Analysis.....	126
Figure B–6: Error in Pressure for Adiabatic Analysis	126
Figure B–7: Error in Energy Conservation for Adiabatic Analysis	126
Figure C–1: Flow Chart for Finite Heat Transfer (FHT) Analysis Program.....	130
Figure C–2: Flow Chart for 4 TH Order Runge-Kutta Integration Loop in FHT Analysis Program	131
Figure C–3: Energy Conservation for Finite Heat Transfer Analysis.....	132
Figure C–4: Normalized Error (using max error) for FHT Analysis	136
Figure C–5: Error in Gas and Matrix Wire Temperatures for FHT Analysis.....	136
Figure C–6: Error in Pressure for FHT Analysis	136
Figure C–7: Error in Energy Conservation for FHT Analysis	136

Figure C-8: Comparison of Gedeon-Wood and Martini's for Regenerator Nu Correlation.....	138
Figure D-1: 2 nd Order Method Calculation Flow Chart	140
Figure D-2: Cooler, Regenerator and Heater Mach Numbers for 4500 RPM.....	141
Figure D-3: Cooler, Regenerator and Heater Reynolds Numbers for 4500 RPM.....	142
Figure D-4: (a) Cooler Friction Factor Correlation Comparison (b) Heater Friction Factor Correlation Comparison	144
Figure D-5: Regenerator Pressure Drop Comparison and Validation	144

LIST OF TABLES

Table 2–1: Ford-Philips 4-215 General Operating Parameters	26
Table 2–2: Heater Specifications for Ford-Philips 4-215 Engine	29
Table 2–3: Regenerator Specifications for Ford-Philips 4-215 Engine	30
Table 2–4: Cooler Specifications for Ford-Philips 4-215 Engine.....	31
Table 3–1: Ideal Performance Summary for Different Gases at the Same Starting Pressure	36
Table 3–2: Ideal Performance Summary for Different Gases with the Same Mass.....	38
Table 3–3: Sinusoidal Volume Variations	51
Table 3–4: Summary of Thermal Cycle Equations for Isothermal Analysis	52
Table 3–5: Ford-Phillips 4-215 Engine Isothermal Analysis Performance.....	56
Table 3–6: Comparison of Engine Performance Results for 1 st Order Methods at 4500 RPM	78
Table 3–7: Summary of 2 nd Order Pumping Pressure Loss at 4500 RPM	84
Table 3–8: Comparison of Engine Performance Results for 2 nd Order Methods at 4500 RPM	91
Table 3–9: Matrix Set Data for Parametric Studies for 60°, 90°, 77°, and 105° Phase Angles.	96
Table 4–2: 2 nd Order Performance Results for Sinusoidal, Fang and Step Functions at 4500 RPM	103
Table 4–3: Design and Performance data for Baseline and Optimize Ford-Phillips Engine	111
Table B–1: Set of Thermal Cycle Equations for Adiabatic Analysis	119
Table B–2: Comparison of numerical result for n=15,000 (number of steps) and 4500 RPMs	124
Table B–3: Set of equations for error and convergence evaluation in the Adiabatic Analysis	124
Table C–1: Set of Thermal Cycle Equations for Finite Heat Transfer Analysis	128
Table C–2: Comparison of numerical results of FHT Analysis, when using ACF=7 and ACF=0	133
Table C–3: Set of equations for error and convergence evaluation in FHT analysis.....	134
Table C–4: Set of Equations for HTC Calculation in Finite Heat Transfer Analysis.	137
Table D–1: Summary of Equations for Pumping Power Loss Calculation.....	145
Table D–2: Summary of Equations for Mechanical Power Loss Calculation	146
Table D–3: Expressions for ϵ and NTU Found in SE Literature	147
Table D–4: Summary of Equations for Regenerator Heat Loss Calculation	147

NOMENCLATURE

Letter Symbols

A	Heat transfer or wetted area [m ²]
C	Heat Capacity [kJ/K]
C_1, C_2, C_3	Constants used in Heywood equation for mean effective pressure (mep) loss
c	Specific heat general use [kJ/kg-K]
C_v	Gas specific heat at constant volume [kJ/kg-K]
C_p	Gas specific heat at constant pressure [kJ/kg-K]
D_h	Hydraulic diameter [cm or mm]
d_w	Matrix wire diameter [cm or mm]
d	Ordinary or exact differential
E	Thermal energy [kJ]
e or ϵ	Error
F	Fluid friction factor; Mechanical Friction Force [kN or N]
f	Engine operating frequency [Hz or 1/s]
f_f	Fanning friction factor
G	Mass flux [kg/s- m ²]
h	Heat transfer convection coefficient [W/m ² -K]
k_f	Fluid thermal conductivity [W/m-K]
K	Minor loss coefficient
L_s	Piston stroke length [cm or mm]
Ma	Mach number
m	Mass [kg]
\dot{m}	Mass flow rate [kg/s]
N	Engine speed used in Heywood equation for mep loss [Rev/s]
NC	Number of cylinders
NR	Number of generators
Nu	Nusselt number
P or p	Pressure [bar, kPa or Pa]

Pr	Prandtl number
Q	Heat [kJ or J]
Q'	Heat per unit mass [kJ/kg]
\dot{Q}	Heat rate [kW]
R	Gas constant [kJ/kg-K]
Re	Reynolds number
r_c	Compression ratio
S	Entropy [kJ/K]
Sc	Schmidt number
T	Temperature [K]
t	Time [s]
U	Internal energy [kJ]; overall heat transfer coefficient [W/m ² -K]
\forall or V	Volume [cc or m ³]
\dot{V}	Volume flow rate [m ³ /s]
Vel	Gas velocity [m/s]
V_p	Average piston velocity [m/s]
W	Work [kJ]
W'	Work per unit mass [kJ/kg]
\dot{W}	Power or output power [kW]
X_{cl}	Clearance length [mm]

Greek Symbols

α	Phase angle [°]
Γ_c	Volume ratio used in Costea's mechanical friction correlation
γ	Ratio of specific heats
Δ	Variable change or differential
ε	Regenerator Effectiveness; pipe relative roughness
η	Cycle efficiency; mechanical efficiency
θ	Crank angle [°]
λ_v	Scaling factor used in Costea's mechanical friction correlation

μ	Gas dynamic viscosity [kg/m-s]
ξ	Normalized error
ρ	Density [kg/m ³]
τ	Temperature ratio
ϕ	Matrix screen porosity

Subscripts

b	Refers to brake power
C or c	Compression or compression space; cold side
E or e	Expansion or expansion space
eff	Effective
g	Gas
h	Heater space
i	Refers to indicated power
k	Cooler space
m	Mean value
mr	Matrix wire solid material
sw	Swept
pl	Pressure loss
mec	Mechanical
ml	Mechanical loss
mf	Mechanical friction
rl	Regenerator (or regeneration) heat loss
w	Wall of heat exchanger
cl	Clearance
H	High temperature reservoir; hot side
L	Low temperature reservoir
R or r	Regeneration or regenerator space

Acronyms

ACF	Accelerating convergence factor
AIP	Air-independent propulsion
CFD	Computational Fluid Dynamics
CHP	Combined heat and power
CLR	Clearance length ratio
CSP	Concentrated solar power
DA	Double acting piston
DSR	Dead space to temperature ratio
FCT	Time fraction for regenerator first blow
FDM	Finite Difference Method
FHT	Finite heat transfer
H ₂	Hydrogen
He	Helium
IC	Internal combustion
LDT	Low temperature differential
LOX	Liquid oxygen
mCHP	Micro combined heat and power
mep	Mean effective pressure
NTU	Number of Transfer Units
RPM	Revolutions per minute
SE	Stirling engine
SES	Stirling Energy Systems
SNL	Sandia National Laboratories
SVR	Swept volume ratio
UWV	Under water vehicle

CHAPTER 1: INTRODUCTION

1.1 Introduction to Thesis Scope

Heat engines are an intrinsic part of our daily life, as they are widely used in the areas of agriculture, transportation and electric power generation. The purpose of a heat engine is the conversion of thermal heat energy to useful mechanical work. Thermal energy is typically provided by the combustion of fossil fuels such as petroleum and natural gas; although alternative sources such as nuclear, geothermal and solar energy can also be used to provide thermal energy. The thermal energy is then transferred to a working fluid whose energy and motion is later transformed to net power output by mechanical means (e.g. reciprocating crank-piston, turbine, etc.). Engine or power systems are usually named and described by a thermodynamic cycle. Some thermodynamic cycles that are more commonly known in thermal-power applications are the Rankine, Brayton, Otto and Diesel cycles. The thermodynamic cycle is said to be closed if it retains the same mass of working fluid at the end of the cycle or open if the mass is renewed. The various types of heat engines can be classified into internal combustion and external heat engines. For internal combustion engines heat is added by means of fuel ignition inside the system boundary. In the case of external heat engines, heat is supplied from any external source (combustion, nuclear, geothermal, solar, etc.) outside the system boundary.

The Otto and Diesel are examples of two internal combustion cycles successfully used in transportation vehicles due to their high specific power output. The Otto cycle, named after German engineer Nikolaus Otto, was successfully developed into a practical engine in 1876. Otto's development was the first meaningful improvement in engine performance, relative to the already existing power generation methods. Today, Otto engines (or petrol engines) have usually an operating efficiency around 30% and are capable of achieving power outputs in the range of 100 to 200 horsepower. Soon after Otto developed his engine cycle (in 1893), Rudolf Diesel designed and produced an internal combustion engine that employed a much higher compression ratio. This allowed the air to reach such elevated pressure and temperature that by simply injecting a spray of fuel it would auto-ignite, thus eliminating the need for a spark to ignite the fuel, as done by the Otto cycle engines. The

nature of this auto-ignited combustion in the Diesel engine makes it more efficient, therefore, requiring a substantially lower amount of fuel to operate in contrast to the Otto engine. Also the Diesel engine cycle is able to run on cruder fossils which are less expensive to make. Typically Diesel engines are able to produce net power outputs that far exceed that of an Otto engine and its thermal efficiency ranges between 40% and 50%. Today both the Otto and Diesel cycles still possess commercial and industrial success. However, increased prices for fossil fuels and the need of cleaner methods in obtaining energy, make them less attractive for the future.

Technically, Rankine and Brayton power systems may be considered as external heat engines because the heat source is located outside the system boundary. But these power systems are composed of separate components and are much larger in scale to be considered as engines. However, there exists an external heat engine that predates the invention of the internal combustion engine and it is called the hot-air engine. The first documented hot-air engine was invented by Sir George Cayley around 1807. This engine substituted air for steam as the working fluid, requiring the use of gas furnaces instead of boilers which were a safety concern at the time. Soon after this development, one of the most ingenious inventions of the 18th century was conceived, a device commonly known as the thermal regenerator. Regenerators are used to recover some of the waste heat from a thermal cycle and reuse it, thus increasing the cycle efficiency. Robert Stirling was responsible for this creation and his 1816 patent included a design of a hot-air engine as a practical application for the use of the regenerator. Therefore the hot-air type engine became to be known as the Stirling engine in honor of Robert Stirling. In contrast to Otto's and Diesel's inventions, the Stirling engine did not become a quick success in commercial and industrial applications. Hence the study and the development of the Stirling engine have been achieved slowly and in a much narrow scope of thermal applications. However, the new demands for renewable heat sources and cleaner energy make this engine more attractive for future development. Therefore, the opportunity for Stirling engines to compete with internal combustion engines exist if innovative Stirling technology is made available to make the engine more reliable, sustainable and efficient.

In this chapter, topics such as the Stirling engine description, history, advantages and

range of applications are introduced. In addition, the research project objective is formally stated at the end of this chapter. Chapter 2 will review the Ideal Stirling cycle, engine mechanical configurations, existing analytical models and the design specifications for the Ford-Phillips 4-215 double-acting (DA) engine. In Chapter 3, the mathematical models using sinusoidal piston motions are explored. Here the different parameters that affect Stirling engine performance are evaluated. In addition, the reliability of the methods is compared as the complexity of the models increases for more realistic assumptions. Finally, Chapter 3 concludes with the description of the proposed analysis studies and the thermal model used in the analysis. The results and assessment of the proposed studies (for optimum volume variation and engine configuration) is given in Chapter 4. Chapter 5 explains the conclusion of this thesis and future work recommendations.

1.2 Stirling Engine Description

Interest in the Stirling engine has increased in the past few years as it has been considered as a plausible alternative to the current internal combustion engines and other currently used power generating cycles. The Stirling Engine promises new advantages that cannot be obtained with the current heat cycles used for producing power. Some of the advantages of the engine are:

- It can work with almost any kind of external heat source, including solar, geothermal and bio-mass.
- The engine can work at very small scales allowing for milli and micro applications.
- It can run silently with minimal vibration.
- The engine operates on the basis of a reversible cycle which makes it a perfect device for heat-pump and refrigeration applications.
- It can be used for combined heat and power (CHP) applications.
- The thermal efficiency for the Ideal theoretical limit is the same as the Carnot cycle efficiency.

All these advantages assure that the potential of the Stirling Engine agrees with the goals of clean, reliable and sustainable methods for obtaining energy. This creates an irony in the

traditional approach for the development of new technology. The reason is that the Stirling Cycle is an old idea; in fact it was first conceived almost two centuries ago.

The Stirling cycle has been practically ignored from today's conventional thermodynamics courses and practically no universal knowledge on its development is spread commercially in the industry. To understand this paradigm, it is important to study the history of the Stirling Engine since its invention in 1816 [1, 2]. The hot air engine is named after Robert Stirling, who re-designed it as a practical application for the thermal regenerator. The regenerator is the actual invention (not the engine itself), stated in his original patent claim in 1816 [1]. His motivation was to develop an alternative to the vapor machines which at the time were unreliable and dangerous. The extremely high pressures at which boilers had to be operated and the poor safety standards in their manufacture resulted often in boiler explosions making the machine a hazard for a working environment. The invention of Robert Stirling not only had the advantage that it operated at a lower effective pressure but it was relatively simpler than the steam engine, thus requiring fewer personnel to operate it [2].

Figure 1-1 shows a drawing from the conceptual sketches of Stirling's original patent [3]. Contrary to Nicolas Léonard Sadi Carnot's heat engine, Stirling's invention did not stay in paper as a hypothetical concept. In 1818 a full-size machine designed on the basis of Stirling's patent was built to pump water from a quarry [2, 3]. The engine was rated at 2 hp working at a maximum temperature of 400 °C as suggested by Organ [3]. But after this successful attempt no further significant progress was made by Stirling on improving the design of his invention. By the early 19th century, interest in the Stirling engine decreased significantly due to the success of the Otto cycle engine incorporation in motor transport and the introduction of boiler codes for the construction of safer steam engines [4]. Increases in oil and energy prices, as well as a greater concern for environmental conservation, has given the Stirling engine a second chance to emerge as a possible solution to these problems. An example of current Stirling technology that uses concentrated solar power (CSP) as a heat source is the SES SunCatcher capable of generating 25 kW [5]. The first to develop a free-piston Stirling engine to work with CSP was William Beale of

Sunpower Inc., a company that has created a range of Stirling power generators operating from 35 W to 7.5 kW [6].

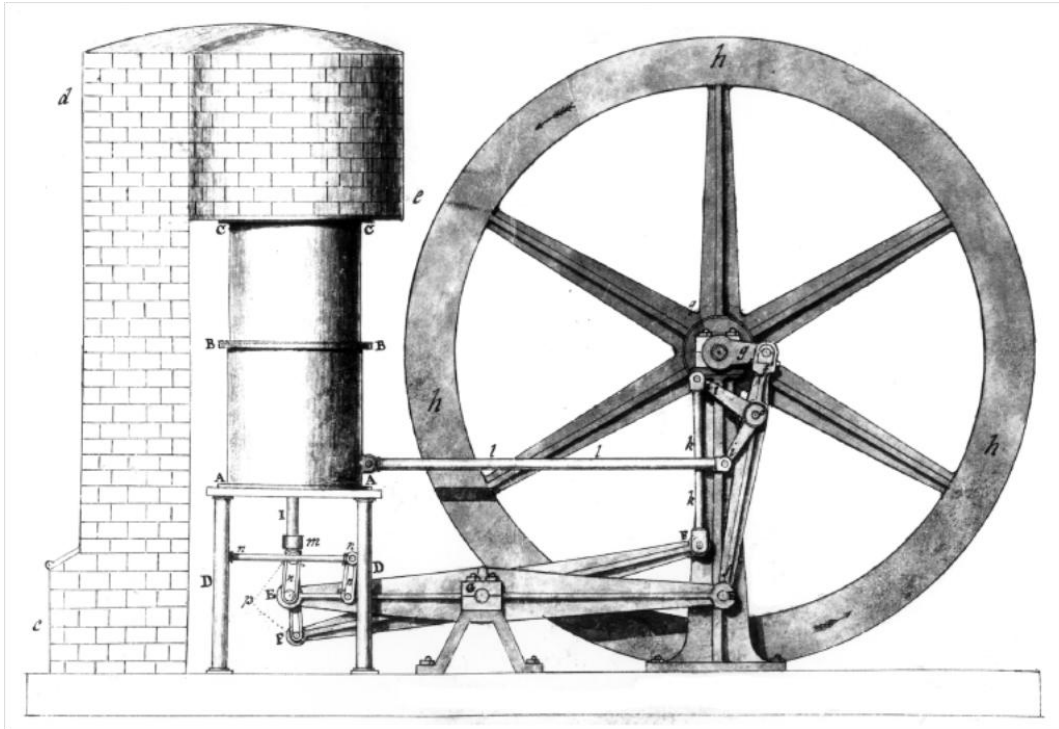


Figure 1- 1: Drawing of the Original Patented Stirling Engine (Organ, [2007])

1.3 Stirling Engine Applications

1.3.1 Concentrated Solar Power

Solar energy can be an excellent heat source for the Stirling engine. Power from the sun can be harnessed efficiently when solar concentrators are used to focus the solar radiation of a larger area to a small concentrated surface or point. Then, the concentrated sunlight is converted to thermal energy to finally be stored or used to produce work for driving a generator to deliver electricity to the power grid.

There are various types of CSP (Concentrated Solar Power) systems that use this renewable technology (Figure 1-2). However, as seen in Figure 1-3, the Solar Dish-Stirling system can achieve a greater concentration of the sun radiation than any of the other CSP systems. These three approaches are shown schematically and described in more detail below. The CSP methods shown here are described in more detail in a CSP Technologies Overview provided by Sandia National Laboratories (SNL) [7].

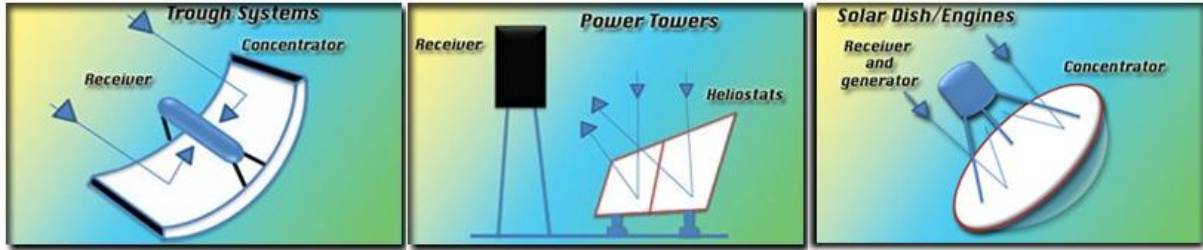


Figure 1– 2: Common Concentrated Solar Power Systems (SNL, [2012])

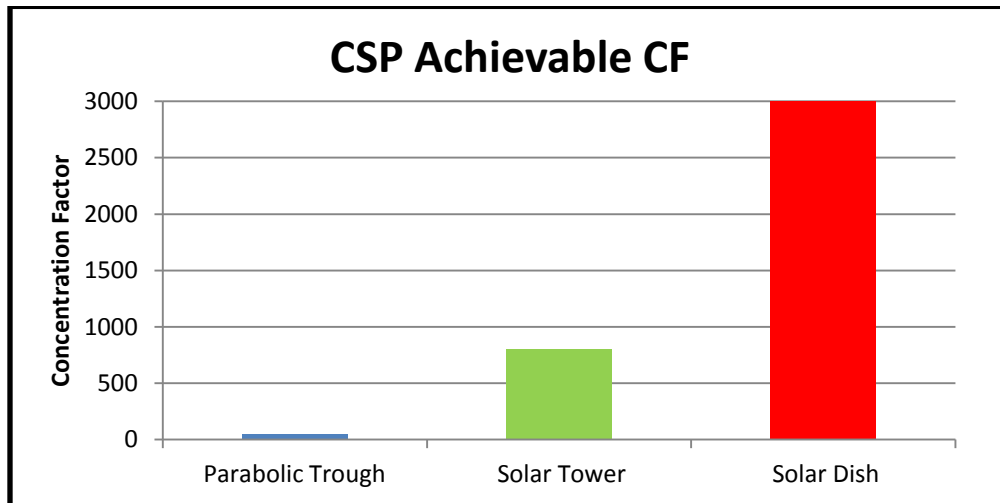
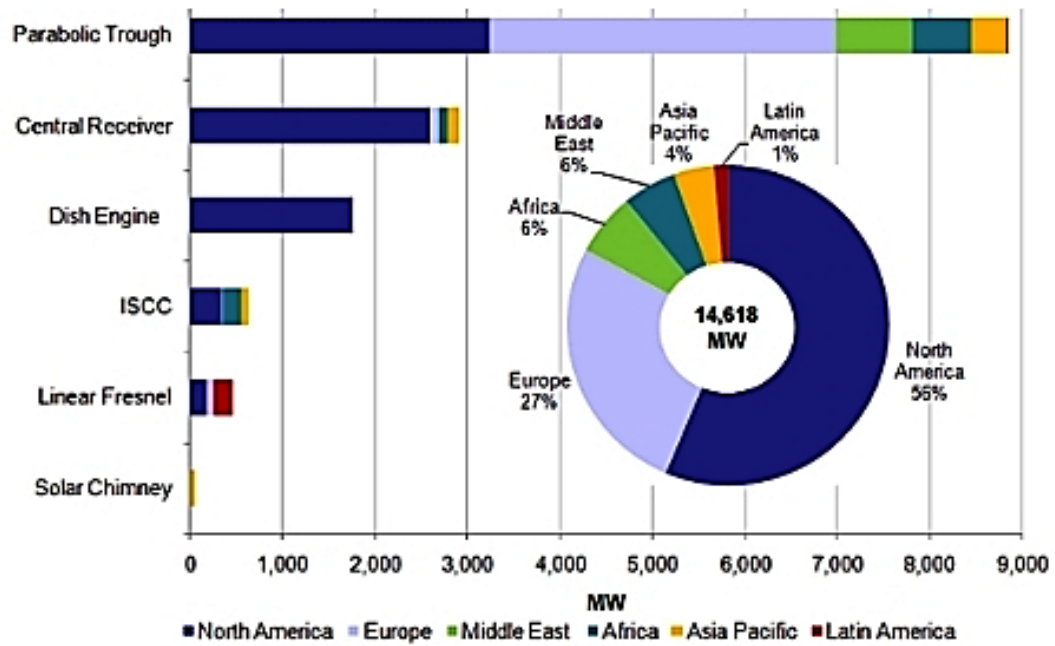


Figure 1– 3: Concentrating Solar Factor for Common CSP Systems

In the case of the solar parabolic dish CSPs, mirrors are used to reflect solar radiation to a receiver. The receiver end then supplies the heat that drives the Stirling engine. The Dish Stirling engine is capable of generating 25 kW of electric power at very high efficiencies, which allows it to compete with photovoltaic panels and other solar renewable energy systems. As shown in Figure 1–4, the Solar Dish Stirling (Fig. 1–5) ranks number 3 in world CSP technologies for delivering electrical energy to power grids [8]. Some of the limitations for the Solar Dish systems are the requirement of large land area, relative high maintenance and typically involve higher initial investment.

Regional CSP Pipeline by Technology



Source: *Emerging Energy Research*

Figure 1– 4: World CSP Energy Production by System Technology (Renewable Energy Focus, [2009])



Figure 1– 5: Solar Dish-Stirling unit (SES, [2007])

1.3.2 Cryocoolers

One of the major advantages that Stirling engine cycle has over any other power cycles is that its path can be reversed. Therefore, when a Stirling machine is supplied with a power input, it can operate either as a heat pump cycle or a refrigeration cycle. Stirling cryogenerators (or cryocoolers) are the most successful application of the Stirling cycle. Most current systems are able to deliver temperatures ranging from $-75\text{ }^{\circ}\text{C}$ to $-250\text{ }^{\circ}\text{C}$ [9] and may even achieve lower cooling temperatures.

The first Stirling-cycle cryocooler was developed at Philips in the 1950s and was commercialized for the production of liquid nitrogen and for other liquefying gas production plants. The Philips Company was very active in improving the design and manufacturing of Stirling cryocoolers and cryogenic cooling systems [1]. This led to the production of extremely efficient refrigeration systems for very low cooling temperature, as required in cryogenic applications. Stirling cryocoolers are durable, highly reliable, require little maintenance, have minimum vibration and noise, compact, lightweight, and run on low input power. Some designs are able to run on less than 100 watts of power [6]. In Figure 1–6 the general design of a Stirling cryocooler is shown [10].

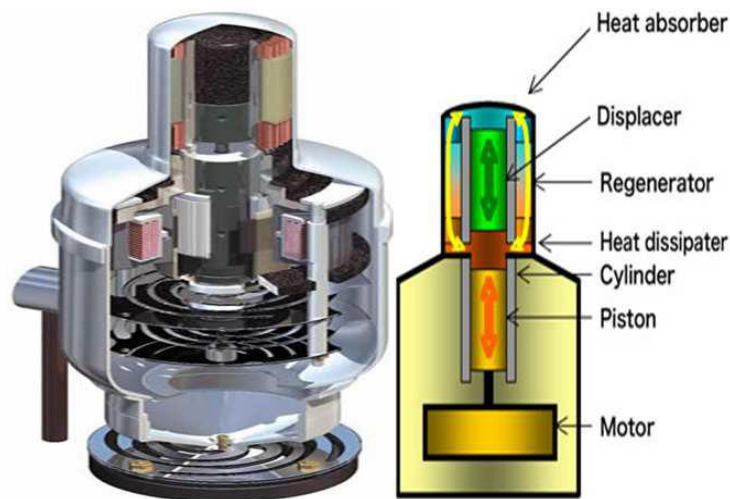


Figure 1– 6: Stirling Cryocooler Design and Schematic (Twinbird Corp, [2007])

1.3.3 Submarines and Underwater Vehicles

One of the not widely known uses for the Stirling engine is its function for powering submarines and UWVs (Under Water Vehicles). The first successful application in this field was reached by Kockums (a Swedish defense contractor) in 1988, when they fitted a

Stirling engine into a section of the Royal Swedish Navy submarine HMS Näcken. The purpose was to create an air-independent propulsion (AIP) system capable of increasing the submerged endurance time of current power battery systems [11].

Kockums AIP systems incorporate a Stirling engine, Oxygen in liquid form (LOX) stored in cryogenic tanks, and diesel as its fuel. The burning of LOX and diesel fuel in a pressurized combustion chamber, allows the exhaust gases to be at higher pressure than the surrounding seawater, thus eliminating the need of a compressor to discharge them [11]. Submerged endurance is primarily determined by the amount of stored LOX. Typically this equipment allows the submarine to stay underwater 2-5 times longer than with a normal battery system. Figure 1-7 illustrates a Kockums' submarine displaying the section where the AIP system is located (right) and how the section looks from the inside of the submarine (left).



Figure 1- 7: Kockums Submarine with Stirling AIP Unit (Kockums, [2009])

More recently, the applicability of the Stirling engine for other manned underwater vehicle (UV) and unmanned underwater vehicles (UUV) has been explored as well. Since the Stirling engine can be designed by scaling, it may also outperform underwater vehicle battery propulsion systems.

1.3.4 Cars and Motor Transport

In the 1970s and 1980s, automobile companies like General Motors and Ford evaluated the possibility of implementing Stirling engines into motor vehicles [12, 13]. The main motivation behind the effort was due to the first “world oil crisis”. This crisis did not only

provoke fossil fuel prices to sky-rocket; it also led to research for potential energy alternatives that could achieve higher efficiencies and lower fuel consumption.

However, the proposed novel Stirling engine solution was not able to achieve the expectations, and the research focus changed into optimizing the Otto and Diesel engines. One of the main problems found using the Stirling cycle engine, was that for a constant power setting it could achieve good performance, however, it could not respond sufficiently fast for adjusting the power (acceleration). As a result, acceleration control typically involved complex solutions [12, 13].

One possibility is to design a hybrid electric car where a Stirling engine could give enough power to run the car for long trips when the car is moving at almost constant speed. And to use a battery system to give the instant acceleration necessary to drive an automobile. This invention could make the car run silent and with lower carbon emissions. Additionally the possibility of achieving high fuel savings with an electric-Stirling engine combination may give it a shot in competing with current hybrid cars.

1.3.5 Micro Combined Heat and Power

Cogeneration technology is widely used in local power and production plants as means of reducing energy cost by combining the generation of useful heat and electric power. This technology is also known as combined heat and power (CHP) and there are two basic concepts behind its approach to achieve an efficient energy process. The first concept is that when electricity is produced locally, the energy losses through long transmission lines are reduced substantially. The second concept is that the heat loss due to the inefficiencies in the power generation process can be employed to heat homes, produce hot water or be applied to any other process that requires heat in a production plant.

In Europe, especially in the United Kingdom (UK), traditional boiler systems are being replaced by a technology that is complementary (smaller system scale) to CHP. The innovative system is being developed for use in residential homes and commercial buildings [14, 15]. The term micro combined heat and power (mCHP) has been given to this technology due to the smaller scale of the application. The significant increases in the cost of energy, as well as more legislation to reduce carbon emissions, which includes

incentives to energy production methods that reduce carbon emissions, have made mCHP as an alternative to replace traditional boilers for means of providing central heating, water heating and electricity.

Generally in a mCHP device, natural gas is consumed by a Stirling engine for means of providing electricity. However, not all the heat is supplied for power generation purposes; around 70% to 80% of the gas energy that is converted into heat will be used for space heating and hot water [14]. A general schematic for a residential home mCHP unit is shown in Fig. 1–8. Usually this device produces much less carbon dioxide than other ways of providing heat and power. In fact, if the capacity of CHP systems was increased to the Government's target of 10,000 MW, the UK could meet one third of its international commitment of carbon dioxide emissions reduction level [15].

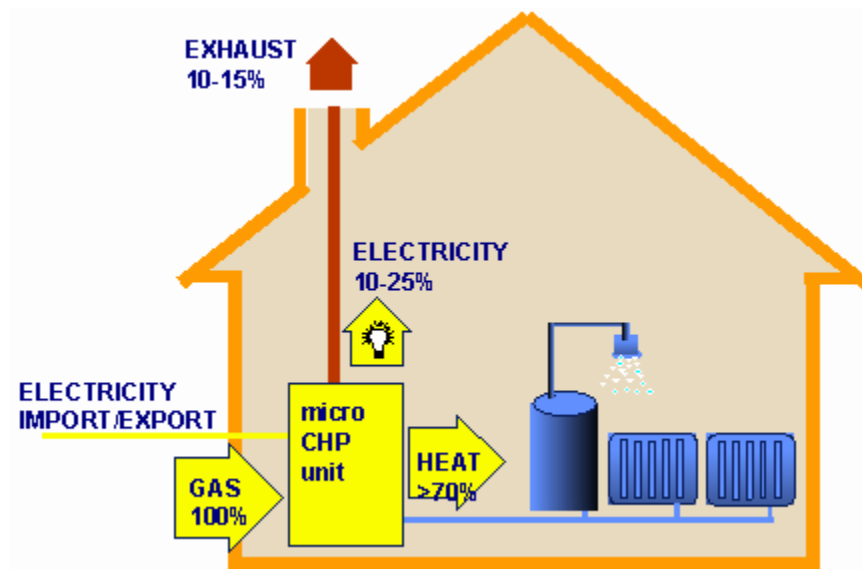


Figure 1– 8: Residential Home Schematic for mCHP unit (Harrison, [2012])

1.4 Thesis Objective

Stirling engine performance is not only tied to the internal processes involved throughout the cycle, but also the types of mechanisms used are an integral part of the power generation process. One of the problems of kinematic Stirling engines is that the sinusoidal volume variations that are produced by typical crank mechanisms do not result in optimum performance because these deviate considerably from the Ideal Stirling cycle thermodynamic processes. Evidently there is a need to investigate which type of volume

variations (in the compression and expansion spaces) would result in optimum engine performance and which types of mechanisms are capable of achieving these variations.

In accordance with this need, the primary goal of this thesis is to improve the thermodynamic efficiency of an Alpha Stirling engine configuration by performing studies on different piston motions that are believed to be more adequate. This can be accomplished by developing an accurate mathematical model of the cyclic behavior of the five internal control volumes (compression space, cooler, regenerator, heater, and expansion space) that is dependent on the piston swept dynamics. Then, the different functions of the volume variation inside the compression and expansion cylinder spaces can be evaluated with respect to the cycle performance they can achieve. The Stirling Cycle analysis will be explored in detail (primarily using the sinusoidal variations) to assess the precision of the models as assumptions become more complex. This will culminate when the 1st and 2nd Order method results are compared. The 2nd Order model will be used to perform a comprehensive comparison between the sinusoidal volume variations and arbitrary function volume variations. The study will focus on the Alpha Stirling engine configuration and the Ford-Phillips 4-215 engine will be considered for a case study analysis. In addition, parametric studies will be conducted to evaluate the thermodynamic and mechanical losses, in order to determine the sensitivity of the engine performance to important design parameters (e. g. heat exchanger size, operating temperature ratio, etc.). Emphasis will be given to swept volume ratio (SVR), clearance length ratio (CLR), and phase angle using the 2nd Order method in Chapter 4.

It has been found that there exists a considerable body of literature that focuses on Stirling engine design. However, the progress that has been made using Stirling engine machines seems limited to a narrow scope of applications (CSP [5-6], Cryocoolers [16], Underwater Vehicles [11]) and overall commercial success has not been reached. Considering the wide range of applications suitable for Stirling engines the possibility of significantly improving and optimizing existing designs must be explored. Typically, thermal system optimization has been traditionally performed separate from the mechanical system optimization. Therefore, the model to be implemented must properly describe thermodynamic relationships like the finite heat transfer effects and the gas

dynamics of the system. This way, not only a better understanding of the already existing mechanisms can be addressed, but also the effects of placing arbitrary piston motions in the variable working spaces. Considering all of these factors will guide future studies into finding a practical mechanism that is capable of achieving optimum volume variations. It is also desired to provide the designer with an analysis model that is simple to implement and at the same time accurate enough to properly evaluate design changes. If this set of tools is more available to designers, development of high performance Stirling engines in the near future may compete with today's available commercial internal combustion engines.

CHAPTER 2: LITERATURE REVIEW

2.1 Stirling Ideal Limit

The maximum theoretical thermal efficiency for the Stirling cycle results in the thermal efficiency deduced for the Carnot cycle. The idealization for the theoretical case is based on the assumption that at any given point in time the pressure and temperature are homogenous within the volume containing the mass of the working gas. The gas is considered to be a perfect gas in all the processes, thus the ideal gas equation of state can be applied at any point of the cycle. The heater and cooler are considered isothermal heat exchangers. The regenerator is assumed perfect, and the processes involving the decrease and increase in temperature are considered isochoric (constant volume) [17]. Based on these assumptions, the Stirling engine cycle consists of the following processes:

- Process 1-2: The working gas is compressed isothermally, while heat is removed to the low temperature reservoir.
- Process 2-3: The working gas is preheated by gaining heat from the regenerator at constant volume.
- Process 3-4: The working gas is expanded isothermally, while heat addition occurs from the hot temperature reservoir.
- Process 4-1: The working gas is precooled by losing heat to the regenerator at constant volume.

Each process described for the Ideal Stirling cycle is presented in the pressure-volume (P- ∇) and temperature-entropy diagrams shown in Figure 2-1.

Each process can be evaluated using the first law of thermodynamics for a closed system. The work-heat relationship for a stationary system using the first law is,

$$\Delta E = \Delta U = \Delta Q - \Delta W \quad (2.1)$$

For the isothermal compression process 1-2 since there is no change in internal energy and since only heat addition and expansion work occurs, the equation results in,

$$Q_{\text{out}} = W_C \quad (2.2)$$

Based on the perfect gas assumption, the compression work for an isothermal process is,

$$W_C = \int_{V_1}^{V_2} P(V)dV = \int_{V_1}^{V_2} \frac{mRT_C}{V} dV = mRT_C \int_{V_1}^{V_2} \frac{1}{V} dV = mRT_C \ln\left(\frac{V_2}{V_1}\right) \quad (2.3)$$

The heat rejection and compression work as determined by Eq. 2.2 and 2.3, respectively, are negative quantities consistent with the sign convention in thermodynamics. Similarly for the isothermal process 3-4 the first law of thermodynamics results in,

$$Q_{in} = W_E \quad (2.4)$$

and the expression for the expansion work yields,

$$W_E = mRT_H \ln\left(\frac{V_4}{V_3}\right) \quad (2.5)$$

For the isochoric processes there is no expansion or compression work, however, there is a change in the internal energy of the working fluid due to internal heat transfer from the regenerator. For process 2-3 there is an increase in internal energy and for process 4-1 there is a decrease. Heat transferred in both processes is given by the following equation,

$$Q_R = mC_V(T_H - T_C) \quad (2.6)$$

where Q_R represents the regenerator heat exchange. Note that the regenerator supplies the same amount of heat in process 2-3, that it receives from process 4-1. The available net work of the cycle is given by,

$$W_{net} = W_E + W_C = mR \left[T_H \ln\left(\frac{V_4}{V_3}\right) + T_C \ln\left(\frac{V_2}{V_1}\right) \right]$$

or

$$W_{net} = mR \ln(r_C) [T_H - T_C] \quad (2.7)$$

where r_C is the compression ratio defined as follows,

$$r_C = \frac{V_4}{V_3} = \frac{V_1}{V_2}$$

Finally, the cycle thermal efficiency can be determined based on the ratio of the net output work for the cycle and heat addition required during the cycle:

$$\eta_{\text{cycle}} = \frac{W_{\text{net}}}{Q_{\text{in}}} = \frac{mR \ln(r_C) [T_H - T_C]}{mRT_H \ln(r_C)} = \frac{T_H - T_C}{T_H} = 1 - \frac{T_C}{T_H} \quad (2.8)$$

By comparison, it is demonstrated that the Ideal thermal efficiency of the Stirling engine cycle is the same as the Carnot cycle thermal efficiency [17].

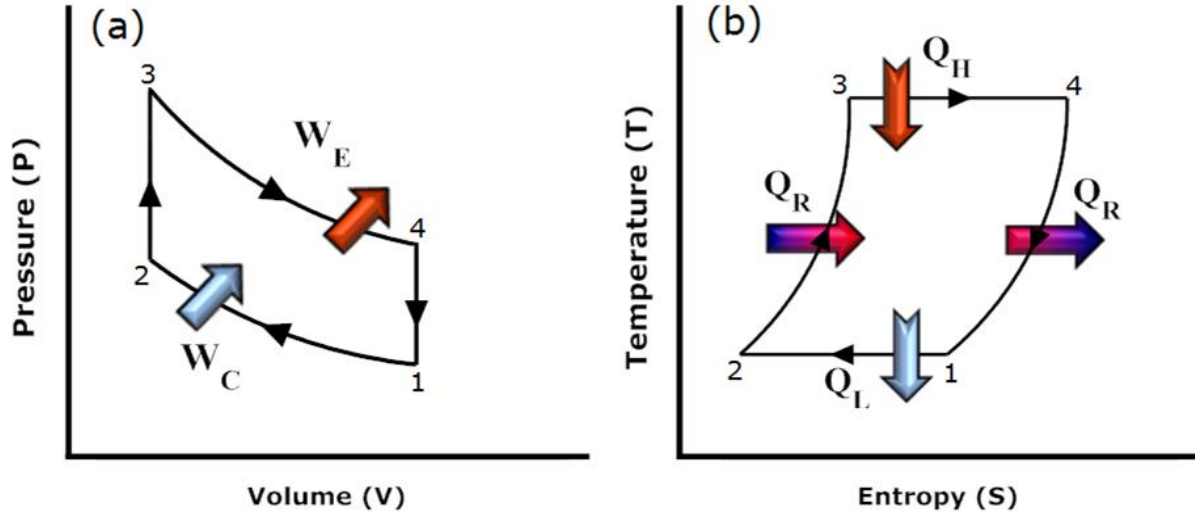


Figure 2-1: (a) Ideal P-V Diagram (b) Ideal T-s Diagram

2.2 Stirling Engine Configurations

There are three basic Stirling engine design configurations: the Alpha-Stirling, the Beta-Stirling, and the Gamma-Stirling. The basic working principle of the three types of engine is the same. The main difference between them is how the internal spaces are linked and their use of piston or displacer mechanisms. A more complete specification of Stirling engine mechanical configuration arrangements is provided by Thombare and Verma [17] and by W. Stine [18]. Here only the details regarding the distinctive spaces (expansion space, heater, regenerator, cooler, compression space) inside the internal volume of the Stirling engine is discussed. Typically Stirling engine designs include some type of regenerator, but some do not have an evident regenerator because they make use of the high surface area of the displacer. This is the case for the Beta and Gamma configurations.

In the Alpha Stirling two separate pistons are used for the compression and the expansion. Each has a separate cylinder space which is connected in series with a cooler, regenerator and heater [17]. The compression piston is located at the cold end, while the expansion piston is located at the hot end as shown in Figure 2-2. As the cycle progresses,

the working gas is displaced between the five different spaces of the internal volume. To model the Alpha configuration analytically, typically the compression space, cooler, regenerator, heater and expansion spaces are divided into individual control volumes. The Alpha Stirling engine typically has the highest specific work output [2, 17], for this reason it is attractive for automotive [17] and CSP applications [19]. Another advantage of the Alpha Stirling engine is its mechanical simplicity compared to the other configurations. But it has two major disadvantages; one is that it needs special sliding seals to contain the working gas. The other disadvantage is more difficult to solve because it involves reliability and durability problems of the piston seals that arise as a result of the high temperatures in the hot expansion space [2].

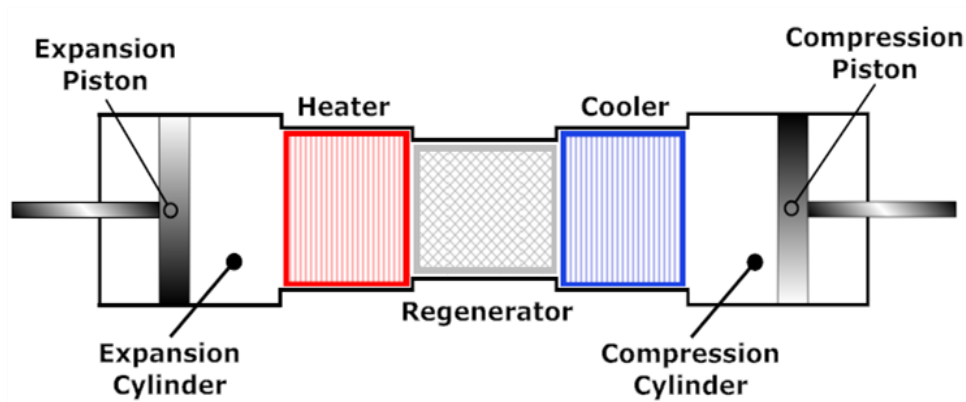


Figure 2-2: Alpha-Stirling

For the Beta Stirling engine configuration (Fig. 2-3) only one piston is used for both the compression and the expansion, and it is called the power piston. A displacer is used to drive the working gas from the cold side to the hot side. The displacer should transport the working gas close to constant volume [2]. In addition the displacer piston should be loose fitted, although it can be mounted to the same shaft as the power piston [2, 17]. The divisions of the internal volume spaces become more complicated in this design. The reason is that there is only one cylinder that is shared by the power piston and gas displacer. Thus, the definition of boundaries across the cylinder volume becomes less apparent than for the Alpha configuration [20]. This makes modeling of the Beta Stirling engine more complex and less flexible. The advantage of this engine is that the hot side is contained within the displacer side, and no seals are required on the displacer [2]. The Beta type

configuration with a slider-crank mechanism has been studied thoroughly (analytically and experimentally) by Karabulut et al. [21-23].

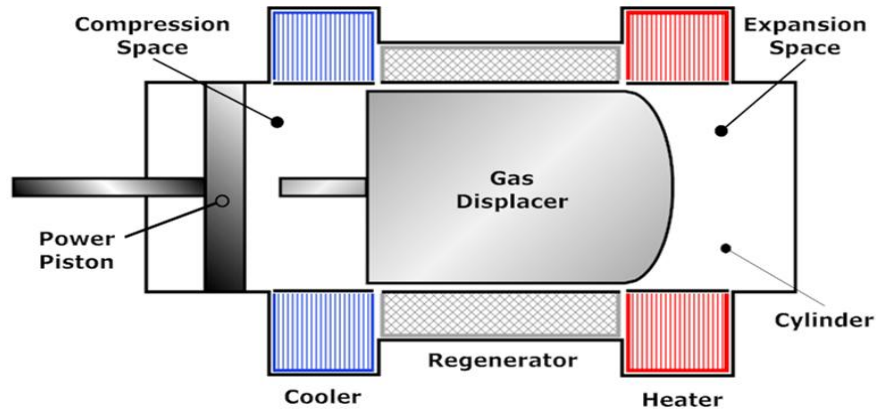


Figure 2-3: Beta-Stirling

A Gamma Stirling engine configuration is similar to the Beta Stirling configuration in that it has a displacer and a power piston. The difference is that the displacer and piston are mounted in separate cylinders [17], as seen in Fig 2-4. This model allows for a more convenient separation between the heat exchangers associated with the displacer cylinder and the power piston cylinder [24]. Since the Beta configuration has only one cylinder, both heat rejection and heat addition has to occur through the same cylinder. This configuration has the same advantages of the Beta Stirling but produces a lower compression ratio because of the larger dead space volume associated with the heat exchangers [24]. Most applications that use Gamma configurations operate at a low temperature difference between the low and high temperature reservoirs, thus requiring large heat exchangers. Because of the low temperature differential (LTD) that Gamma Stirling engines operate on, these engines are also classified as LTD Stirling engines [25-27].

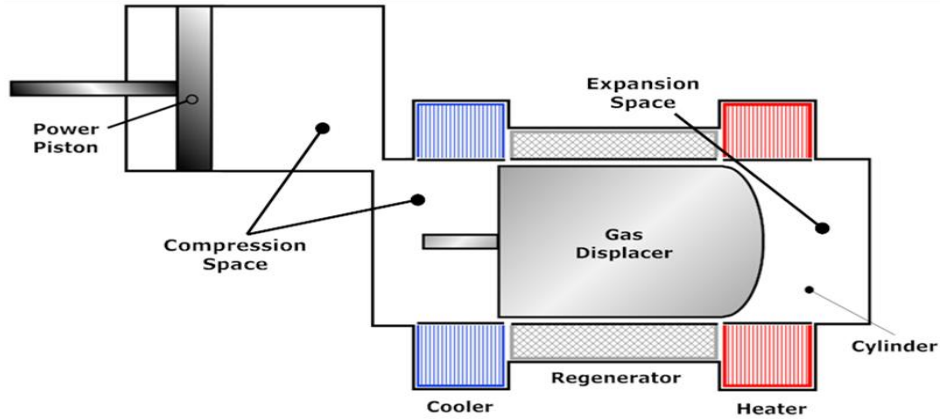


Figure 2-4: Gamma-Stirling

Many real practical Stirling machines have variations of the three basic configurations implemented in their design. Fraser [19] describes the Rinia-Siemens arrangement as a configuration that uses both the front and back face of the pistons (double-acting piston) connected to each other as seen in Figure 2-5. Fraser also states that the Rinia-Siemens arrangement significantly improves the engine efficiency compared to the common Alpha configuration.

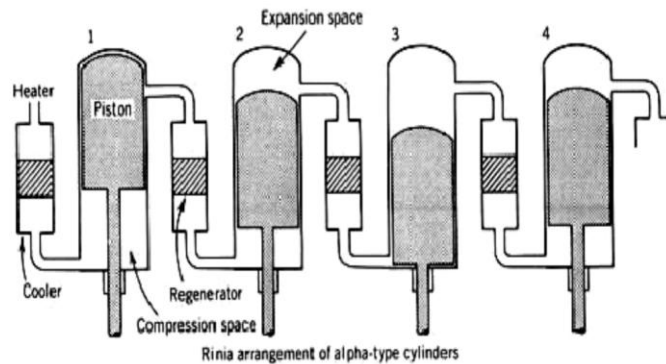


Figure 2-5: Rinia-Siemens engine configuration (Fraser, [2008])

A radical variation of the Beta configuration was devised by William Beale, the free-piston Stirling engine (Fig. 2-6), in which all the mechanical linkages of the power piston and the displacer are eliminated [8]. The movement of the displacer is caused by the variation of gas pressure inside the cylinder while the power piston movement is controlled using a gas spring [4]. The power is extracted from the engine by attaching a magnet to the piston which generates power through a linear alternator as it moves back and forth. Since the engine has only two moving parts (power piston and displacer) low cost is achievable due to its mechanical simplicity, low maintenance, reliability and durability [8].

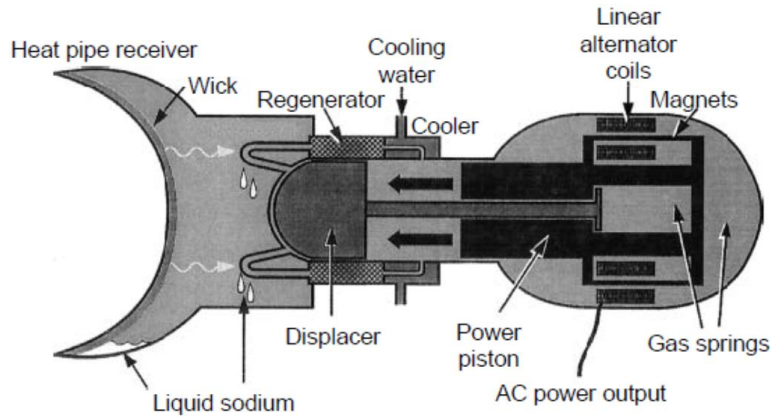


Figure 2-6: Beale free-piston engine configuration (Stine, [2007])

An interesting offshoot of the Gamma Stirling engine was developed for an underwater propulsion vehicle [28]. The design consists of two parallel displacers (having each an individual heater) connected to a double acting Bingham piston, as illustrated in Figure 2-7.

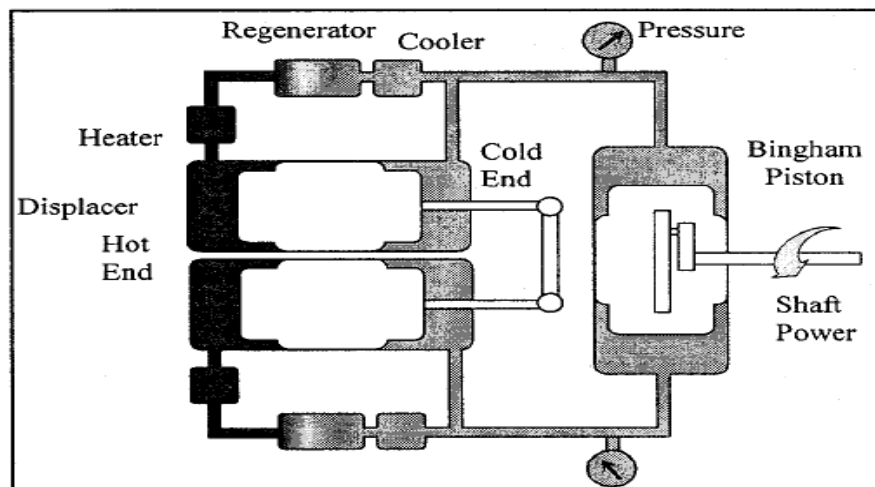


Figure 2-7: Double acting Bingham engine configuration (Reader et al., [1998])

2.3 Stirling Engine Analysis Methods

There are various design methods and analysis approaches for Stirling engines found in the literature. These are typically classified according to the level of complexity in the model assumptions. All of them one way or another attempt to describe the processes occurring in the cycle so that proper analysis can be performed in the design. Figure 2-8 shows how the individual processes for the basic components in a Stirling engine are linked as suggested by Martini [29, 30]. Thus, appropriate mathematical modeling should attempt to correctly describe the processes illustrated in the Flow Diagram shown in Figure 2-8.

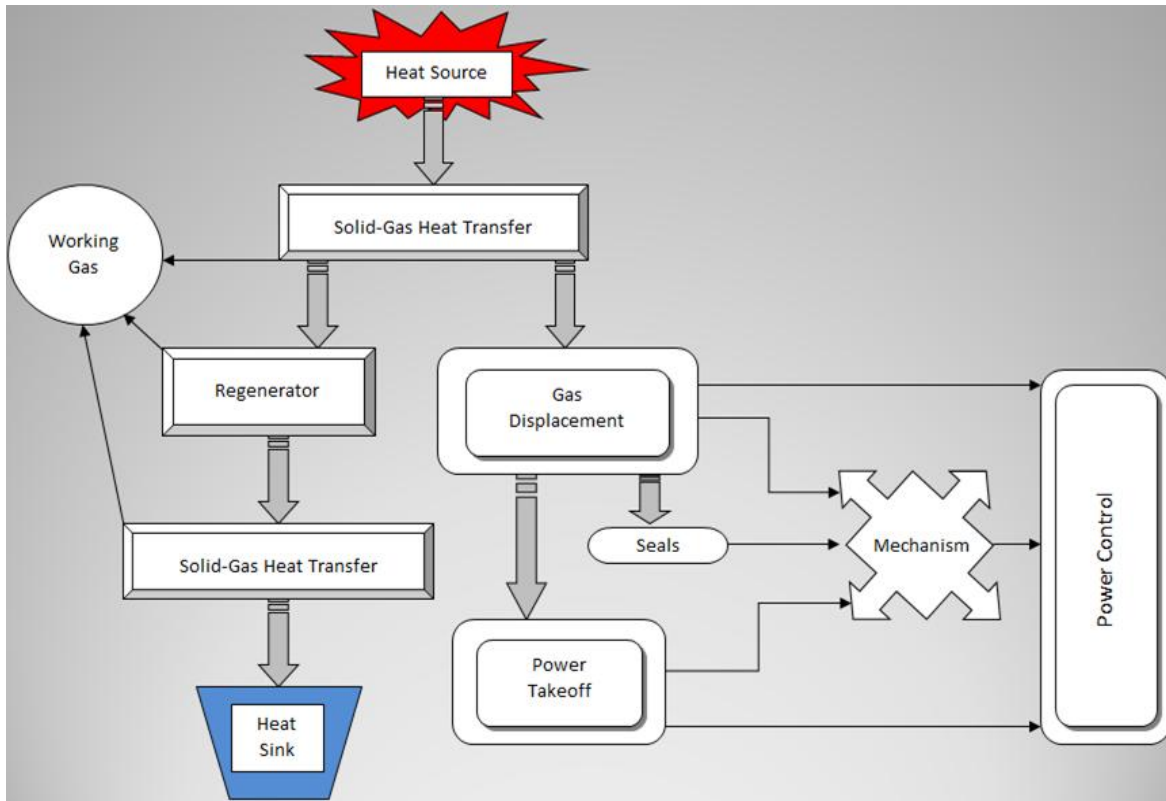


Figure 2-8: Design Block Diagram (Martini, [1983])

Chen and Griffin [31] classified and described the various mathematical models into four major categories based on the degree of sophistication applied in the analysis techniques. Martini [29] has also published a full technical report which describes and categorizes the mathematical methods in a similar manner. The mathematical model categories described by these investigators is listed as:

- (1) First Order Methods (approximate)
- (2) Second Order Methods (decoupled)
- (3) Third Order Methods (nodal)
- (4) Method of Characteristics

However, current Stirling engine literature describes a new classification that uses today's progress on Computational Fluid Dynamics (CFD) for Stirling engine analysis. Mathematical models that use CFD techniques are classified as Fourth Order methods [32].

In First Order methods, analytical models can be used for rough estimates in evaluating the Stirling engine performance. Calculations of net output work and engine efficiency may start using the Ideal cycle analysis in which no losses are considered. However, practical

engine considerations are commonly used by investigators in order to obtain useful results. The approaches either apply correction factors that have been determined experimentally (Schmidt or Beale Number), or apply simple and acceptable loss considerations in the mathematical expressions, approximate relationships between system parameters and idealized results can be established [31].

Analysis using Second Order methods use numerical procedures to solve a set of ordinary differential equations derived from conservation laws and the mechanism kinematics. Second Order methods are found to be useful for simplistic engine design optimization [29-31]. The reason is that although Second Order methods also begin with simplified models (e.g. Isothermal, Adiabatic) the individual loss mechanisms are identified and quantified in a more realistic manner and then subtracted from the Idealized performance parameters. Loss terms can be divided into two categories [29-30, 33]:

I. Power Losses:

1. Mechanical frictional losses
2. Gas leakage through imperfect seals
3. Pressure drop in the regenerator and heat exchangers
4. Hysteresis losses in compression and expansion cylinders

II. Heat Losses:

1. Wall heat conduction
2. Gas-solid heat transfer
3. Temperature swing (oscillation) in regenerator
4. Imperfect regeneration and thermal lag
5. Shuttle loss (heat conduction in piston or displacer)

It is assumed that all of the energy losses are independent of one another (decoupled). For the Second Order method, the net work output rate is equal to the Ideal net power output minus the power losses, the heat input is the Ideal heat input plus the heat losses, and finally the net cycle efficiency is the 2nd Order net output work divided by the 2nd Order net heat input [29, 30]. Chen and Griffin [31] also sub-divide the 2nd Order category according to the following simplified cycle analysis used in the variable volume working spaces: isothermal, adiabatic and semi-adiabatic processes. Snyman et al. [20] tested the Adiabatic and SIMPLE models developed by Urieli [4] for the Beta type engine developed by

Heinrici [20]. A prototype of the Beta Stirling engine was constructed and tested experimentally. Results between numerical predictions and experiments were in fairly good agreement, when the loss mechanisms are incorporated into the analysis.

The premise of Third Order mathematical modeling is that the different processes, in which the loss mechanisms are occurring, do in fact interact and considerably affect each other. Therefore, Third Order design methods attempt to compute the complex processes occurring in a Stirling engine without decoupling the energy losses from the cycle analysis calculations. Discretization techniques are required for numerical calculation and solution of the problem. The basic procedure is to divide the engine internal volume into discrete control volumes, then the equation of state plus the differential equations of conservation of mass, momentum and energy are applied to each control volume, and finally a system of ordinary differential equations is solved by a numerical method. A recent study on the performance characteristics of a Beta Stirling engine was done in 2006 by implementing the finite difference approach with forward differentiation [23]. The engine was modeled by dividing the internal volume in 103 cells and the equations for the kinematic relations were shown. However, it is not clear how the losses were incorporated in the analysis. An important result shown in this study is how the heating and cooling load is raised drastically as the working gas mass is increased, as a result, an optimal mass for the working fluid exists in a real engine. Third Order analysis is more rigorous, therefore, requiring relatively larger computational resources than the Second and First Order methods. However, with present computers, solutions can be achieved in significantly short times. More exploration on previous implementations of Third order methods is required to understand if results are significantly more accurate than 2nd Order methods [34].

The final method discussed here is the Method of Characteristic, which is less common in Stirling engine analysis [31]. Only a few investigators have developed their analytical studies using this approach. In mathematics, the method of characteristics is applied to a system of nonlinear partial differential equations so the system of equations is transformed into a system of ordinary differential equations which can be solved as an initial value problem. This transformation is valid only along certain curves of the domain, which are called the characteristic curves of the equation. This mathematical approach is commonly

used in gas dynamics where the resulting partial differential equations are shown to be of the hyperbolic type [35] and discontinuous wave propagation is present [34]. For unsteady one dimensional flow, the characteristic curves are found in the position-time (x, t) plane where time and position partial derivatives are discontinuous. After the conservation laws are expressed as the total differential of fluid properties, a matrix system is obtained in which the fluid properties are the dependent variables. Then, the solution of the characteristic curves is obtained by setting the coefficient matrix to zero [31]. Researchers in this area, claim that the discontinuous nature from the heat exchangers and the oscillatory wave motion of the gas makes this method more appropriate for Stirling engine analysis. Chen and Griffin have stated that this method has been successfully used by investigators such as Organ [3] and Larson [35] in their Stirling engine models.

Recently, new investigations have been performed using CFD in Stirling engine analysis. This development is now considered as another category (Fourth Order method) of Stirling engine analysis methods in the present literature. The name, Fourth Order methods, is perfectly suited for the category since it follows Third order methods chronologically and also has an increased complexity of the formulation, since it involves the solution of the Navier Stokes equations in 2D or 3D space with dynamic modeling. Since this approach is relatively new in the field of Stirling engine analysis only a few articles and reports are available. Dyson et al. [32, 33] gives a comprehensive overview on Stirling computational methods and makes the case for the need of fourth order methods. Turbulence modeling, transitional effects and the multidimensional characteristics of the velocity, temperature and pressure fields especially in intermediate zones where components are connected cannot be properly described with Third or lower order methods of analysis. Dyson et al. [32, 33] provided simulation results for a dual opposed free Stirling convertor (a device contemplated for NASA space missions using nuclear thermal energy). A project that performed CFD simulations on a Stirling cryocooler using Fluent commercial software was performed by Sahu [36]. The modeling process is presented in detail and temperature contours with velocity vectors are shown in the results. In addition, cyclic temperature variation of the cooler and cyclic pressure in the compression space is shown to have a sinusoidal behavior as expected for a crank shaft mechanism. Fourth Order methods assure

a more detailed and comprehensive view of the physics involved in the actual fluid flow and heat transfer involved in Stirling engines. However, problems have been found in correctly modeling the regenerator and incorporating a dynamically deforming mesh with cyclic boundary conditions [32].

2.4 Case Study: The Ford-Philips 4-215 Stirling Engine

Engine parameters for the 1st and 2nd Order analyses in chapter 3 are defined according to the design of the Ford-Philips 4-215 engine. The Ford-Phillips 4-215 is a double acting (DA) swashplate driven engine (based on the Rinia- Siemens arrangement), developed by collaboration between Ford Motor Company and N.V. Phillips in early 1970's [13, 37]. The goal of the program was to investigate the capability of using Stirling engines in automotive applications [37]. The idea was to design, manufacture and test a Stirling engine for a Ford Torino. The final product was a 127 kW (170 hp) power rated engine, running at speeds of 600-4500 RPM (Torino transmission was unchanged) without requiring major modification to the chassis [13, 37]. Phillips decision to use a DA swashplate design was based on the previous Philips 4-65 experimental configuration that delivered high specific power and compactness. The 4-65 was the first DA swashplate experimental engine developed by Phillips and test data showed excellent improvements in comparison with contemporary Stirling technology at the time [13]. A photo of the actual Ford-Philips 4-215 engine is shown in Fig. 2-9 (a) and the corresponding engine cross-section in Fig. 2-9 (b).

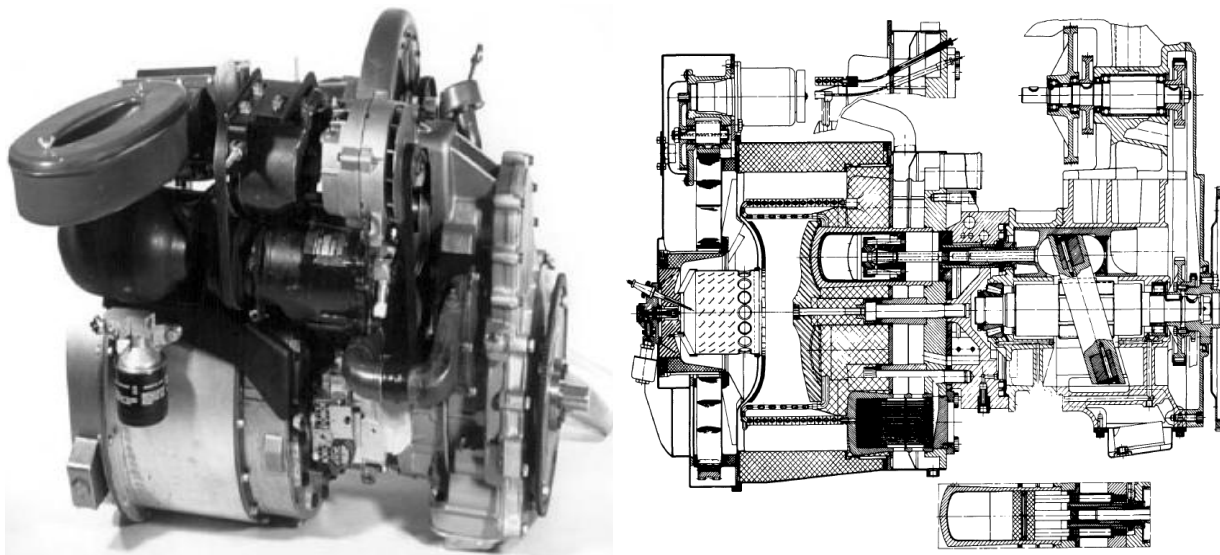


Figure 2-9: (a) Ford-Philips 4-215 Engine (Organ, [2001]) (b) Ford-Philips 4-215 Engine Cross-Section (Van Giessel et al., [1977])

2.4.1 Piston and Cylinders

The general engine configuration and operational parameters are displayed in Table 2-1. Four cylinders are used in the Ford-Philips 4-215 engine design, expansion and compression spaces are divided by the pistons. Each piston in the DA swashplate machine does expansion work on the hot side of the cylinder and compression work on the cold side of the cylinder. In other words the pistons generate power at one cylinder while displacing the gas in the adjacent cylinder. The total internal engine volume is 2680 cc, of which 870.6 cc is used for swept volume, 214.2 is for cylinder clearance and the rest is for heat exchange. Note that the swept volume and clearance volume are the same for either expansion or compression space.

Table 2-1: [Ford-Philips 4-215 General Operating Parameters \(Urieli, \[1984\]\)](#)

Parameter	Data
Working gas	Hydrogen (H ₂)
Gas mass	16.3×10 ⁻³ kg
Mean pressure	150 bar
Bore diameter	73 mm
Stroke length	53 mm
Number of cylinders	4
Total clearance volume	214.2 cc
Total swept volume	870.6 cc
Phase angle	90°
Heater temperature	1023 K
Cooler temperature	337 K

The material selected for the engine cylinder housing was the low-nickel carbon steel CRM-6D developed by Chrysler in 1963 [13]. This material in particular satisfies the following requirements: (1) chemically inert and impermeable to hydrogen at high temperatures and pressures; (2) structurally stable at temperatures of 1023 K; (3) resistant to oxidation; (4) compatible with the brazing process of the engine head assembly. The cylinders are fabricated by precision investment casting, followed by machining of the internal surface [13, 37].

Materials and construction for the piston consist of a base made from chrome-nickel steel (which contains the clamp mechanism for securing the piston to the piston-rod) and a heat resistant hollow dome made of cast CRM-6D [13]. Rulon, a Teflon material reinforced with glass-fiber, is used for dry running of the piston rings [13, 37]. Due to the phase shift of 90° there are pressure fluctuations on the piston faces. This will cause undesirable effects on the pistons rings. This is avoided by using two piston rings in each piston and keeping the pressure between them at minimum cycle pressure [37]. To maintain wear resistance and high fatigue strength requirements, piston rods are made of nitride steel (BS 970), case hardened to 66 Rc. The 4-215 DA engine swashplate is made from nodular cast iron and has a slightly conical shape to establish a hydrodynamic oil film against the flat face of the sliders [37]. The swashplate has a 17° angle (angle between plate and the plane perpendicular to axis of rotation) and is screwed to the main shaft so that axial adjustment of the assembly can be made [13, 37]. Figure 2–10 shows the piston-swashplate system.

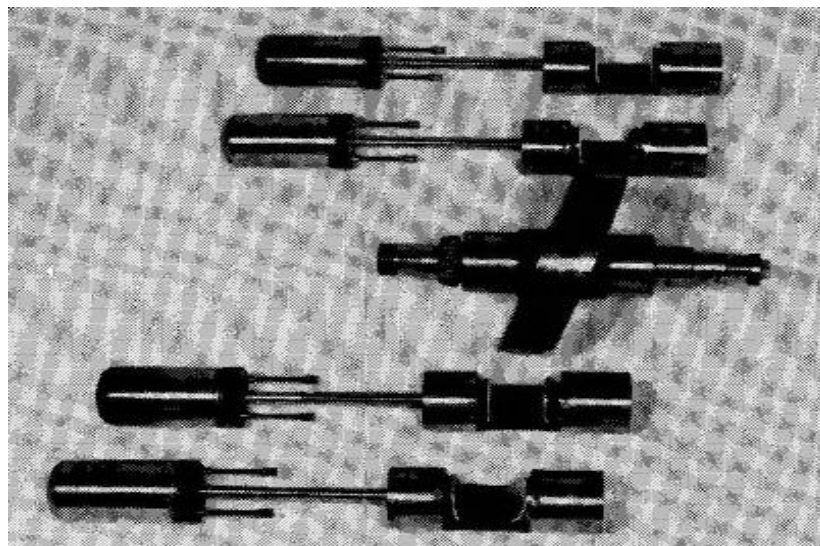


Figure 2–10: Piston-Swashplate Drive System (Van Giessel et al., [1977])

2.4.2 Heating System

External heat is provided by means of continuous ignition of fuel. The combustion process occurs on a simple combustion chamber assembly that is composed of a conical burner can, a fuel nozzle and an igniter. A 40mm ceramic disk rotating at 8 RPM is used as regenerative pre-heater in a heat recovery system. The regeneration from the pre-heater allows for approximately 45% of fuel economy [29]. Both a uniform flow pattern and

recirculation are achieved by the combination of a 48-blade swirler and the conical shape of the burner can [13]. In concept the Ford-Philips 4-215 burner functions similarly to those found in gas engines. However, the ignited gas-mix (or flue) is separate from the gas that does work on the engine. Therefore, the external heat of combustion must be transferred to the working gas (hydrogen) by means of a heat exchanger (heater).

The actual Ford-Philips 4-215 engine heater head arrangement and connection of heater tubes to the cylinder heads is shown in Figure 2–11. Since the four engine cylinders are grouped around a central axis, the heater tubes are clustered in a symmetric cylindrical cage to allow a single burner to serve all four cylinders [29] as observed in Fig. 2–11 (a). Each cylinder has a set of 22 heater tube, each tube having 4 mm in internal diameter and 462 mm in length. The heater parameters are summarized in Table 2–2. The helical configuration of the tubes makes the heater cage flexible so intermittent operation does not give rise to fatigue failure. Giessel et al. [37] point out that from experience rigid cages are avoided on Stirling engines, since the stiffness is a critical parameter in determining the life of the heater tubes because of the intermittent loads.

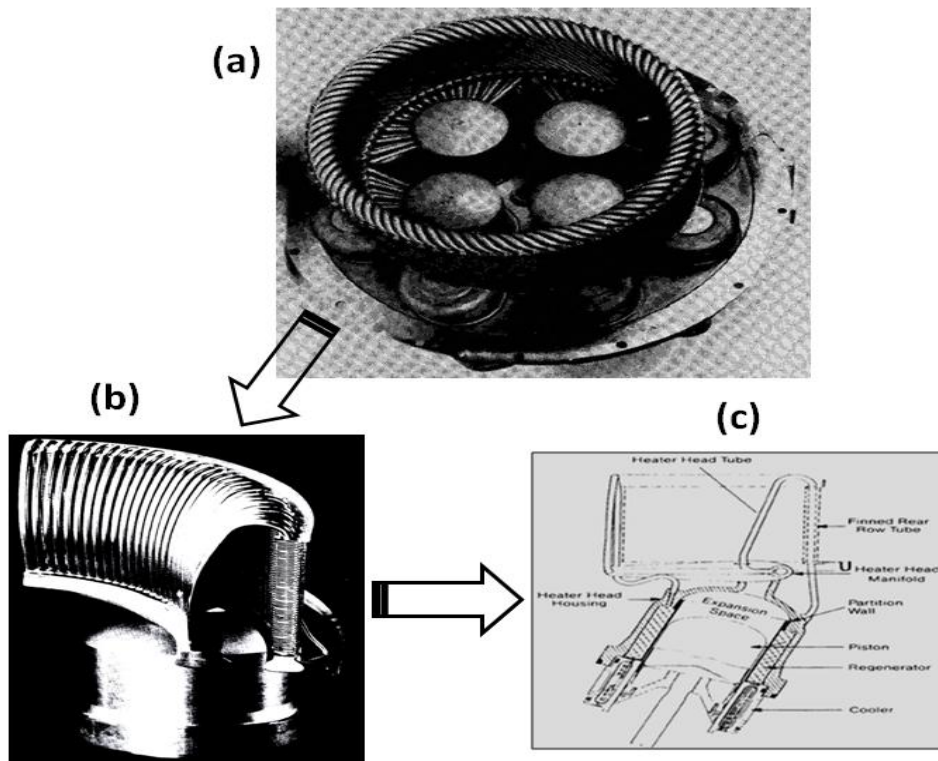


Figure 2–11: (a) Ford-Philips 4-215 Heater Head Design (Van Giessel et al., [1977]) (b) General View of Heater Tubes mounted in Cylinder (Nightingale, [1986]) (c) General Heater Cross-Section (Nightingale, [1986])

Table 2-2: Heater Specifications for Ford-Philips 4-215 Engine (Urieli, [1984])

Parameter	Data
Total volume	510.9 cc
No. of tubes per cylinder	22
Tube ID	4 mm
Tube length	462 mm
Free flow area per tube	12.7 mm ²
Wetted area per tube	58.1 cm ²
Heater temperature	1023 K

The heater must satisfy similar requirements to the ones mentioned for the cylinder housings. However, the material used for the heater must withstand temperatures approaching 1073 K [13]. For this reason the heater tubing is made from a solid-solution-hardened alloy steel designated N-155 or Multimet. The second row of tube (or second pass) is covered in fins made from AISI 310 stainless steel [13, 38].

2.4.3 Regenerator and Cooler

Two regenerator-cooler units per cylinder are used in the Ford-Philips 4-215 engine configuration. The regenerator is a porous device used for heat storage at hot side of the cycle, while the cooler is a heat exchanger used for rejecting heat at the cold side of the cycle [29]. The regenerator cooling units of the actual engine are shown in Fig. 2-12 (a).

The regenerators are made from layers of standard disk wire gauzes stacked tightly together. Gauze material has to be free of oxidation in order to maintain the high effectiveness during the life of the engine. General regenerator design specs can be found on Table 2-3. The regenerator casings uses the same CRM-6D material that the engine cylinders, as indicated by Hargreaves (1991) [13]. It is believed that the regenerator matrix material is a type of stainless steel alloy compatible for brazing with CRM-6D; however, the available sources do not specify the material used for the regenerator gauzes.

Cooler tubes are constructed of stainless steel, measuring 1.8 mm outer diameter and 0.45 mm in wall thickness. The tubes are brazed into end plates of 3.0 mm thickness [13, 37]. Each cooler unit consists of 371 tubes, as seen in Fig 2-12 the regenerator outer casing

extends to the cooler. Basically the external cooler configuration is a two pass Shell & Tube heat exchanger (Fig. 2–12 (d)). Coolant water flows at 337 K across the cooler tubes with a lateral partition to provide flow separation between the first and second passes [29]. The important cooler specifications are given in Table 2–4.

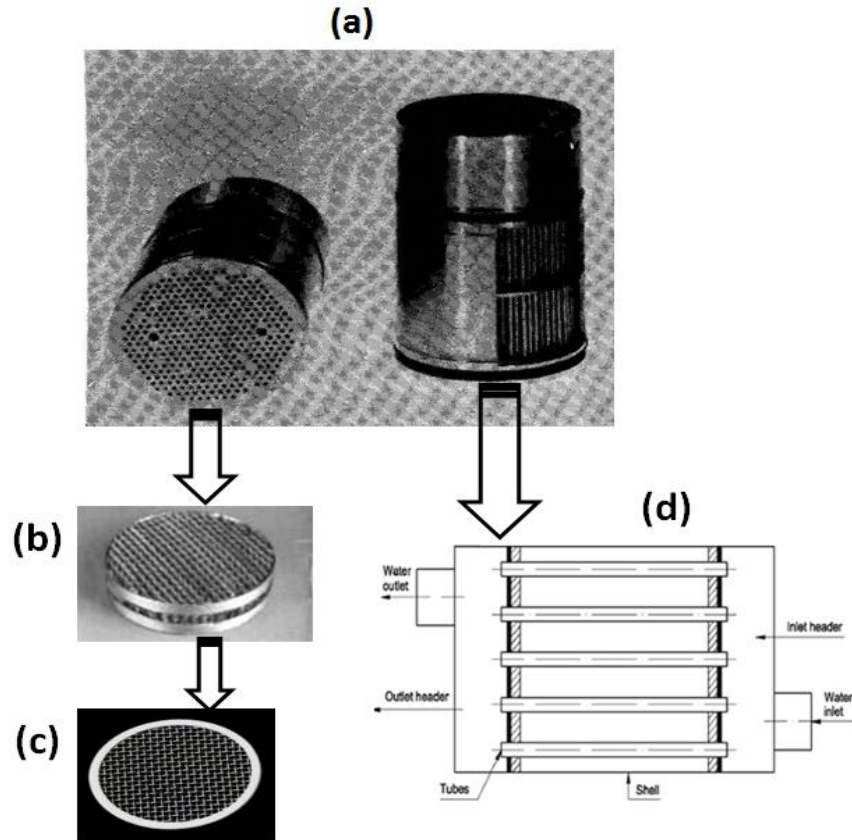


Figure 2–12: (a) Ford-Philips 4-215 Regenerator-Cooler Unit (Van Giessel et al., [1977]) (b) General Regenerator Gauze Stack (c) General Single Wire Gauze (d) General Cooler Shell & Tube Arrangement

Table 2–3: Regenerator Specifications for Ford-Philips 4-215 Engine (Urieli, [1984])

Parameter	Data
Total volume	705.8 cc
No. of regenerators units per cylinder	2
Regenerator housing diameter	73 mm
Regenerator length	34 mm
Matrix wire diameter	36 μm
Screen porosity	0.62
Hydraulic diameter	58.7 μm
Mesh size (#Screens)	200

Table 2-4: Cooler Specifications for Ford-Philips 4-215 Engine (Urieli, [1984])

Parameter	Data
Total volume	164.3 cc
No. of cooler units per cylinder	2
No. of tubes per cooler	371
Tube ID	0.9 mm
Tube length	87 mm
Free flow area per tube	0.64 mm ²
Wetted area per tube	2.5 cm ²
Cooler temperature	337 K

2.5 Previous Work

It has been observed that the sinusoidal motion does not follow the intended Stirling cycle processes appropriately. Previous work has been done in order to obtain a motion that approximates the Ideal processes more closely. Here, two different studies of alternative mechanisms that deviate from the typical sinusoidal volume variations are we described. Both studies found in the literature, are based on the assumption that if the volume variations followed the Ideal variation, which is linear, the PV diagram should result in a larger area and therefore higher efficiency. However, no comprehensive thermal analysis was done in these studies to back up their claims.

Dehelean et al. [38-40], studied the implementation of a slider/bar mechanism to dwell (or damp) the compression piston during the expansion phase of the Alpha Stirling engine. The studies are viewed from a mechanical analysis perspective. In Fig. 2-13 (a), the general schematic of the four bar mechanism is displayed. The authors state that the mechanism results in a dwell of the compression piston during the expansion process, as shown in Fig. 2-13 (b) for crank angles between 200° and 300°. Intuitively, the dwell of the compression piston suggests that the area of the P- \forall diagram should increase. Since the compression volume is kept close to the minimum, the expansion process occurs mostly in the expansion cylinder, therefore, improving the efficiency; although no thermodynamic results are presented, qualitatively this is true from the perspective of the Ideal Stirling cycle theory.

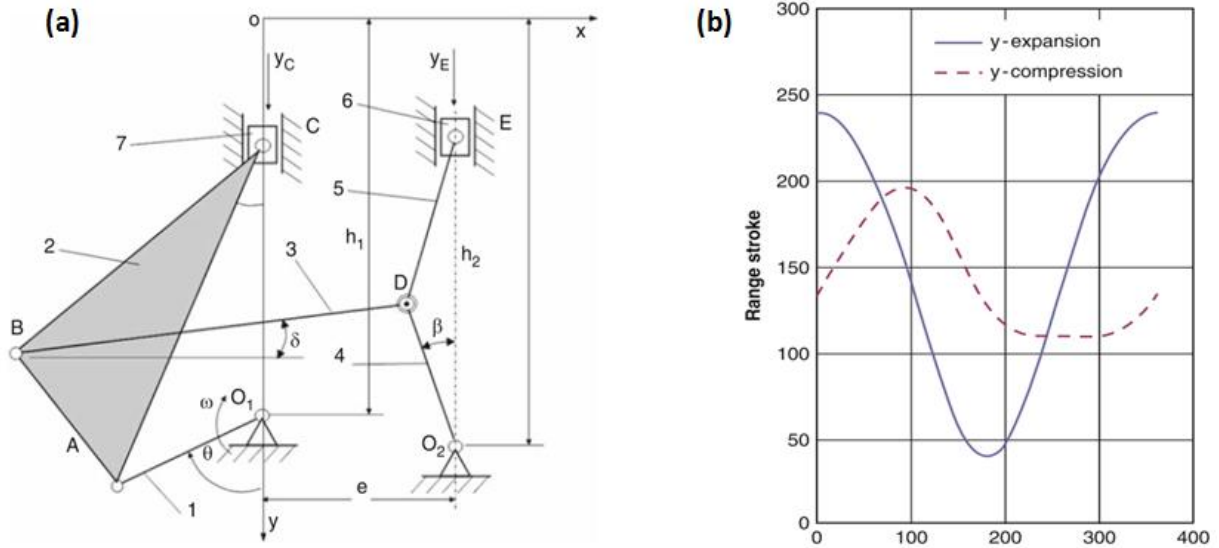


Figure 2-13: (a) Four Bar Dwell Mechanism (b) Resulting Piston Dwell Displacement (Dehelean and Coupe, [2009])

The second mechanism alternative (for Alpha Stirling Engines) proposed in the literature comes from Fang et al. [41]. In this study, the authors evaluate the potential for an elliptic drive mechanism to follow the linear motion of the Ideal Stirling cycle. Different drive schemes were compared using a simple computer model of a Rider-type engine. As mentioned earlier, the sinusoidal volume variations are inadequate in terms of the Ideal process, since they deviate largely from the Ideal motion. The work done by Fang et al., showed that a motion derived from an elliptical drive results in a closer approximation to the Ideal motion (Fig. 2-14 (a)). The general design of the drive capable of this elliptical volume variation is shown in Fig. 2-14 (b). It is stated [41] that the motion design can be made possible by the use of elliptic gears. More information can be found regarding the elliptical gear design in US patent #5557934, granted on Sept 24, 1996 [42], which is related to Fang’s work. The $P-v$ diagram presented by Fang et al. [41] that resulted from the elliptic drive motion seems to be promising result. Nevertheless, the Adiabatic analysis was used in the thermodynamic model and the only numerical result compared to the sinusoidal motion is the peak pressure, which resulted in a 16% increase for the elliptic drive.

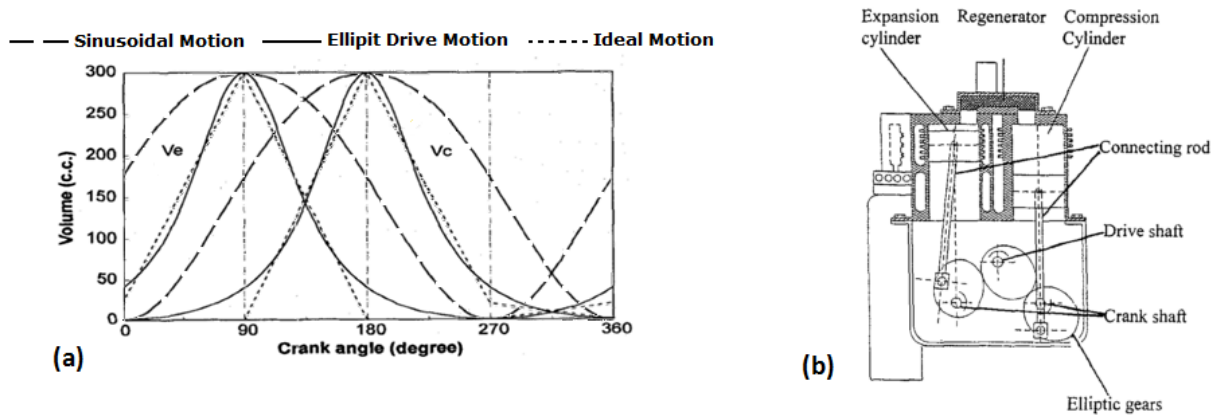


Figure 2-14: (a) Sinusoidal, Elliptic Drive, and Ideal Motions (b) Elliptical Drive General Design (Fang et al., [2009])

The present study will further expand on the work performed by Fang et al., by incorporating the power and thermal losses of the 2nd Order method and providing a comprehensive comparison between the sinusoidal and elliptic drive motions.

CHAPTER 3: STIRLING CYCLE ANALYSIS & STUDIES

3.1 Ideal Cycle Analysis

3.1.1 Ideal Stirling Cycle Example Problem

To start exploring the Ideal Stirling cycle, the example devised by Martini [29] is reviewed here and further developed. In Martini's example only hydrogen was used as the working gas and the problem is formulated on a mole basis. Here the problem is performed on a mass basis and considers air, helium and hydrogen as working gases. The following assumptions are made:

- The cold heat sink temperature is 300 K
- The hot temperature of the heat source is 900 K
- Minimum volume (un-swept volume) is 50 cm³
- Maximum volume (swept volume) is 100 cm³
- The starting pressure (minimum pressure) is 10 MPa

When applying the ideal gas equation of state to the four processes occurring in the Ideal Stirling Cycle (see Fig. 1-2 (a)) we find that the state variables for the cycle are a function of the starting pressure, the compression ratio, and the temperature ratio:

$$p_1 = p_{min} \quad (3.1)$$

$$p_2 = p_{min} \cdot r_c \quad (3.2)$$

$$p_3 = p_{min} \cdot r_c \cdot \tau \quad (3.3)$$

$$p_4 = p_{min} \cdot \tau \quad (3.4)$$

where

$$r_c = \frac{V_{max}}{V_{min}} ; \tau = \frac{T_H}{T_L}$$

are the compression volume ratio and operating temperature ratio, respectively. This implies that after the minimum cycle pressure has been established the Ideal cycle pressures p_2 , p_3 , and p_4 will be dependent on the volume and temperature ratios. Furthermore the path followed by the pressure and volume is independent of gas properties. With equations 3.1 to 3.4 and the assumed data for the hypothetical case given by Martini; air, helium and hydrogen P- \forall diagrams are interposed in Figure 3-1.

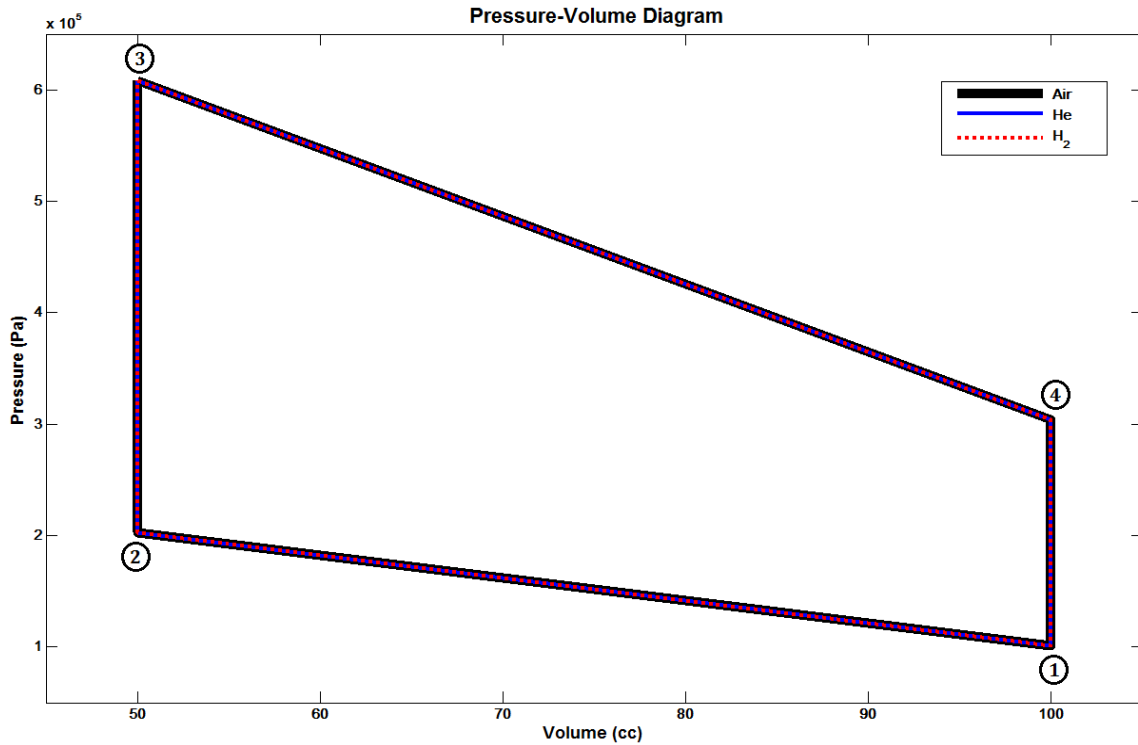


Figure 3-1: Ideal Cycle P-V Diagram for Gases at the Same Starting Pressure

Although the pressure relations established for the Ideal Stirling cycle will not depend on gas properties, the minimum pressure (also known as starting or charge pressure) will depend on the gas constant, the amount of mass, the cold sink temperature and the maximum volume. Therefore the equation of state will require higher mass quantities of helium and air for the starting pressures to be equal to the hydrogen minimum pressure, since both air and helium have lower gas constants than hydrogen. The ideal gas equation of state and equations 2.4 to 2.8 were used to determine the required gas mass and performance parameter values that are summarized in Table 3-1.

It is important to highlight that although the analysis for the Ideal cycle pressures, have a degree of independence from gas properties, the heat transfer from the regenerator to the working gas in fact does depend on the fluid properties. The regenerator, generally, is a matrix composed of metal wire gauzes stacked together to form an internal porous heat exchanger. Regeneration heat is the heat either supplied or received by the working gas in process 2-3 and 4-1, respectively. The results in Table 3-1 show that the regenerator heat for air and hydrogen is about the same, while the regenerator heat for helium is less. By means of a T-ΔS diagram this result can be better understood. As shown in Figure 3-2, the

change of the total entropy for the two isochoric processes is less for helium than that for air and hydrogen. Recalling Eq. 2.5 from Chapter 2, the basic representation of the isochoric heat exchange between the gas and the regenerator, is seen by the slope (mC_v) of processes 2-3 and 4-1 in Figure 3-2. Thus for comparison of the heat transfer needed (in the regenerator) for different gases, either the T- ΔS diagram or the constant volume heat capacity (mC_v) will reflect the amount of heat exchange in the heat regeneration process.

Table 3-1: Ideal Performance Summary for Different Gases at the Same Starting Pressure

Working Gas	Air	Helium	Hydrogen
Mass (kg)	0.0119	0.0016	0.0008
Heat Input (kJ)	2.0794	2.0794	2.0794
Net Work (kJ)	1.3863	1.3863	1.3863
Regenerator Heat (kJ)	5.5817	3.8615	5.2366
Thermal Efficiency (%)	66.7	66.7	66.7

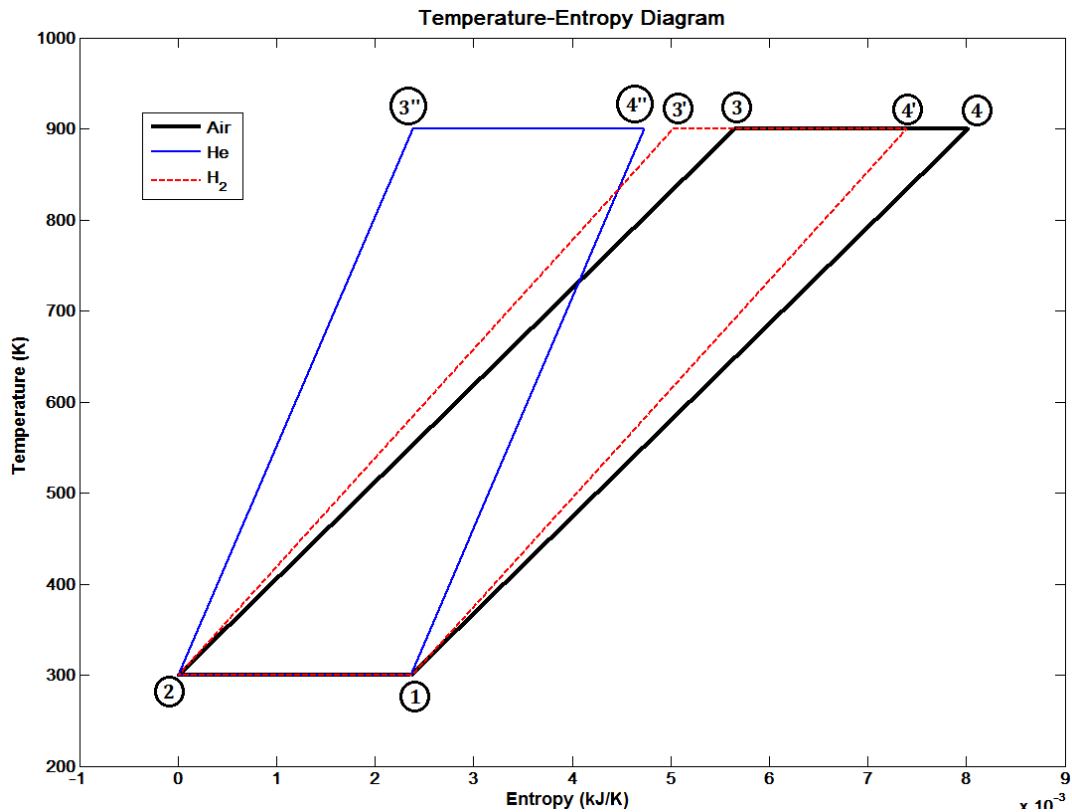


Figure 3-2: Ideal Cycle T- ΔS Diagram

To explore the effects of fixing the mass of the working gas instead of the initial cycle pressure, a mass of 0.0016 kg was selected for all gases. The new P- ∇ diagram is shown in Figure 3-3 and the results are summarized in Table 3-2. Two obvious observations can be

made from the results; one is that the starting (or charge) pressure is highest for hydrogen since it has the larger gas constant of the three gases and air has the lowest charge pressure since it has the lowest gas constant. The other observation is that the cycle mean pressure is affected in the same manner. Therefore the pressure at the following states increases proportionally due to the magnitude of the gas constant. The overall outcome is a greater area enclosing the cycle for hydrogen meaning it produces more net work for a same amount of mass than either helium or air.

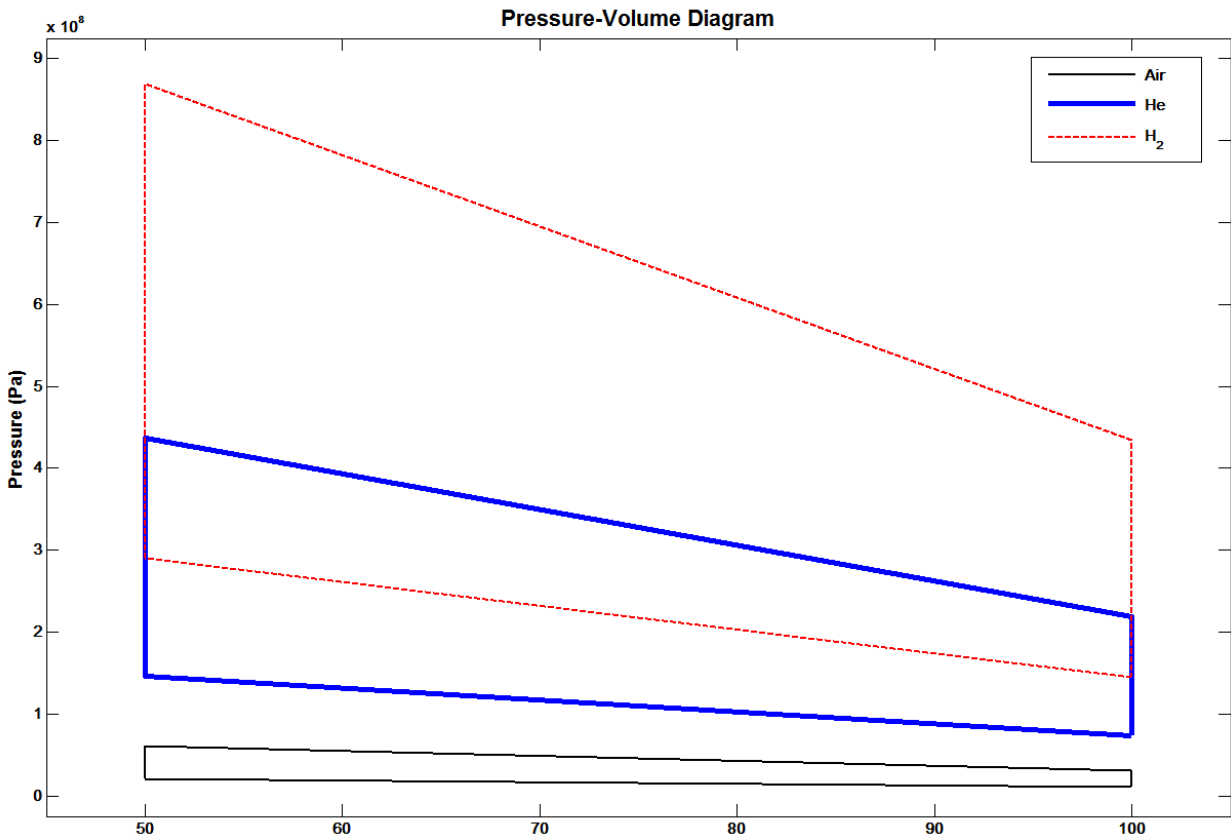


Figure 3-3: Ideal Cycle P-V Diagram for Gases with the Same Cycle Mass

Here as in the previous case a T-ΔS diagram is needed to better understand the Ideal heat transfer occurring in the regenerator. The large value for helium and hydrogen imply more per unit mass heat transfer required in the regenerator. Therefore, optimal regenerator designs may be required in Stirling engines that use hydrogen or helium, than for one using air. Also note that the cycle efficiency is still determined by the temperature ratio and even though hydrogen is capable of producing more work than air or helium, more heat input is also required.

Table 3–2: Ideal Performance Summary for Different Gases with the Same Mass

Working Gas	Air	Helium	Hydrogen
Mass (kg)	0.0016	0.0016	0.0016
Heat Input (kJ)	0.2802	2.0196	4.0192
Net Work (kJ)	0.1868	1.3464	2.6795
Regenerator Heat (kJ)	0.7520	3.7504	10.122
Thermal Efficiency (%)	66.7	66.7	66.7

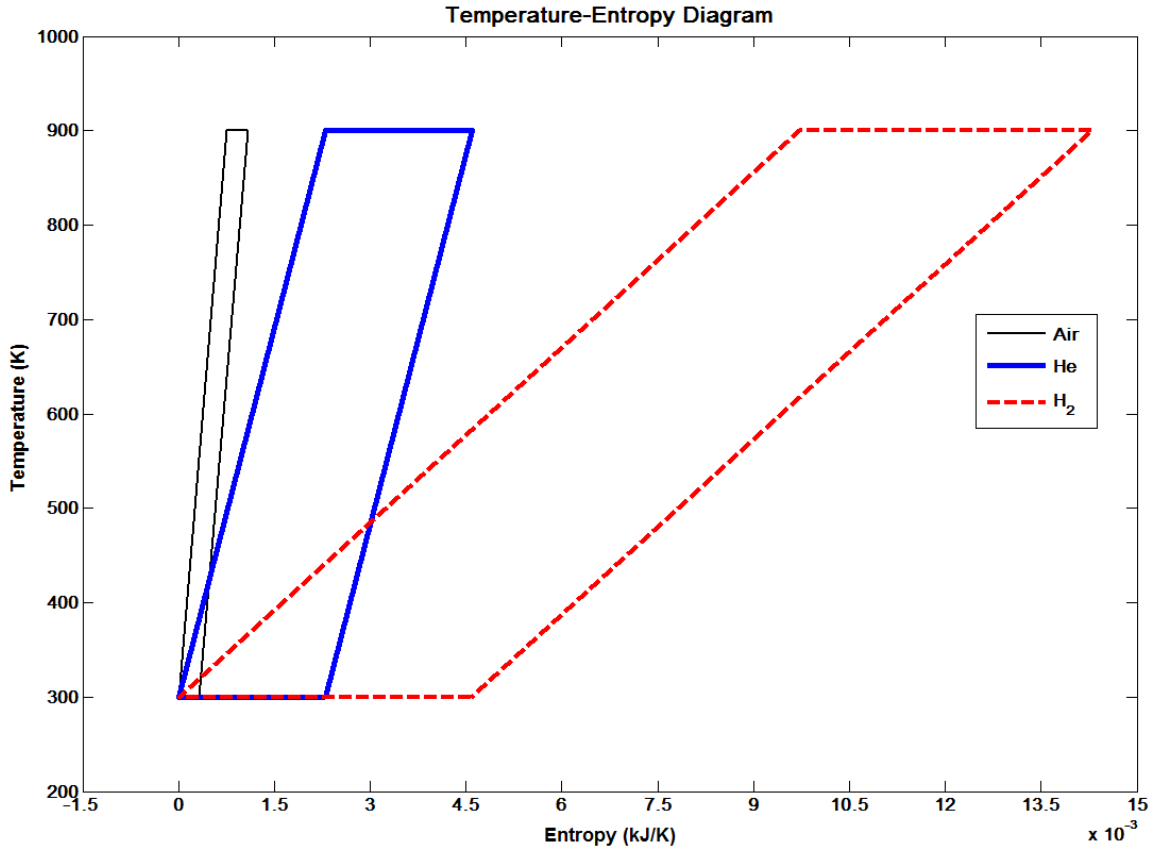


Figure 3–4: Ideal Cycle T-ΔS Diagram for Gases with the Same Mass

3.1.2 Preliminary Parametric Studies

The relations for regenerator heat, net output work and efficiency specified in Chapter 2 are presented here again to verify the effect of temperature ratio and compression volume ratio on cycle performance. The formulas are:

- Regeneration Heat transfer

$$Q_R = mC_V(T_H - T_C) = mC_VT_C(\tau - 1) \quad (3.5)$$

- Net work

$$W_{net} = W_E + W_C = mRT_C(\tau - 1)\ln(r_c) \quad (3.6)$$

- Cycle efficiency

$$\eta = \frac{W_{net}}{Q_H} = 1 - \frac{T_C}{T_H} = 1 - (1/\tau) \quad (3.7)$$

Using Martini's example as a base for the parametric analysis, Figure 3–5 to Figure 3–9 were generated. Figure 3–5 shows the linear dependence of the regenerator specific heat transfer required for the Ideal cycle as a function of the operating temperature ratio. From the graph it can be observed that the high slope for hydrogen corresponds to its large specific heat value, which is about 13 times greater than the specific heat of air. In the case of helium, its specific heat is only about 5 times larger than air.

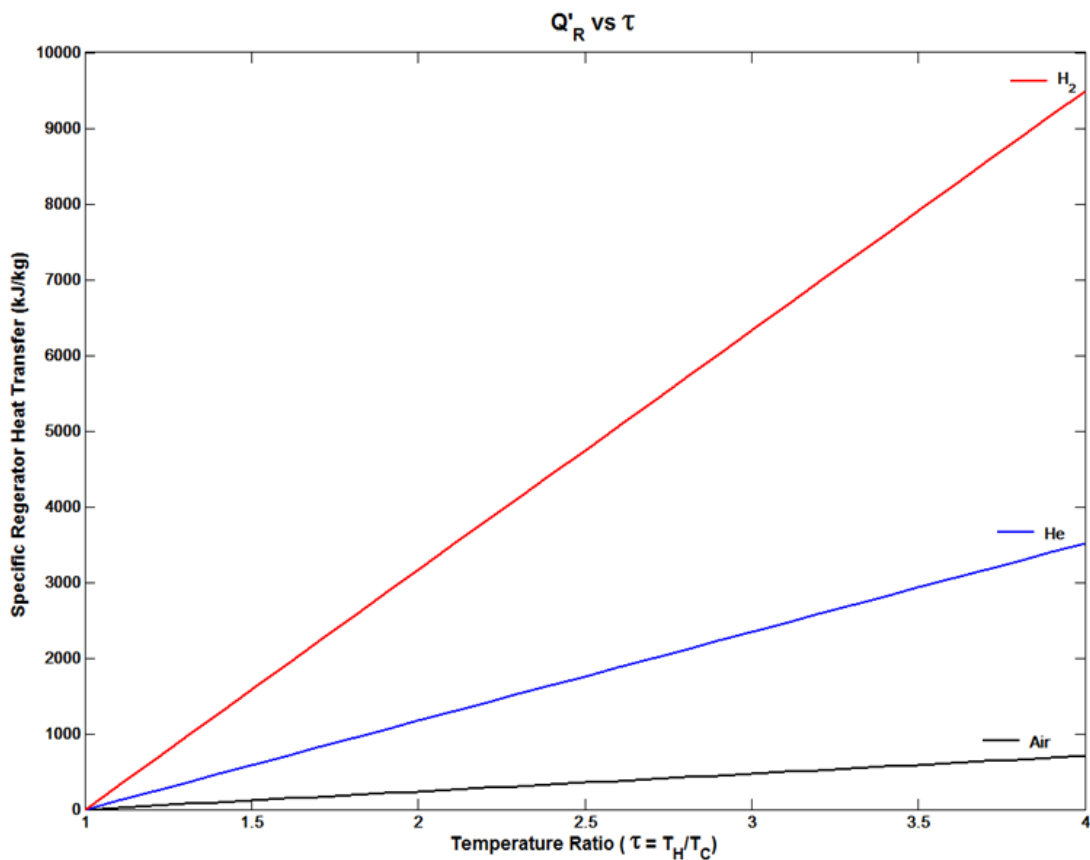


Figure 3–5: Regenerator Specific Heat Transfer as a Function of Temperature Ratio

The specific net work output does not only depend on temperature ratio and the fluid properties, but it also depends on the compression (or swept) volume ratio. Figure 3–6 illustrates the logarithmic dependence on the volume ratio. Curves were plotted for air, helium and hydrogen and considering the operating temperature ratio 900 K : 300 K given in Martini's example. The increased specific net work for higher compression volume ratios

for hydrogen is substantially larger than that of air, and helium also exhibits a considerable increase when comparing it to air.

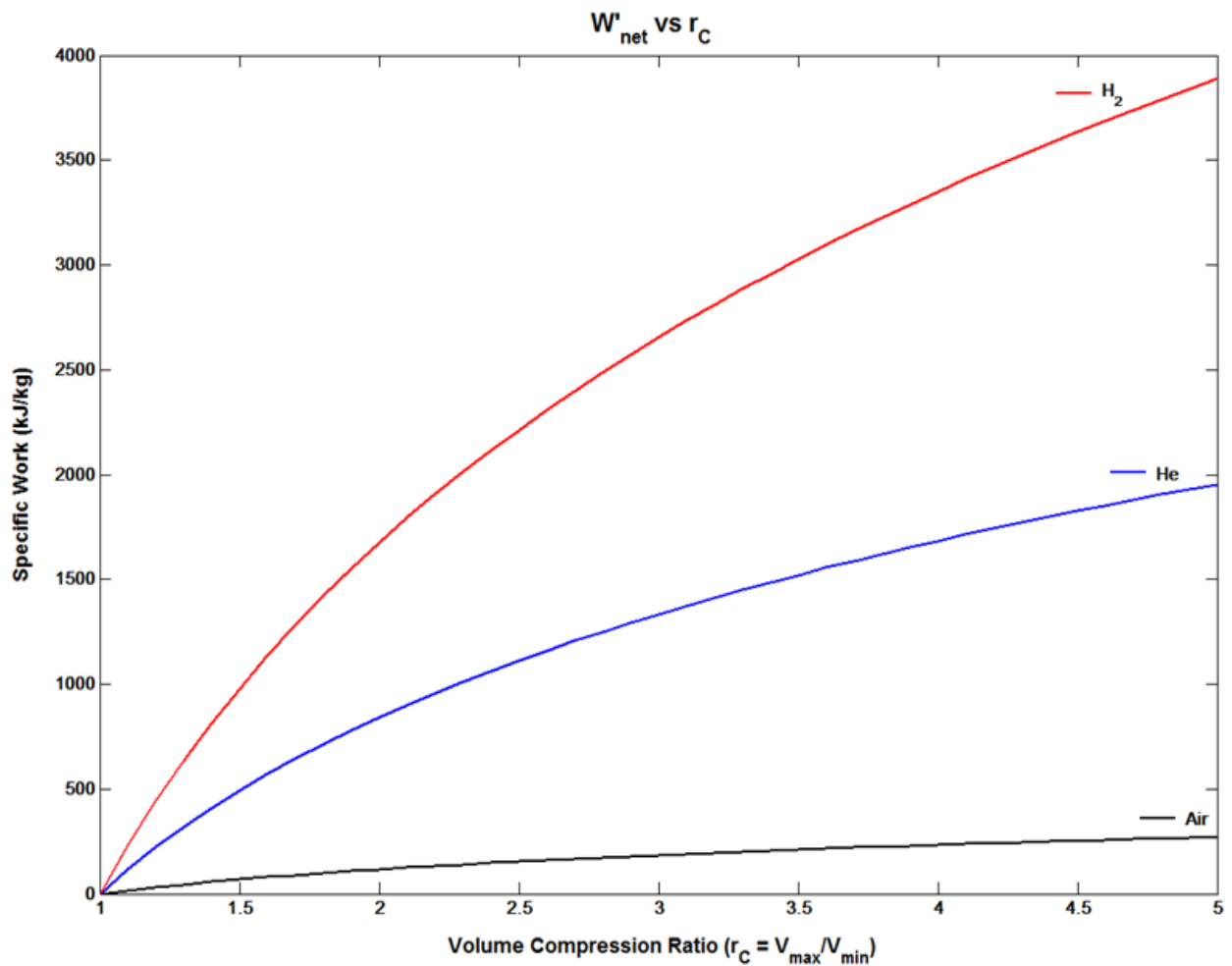


Figure 3-6: Specific Net Work as a Function of Compression Volume Ratio

In Figure 3-7 the specific net output work is plotted as a function of the operating temperature ratio for the value of volume ratio equal to 2, which is the one for Martini's example. The curves in Figure 3-7 are similar to those of Figure 3-5 (regenerator specific heat transfer). The difference here is that the high value of the hydrogen gas constant is what accounts for the large slope behavior, instead of the specific heat. Hydrogen has a gas constant 14 times larger than that of air, and the helium gas constant is about seven times larger. Figure 3-8 shows surface plots of the specific net work for air, helium and hydrogen, as functions of volume and temperature ratios. As expected, the net work output increases for both increasing compression volume and temperature ratios. Finally, cycle thermal efficiency is plotted against the temperature ratio in Figure 3-9. This is the same as the

Carnot thermal efficiency since the Ideal Stirling cycle yields the same equation for thermal efficiency.

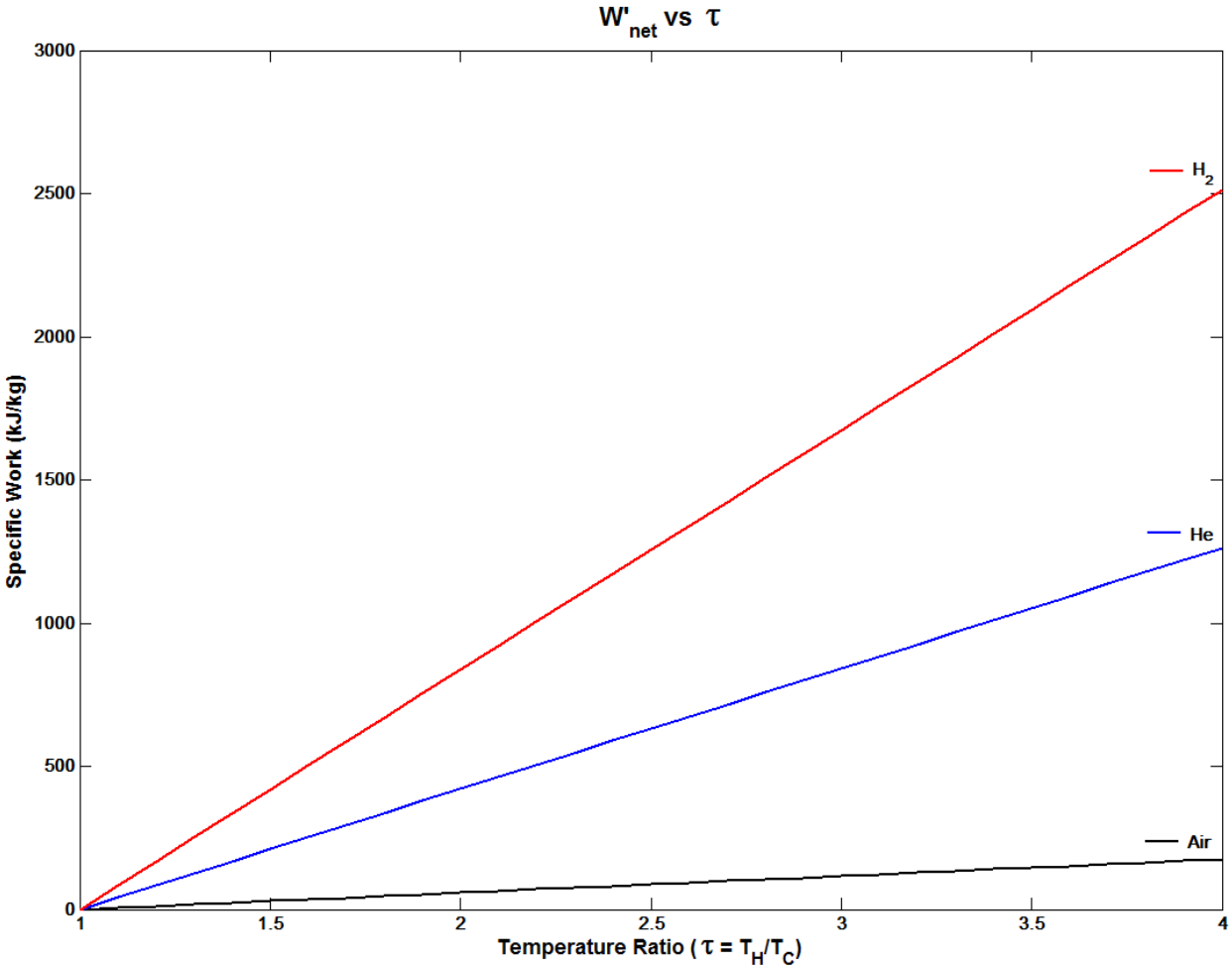


Figure 3-7: Specific Engine Work as a Function of Temperature Ratio

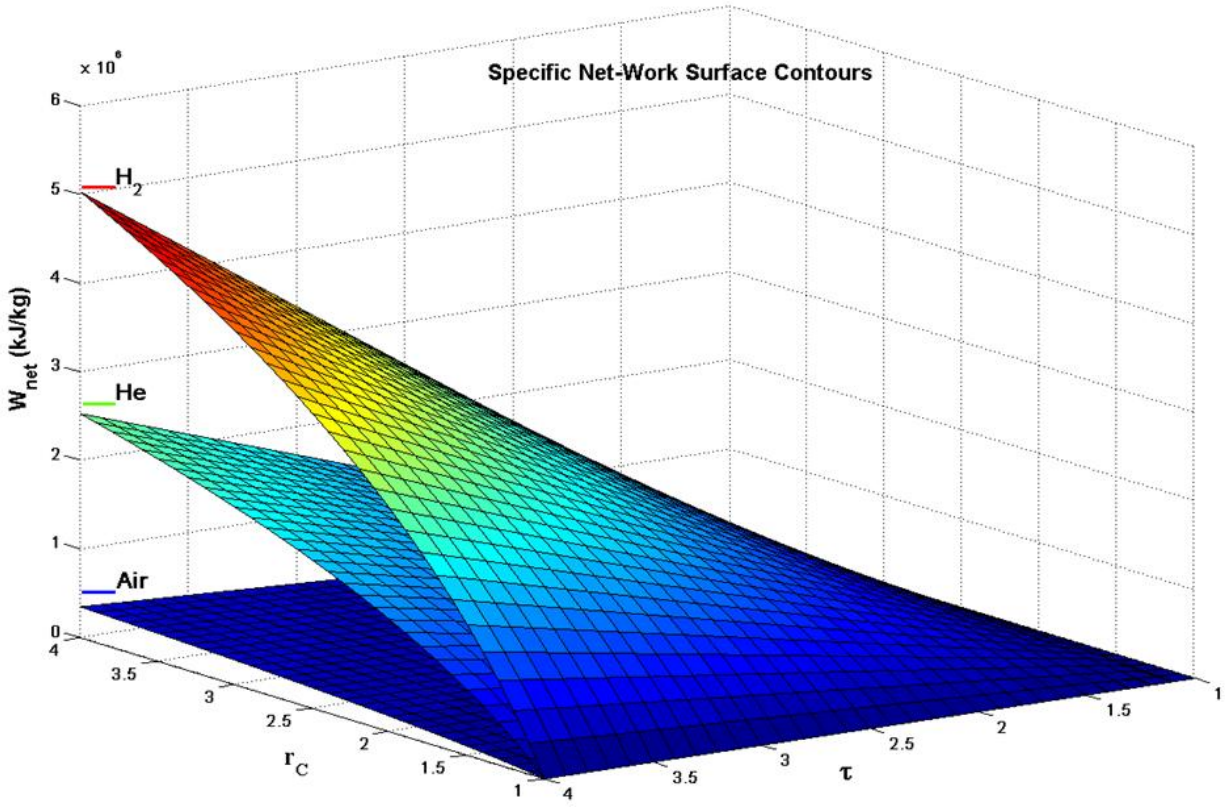


Figure 3-8: Specific Net Work as a Function of Compression Volume and Temperature Ratios

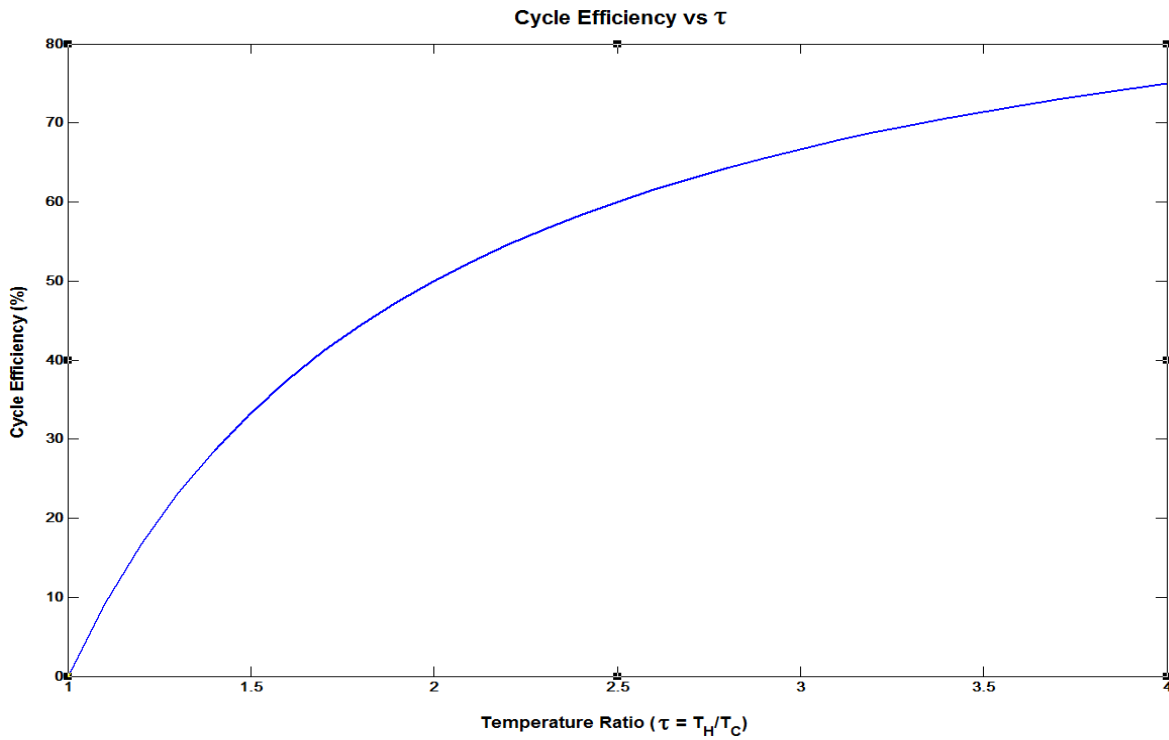


Figure 3-9: Thermal Efficiency as a function of Temperature Ratio

3.1.2 Working Gas Selection

The analysis shown until now compares air, helium and hydrogen as the working gas alternative for the Stirling engine. In general, hydrogen and helium are chosen over air because of the higher specific output they provide for the same operating conditions. However, it has been claimed that an engine using hydrogen or helium can be scaled, based on similarity, to produce the same performance with air.

This can be better understood by means of Figure 3-10 where a diagram illustrates simulated Stirling engine efficiency as function of specific horsepower output per liter of swept volume for air, helium (He) and hydrogen (H₂). It is evident that the engine can be scaled to have the same efficiency; however, the same cannot be said about output power. Hydrogen will always have a higher capacity to do work per unit mass as what is observed from Figure 3-6 to Figure 3-8. From Figure 3-10, it can also be observed that the curve of helium and hydrogen approach each other as the engine becomes more efficient (low specific power output).

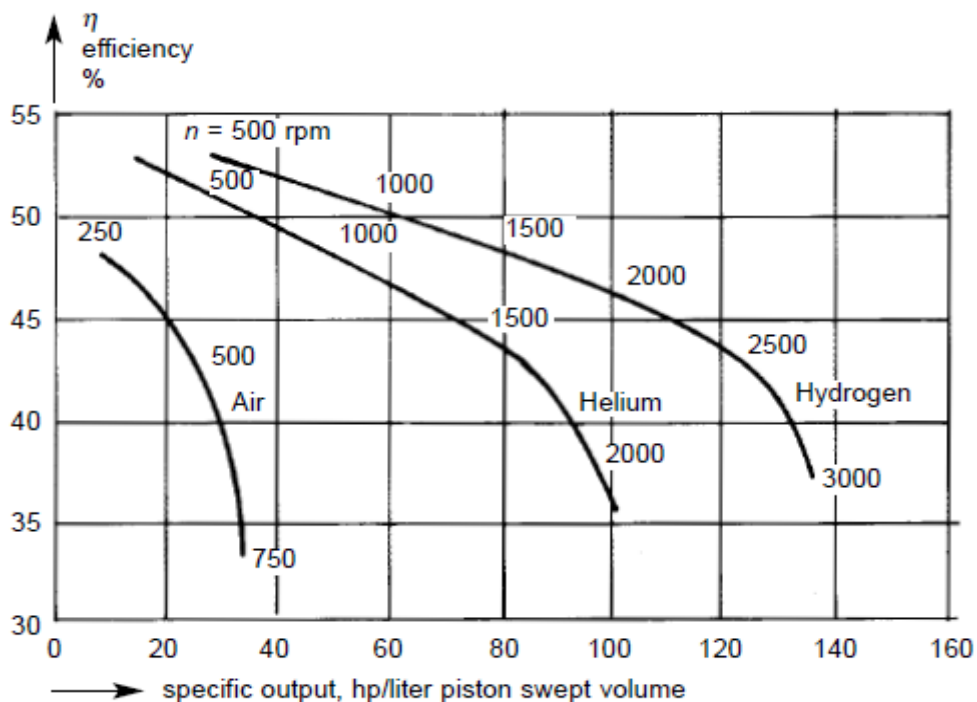


Figure 3-10: Computer Simulated Effect of Working Fluid on the Thermal Efficiency (Organ & Finkelstein, [2001])

Although the concept of similarity is very useful when an existing engine design has to be modified for the use of another other working gas. The diagram does not support the

argument that air can be scaled to achieve the same performance of helium or hydrogen since for the same efficiency He and H₂ have larger outputs and for the same outputs He and H₂ operate at higher efficiencies. Therefore there is in fact superiority of the lighter gases over the use of air, which contrasts with the conclusions of Finkelstein et al. [1]. For this reason the majority of engines in general use either He or H₂ as the working gas. The Ford-Philips engine used in the case study contains H₂ as the working gas, and the following sections will focus on the results using hydrogen as the working gas.

3.1.3 Imperfect Regeneration

Now the effects of having imperfect regeneration are evaluated. Today high efficiency regenerators are available; however, the regenerator heat transfer ineffectiveness can lead to major cycle inefficiencies [29]. It is important to study the regenerator effectiveness in the Stirling engine in order to predict loss in performance. To achieve this, the methodology presented by Martini [29] was implemented. The regenerator effectiveness as the gas moves from the cold side to the hot side of the engine is defined as:

$$\varepsilon = \frac{T_R - T_C}{T_H - T_C} \quad (3.8)$$

This means that an additional heat input term must be accounted for, then

$$Q_{in} = Q_H + Q_{R \rightarrow G} = mRT_H \ln(r_c) + mC_V(T_H - T_R)$$

Note that when $T_R = T_H$ perfect regeneration occurs ($\varepsilon = 1$) and the additional term in the heat input decreases to zero. However, for imperfect regeneration:

$$T_L < T_R < T_H$$

and the efficiency of the cycle is now determined by:

$$\eta = \frac{T_H - T_C}{T_H - \left(\frac{C_V}{R}\right)\left(\frac{T_H - T_C}{\ln(r_c)}\right)} = \frac{T_H - T_C}{T_H - \left(\frac{1}{\gamma - 1}\right)\left(\frac{T_H - T_C}{\ln(r_c)}\right)} \quad (3.9)$$

Substituting the temperature ratio, specific heat ratio in Eq. 3.8, the following expression for the thermal efficiency is obtained,

$$\eta = \frac{(\gamma - 1)(\tau - 1)\ln(r_c)}{(\gamma - 1)\tau\ln(r_c) - (\varepsilon - 1)(\tau - 1)} \quad (3.10)$$

where γ is the ratio of specific heats.

$$\gamma = \frac{C_P}{C_V}$$

In contrast to the Ideal case, where the efficiency only depends on the operating temperature ratio of the cycle (Eq. 3.7), Equation 3.10 shows that the thermal efficiency for the cycle depends on fluid properties, compression volume ratio, temperature ratio and the effectiveness of the regenerator. However, imperfect regeneration will approach the Stirling Ideal limit as $\varepsilon \rightarrow 1$. In Figure 3–11 to Figure 3–14 the effect of regenerator effectiveness, in combination with different compression ratios and temperature ratios is explored.

Figure 3–11 shows how the efficiency is affected from the Ideal case to the scenario where no regeneration is achieved (no regenerator exists). The values presented are for the initial example, in which the volume and temperature ratio are 2 and 3, respectively. The efficiency drops from 67.7% (Ideal) to just below 20% for zero regenerator effectiveness, meaning that the cycle will be able to achieve some work at the expense of large amount of heat input. It is also observed that for an effectiveness of 0.6 the efficiency drops to about half of its Ideal value. Therefore, small deviations from the Ideal regeneration effectiveness affect the cycle thermal efficiency significantly. Typical high performance Stirling engines used regenerators with effectiveness of about 0.9 and even higher.

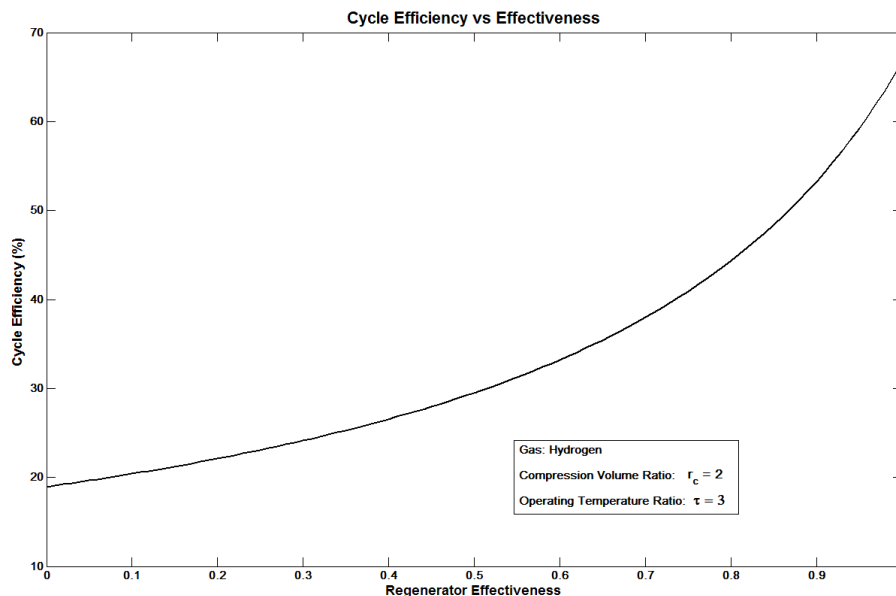


Figure 3–11: Cycle Efficiency vs Regenerator Effectiveness

In Figure 3–12 various curves are plotted to verify the effect of temperature ratio on regenerator effectiveness and cycle efficiency, at a constant volume ratio. From either the Ideal Stirling thermal efficiency (or Carnot's) it is concluded that it is not possible to operate the engine with reservoirs having the same temperature [43]. Therefore zero efficiency would always occur and the regenerator heat transfer is irrelevant. For this reason, Figure 3–12 starts with an operating temperature ratio of 1.5. When τ is 1.5, the efficiency drops to about 15% when having no regenerator but it is able to achieve a maximum efficiency of only about 33% in the Ideal regeneration. As the temperature ratio increases, the effect that the effectiveness has on the efficiency is decreased. Furthermore when $\tau \rightarrow \infty$, the thermal efficiency for the Ideal cycle with regeneration tends to an asymptotic limit. Based on present day material capabilities maximum operating temperature ratios should be between 4 and 5 times ambient temperatures (absolute scale).

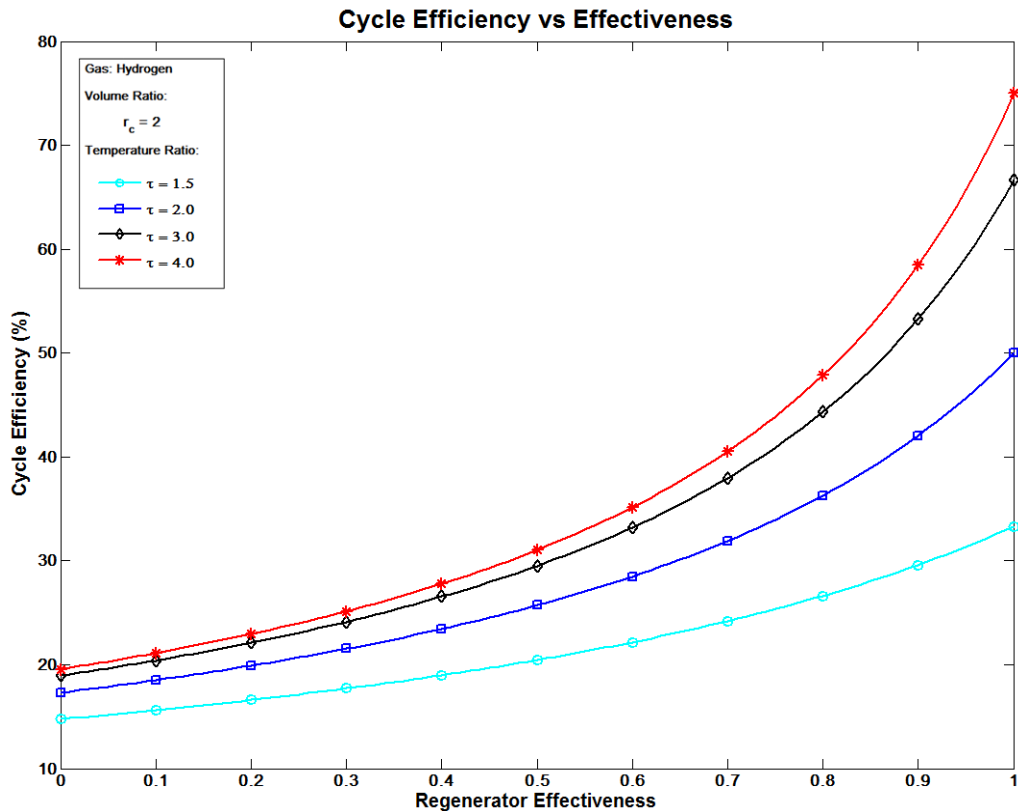


Figure 3–12: Cycle Efficiency as a Function of Regenerator Effectiveness and Temperature Ratio

For Figure 3–13 various curves are traced to illustrate the effect that the compression volume ratio and the regenerator effectiveness have on the cycle thermal efficiency, at a

constant temperature ratio. Based on common sense there must be swept volume ($r_c > 1$) for the gas displacement to produce work. Otherwise, no work could be produced yielding zero efficiency independently of regeneration effectiveness. Therefore we also start here with a value of 1.5 in the volume ratio parameter, which yields close to 12% cycle efficiency when having no regenerator and reaches 67.7% in Ideal regeneration. As the volume ratio increases a significant improvement in thermal efficiency is seen for the case of zero regenerator effectiveness. To acknowledge this fact, we can come to the conclusion that in practice, the working spaces themselves account for some regeneration (however small it may be). Therefore larger swept volumes will have the capacity to have better engine performance at low or no regeneration capacity and smaller swept volume will performed poorly at low or no regeneration capacity. As in the case of increasing temperature ratios, increasing volume ratios also decreases the effect that regenerator effectiveness has on the thermal efficiency. The final relevant observation from Figure 3–14 is that all curves converged to a single point when $\epsilon \rightarrow 1$. In this limit, the cycle efficiency only depends on temperature ratio (which is precisely the Ideal Stirling cycle thermal efficiency).

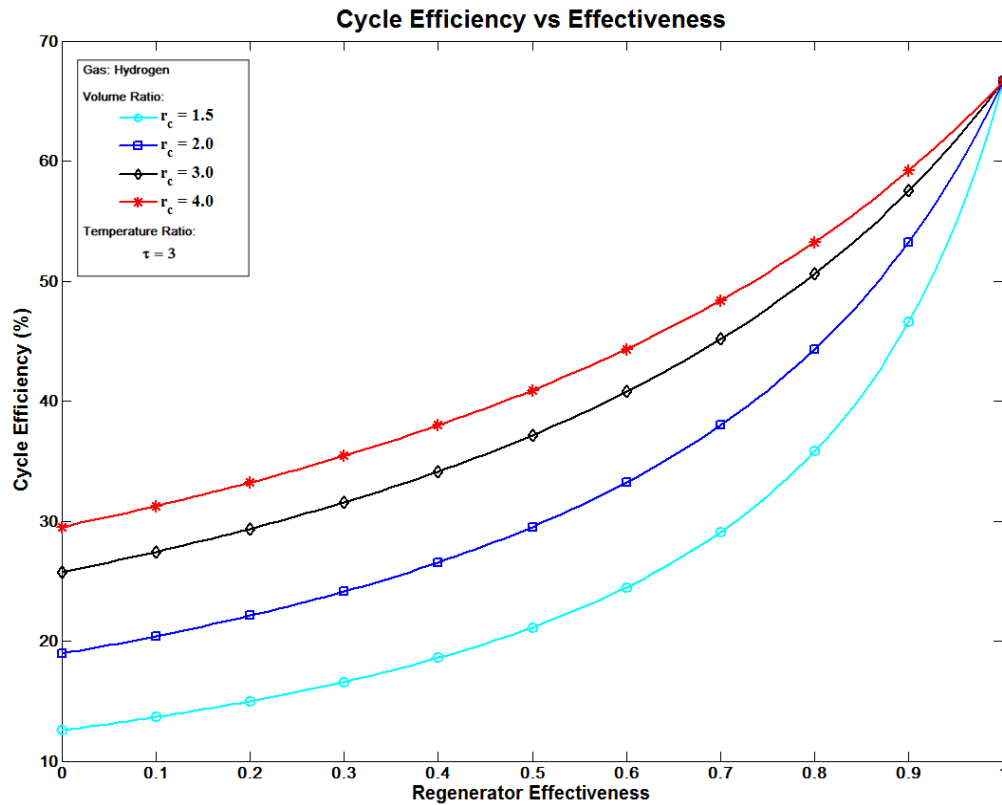


Figure 3–13: Cycle Efficiency as a Function of Regenerator Effectiveness and Compression Volume Ratio

Similarly as for the Ideal specific work for different working gases (Figure 3–8), Figure 3–14 displays the behavior of cycle thermal efficiency having imperfect regeneration as a simultaneous function of compression volume and temperature ratios. The different contour surfaces display the effect of regenerator effectiveness as it increases from 0 to the Ideal limit. Note that in the Ideal regeneration limit the thermal efficiency surface collapses to a curve with dependence on τ only (again this is the Ideal Stirling cycle efficiency). However, both the zero regeneration and the Ideal regeneration surfaces form an envelope that encloses the thermal efficiency of the actual engine according to the size of the swept volume spaces and difference in operating temperatures for the heat source and heat sink.

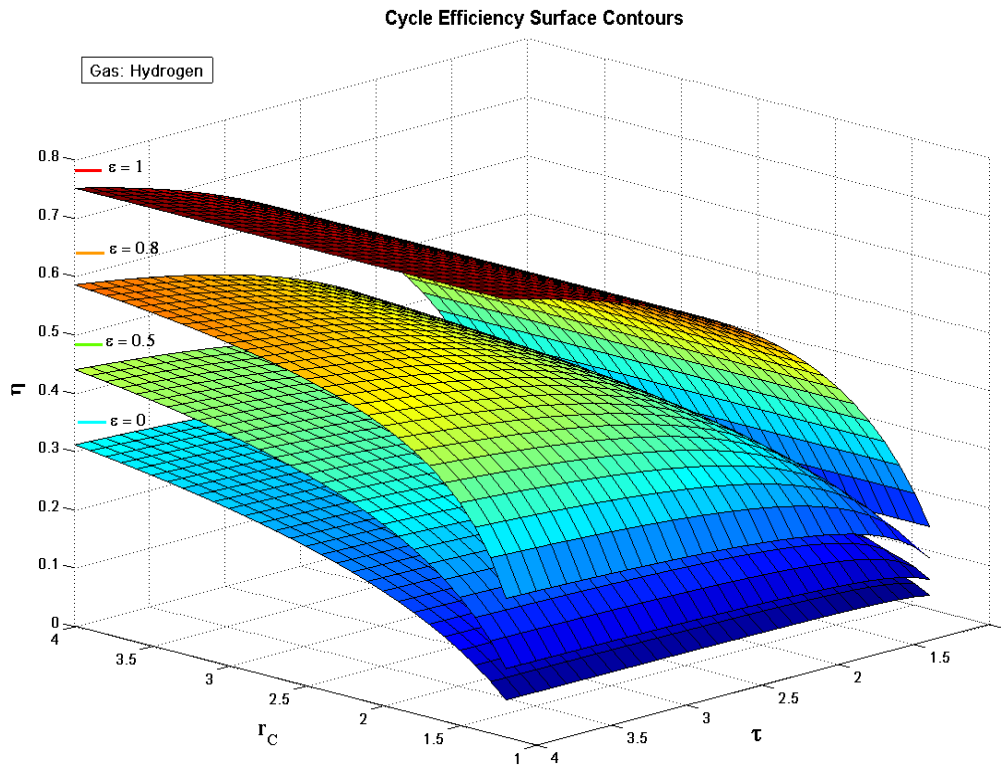


Figure 3–14: Cycle Efficiency vs Regenerator Effectiveness Surface Contours

3.2 First Order Methods

In Section 3.1, the four ideal gas processes (isothermal-compression, isochoric heating, isothermal expansion and isochoric cooling) were viewed as separate independent processes. Although the effects of gas properties (gas selection), volume compression ratio (r_c), temperature ratio (τ), and regenerator effectiveness (ϵ), are shown to affect the cycle

thermal efficiency. However, the Ideal cycle analysis is unable to predict how the piston motion, which controls volume variations, affects the cycle. First Order methods are useful in determining a more realistic cycle behavior and performance parameters than what can be determined with an Ideal cycle analysis. One of the main reasons is that now the type of motion used for the gas displacement will play an important role on the results. Also the fact that the individual gas processes actually overlap [29], since the complete mass of the working gas will be always divided in the five components of the engine (expansion space, heater, regenerator, cooler, and compression space) during the whole cycle is also considered in the analysis. In this section three methods of analysis are developed and compared:

- (1) Isothermal Analysis
- (2) Adiabatic Analysis
- (3) Finite Heat Transfer Analysis

Each method will be analyzed and discussed using the Ford-Phillips 4-215 engine as the case study, the engine is described in Section 2.4. This chapter will only deal with the Alpha Stirling engine configuration and purely sinusoidal volume variations. The sinusoidal variation will be used later as our baseline for the engine optimization studies (Chapter 4). After discussing the Isothermal, Adiabatic and Finite Heat Transfer analyses, Section 3.3 will deal with 2nd Order methods to account for pressure and mechanical losses.

3.2.1 Isothermal Analysis

The Isothermal analysis was the first theoretical thermodynamic analysis developed for Stirling engines. Professor Gustav Schmidt was responsible for this mathematical study and published it in 1871 [4]. Schmidt's mathematical model has become the classic ideal standard for which Stirling engines are compared rather than Ideal cycle analysis. Schmidt was able to develop a closed form solution for cycle work (Eq. 3.11) by assuming isothermal working spaces, ideal heat exchangers (isothermal heat exchange), perfect regeneration and integrating the sinusoidal volume variations through the complete cycle.

$$\oint p(\forall) d\forall = \int_{\theta=0^{\circ}}^{\theta=360^{\circ}} p d\forall = Sc \cdot p_m \cdot V_{sw} \quad (3.11)$$

In Eq. 3.11, Sc is the Schmidt number, p_m the mean cycle pressure and V_{sw} is a constant associated with the swept volume (see Appendix A.1 and A.2). Although the analytical solution for the Isothermal analysis is available, a numerical solution may be required for other types of motion that are non sinusoidal [4]. In addition, when analyzing non sinusoidal mechanisms, different analytical expressions should arise from the closed form integrand in Eq. 3.11.

Discretization:

The discretization of the analytical model for the engine will be configured as the five space component model, in which the compression, cooler, regenerator, heater and expansion spaces are considered as individual homogenous cells. Therefore, the working gas at any point in time (in each cell) is represented by its instantaneous mass, temperature, volume and pressure. Figure 3–15 depicts the temperature distribution in the five spaces for the Isothermal model. The compression space and cooler are at the cold heat sink temperature T_k , the expansion space and heater are at the hot source temperature T_h , and the ideal regenerator has a linear temperature distribution. The thermodynamic analysis assumptions are listed below.

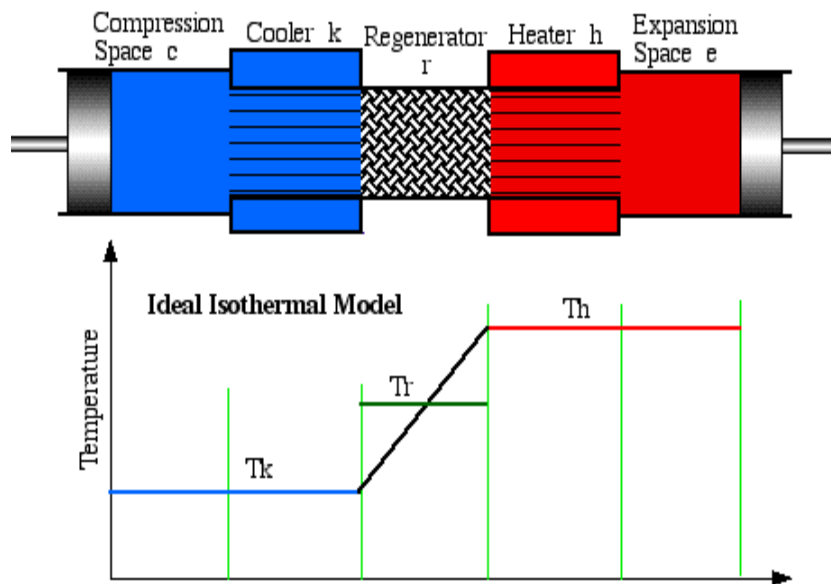


Figure 3–15: Five Component Model for Isothermal Analysis (Urieli, [2011])

Assumptions:

- The engine is operated at steady state cycles.
- Engine rotational speed is maintained constant.

- The working gas (hydrogen) is considered as a perfect gas and the equation of state is applied.
- No seal leakage, thus the hydrogen mass is constant over the complete cycle.
- Uniform pressure through all engine components.
- Kinetic and potential energy changes for the fluid are ignored.

Mathematical Model:

The first step taken here is to express the general equations used for the Isothermal model and include the sinusoidal piston-crank mechanism equations for the net cycle work integration. The Isothermal model equations are taken from Urieli [4]. His analytical model is expressed in a different manner than what was obtained by Schmidt. A numerical integration technique was used to verify the analytical expressions derived by Urieli. Both the analytical equations and the numerical code (developed using the trapezoidal rule) were found to give almost identical results.

The piston-crank mechanism used in the Ford-Phillips 4-215 engine allows sinusoidal volume variation in the compression and expansion spaces. Therefore the volume variations can be expressed by the following functions,

$$V_c = f(\theta) \text{ and } V_e = f(\theta + \alpha)$$

Where θ is the crank angle and α is the phase angle (relative angle between the expansion and the compression piston). It is assumed that when θ is zero, corresponds to the maximum volume in the compression space. Then, we can define the volume variations with the expressions given in Table 3-3.

Table 3-3: Sinusoidal Volume Variations

Compression Space Volume Motion	Function	$V_c = V_{cl,c} + \frac{1}{2}V_{sw,c}(1 + \cos \theta)$	(3.12)
	Derivative	$\frac{dV_c}{d\theta} = -\frac{1}{2}V_{sw,c} \sin \theta$	(3.13)
Expansion Space Volume Motion	Function	$V_e = V_{cl,e} + \frac{1}{2}V_{sw,e}(1 + \cos(\theta + \alpha))$	(3.14)
	Derivative	$\frac{dV_e}{d\theta} = -\frac{1}{2}V_{sw,e} \sin(\theta + \alpha)$	(3.15)

To get an expression for net cycle work we need to solve the integral of pressure volume

differential as functions of crank angle variation. The formulas for cycle performance are summarized in Table 3-4. The complete steps to obtain the analytical solution are rather extensive, for details refer to Appendix A of Urieli's "Stirling Cycle Engine Analysis" [4]. The Appendix A.1 included in this thesis, is made for the sole purpose of defining the simplifying terms (for example b and c) in the Isothermal analysis cycle equations.

Table 3-4: Summary of Thermal Cycle Equations for Isothermal Analysis

Instantaneous Pressure	$p = \frac{m \cdot R}{\left(\frac{V_c}{T_k} + \frac{V_k}{T_k} + \frac{V_r \ln(T_h/T_k)}{(T_h - T_k)} + \frac{V_h}{T_h} + \frac{V_e}{T_h}\right)}$	(3.16)
Mean Cycle Pressure	$P_m = \frac{mR}{s\sqrt{(1 - b^2)}}$	(3.17)
Heater Heat & Expansion Work	$Q_h = W_e = \oint p \left(\frac{dV_e}{d\theta}\right) d\theta = \frac{\pi V_{swe} mR \sin(\beta - \alpha)}{c\sqrt{1 - b^2}} (\sqrt{1 - b^2} - 1)$	(3.18)
Cooler Heat & Compression Work	$Q_k = W_c = \oint p \left(\frac{dV_c}{d\theta}\right) d\theta = \frac{\pi V_{swc} mR \sin \beta}{c\sqrt{1 - b^2}} (\sqrt{1 - b^2} - 1)$	(3.19)
Cycle Net Work	$W_{net} = W_e + W_c = \Pi \cdot P_m \{V_{swc} \sin \beta - V_{swe} \sin(\beta - \alpha)\}$	(3.20)
Cycle Efficiency	$\eta = \frac{W_{net}}{Q_h} = 1 - \frac{T_k}{T_h}$	(3.21)

Thermal Results:

Figure 3-16 to Figure 3-18 show the sinusoidal volume variations, cycle pressure variation, and the pressure-volume diagram for the Isothermal model. From Figure 3-17 it can be implied that the cycle behavior depends on motion, since the variation in the thermal results adopt the sinusoidal behavior from the mechanism. In Figure 3-16 the sinusoidal variations of the compression and expansion space volume are shown along with the combined dead space volume occupied by the heater, regenerator and cooler. As shown in the figure the required space for heat exchange is considerable when compared with the actual space used for work in the Ford-Phillips 4-215 engine. The space used for heat exchange is called dead space volume because it is unusable in terms of work. The amount of unused space adversely affects the capacity of the engine to produce work. The

effect of dead space volume will be further explored in the following section.

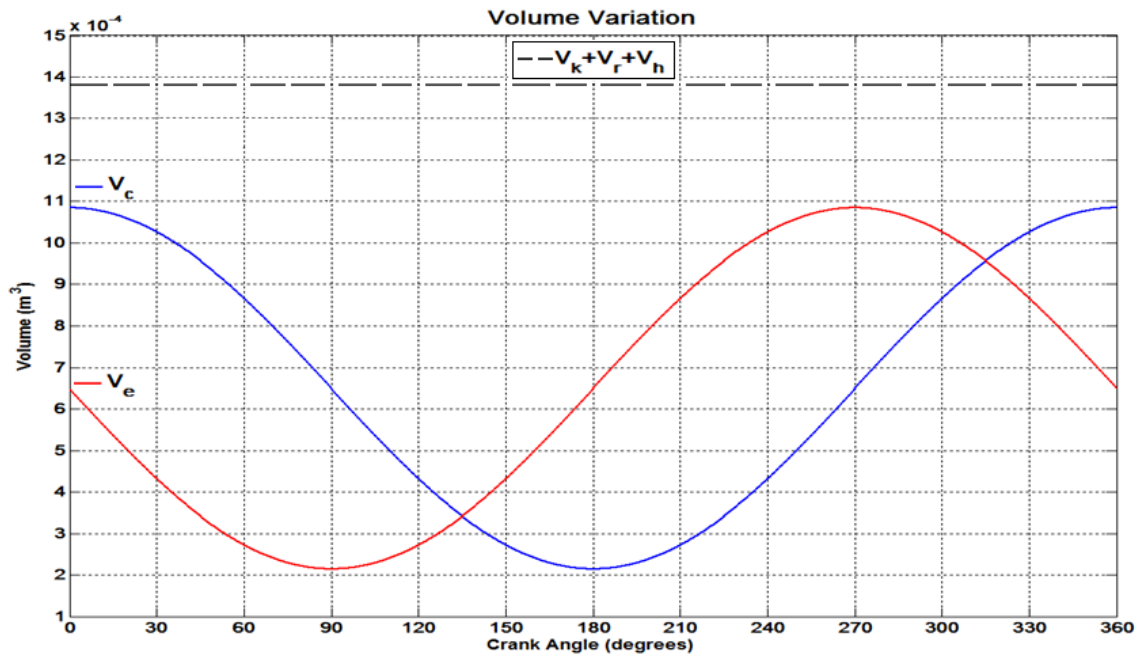


Figure 3-16: Sinusoidal Volume Variation

From Figure 3-17 it can be observed that the minimum and maximum pressure occurs close to the crank angle of maximum and minimum volume, respectively. However, they do not coincide exactly. The minimum and maximum volume occurs at crank angles of 135° and 315° , respectively. In the case of maximum and minimum pressures, these occur at 161.64° and 341.64° , respectively. Therefore there is an approximated 27° degree lag for the pressure relatively to the volume variation. This is reasonable since the mass is divided in five components which are at different thermodynamic states at each point in time.

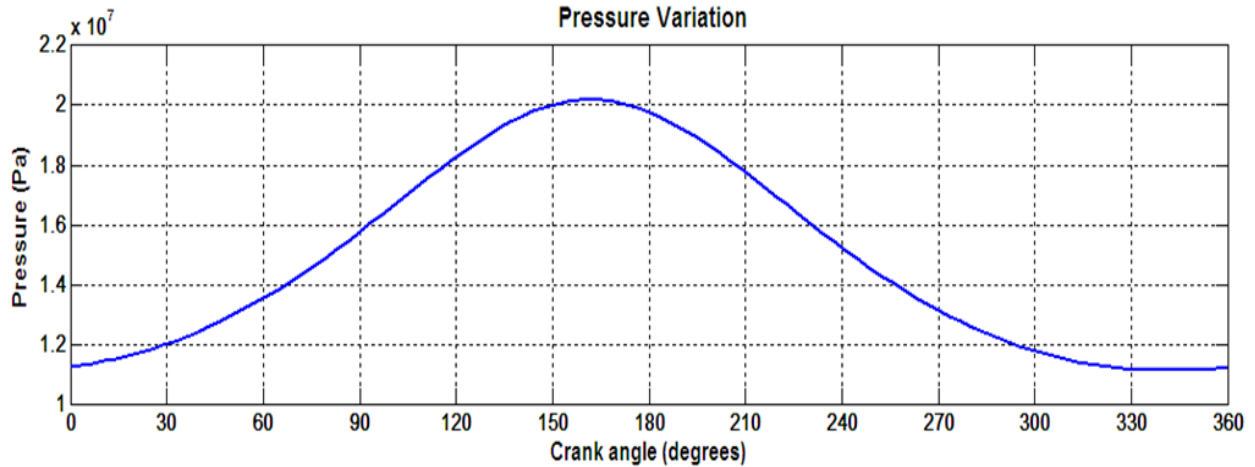


Figure 3–17: Sinusoidal Pressure Variation over the Cycle for Isothermal Analysis

If Figure 3–16 and Figure 3–17 are combined in a single plot, the engine indicator diagram (P- \forall diagram) in Figure 3–18 is obtained for the Isothermal model. The integration of the enclosed P- \forall area is the net work of the cycle and should give the same result as Eq. 3.20. The cycle performance parameters are summarized in Table 3–5. Finally, Ideal vs. sinusoidal motion and P- \forall diagrams are shown (using Ford-Phillips 4-215 engine data) in Figure 3–19 and Figure 3–20, respectively. Note that for creating the Ideal motion in Fig. 3–19, it was assumed that each ideal process has the same duration in the cycle.

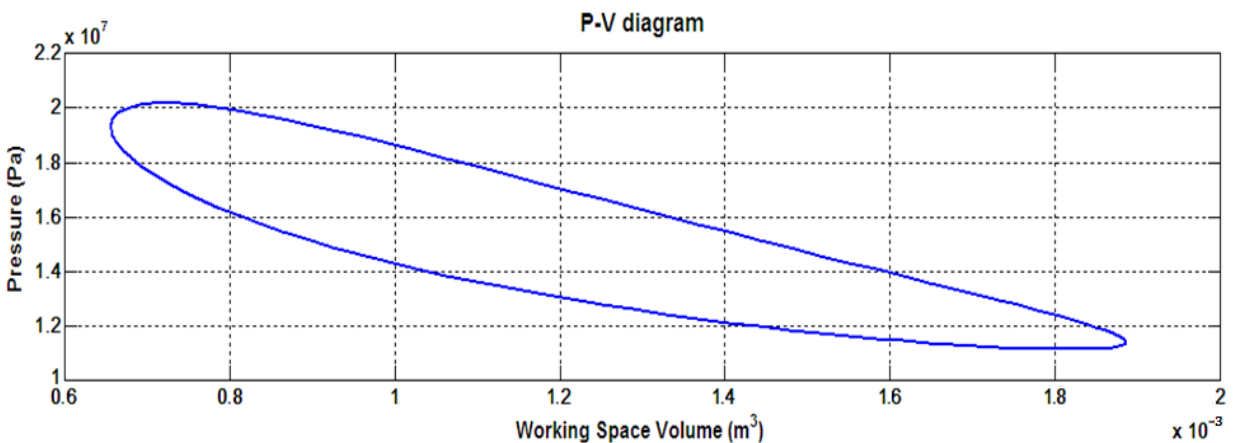


Figure 3–18: P- \forall Diagram for Sinusoidal Volume Variation for Isothermal Analysis

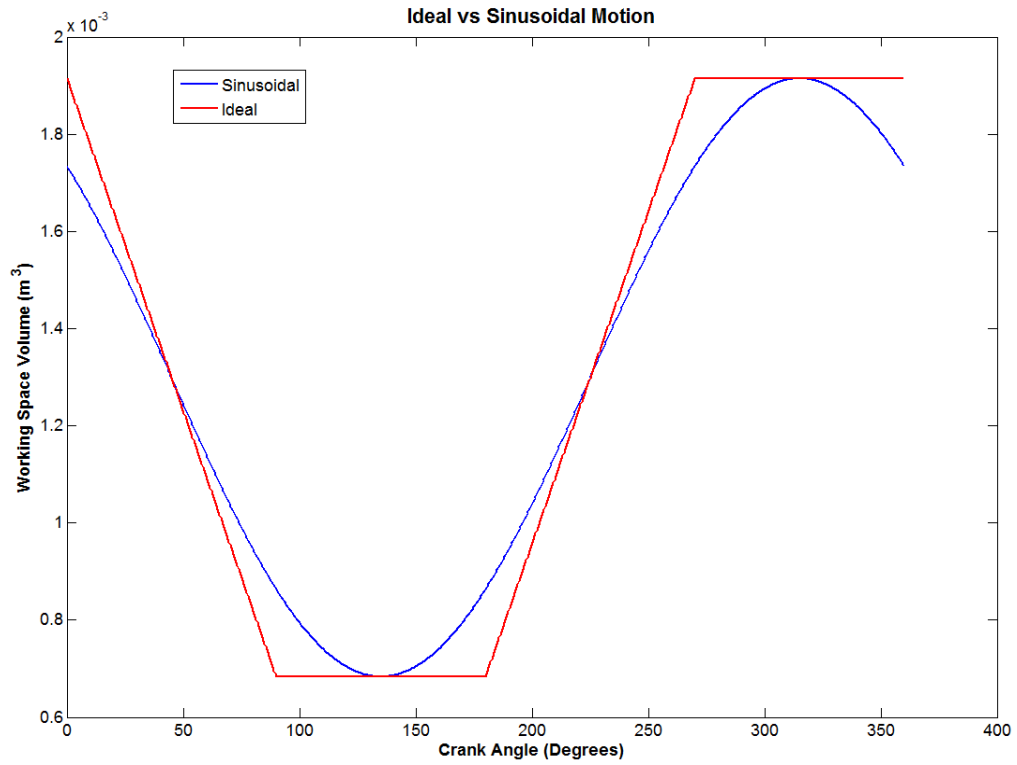


Figure 3-19: Ideal and Sinusoidal motion

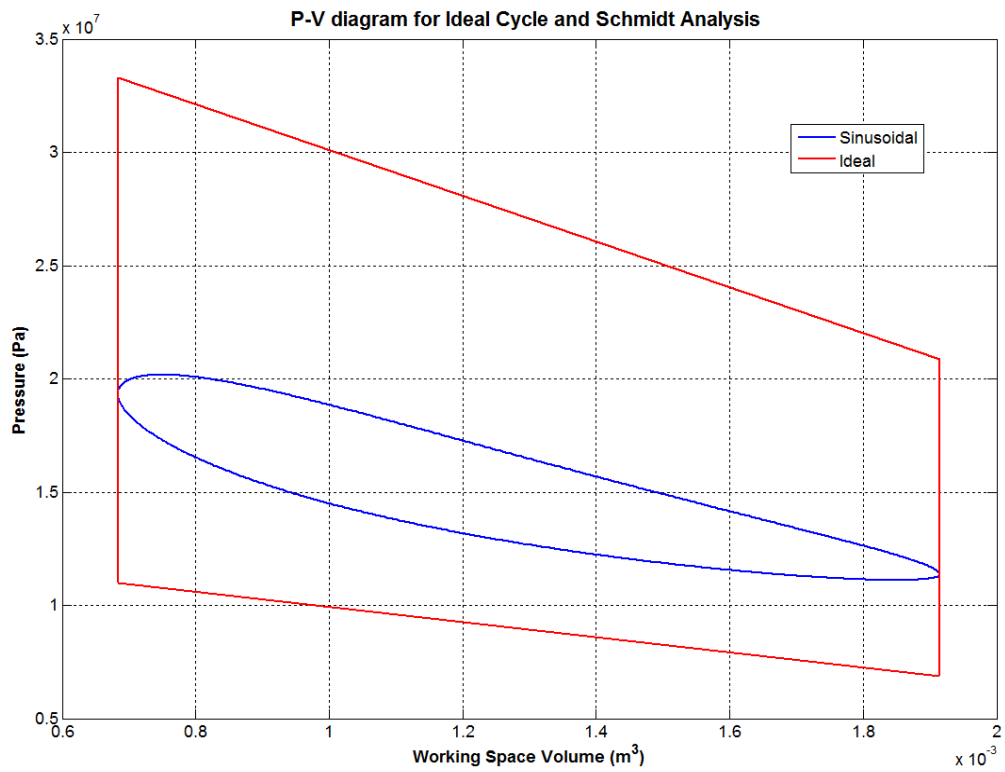


Figure 3-20: Ideal Cycle and Sinusoidal P-V Diagram

Table 3-5: Ford-Phillips 4-215 Engine Isothermal Analysis Performance

Parameter Name	Symbol	Value/Result
Swept Volume (m ³)	V_{sw}	8.706×10^{-4}
Phase Angle (deg)	α	90°
Mass (kg)	m	16.2×10^{-3}
Mean Pressure (bar)	p_m	148.8
Heater Heat Input (kJ)	Q_h	5.725
Net Work (kJ)	W_{net}	3.840
Efficiency (%)	η	67.06

3.2.2 Further Parametric Studies

When the effect of a sinusoidal crank mechanism is implemented, it is possible to determine how cycle behavior is affected by phase angle and dead space volume. These parameters directly affect engine performance; however, it is not possible to examine them from the Ideal cycle analysis. Consequently, the Isothermal model can be used for further preliminary parametric analysis and idealized optimization can also be explored on net cycle work. Although, with the limitation that cycle efficiency obtained for the Isothermal analysis remains the same as Carnot efficiency (independent of volume variation). As previously stated, the Ford-Philips 4-215 engine will serve as the baseline for the engine parameter data. Although this is still a simplified case study, results will serve to view further deviations between the Ideal cycle analysis and the Isothermal model.

In Figure 3-21 the net cycle work is plotted as a function of the phase angle. The results show that as the phase angle increases from 0° to approximately 90° the net work also increases and reaches a maximum and then it starts to decrease. The maximum occurs at a phase angle of 87.8° with a net cycle work of 3.87 kJ. The optimum phase angle obtained is fairly close to the 90° given by the design parameter of the Ford-Philips 4-215 engine. In addition the difference between the net cycle work given for the 90° angle and optimum value found is really small, thus for obvious manufacturing simplicity it is better to have a 90° phase angle.

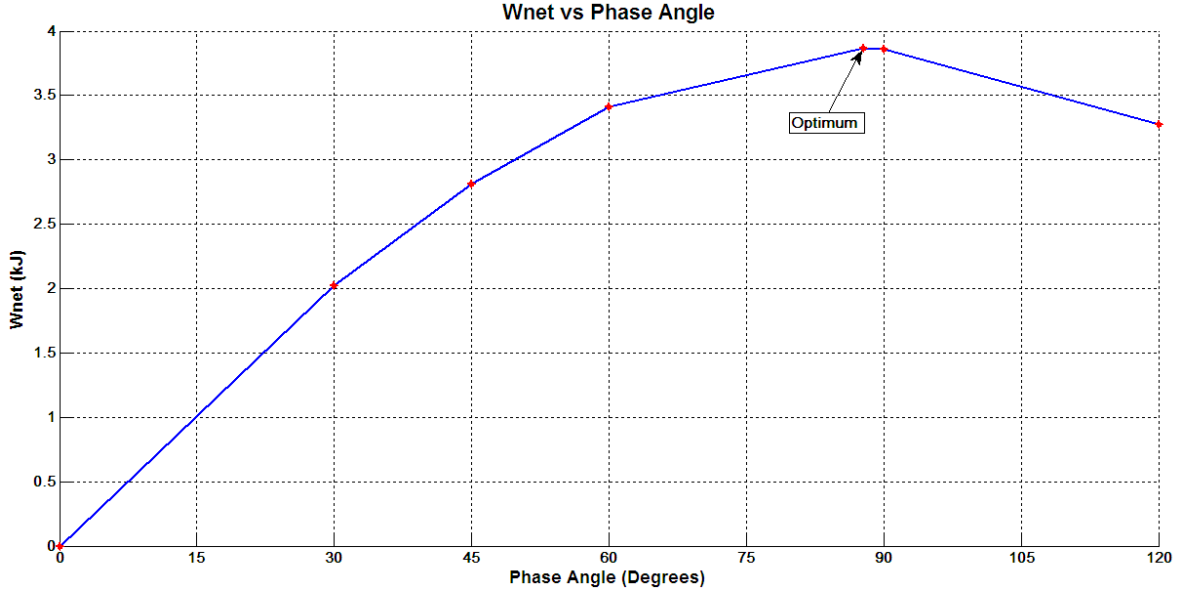


Figure 3-21: Net Cycle Work for Phase Angle Variation

The final parametric study includes the effect of the heat exchange volume or as referred previously dead space volume. Since the SE engine is an external heat engine it requires space for heat transfer. This space does not contribute to the production of work, and therefore it is commonly referred to as dead space volume. Presented here is the cycle net work as function of dead space volume by using the following approach:

- Heater, regenerator, cooler and clearance volumes make up the total dead volume space in the engine.
- Equation 3.16 can be combined with the Schmidt integral (Eq. 3.11) so the cycle pressure can be expressed as a function of dead space volume to heat exchanger temperature ratio (Eq. 3.22).
- The heat exchanger temperatures in the analysis are assumed to be constant.

The equation for dead space volume to temperature ratio is:

$$DSR = \frac{V_{cle}}{T_h} + \frac{V_h}{T_h} + \frac{V_r}{T_r} + \frac{V_k}{T_k} + \frac{V_{clc}}{T_k} \quad (3.22)$$

And the effective regenerator temperature [4] is calculated from:

$$T_r = \frac{T_h - T_k}{\ln(T_h/T_k)} \quad (3.23)$$

The DSR value for the Ford-Phillips 4-215 is approximately $3 \times 10^{-6} \text{ m}^3/\text{K}$, this is the engine data point displayed on Figure 3-22. As the dead volume increases indefinitely the

net cycle work approaches zero since the working space volume becomes insignificant when compared to heat exchange volume. The gas inside the engine might move (due to thermal gradients), however, it will reach the point where it is unable to move the pistons. On the contrary, when the DSR decreases there is a monotonic increase in W_{net} with respect to the engine data point. Figure 3–22 suggested that much improvement may be done to decrease the size of the heat exchangers in the Ford-Phillips 4-215, and that in general heat exchangers used in SE still present a major area for engine optimization. In Figure 3–23, the P- \forall diagram for the DSR of the engine data point is shown. In addition, P- \forall diagrams for values of 1/3, 1 1/2, and twice the engine DSR are included to illustrate the effect of reducing or increasing dead space volume.

The parametric study done for the Isothermal model showed that the optimized values of net cycle work can be attained by evaluating the parameters of interest individually. However, it is necessary to incorporate a thermal model in the analysis that considers more realistic assumptions. Then, more practical results can be obtained and optimization procedures become more valid. The more realistic methods given in the literature do not have analytical solutions to the performance parameters; therefore these functions have to be solved by numerical methods. This is important to note when developing the optimization procedure for the volume variation in the engine.

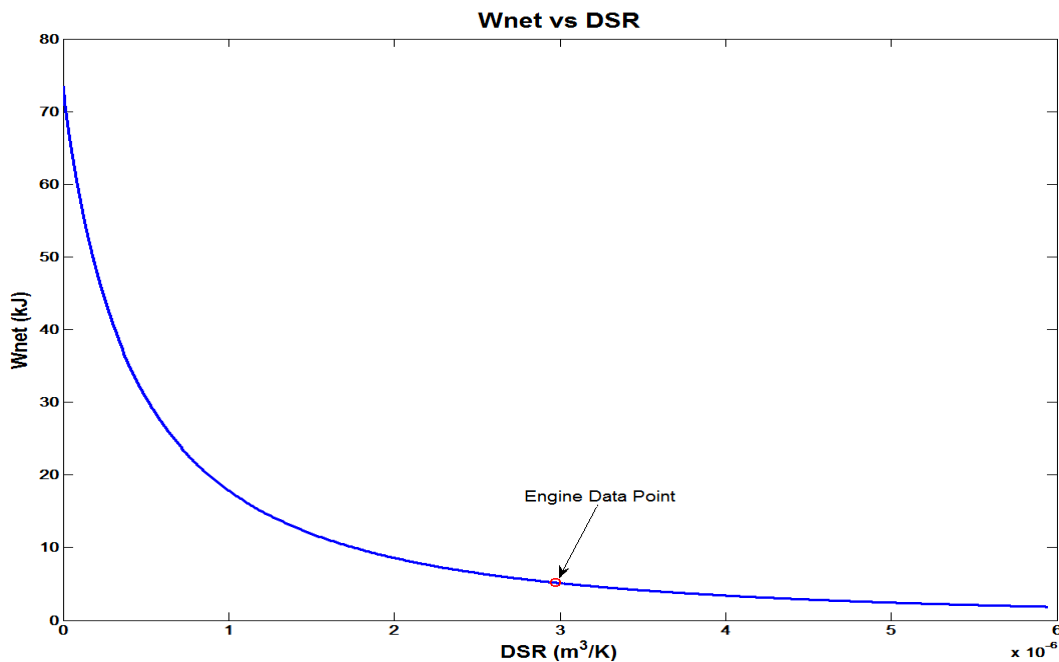


Figure 3–22: Dead Space Volume Effect on Cycle Net Work

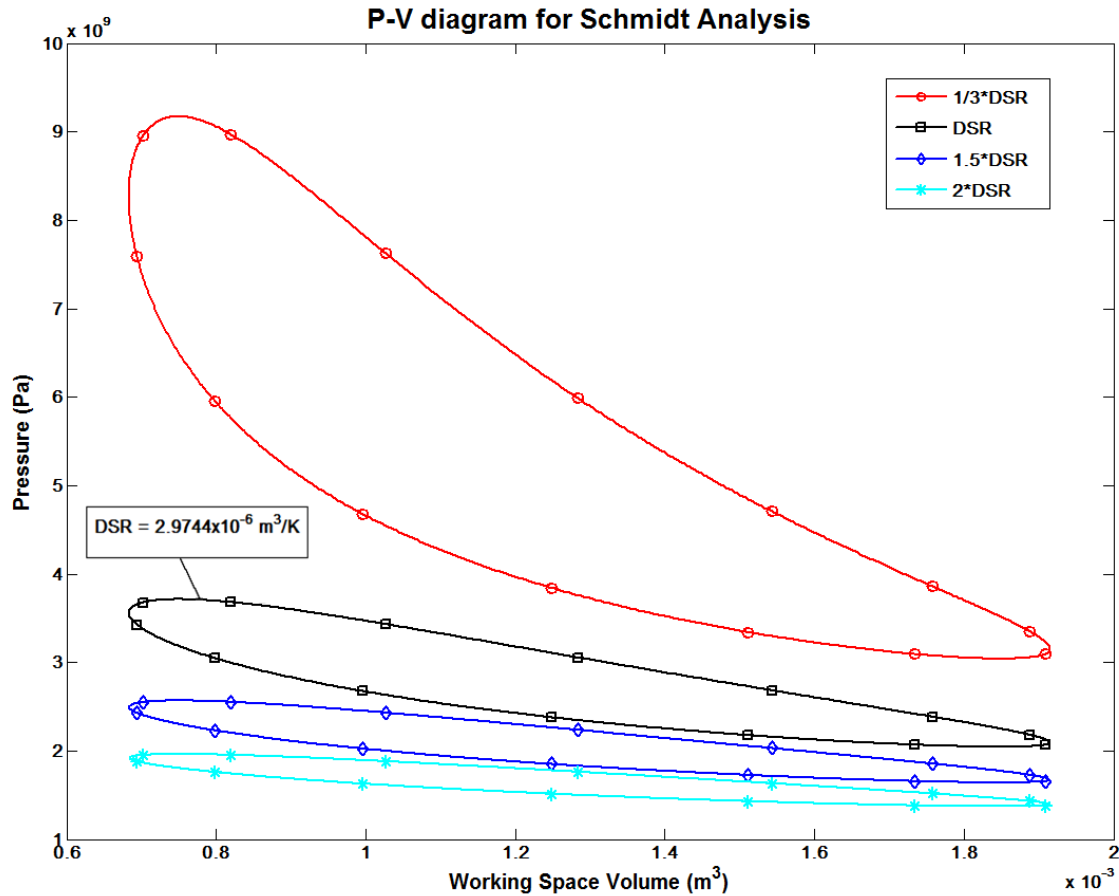


Figure 3–23: Dead Space Volume Effect on P-V Diagram

3.2.3 Adiabatic Analysis

The preceding section (3.2.1) considered the case in which the engine working spaces were isothermal, therefore the gas at the compression space is maintained at the cooler temperature (T_k) and the gas at the expansion space is maintained at the heater temperature (T_h). For analysis purposes this leads to redundant heat exchangers in the machine, since the solution is forced through the cycle to be the same as the work terms (Eq. 3.18 and Eq. 3.19). The correct approach in analysis assumptions cannot allow all the heat transfer to occur through the boundaries of the working spaces. This is neither the case from a practical sense, because highly effective heat exchange cannot be attained in the cylinders that are designed for gas compression and gas expansion. It has been observed that in real machines the behavior inside the working spaces tends to be close to adiabatic (almost no heat exchange) and not isothermal [4]. With this assumption cycle analysis and design becomes more relevant since heat must be convected through the heat exchangers.

The implication of this assumption should result in a cycle variation of temperatures T_k and T_h . Furthermore the solution for all unknown cycle parameters is to be solved numerically.

Discretization:

The number of discrete cells or control volumes used in the Adiabatic analytic model is the same that the one used for the Isothermal analysis (five control volumes). The difference for the Adiabatic model is that the compression and expansion spaces will have a temperature variation due to the adiabatic modeling of the control volume that confines the spaces. The expected adiabatic behavior of the expansion and compression spaces is illustrated in Figure 3–24. As shown, the temperature for the heater and cooler remain isothermal, and regenerator temperature distribution is linear. Basically, most of the analysis assumptions are the same as in the Isothermal analysis. However, some additional assumptions are necessary for solving the Adiabatic model, these are provided next.

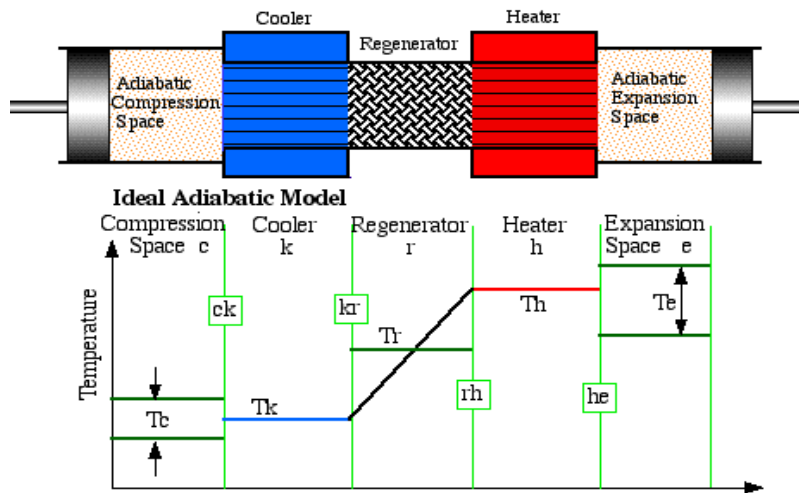


Figure 3–24: Five Component Model for Adiabatic Analysis (Urieli, [2011])

Assumptions:

- Adiabatic compression and expansion.
- External heat transfer between the working gas and the heater or cooler control volumes (Q_h and Q_k).
- The regenerator heat (Q_r) is transferred internally from the regenerator matrix to the gas and vice versa, however, its enclosure is adiabatic.
- The enthalpies flowing across the interfaces ck and he (see Figure 3–24) carry the respective adjacent upstream cell temperatures, therefore the interface tempera-

tures at the boundaries ck and he are defined according to the following flow equations,

$$\text{if } \dot{m}_{ck} > 0 \Rightarrow T_{ck} = T_c ; \quad \text{else} \Rightarrow T_{ck} = T_k \quad (3.24)$$

$$\text{if } \dot{m}_{he} > 0 \Rightarrow T_{he} = T_h ; \quad \text{else} \Rightarrow T_{he} = T_e \quad (3.25)$$

The reasoning behind Eq. 3.24 and 3.25 is similar to the upwind differencing scheme (typically implemented in CFD or FDM) where the adjacent values of cell in the flow field are determined based on the flow direction.

Mathematical Model:

The algebraic equations used for the Adiabatic analysis are summarized in Table B-1 of Appendix B. This is a non-linear system of equations that has to be solved numerically, for the specific engine configuration at a specific engine operating condition (e.g. engine speed). The equations listed in Table B-1 establish 23 variables, of which 7 are derivatives that need to be solved in time (or θ) in order to obtain the thermal solution throughout the complete cycle. The 7 derivatives that have to be integrated numerically are: cycle pressure (p), compression space mass (m_c), cooler heat (Q_k), regenerator heat (Q_r), heater heat (Q_h), compression work (W_c) and expansion work (W_e). In this analysis, the expansion space mass is forced to satisfy conservation of mass for the entire thermodynamic system. This is the typical Adiabatic analysis setup that was developed by Urieli [4]. However, the term for mass rate of change inside the expansion space is also calculated. The reason behind the calculation is that the heat rate equations B.22 and B.23 in Table B-1 depend on the expansion space mass accumulation rate. This approach for solving the heat transfer rates is different than typical Adiabatic analysis presented by Urieli [4], where the heat rates are expressed in terms of the pressure rate of change and the mass flow rates. The solution of the numerical system of equations for the Adiabatic analysis required the variables and derivatives to be solved sequentially in every time step. A limitation with this approach is that the interface temperature for the boundaries ck and he change abruptly (Fig. 3-24) twice in the cycle according to the change in flow direction in the compression and expansion spaces.

The energy terms are assumed zero at the beginning of the cycle, and the initial values for pressure and compression space mass are attained from the Isothermal analysis. With

the assumed initial conditions, the system of ordinary differential equations is reduced to an initial value problem. The classical fourth order Runge-Kutta method [44] was selected for the numerical integration. The boundary (or interface) temperatures are set as $T_{ck} = T_k$ and $T_{he} = T_h$ in the initialization. However, $T_{he} = T_h$ when the cycle starts as it will be seen later (Figure 3–26). Convergence criteria incorporated the evaluation of the compression and expansion temperature at the start and end of the cycle, the cycle pressure at the start and end of the cycle, regenerator heat and conservation of energy (see Appendix B).

Thermal Results:

The convergence criteria used considers that values of cycle pressure (p), compression space temperature (T_c) and expansion space temperature (T_e) at the end of the cycle must equal the initial values at the start of the cycle to establish steady state. Energy conservation using the First Law of Thermodynamics was also applied, and the normalized convergence criteria were set to 10^{-5} . The analysis program required 19 iterations for convergence. Previous works [4, 45] have achieved faster convergence, however, since a more conservative approach is used in the present study this should be expected. Results for the Adiabatic analysis are presented from Figure 3–25 to Figure 3–30.

The gas temperature during the cycle is shown for each engine component in Figure 3–25. The heater and cooler temperatures were assumed isothermal through the cycle so they have constant values of 1023 K and 337 K, respectively. A constant value of 617.8 K is given in the diagram for the regenerator effective temperature and it is obtained from Eq. 3.23. The regenerator is assumed to have a linear temperature distribution as observed in Figure 3–25. And since the cooler and heater temperature remain constant during the cycle, the effective regenerator temperature does not change during the cycle. It is observed that a large cyclic temperature variation occurs for the expansion space temperature. Its lowest value is 856 K and it reaches a maximum temperature of 1041 K. However, the expansion space temperature for most of the cycle is below the heater temperature. The compression space temperature variation is relatively less than what is observed in the expansion space. Also there is a large period of time in the cycle where the temperature T_c is less than T_k . The average value for temperature T_c is 344 K which is close to the cooler temperature T_k .

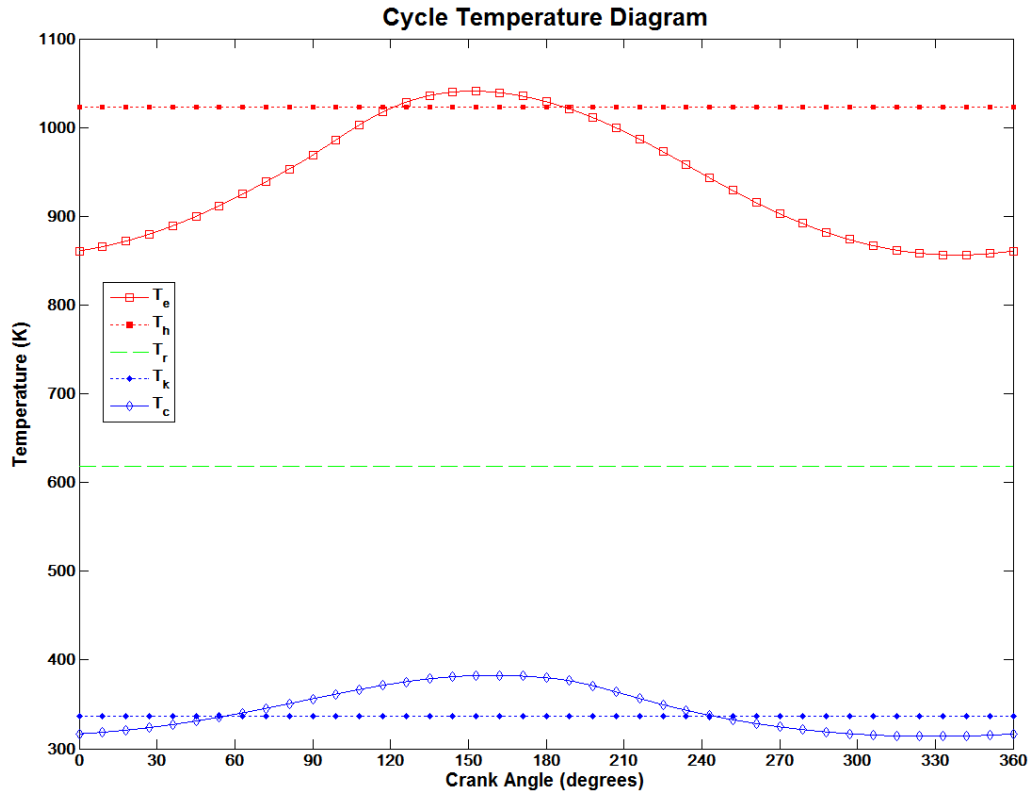


Figure 3–25: Gas Temperature Diagram for Adiabatic Analysis

Figure 3–26 is a plot for the interface temperatures between the boundary of the Compression Space (ck) and the Cooler and the boundary between the Heater and the Expansion Space (he). These curves become relevant for analyzing flow reversal and heat exchange in the cooler and heater since the enthalpies transported to the boundary depend on temperatures T_{ck} and T_{he} .

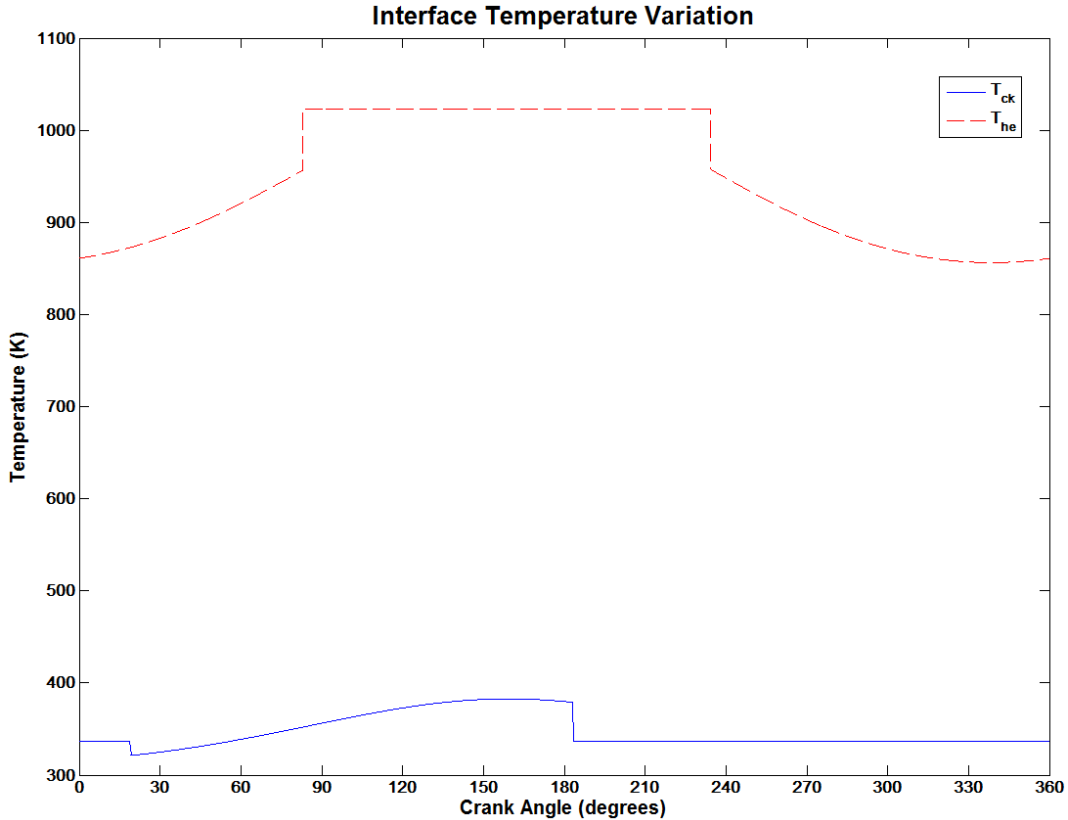


Figure 3-26: Adiabatic Analysis Interface Temperatures

The normalized cycle pressure and normalized compression space mass are illustrated in Figure 3-27. Cycle pressure and compression space mass were normalized using the respective maximum values during the cycle. Both curves demonstrate that the cycle behavior of these parameters is also sinusoidal (similar to the Isothermal analysis), therefore, parameter values for a real Stirling machine are dependent on piston motion. The lag between volume variation and cycle pressure is comparable to the one obtained in the Isothermal model. Figure 3-27 can also be used to demonstrate that the compression space mass is inversely proportional to the cycle pressure and that there is also a lag between them. The lag between the maximum pressure and minimum compression space mass is about 24° , while the lag between minimum pressure and maximum compression space mass is about 40° . The lag for the difference between the minimum p and maximum m_c is about twice and is reasonable because m_c also depends on T_{ck} which takes a constant value (T_k) from about 80° to 230° (range where the maximum p and minimum m_c occur) and varies for the rest of the cycle (range where the minimum p and maximum m_c occur).

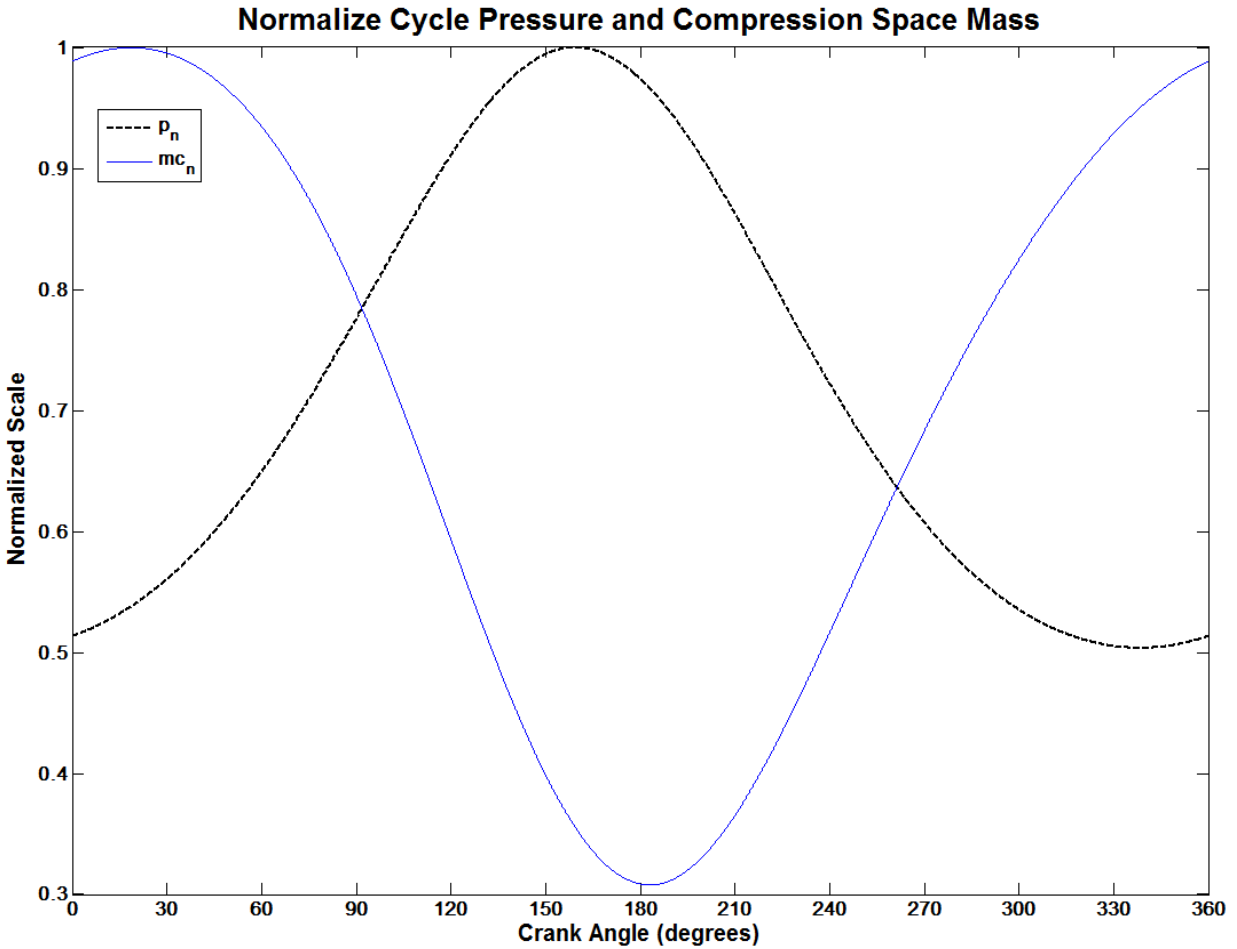


Figure 3-27: Normalized Pressure and Compression Space Mass for Adiabatic Analysis

Figure 3-28 and Figure 3-29 exhibit the cycle mass variation and mass flow rate variation for the Adiabatic analysis, respectively. A large amount of mass from the working gas will tend to accumulate in the compression space since its temperature is about 3 times lower than the expansion space and its swept volume is about six times greater than the cooler volume. The increasing pressure will then move the mass to the other components of the engine, particularly the regenerator and the expansion space. The regenerator has relatively more mass than the other heat exchangers, which might be expected in terms of heat exchanger volume. However, it is not intuitively obvious to observe almost identical mass variation for the heater and cooler. The justification of this result is explained using the ideal gas law and noting that:

$$\frac{V_h}{T_h} \div \frac{V_k}{T_k} \approx 1$$

For the regenerator this factor is more than twice than for the heater and cooler. Certainly this is not coincidence and there is a design aspect concerning this ratio in terms of gas content and engine size. Higher flow rates occur at the regenerator boundaries. Also note that for the heat exchangers, flow might be entering or exiting from both boundaries in a period of the cycle. Flow reversals in and out of the control volumes can be observed by plotting the interface temperatures (see Figure 3-26). They occur at the jump discontinuities, and they coincide with flows changing from positive to negative values (or vice versa) in the cycle mass flow diagram (Figure 3-29).

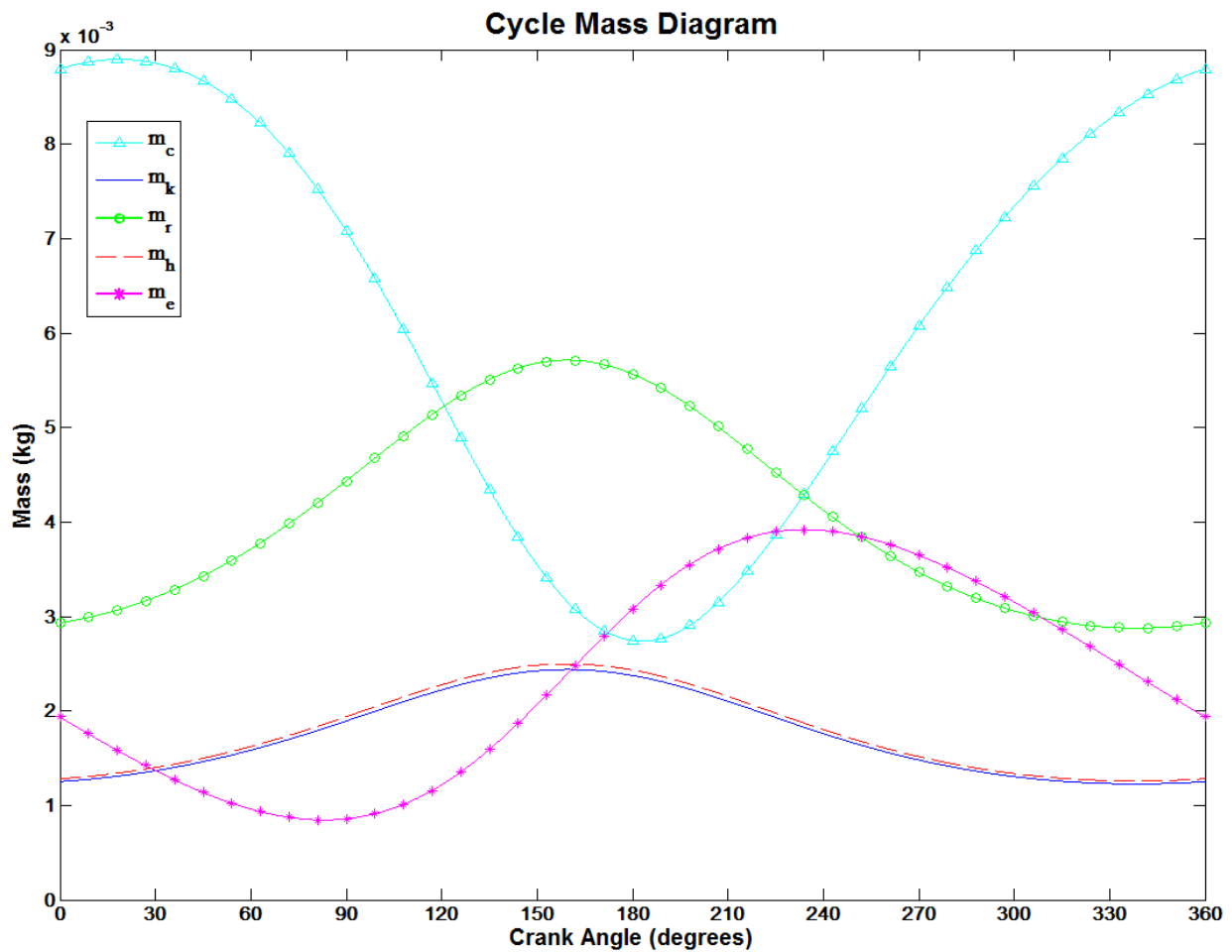


Figure 3-28: Cycle Mass Variation for Adiabatic Analysis

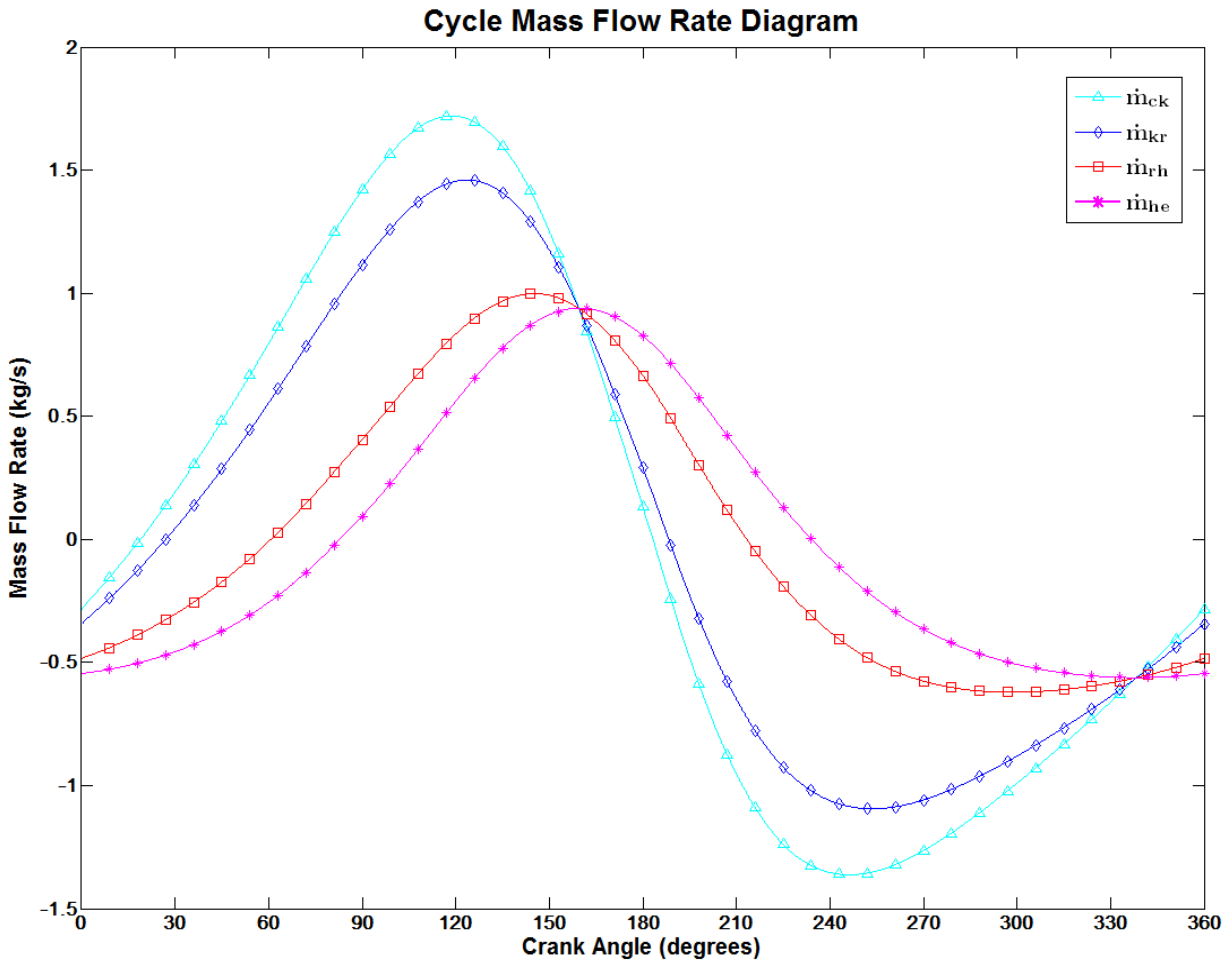


Figure 3–29: Cycle Mass Flow Rate Variation for Adiabatic Analysis

The importance of heat transfer in the regenerator is shown in Figure 3–30 where it appears to be two times greater than the net output work during most part of the cycle. It can also be observed that at the end of the cycle the regenerator heat is zero, which means that internal heat exchange is a reversible process where the heat accumulated will be transferred back to the working gas. This is an expected result based on the assumption that the regenerator (as a system) is an adiabatic component with respect to the surroundings. As a result, no residual heat should be present at the end of the cycle. The Adiabatic cycle efficiency was reduced to 61.8% from the 67.1% obtained in the Isothermal model. Conversely a slightly higher cycle net work (3,980 J) was obtained for the Adiabatic analysis compared to the Isothermal results (3,863 J). This can be justified if the working spaces are viewed as cells that undergo polytropic processes. Because the polytrophic constant for an adiabatic or quasi adiabatic process is higher, any adiabatic process will

tend to produce higher pressure variations per unit volume change than the ones produced by an isothermal process. The numerical solution can either be obtained by integration with respect to time or crank angle (θ), since the engine angular speed relates both variables and for the Adiabatic analysis it does not affect the results for sufficiently small steps of integration. The time dependence will become more relevant in the next section where non-ideal (or finite heat exchange) is considered in the cooler, regenerator and heater. In the following section, comparison of the three models used for the 1st Order method will be explored as well.

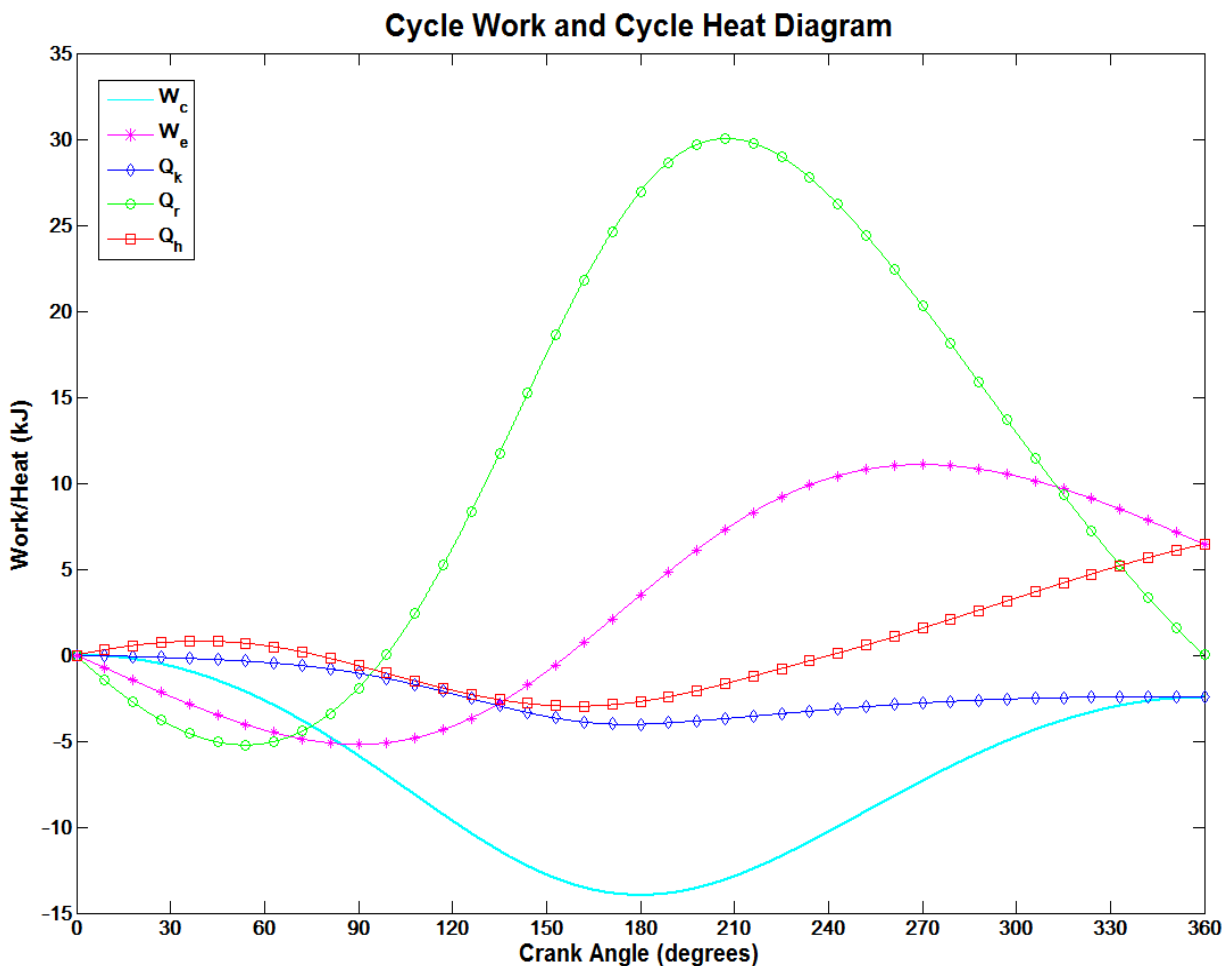


Figure 3-30: Cycle Work and Heat Diagram for Adiabatic Analysis

3.2.4 Finite Heat Transfer Analysis

If a 2nd Order method is used with any of the previous Isothermal or Adiabatic analyses, one will find that even when considering accurate engine losses the net engine performance will be over predicted. Therefore another important aspect needs to be

accounted for in the Stirling cycle analysis. Stirling engines are based on a thermal cycle working at a temperature differential (ΔT), if the ΔT increases the performance increases, in contrast a decrease in ΔT will result in lower performance. One of the main idealizations in the previous analysis is that the gas inside the heater volume is maintained at the heater wall temperature (T_{wh}) and that the gas inside the cooler volume is maintained at the cooler wall temperature (T_{wk}). This assumption requires an ideal infinite overall heat transfer coefficient (either infinite surface area or an infinite convection coefficient). In practice, heat exchangers interact with external thermal reservoirs; therefore, thermodynamic laws require thermal non-equilibrium for heat transfer to exist between the heat exchanger wall and the working gas. The result from the non-idealization is a T_h at a lower value than T_{wh} and a T_k at a higher value than T_{wk} , and since the temperature differential of the working gas is reduced a lower performance is obtained.

The analysis included in this section will consider forced convection heat transfer between the gas and the heat exchangers. The instantaneous convective heat transfer rate is calculated using Newton's law of cooling as:

$$\dot{Q} = hA(T_w - T_g) \quad (3.26)$$

The term Finite Heat Transfer analysis is given because now a determinate value of the overall heat transfer coefficient is considered in the heat exchangers, although the term non ideal heat exchangers is more commonly used in literature [4]. Another important aspect, is that various parameters for the Finite Heat Transfer analysis such as Reynolds number (Re), heat transfer convection coefficient (h), and heat transfer rate (\dot{Q}) are time dependent. Therefore, it is more convenient to solve all the unknown cycle parameters in the system of equations with respect to time rather than crank angle. Another noteworthy observation is that the average gas velocities in the heater, regenerator and cooler will be different at any instant of the cycle, due to the difference in temperature in the heat transfer spaces. Figure 3-31 plots the internal heat transfer coefficient of the heater, regenerator and cooler, vs. engine speed using the design heat exchanger data for the Ford-Phillips 4-215 engine (Section 2.4).

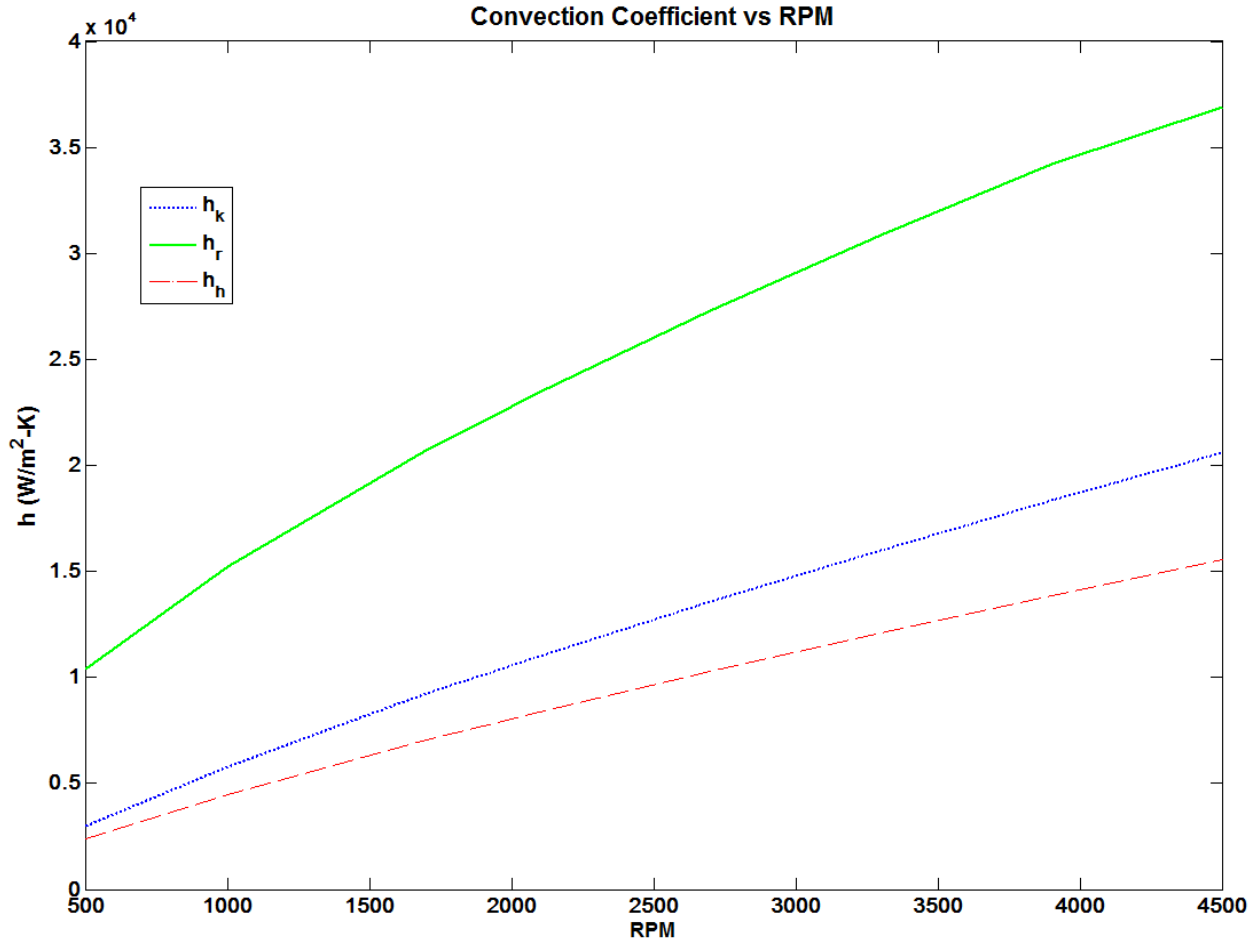


Figure 3-31: Internal Heat Transfer Characterization of the Ford-Phillips 4-215 engine

Discretization:

Instead of the five space component discretization model, the discretization for the Finite Heat Transfer analysis divides the regenerator into two or more cells as seen in Figure 3-32. As in the Isothermal and Adiabatic thermal models the regenerator gas temperature distribution is assumed linear. This allows for all the regenerator interface temperatures to be extrapolated by means of the effective gas temperature in each cell (T_{r1} and T_{r2} for two regenerator cells). The linear regenerator gas temperature distribution comes from the Quasi Steady Flow assumption. The actual gas flowing through the heat exchangers is periodic and unsteady. However, a quasi steady flow is assumed. Since flow conditions are assumed to be at quasi-steady state for small enough increments in time. Nevertheless the gas temperatures inside the heat exchangers (including the regenerator) can vary significantly over the cycle. The heater and cooler wall temperatures are

maintained isothermally at 1023 K and 337 K, respectively. The regenerator matrix cell temperatures are calculated using:

$$\frac{dT_{wr1}}{dt} = \frac{-\dot{Q}_{r1}}{\nabla_{mr}\rho_{mr}c_{mr}} \quad (3.27)$$

$$\frac{dT_{wr2}}{dt} = \frac{-\dot{Q}_{r2}}{\nabla_{mr}\rho_{mr}c_{mr}} \quad (3.28)$$

where ∇_{mr} is the solid volume of the matrix wire, ρ_{mr} is the density and c_{mr} is the specific heat of the matrix material. The equation for the temperature change of the matrix wire takes into account the thermal lag that exists between the regenerator matrix and the gas flowing in the regenerator volume. This is a proper way to describe the interaction between the matrix and gas inside the regenerator but the accuracy of the results is typically dependent of the number of regenerator cell divisions [4].

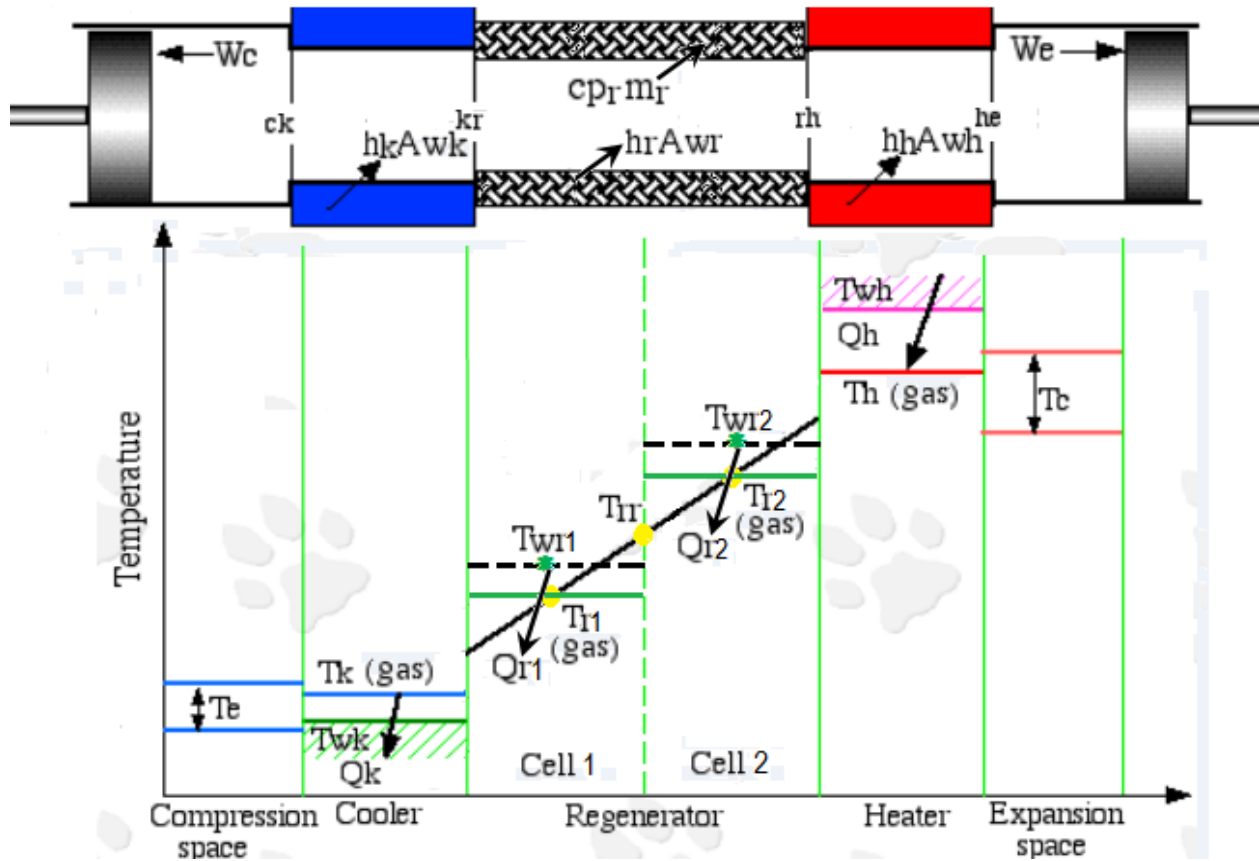


Figure 3-32: Five Component Model for Finite Heat Transfer Analysis (Modified from Urieli, [2011])

Assumptions:

- Quasi-steady flow model.
- Forced convection heat transfer inside the heat exchangers; with no external heat losses.
- Linear regenerator gas temperature distribution at any time instant. The following gas temperature extrapolation is conducted at the regenerator interfaces using the linear distribution:

$$T_{rk} = 1.5T_{r1} - 0.5T_{r2} \quad (3.29)$$

$$T_{rr} = 0.5(T_{r1} + T_{r2}) \quad (3.30)$$

$$T_{hr} = 1.5T_{r2} - 0.5T_{r1} \quad (3.31)$$

- Heater and Cooler wall temperatures remain constant cyclically and spatially.
- For the regenerator matrix, the heat conduction parallel to the flow direction is negligible compared to the heat conducted normal to the flow direction.
- The energy advection across the interfaces depends on the respective adjacent upstream cell temperatures. Temperature at the interfaces *ck* and *he* are determined using Eq. 3.24 and 3.25, similarly for interfaces *kr* and *rh* these are determined based on the following equations,

$$\text{if } \dot{m}_{kr} > 0 \Rightarrow T_{kr} = T_k; \quad \text{else} \Rightarrow T_{kr} = T_{rk} \quad (3.32)$$

$$\text{if } \dot{m}_{rh} > 0 \Rightarrow T_{rh} = T_{rh}; \quad \text{else} \Rightarrow T_{rh} = T_{hr} \quad (3.33)$$

Mathematical Model:

To model the convection heat transfer in the cooler and heater the Nusselt number (Nu) was calculated using the Gnielinski correlation [46], which should provide a reasonable estimation of the convection coefficients for circular heat exchangers used in Stirling engines. This correlation is convenient since it applies for cooling and heating at a constant (or uniform) temperature and is valid over a wide range of Reynolds numbers, including the transition region. The regenerator is characterized by flow through porous media; consequently classic pipe flow correlations are not applicable. In the regenerator, flow development, turbulence and other flow factors are dependent on the Reynolds number as well on the matrix porosity. Pittman [47] used the correlations of Gedeon and Wood for friction and heat transfer correlations in wire screen and metal felt regenerator matrices under oscillating flow conditions to calibrate other correlations developed under steady

state conditions. The Gedeon and Wood Nusselt number (Nu) correlation is defined by the Reynolds number, Prandtl number (Pr) and porosity (ϕ) [47]. An alternative correlation methodology is given by Martini [29]. However, to apply Martini's correlation involves interpreting data from a graphical representation in which various curves are given for different matrix porosities. The Gedeon-Wood correlation is preferred in the regenerator Nusselt number calculation, since the data is more recent, and the correlation is applicable for a wide range of porosity values (0.62 to 0.78) that are typical for regenerator wire screens. A comparison between Gedeon-Wood and Martini is demonstrated in Appendix C.2. The curves presented in Figure C-8 are for the matrix porosity of the Ford-Phillips 4-215 regenerator ($\phi = 0.62$) and the matrix porosity for which Martini's [29] gives a correlation equation ($\phi = 0.717$). The correlations and equations used in order to calculate the heat transfer coefficients in the Finite Heat Transfer analysis are presented in Table C-3 of Appendix C.2.

The algorithm flow chart (Fig. C-1 and C-2) used to solve the Finite Heat Transfer problem is shown in Appendix C.1. In addition Appendix C.1 contains the system of equations for the Finite Heat Transfer analysis (Table C-1). Table C-1 contains 37 equations for which 14 are differential equations. Compared to the Adiabatic model 6 additional variables have to be integrated with respect to time over the cycle: heater mass (m_h), cooler mass (m_k), regenerator cell masses (m_{r1} and m_{r2}), regenerator matrix cell temperatures (T_{wr1} and T_{wr2}). Also the regenerator heat is divided between two cells (Q_{r1} and Q_{r2}). The regenerator net heat is obtained by simply adding both values.

The approach used for solving the system of equations in the Finite Heat Transfer model is basically the same as the Adiabatic analysis previously shown. However, the 4th order Runge-Kutta method should be checked for stability, convergence and accuracy owing to the larger size of the system of equations. The heat transfer coefficient is evaluated at each time step. Also, divergence problems may occur for analysis at low engine RPM. Urieli points out that cycle convergence using the 4th order Runge-Kutta method will be rather slow, requiring several hundreds of iterations to achieve cyclic steady state [4]. The slow convergence is associated with the high thermal capacitance in high performance regenerators, which minimizes the matrix temperature variation. Urieli suggests a

convergence accelerating technique that uses the net residual regenerator heat transfer between the gas and matrix. This is done to modify the matrix cell temperatures at the end of each cycle as described in the following equations,

$$T_{wr1}^{j+1}(0^\circ) = T_{wr1}^j(360^\circ) - ACF[Q_{r1}^j(360^\circ)/C_{mr1}] \quad (3.34)$$

$$T_{wr2}^{j+1}(0^\circ) = T_{wr2}^j(360^\circ) - ACF[Q_{r2}^j(360^\circ)/C_{mr2}] \quad (3.35)$$

where Q_{r1}^j and Q_{r2}^j are the net residual heat of the regenerator cells at the end of cycle, C_{mr1} and C_{mr2} are the regenerator heat capacities of the regenerator cells and ACF is an arbitrary factor used to accelerate the convergence. Another accelerating technique was used by Shock [48, 49] in his nodal analysis of SE. The technique is described to divide the matrix regenerator heat capacity by accelerating factors that diminish to unity with time. However, few mathematical details are given on how Shock's method was implemented.

Thermal Results:

The thermal results presented for the Finite Heat Transfer analysis were obtained at 4500 RPM. Computing time per iteration cycle and the total number of iterations for convergence significantly increased relative to the Adiabatic model. Urieli's approach for accelerating convergence was applied [4], and after determining (by trial and error) an optimum ACF value of 7, cycle iterations were reduced from 427 (when ACF=0) to 63. Cycle gas temperatures, temperatures at interfaces, work and heat are presented in Figure 3–33 to Figure 3–35.

The gas temperature variation through the cycle as well to the wall temperatures of the heat exchangers are shown in Figure 3–33. One aspect that highlights the importance of finite heat transfer is observed in Figure 3–33, where the heater gas temperature variation (~142K) is as large as the temperature variation at the expansion space (~195K). Thus pointing out that the heater is a limiting component in the Stirling engine and that the Ford-Phillips 4-215 heater can be further optimized. The cooler temperature change (~30K) is relatively small compared to the change in compression space temperature (~72K). The Ford-Phillips 4-215 cooler seems to have a more appropriate heat exchanger design regarding minimization of gas temperature variation. The regenerator is shown to be the superior component with its high effectiveness, having a temperature differential of less

than 2.5K (between matrix and gas) and a gas temperature cycle variation of approximately 25K. As predicted in the beginning of this section, in real Stirling machines there is substantial temperature difference for the gas from that of the heat exchangers walls (especially in the heater) that will ultimately lower engine performance.

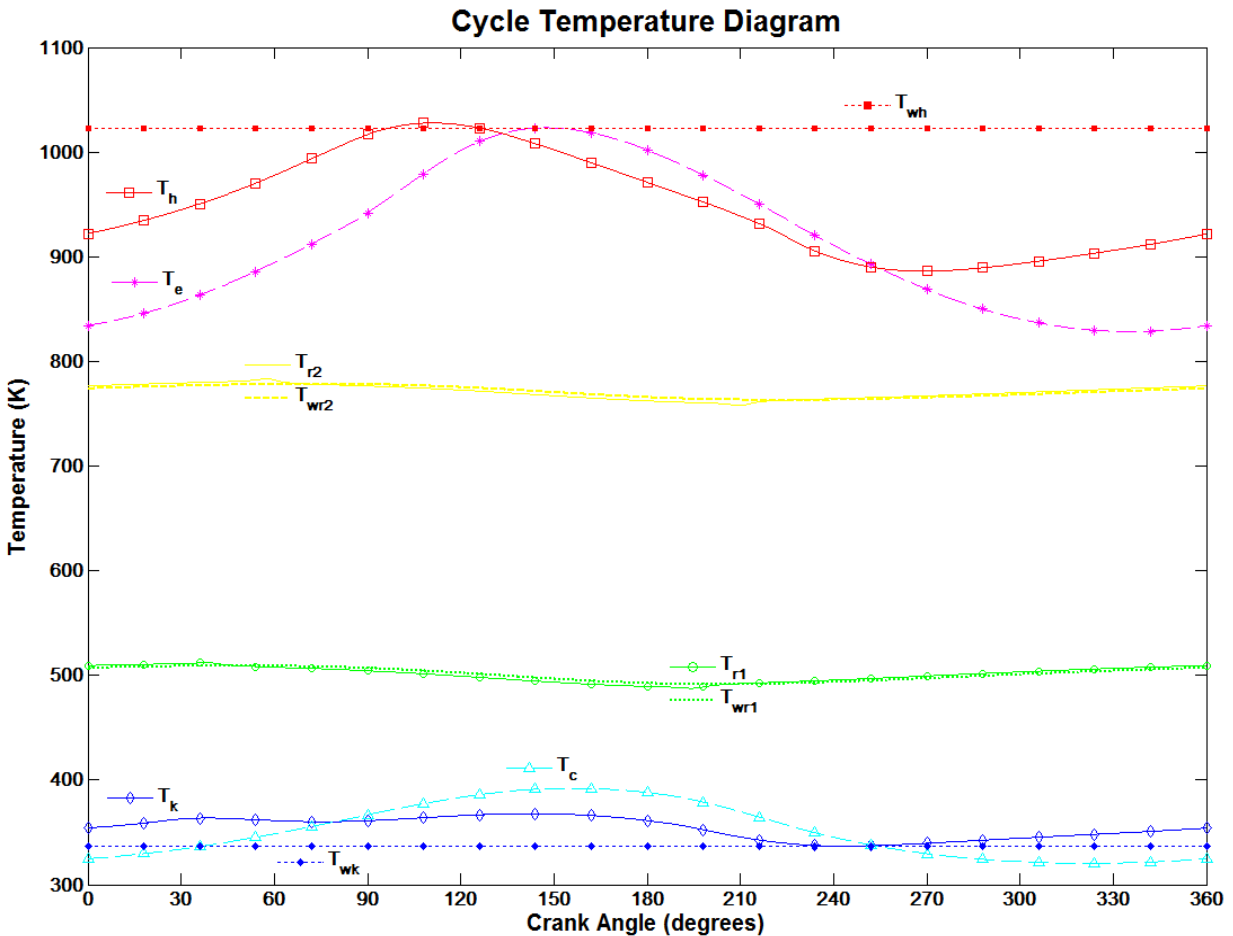


Figure 3–33: Cycle Temperature Diagram for Finite heat Transfer Analysis

Figure 3–34 shows the interface temperatures versus crank angle using the Finite Heat Transfer model. In contrast with the Adiabatic model, interface temperatures do not remain constant in some range within the cycle (refer to Figure 3–26) since the gas in the heater and cooler are no longer isothermal. The temperature response of the interface T_{rr} is an added benefit of this formulation as compared to the previous models. The gas temperature at the regenerator mid location experiences very small variation during the cycle. As for the Adiabatic analysis, the plot is useful in determining the flow reversals and the effect on enthalpy transport through the boundaries.

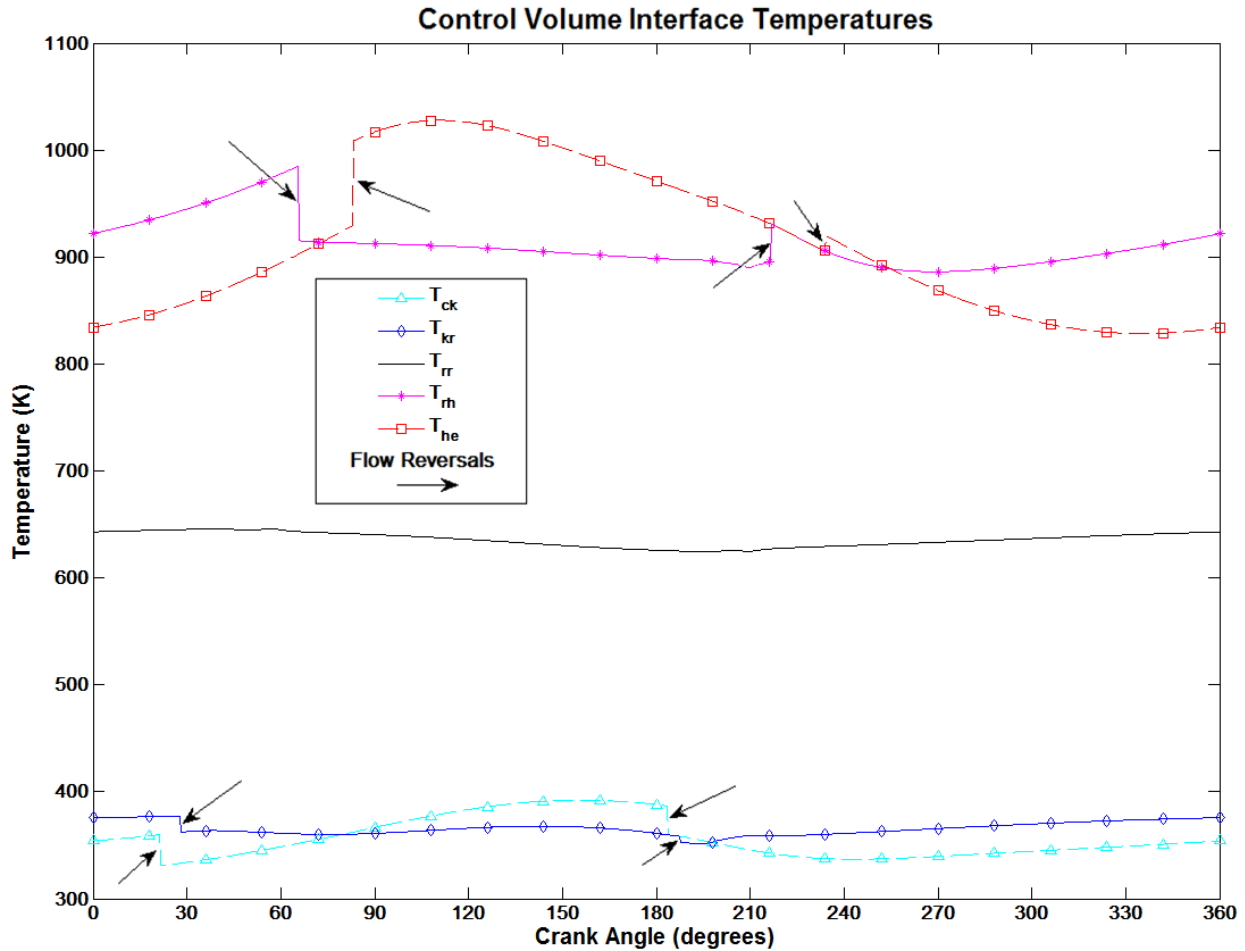


Figure 3–34: Control Volume Interface Temperature Variation for Finite Heat Transfer Analysis

To have a better understanding of how the progress is made toward the real solution of engine performance (by implementing more realistic assumptions), results for the Finite Heat Transfer model are compared with the Adiabatic and Isothermal models. Cycle work and heat as a function of crank angle for the Finite Heat Transfer and Adiabatic analyses are presented in Figure 3–35. Compression and expansion work are observed to have a similar variation along the cycle for both cases. This means that in general, the working space thermal modeling and the piston motion (working space volume variation) will determine the behavior of cycle work.

For the heat exchangers this is not case since the design will affect both the overall heat transfer coefficient and the gas temperature (e.g. size of heat transfer area). The heat load from the heater has increased and is maintained for a longer period in the cycle in comparison with the Adiabatic analysis, in order to achieve somewhat less expansion work.

The opposite occurs in the cooler, and to an extent, more compression work is done. The regenerator heat through the cycle is reduced by roughly 20% relative to the Adiabatic model. Although a lower value would be expected, due to the difference in matrix and gas temperature, accuracy in the regenerator may be evaluated by adding more regenerator cells. Following the approach implemented in discretization methods, cells can be added until the results remain unchanged. Higher accuracy comes at the expense of increased computing time, and for optimization purposes only a regenerator divided into two cells will be considered. Further discretization will require the other heat exchangers to be divided into cells as well for the analysis to be consistent and meaningful. Increased discretization of the control volumes is used to consider the spatial (or axial) variations in the engine and is applied in Third Order methods, which are out of the scope of this work.

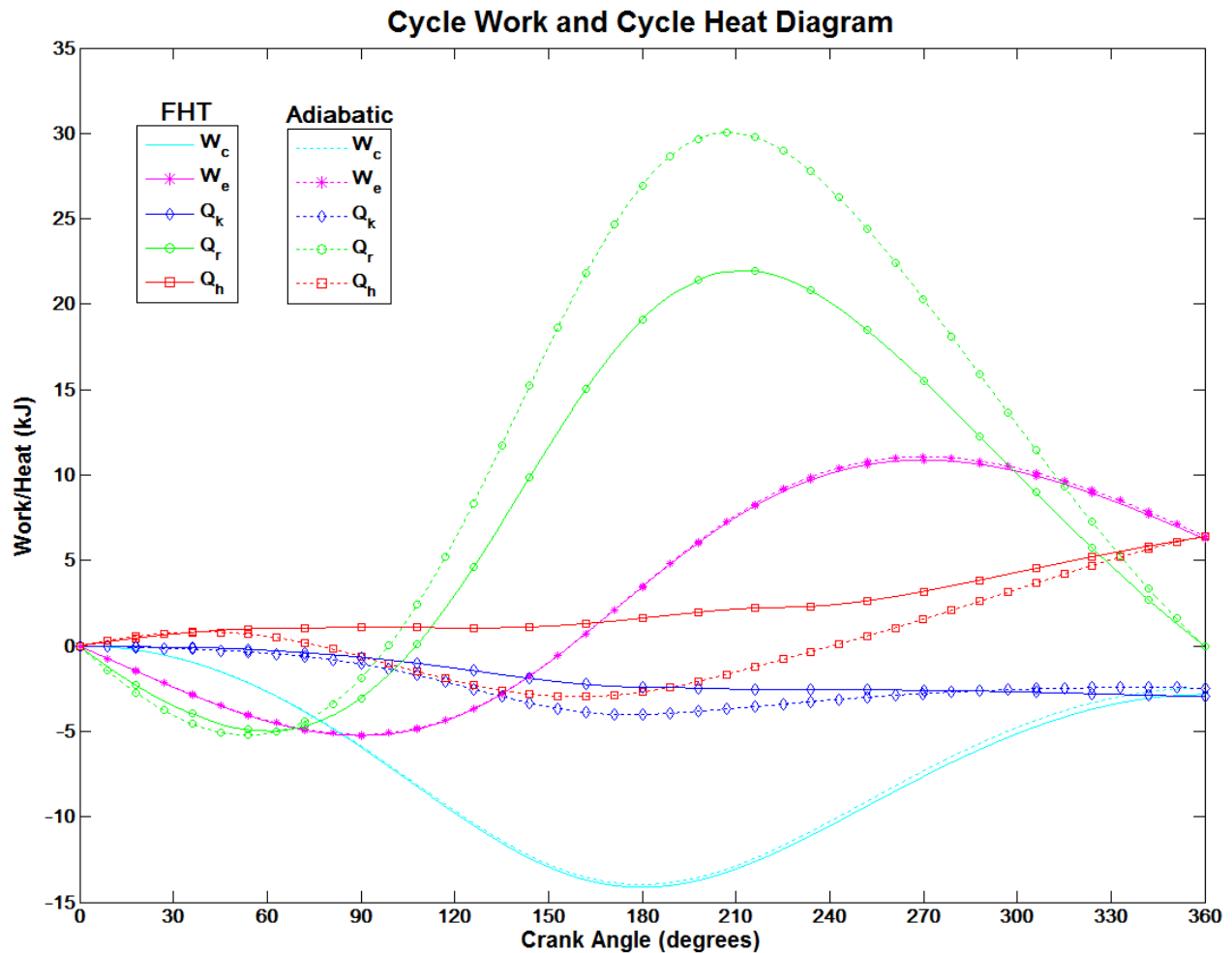


Figure 3-35: Cycle Work and Heat Comparison between Finite Heat Transfer & Adiabatic Analysis

The power of the engine running at 4500 RPM was estimated at 256 kW with 53.53% efficiency. The irreversibilities considered in the Finite Heat Transfer model affect both the cycle work and efficiency and shows that internal heat transfer is an important aspect of the Stirling engine design that should not be overlooked. The results of the three analyses considered here for 1st Order methods are compared using the Ford-Phillips 4-215 field engine data (at 4500 RPM) provided by Urieli [4] and Hargreaves [13]. The results for the three methods considered show a significant difference when compared to the engine test data. This indicates that improvements to the methodology should be implemented with the objective of improving the predictive capability of the numerical model. This is the motivation for developing a 2nd Order method as it will be discussed in the next section.

Table 3–6: Comparison of Engine Performance Results for 1st Order Methods at 4500 RPM

Performance Parameter	1 st Order Methods			¹ Engine Test Data
	Isothermal	Adiabatic	Finite Heat Transfer	
Cycle Mean Pressure (bar)	148.8	148.95	147.54	150
Heat Input (J)	5724.9	6443.8	6391.7	² 8720
Net Cycle Work (J)	3840.0	3979.9	3421.5	2093
Engine Power (kW)	288	298	256.5	157
Cycle Efficiency (%)	67.1	61.76	53.53	³ 24

¹ Performance Data [Urieli, 1984] ² Calculated from Cycle Efficiency and Engine Power ³ Muschel Diagram Efficiency [Hargreaves, 1991]

The P- ∇ diagram is used in Figure 3–36, to further analyze the results from the 1st Order method models. The Ideal cycle encloses the larger area, restricted by the minimum and maximum volume limits, in the horizontal axis, and the heater (high) and cooler (lower) temperature in the vertical axis. The larger area is determined by the heater and cooler isothermal temperatures that the entire gas is assumed to be at during the expansion and compression processes, respectively. In the Isothermal analysis, although the Ideal efficiency is maintained due to the working spaces being isothermal, the gas is now only homogenous at the individual cells. Therefore, gas thermal mixing occurs and the regenerator temperature will significantly reduce the “effective” temperature. This explains that the Isothermal analysis is enclosed by vertical limits inside the Ideal P- ∇ diagram. The same can be said for the Adiabatic and the Finite Heat Transfer (FHT) analysis. However,

since the temperature at the working spaces is no longer isothermal, the efficiency decreases from the Ideal limit.

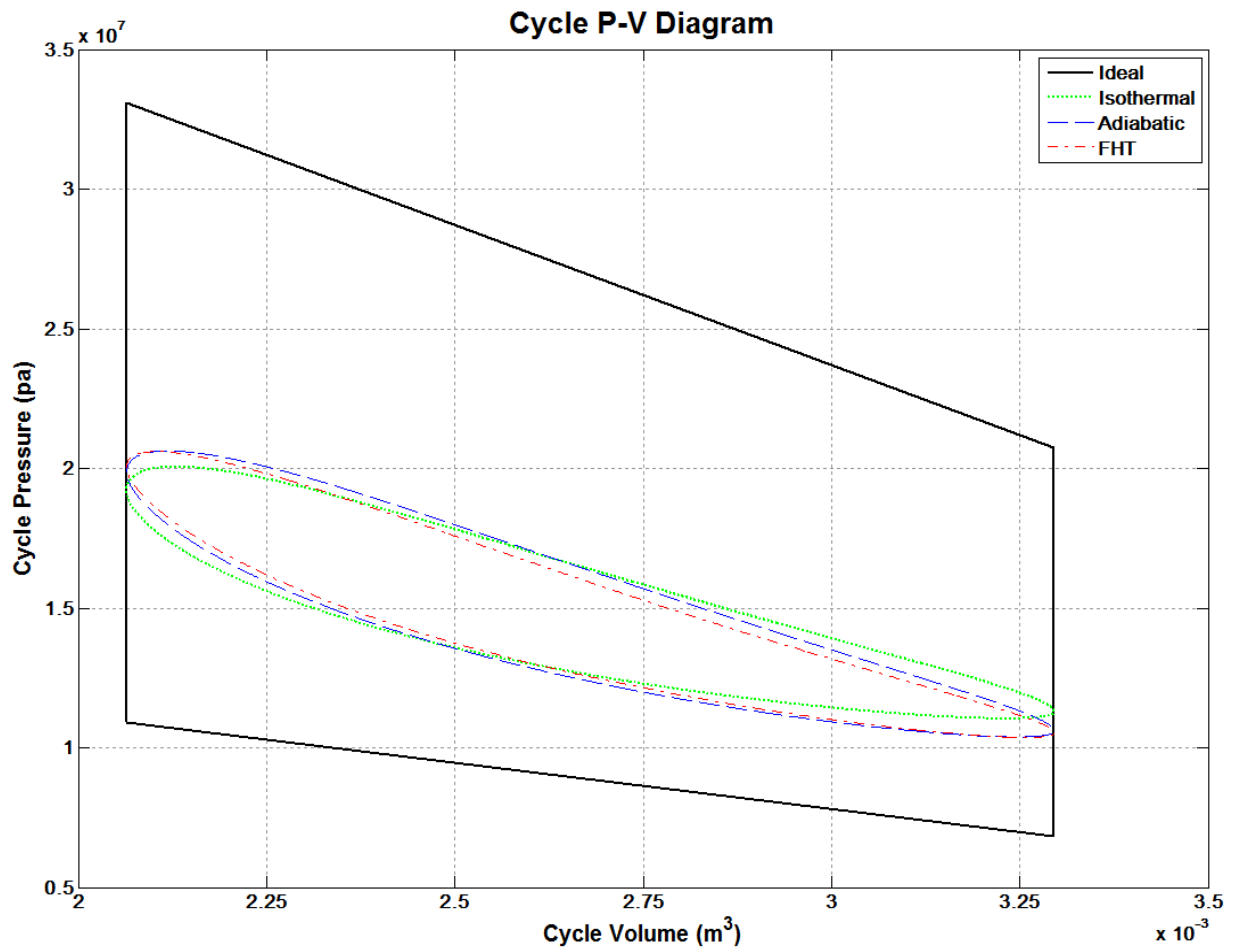


Figure 3–36: Ideal Cycle, Isothermal, Adiabatic, and Finite Heat Transfer P-V Diagrams

3.3 Second Order Methods

In 2nd Order methods the different performance losses are assumed to be decoupled and thus the loss calculations are performed separately from the engine cycle processes [29-31]. The intent of this methodology is to account for pressure loss due to gas friction in the heat exchangers, mechanical friction from piston and cylinder, heat losses in the regenerator and any other energy wasted in the engine.

The procedure is shown in Figure D–1 by means of a flow chart in Appendix D.1. Once the engine performance is obtained from a 1st Order method (e. g. Adiabatic), all the necessary (or significant) energy deficits are estimated by the respective equations that govern their loss mechanisms. Then, the losses that reduce the engine ability to do work

are grouped into power losses, and the losses related to heat transfer are grouped into heat losses (refer to sect 2.3). Finally, the 1st Order Method results are modified by subtracting the power losses to the Ideal net work and by adding the heat losses to the Ideal heat input. As a result, lower net output work and lower cycle efficiency are obtained. This approach makes the 2nd Order method a reasonable model to implement for engine optimization.

The following analysis considers the pressure drop in the heat exchangers due to flow friction, mechanical friction, and heat loss from the regenerator as loss mechanisms that affect engine performance. The Adiabatic results are used for the 2nd Order loss calculations. Each topic will be discussed separately in the subsequent sections (3.3.1-3.3.3) and the final 2nd Order performance predictions are presented in Section 3.3.4.

3.3.1 Pressure Losses

In this study, pressure loss refers to the pressure drop the actual heat exchangers will experience due to fluid friction. To consider the pressure loss due to fluid friction, both minor and major losses associated with the geometry of the heater and cooler and the regenerator matrix need to be considered. Figure 3–37 depicts diagrams of the basic cooler (a) and heater (b) geometry with the respective major and minor losses. The cooler design for the Ford-Phillips 4-215 engine consists of two shell and tube heat exchangers connected in parallel to the compression space by a manifold. Each shell and tube has 371 parallel tubes that extend to the regenerator casing. As seen in the diagram, entrance contraction and exit expansion will cause minor losses in the cooler and major losses will be present along the cooler tubes. From the cooler design specifications (Table 2–4) and the diagram, it can be inferred that the parallel shell and tube design will minimize the pressure drop in the cooler. Heat is supplied from a helical heater-tube cage [13] made of a total of 88 individual heater tubes [29]. The heater tubes are configured symmetrically; therefore, there are 22 per cylinder. For the heater, minor losses will consist of the loss coefficients for the 180° bend and either exit or entrance loss depending on the direction of the flow. Note that the losses at the expansion and compression cylinders are insignificant due to the small velocities. The Ford-Phillips 4-215 heater design data is specified in Table 2–4 (Chapter 2).

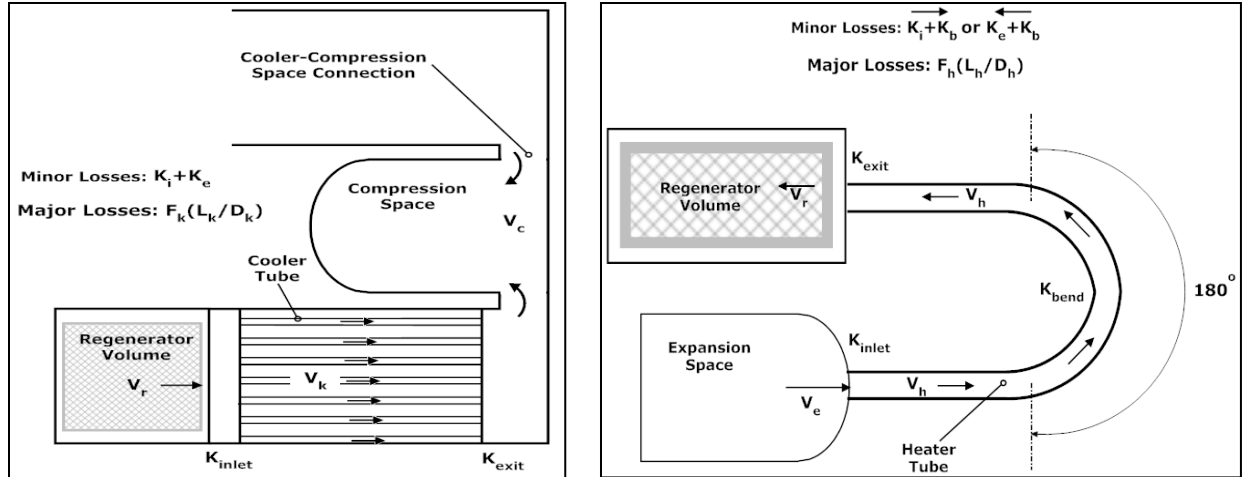


Figure 3-37: (a) Cooler Diagram Depicting Major & Minor Losses (b) Heater Diagram Depicting Major & Minor Losses

The pressure drop in the regenerator is another aspect that causes considerable engine power loss. Flow through the regenerator matrix is governed by the physics of flow through porous media. Gas flow inside porous materials is generally irregular and difficult to analyze. However, since the regenerator wire screens used in typical Stirling engines are axisymmetric and the regenerator matrix is formed by stacking multiple screens of the same type; flow behavior is more predictable than irregular mediums. In the design methodology devised by Martini in the *Stirling Engine Design Manual* [29], a graphical correlation for the Fanning friction factor for woven wire screens and screens with crossed rods is shown as in Figure 3-38. Martini also suggested equations 3.36 to 3.38 as an approximation for screens with porosities ranging from 0.6 to 0.83 (values that are typical for porous matrices in regenerators).

$$\log(F_r) = 1.73 - 0.98 \cdot \log(Re); \quad Re < 60 \quad (3.36)$$

$$\log(F_r) = 0.714 - 0.365 \cdot \log(Re); \quad 60 < Re < 1000 \quad (3.37)$$

$$\log(F_r) = 0.015 - 0.125 \cdot \log(Re); \quad Re > 1000 \quad (3.38)$$

The Reynolds number (Re) for the regenerator is defined as follows,

$$Re_r = \frac{\rho_r Vel_r D_{h,r}}{\mu_r} = \frac{G_r D_{h,r}}{\mu_r} \quad (3.39)$$

Where ρ_r , μ_r , Vel_r , G_r and $D_{h,r}$ are the density, kinematic viscosity, average porous velocity, mass flux, and hydraulic diameter, respectively. The regenerator Re (Eq. 3.39), at glance

appears to be the same as for pipe flows. However, the hydraulic diameter ($D_{h,r}$) is determined by the matrix wire screen porosity (ϕ) and wire diameter (d_w),

$$D_{h,r} = d_w \frac{\phi}{(\phi - 1)} \quad (3.40)$$

Martini's correlation was compared to the Pinker and Herbert's correlation [50] for wire screens without entrance/exit effects. In addition the Darcy and Darcy-Forchheimer Laws for unidirectional permeable flow are used to validate the correlations. The comparison of regenerator pressure drop correlations to the porous medium Laws is shown in Figure D-6 (Appendix D.2), for a constant engine speed of 4500 RPM. Martini's correlation approximates the Darcy and Darcy-Forchheimer curves. However, the Pinker and Herbert correlation underestimates the results by more than a factor of three. It can be inferred that the underestimation is due to the fact that the correlation does not consider entrance and exit effects. For the pressure drop evaluation in the 2nd Order method, Martini's correlation is preferred not only for being more accurate. Also, Pinker and Herbert's correlation is developed for fluid flow in electronic equipment design [50] and Martini's correlation [29] maintains the consistency of SE analysis methods. The correlation comparison and validation is discussed with more detail in Appendix D.2.

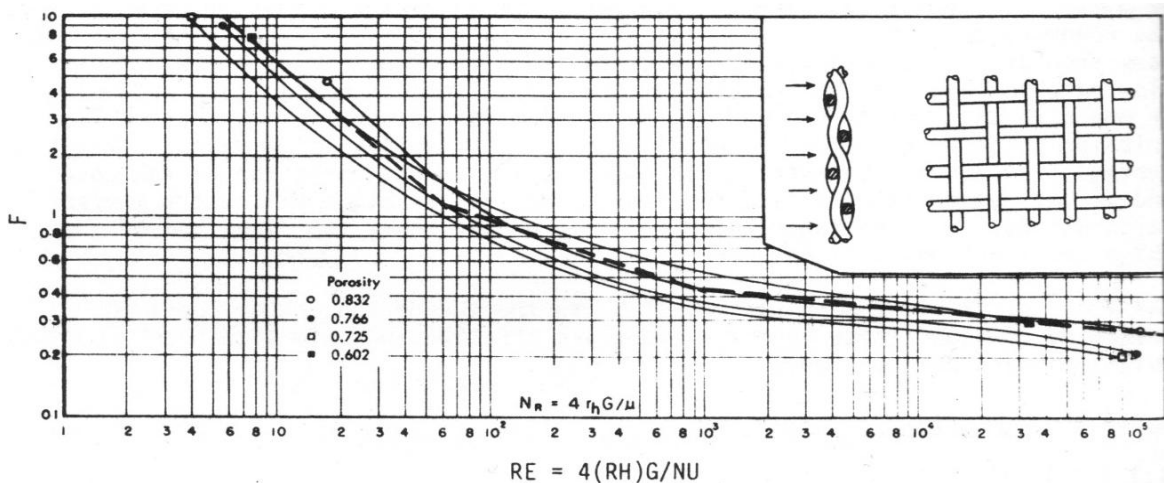


Figure 3-38: Flow through a Woven-Screen Matrix (Martini, [1983])

The characterization of the pressure drop and the pumping power loss associated with the cooler, heater and regenerator is shown in Figure 3-39 (a) and (b), respectively. The results are for the engine operating at 4500 RPM. The pressure drop in the heater is large

compared to the regenerator and cooler owed to the long tube size required for the heater tubes, since a small number of parallel tubes are used (22 tubes). The pressure deficit in the cooler is about 22% less relative to the regenerator. To determine the pumping power losses the following expression is used,

$$\dot{W}_{pl} = \Delta p_{loss} \cdot \dot{V} = \Delta p_{loss} \cdot \left\{ V \left(\frac{\dot{m}}{m} \right) \right\} \quad (3.41)$$

The resulting pumping power loss is also a function of the volumetric flow rate at the respective heat exchanger. As seen in Table 3–7 the volumetric flow rate changes are comparable for heat exchangers. The amount of difference is directly related to air density occurring at the cooler, regenerator and heater since the gas experiences large temperature changes as it crosses the boundaries. The pumping power loss in Figure 3–39 (b) shows that the high pressure drop in the heater also results in the highest pumping power loss (about 3 times that of the regenerator). The total \dot{W}_{pl} is the sum of the individual power losses [29].

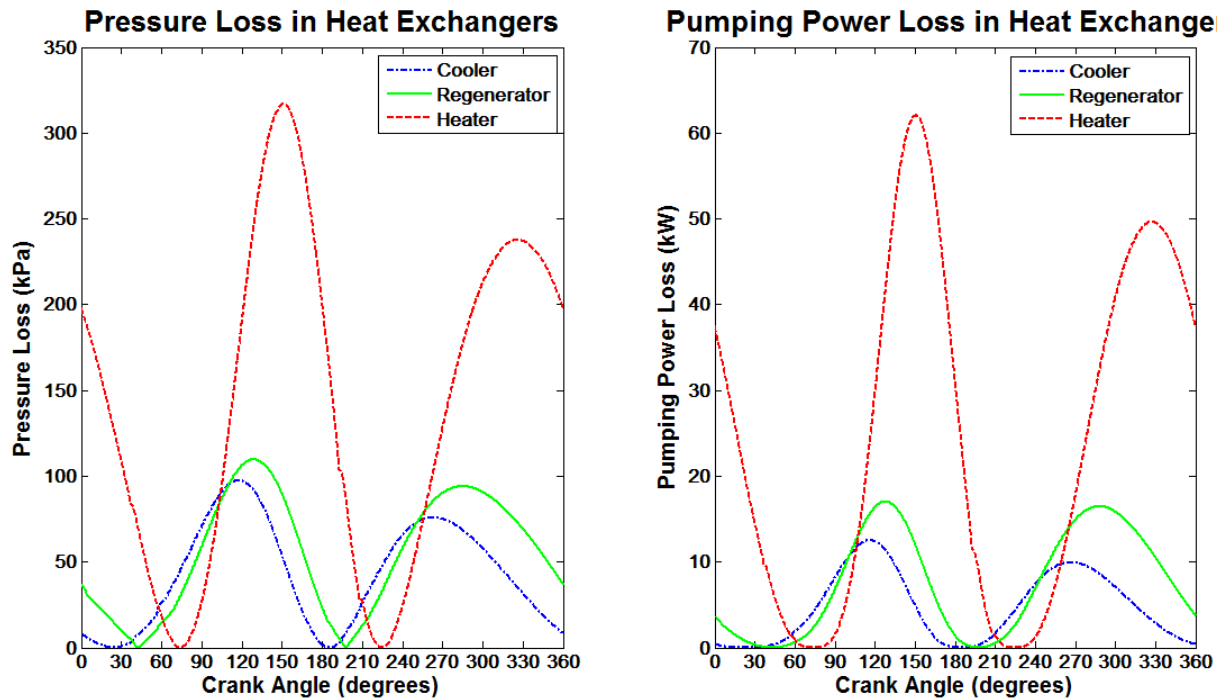


Figure 3–39: (a) Pressure Drop in Heat Exchangers (b) Pumping Power Loss in Heat Exchangers

Table 3–7: Summary of 2nd Order Pumping Pressure Loss at 4500 RPM

Parameter	Cooler	Regenerator	Heater
Average Re	3.88×10^4	92.98	5.61×10^4
Average ΔP (kPa)	42.94	54.79	140.4
Average \dot{V} (m ³ /s)	8.37×10^{-2}	1.07×10^{-1}	1.31×10^{-1}
Average \dot{W}_{pl} (kW)	4.73	7.52	24.02

3.3.2 Mechanical Losses

Mechanical friction associated with various surfaces that are in contact and dynamically rubbing each other (e.g. piston ring-cylinder, rod-piston connection, etc.) are also responsible for a significant amount of engine power loss. The approach followed here does not attempt to find an accurate prediction. Since a laborious analysis will depend on engine detail that might not be available. Another reason to consider a general estimate for mechanical power loss is that a detailed approach for a current mechanical scheme will not be applicable for a new mechanical design. Therefore a more general approach that applies to a wide range of Alpha SE was adopted. Results are much less accurate, rather reasonable according to the purpose of this study.

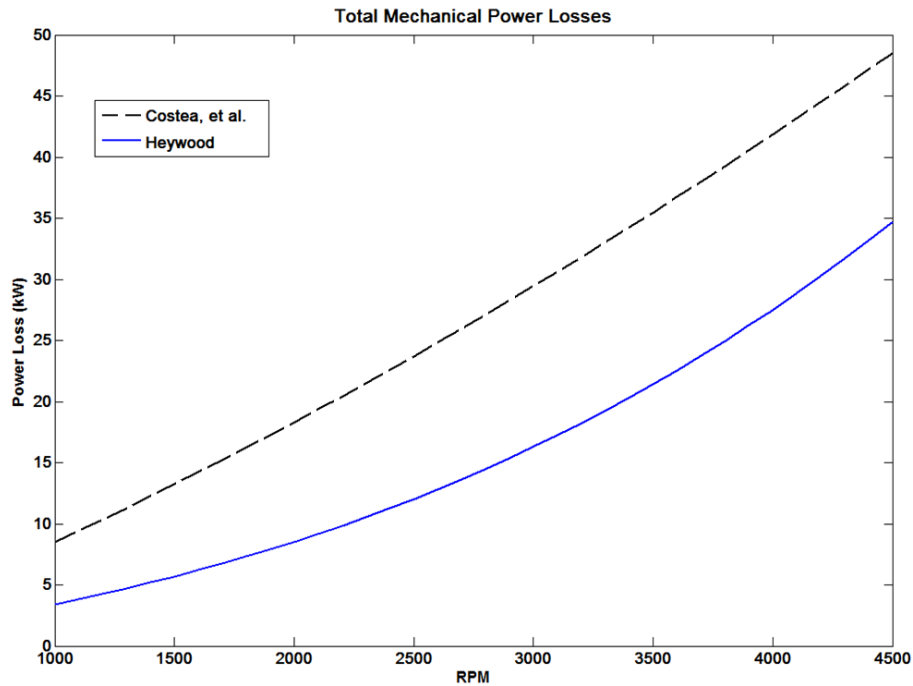


Figure 3–40: Mechanical Power Loss Estimation

Figure 3–40 shows a comparison between correlations given by Heywood [51] and Costea et al. [52] for mechanical friction loss estimation. Both formulas are further explained in Appendix D.3. The expression provided by Heywood [51] was derived for internal combustion (IC) engines that are spark ignited and considers that the total mechanical loss is divided in the following categories:

- *Boundary Friction*: Dry friction resulting from surface to surface contact.
- *Hydrodynamic Friction*: Viscous friction in well lubricated surfaces that are in relative motion.
- *Turbulent Dissipation*: Work associated with driving the engine accessories (pumping and moving fluids).

It is shown that for IC engines, boundary friction is a constant value independent of engine speed, that hydrodynamic friction is directly proportional to engine speed, and that turbulent dissipation depends on the engine speed squared [51]. With this approach, Eq. 3.42 can relate the loss in mean effective pressure (or mean pressure for SE) to engine speed in revolutions per second.

$$\Delta p_{ml} = C_1 + C_2 N + C_3 N^2 \quad (3.42)$$

The constants in the equation (C_1 , C_2 , and C_3) are found from engine data obtained from either a firing engine test (indicated and brake power are measured) or direct motored engine test (power consumed by friction is measured) [13]. For both SE and IC engines these standardized tests are used to measure the mechanical efficiency. Also Costea et al. [52] provide estimation for the mechanical friction present in the components of a solar SE. Costea et al. claims to have adapted the experimental estimates for IC to actual data from Stirling engines. Costea’s loss estimation over predicts the predicted values by Heywood (Fig. 3-45) significantly. However, considering that Hargreaves states an estimated value of 37 kW for overcoming friction and drive engine auxiliaries at the design 127 kW brake power [13], the magnitude of Costea’s loss estimates agrees with considerations taken in the Ford-Philips 4-125 general design. Based on these findings, the Costea’s mechanical friction loss model was used to estimate mechanical power loss in this study. After obtaining the power loss due to mechanical friction (from Costea et al. [52]), the indicated

power is simply the brake power output plus the power loss. Therefore, the efficiency (ratio of brake power to indicated power) can be express as:

$$\eta_{mec} = \dot{W}_b / \dot{W}_i = \dot{W}_b / (\dot{W}_b + \dot{W}_{ml}) \quad (3.43)$$

Brake power and percentage mechanical loss for the Ford Philip's 4-215 DA swashplate engine is displayed on Figure 3-41 (a) and (b), respectively. The brake power is obtained from engine data provided by Urieli [4] when the engine is working at a mean pressure of 150 bar and constant engine speeds, ranging from 1700 to 4500 RPM. According to the purpose of this work, the mechanical loss has more relevance than the mechanical efficiency, since the individual engine power and heat losses should be compared. Another reason is that the estimated mechanical efficiency might not be meaningful due to the high degree of approximation in the approach. The mechanical loss is calculated as follows,

$$\%W_{ml} = \dot{W}_{ml} / \dot{W}_i = 1 - \eta_{mec} \quad (3.44)$$

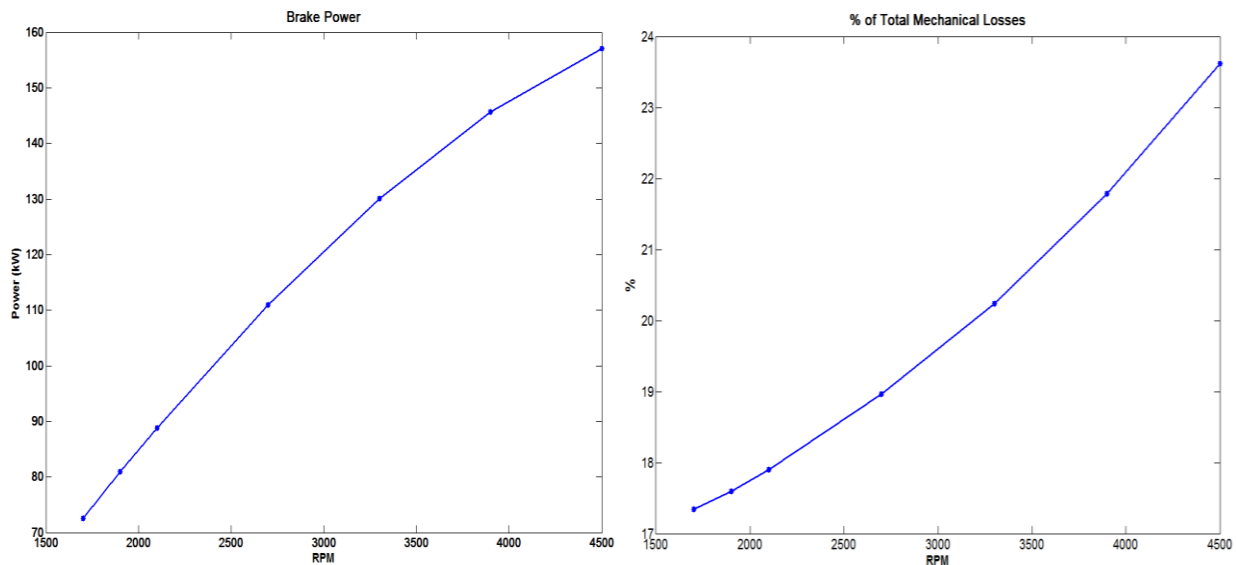


Figure 3-41: (a) 4-215 DA Brake Power (b) 4-215 DA Mechanical Loss from Costea

Although the author of this work recognizes that precise values of mechanical losses give more validity to the final net performance prediction, measurement data on indicated power, mechanical efficiency or mechanical friction power expenditure was not available for the Ford Philips 4-215 engine. However, according to data presented by Hargreaves [13] for a Stirling engines operating close and above 1000 RPM tend to have mechanical losses around 15%. In the case of the Philips Allison 9-30 engine, the curve surpasses 20% losses

at approximately 2700 RPM [13]. Kagawa et al. [53] is another literary source that published considerably high power losses for the NS03T engine mechanical system. The NS03T was a V type Alpha SE studied during the 1980s for endurance and performance improvement. The detailed mechanical analysis of the NS03T (operated at a considerable lower RPM) showed mechanical losses comparable to the results of Figure 3–41 (b) for the Ford Philips 4-215 engine.

It is recommended that before implementing any approximation on mechanical losses, the analyst or designer uses good judgment on the degree these losses will affect the particular configuration under consideration. For example, the Beale free-piston engine (refer to Figure 2–7) has no mechanical linkages. For this type of SE the only possible mechanical losses is friction caused by the power piston and the seal at the cylinder wall and whatever external gas leakage may be present. With this in mind, it is reasonable for a 2nd Order analysis not to consider the mechanical losses for a free-piston engine.

3.3.3 Heat Losses

In this section heat losses are referred to all the thermal heat energy that is not useful to the working gas and is wasted on the engine. As a consequence of heat loss, cycle thermal efficiency decreases by placing an additional load on the heat source. Therefore, it is assumed that heat supplied through the heater is actually the basic input to maintain the heater temperature (or operating temperature) plus the heat wasted on the engine.

One such loss is the regenerator heat deficit that arises from the fact that not all energy from convection can be effectively transferred from the regenerator to the gas and vice versa. In all previous analysis the regenerator was assumed to be perfect, meaning that it was 100% effective. As discussed in Sect. 3.1.3, the deviation encountered in imperfect regeneration can significantly reduce the engine efficiency. Figure 3–42 shows the effect that imperfect regeneration has on the temperature profile of the regenerator. For point of reference, it is assumed that the first blow is when the gas is flowing from the cold side to the hot side of the regenerator. In this case the gas flowing from the cooler at T_k will not effectively absorb all the heat from the regenerator and therefore exits at a lower temperature than T_h . In the second blow the gas supplied at T_h from the heater does not

effectively transmit all the energy to the heater and therefore exits at a higher temperature than T_k . The impact from the regenerator ineffectiveness, is a higher supplied heat requirement over the cycle by the heater and an extra cooling load burdened on the cooler [54], which can be quantified by Eq. 3.45 and 3.46, respectively.

$$Q_h^{2nd} = Q_h^{1st} + Q_{rl} = Q_h^{1st} + Q_r(1 - \varepsilon) \quad (3.45)$$

$$Q_k^{2nd} = Q_k^{1st} - Q_{rl} = Q_k^{1st} - Q_r(1 - \varepsilon) \quad (3.46)$$

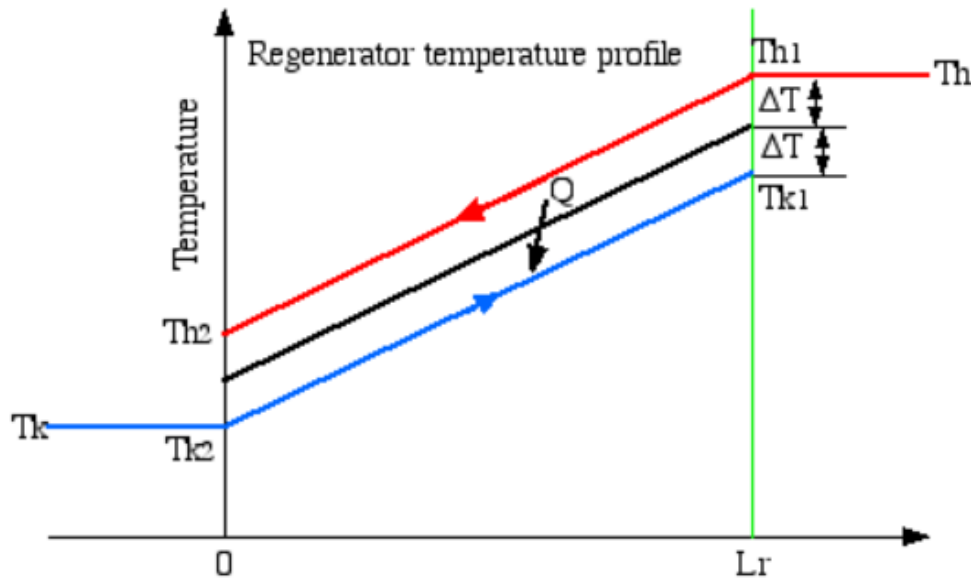


Figure 3-42: Regenerator Temperature Profile for Imperfect Regeneration (Modified from Urieli, [2011])

The behavior of cycle efficiency vs. regenerator effectiveness (ε) was studied in Section 3.1.3, by applying arbitrary ε values from 0 to 1 for different engine compression ratios and temperature ratios (refer to Figure 3-11 to Figure 3-14). In the 2nd Order Method it is desired to obtain a value from engine parameters associated with the heat transfer in the regenerator. Many authors have used the concept of Number of Transfer Units (NTU) along with their own concepts of maximum theoretical enthalpy change in order to define regenerator effectiveness. Various general expressions found in the literature for regenerator NTU and ε are resumed in Table D-3. More information is given in Appendix D.4 on the methodology used in the application of the NTU and ε expressions in order to find the regenerator heat loss.

Results for each expression are demonstrated in Figure 3-43, where NTU and ε variation at first blow (cold to hot regenerator flow) is considered at 4500 RPM. Urieli and

Martini's expressions for NTU are similar except for the use of C_p or C_v , which is the major cause behind their differences. In contrast, Organ-Finkelstein has a completely different behavior in the first blow. The reason is that the convective effect (heat transfer coefficient) dominates the change in transferred heat. The convective effect is the same for the three correlations (see equations D.13 (a) to D.13 (c)). However, the change in transferred heat is expressed significantly different in Organ-Finkelstein's correlation, since the engine operating frequency (Hz) and the instantaneous regenerator gas mass determined it. In contrast, the flow quantities for Urieli and Martini's correlations come from average values at the boundaries. The result obtained from Organ-Finkelstein agrees more with practical sense, since the most effective heat transfer should occur at some point between the start and end of the first blow, that is indicated when the highest NTU (or effectiveness) occurs.

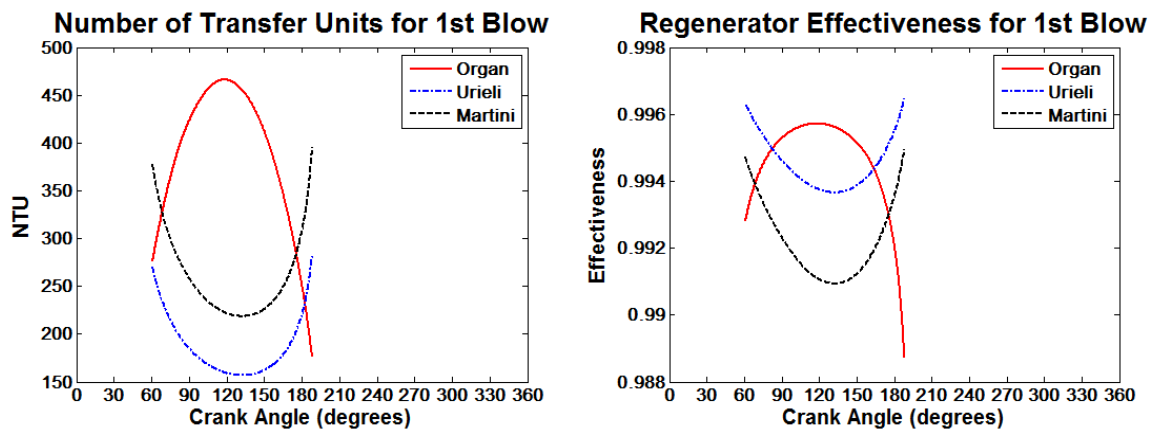


Figure 3-43: (a) Regenerator NTU for First Blow at 4500 RPM (b) Regenerator Effectiveness for First Blow at 4500 RPM

It was found that in some instances (specially, at high engine operating frequencies) the Organ-Finkelstein approach overestimated the regenerator heat loss. As a result, the present study uses Martini's estimation of the regenerator heat loss (or reheat loss) to account for 2nd Order cycle efficiency degradation. The reheat loss is calculated by using the peak regenerator heat from the cycle and the minimum regenerator effectiveness. Many other heat losses are present in a SE, some examples are: axial conduction along regenerator case, radial and axial conduction in the heater and cooler, and heat lost externally to other parts of the engine. These examples and other heat losses will contribute in an additional heat load on the heater which inevitably results in a decrease of thermal efficiency.

3.3.4 Net Performance Prediction

From a 2nd Order method analysis perspective, the net performance prediction of the engine is given by subtracting the power losses to net cycle output power and by adding the heat losses to the input heat predicted in the 1st Order analysis. Therefore the final predicted work rate, heat input and efficiency are calculated according to Eq. 3.47 through 3.49, respectively.

$$\dot{W}_{net}^{2nd} = \dot{W}_{net}^{1st} - \dot{W}_{loss} = \dot{W}_{net}^{1st} - \dot{W}_{pl} - \dot{W}_{ml} \quad (3.47)$$

$$Q_{in}^{2nd} = Q_{in}^{1st} + Q_{loss} = Q_{in}^{1st} + Q_{rl} \quad (3.48)$$

$$\eta_{2nd} = \frac{\dot{W}_{net}^{2nd}}{\dot{Q}_{in}^{2nd}} = \frac{\dot{W}_{net}^{1st} - \dot{W}_{pl} - \dot{W}_{ml}}{(Q_{in}^{1st} + Q_{rl})f} \quad (3.49)$$

The 2nd Order net performance prediction for the engine running at 4500 RPM is summarized in Table 3–8. The results show that the efficiency obtained from the FHT analysis is reasonably close to the efficiency provided by Hargreaves [13]. And the results become less accurate for the Adiabatic and Isothermal models. Although the Isothermal analysis is ideal, the use of the 2nd Order method gives the analysis usefulness in design application, provided that power and thermal losses are accurately predicted. The current 2nd Order method with the FHT analysis gives a close estimation of the net work (within 9.5% of the actual value). However, for the heat input the difference from the test data is large (27.4%). In the model for 2nd Order method, only the regenerator heat loss is considered, nevertheless, in the actual engine wall conduction, shuttle loss, external heat loss to environment and other significant thermal losses are present. In order to achieve results to match the actual data, more loss terms need to be considered in the 2nd Order method. However, if more loss terms are added, it is advised that the calculations be refined since it involves the risk of over predicting the losses for the engine.

In Figure 3–44 the net power from the Adiabatic and Finite Heat Transfer analysis is compared to the break power of the Ford-Philips 4-125 engine. The various power loss mechanisms are accounted for and identified in the diagram. As seen, the loss due to heat transfer is not only significant, moreover is has an order of magnitude comparable to the

engine mechanical loss. At low RPMs the pressure loss is small and increases significantly after 3500 RPM, relative to the other losses. This is further corroborated in Figure 3–45 where the percentage of pumping pressure loss (with respect to Adiabatic power) is less than 4% at 2000 RPM and increase to about 13% at 4500 RPM.

Table 3–8: Comparison of Engine Performance Results for 2nd Order Methods at 4500 RPM

Performance Parameter	2 nd Order Methods			¹ Engine Test Data
	Isothermal	Adiabatic	Finite Heat Transfer	
Cycle Mean Pressure (bar)	148.78	148.03	147.55	150
Heat Input (J)	5981.6	6700.9	6606.2	² 8720
Net Cycle Work (J)	2727.2	2807.1	2290.8	2093
Engine Power (kW)	203.9	210.5	171.7	157
Cycle Efficiency (%)	45.59	41.89	34.68	³ 24

¹ Performance Data [Urieli, 1984] ² Calculated from Cycle Efficiency and Engine Power ³ Muschel Diagram Efficiency [Hargreaves, 1991]

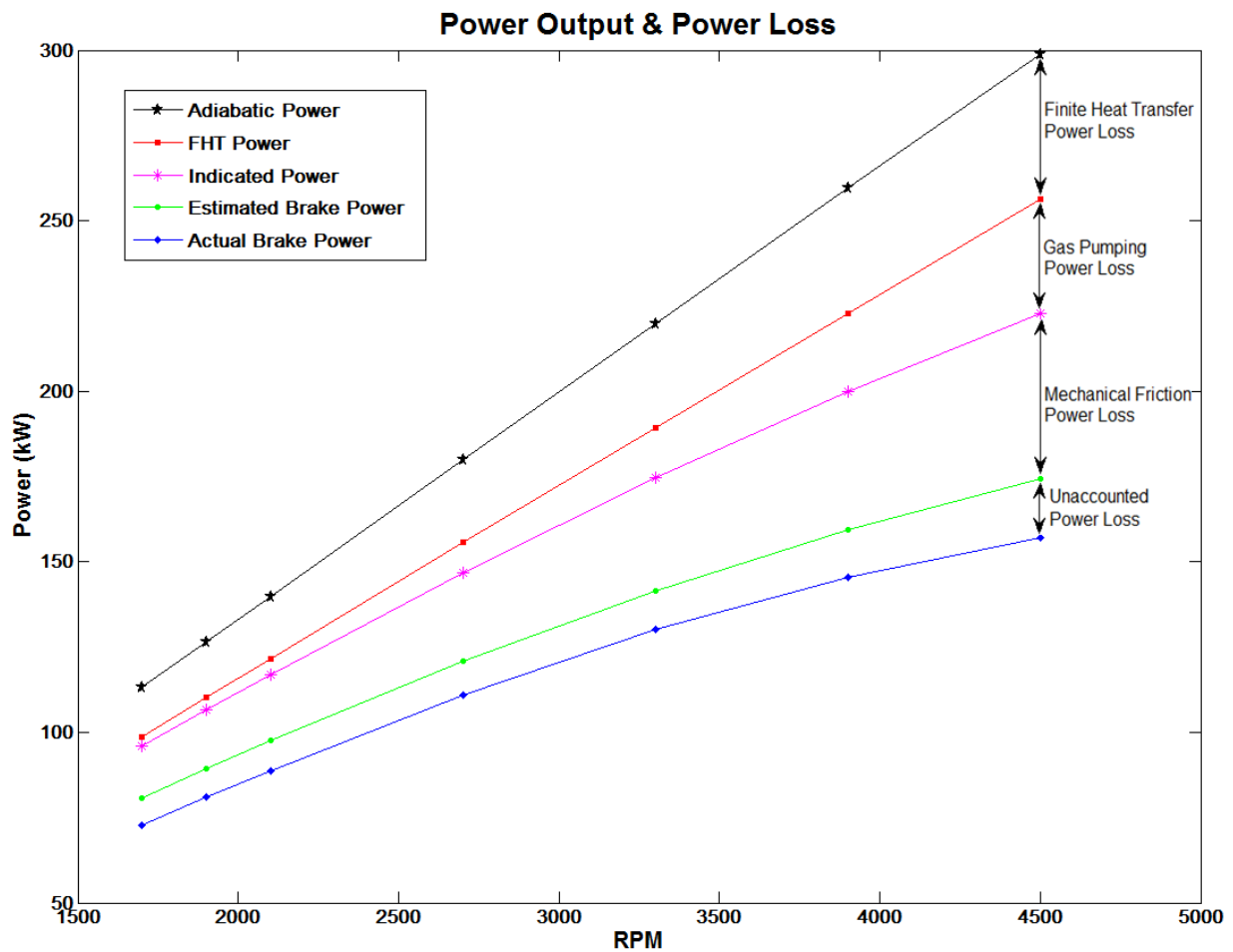


Figure 3–44: Power Output & Power Loss Mechanisms as Function of RPM

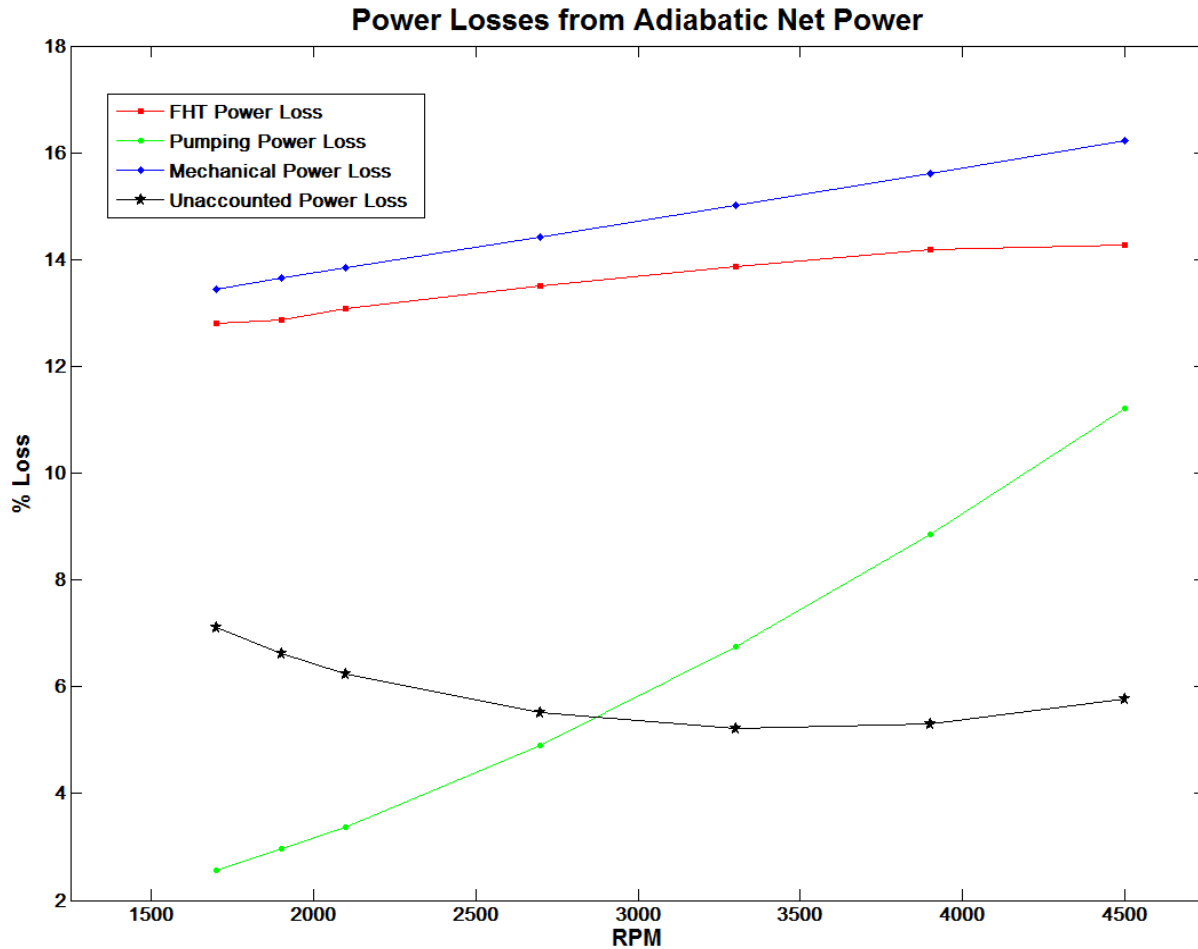


Figure 3-45: Power Loss Percentile from Adiabatic Power as Function of RPM

According to Martini, the 2nd Order conjecture of dividing the power losses and the heat losses into numerous decoupled processes that are later superimposed on 1st Order engine performance was first investigated in the Vuilleumier cycle analysis [29]. The Vuilleumier cycle is used for refrigeration machines that are thermally driven and have components very similar to a SE. Citing directly from Martini’s Stirling Engine Design Manual [29]:

“The idea of separating power output and the heat losses into a number of superimposed processes has been used by a number of investigators of the Vuilleumier cycle. The details of this analysis have been given in a number of government reports. The Vuilleumier cycle is a heat operated machine which uses helium gas and regenerators very similar to the way the Stirling engine is constructed. This super position analysis has worked well in Vuilleumier cycle machines. In a RCA report the measured cooling power using this method of analysis was found to be within 8.9% of that calculated.”

Using the basis of the quoted paragraph from Martini [29], the author of this work does not intend to proclaim the 2nd Order method is well validated or accurate, rather to inform that it has been used comprehensively in external heat engines. There are many advantages of using a 2nd Order method in the design optimization of a SE since each loss can be evaluated individually. Another benefit is the reduction in computing resources needed for the calculation of a single cycle performance case. Optimization procedures often require large number of iterations, thus lengthy and complex analysis tools tend to be more time expensive. For this reason the 2nd Order method, with the losses described in sections 3.3.1 to 3.3.3, using the Finite Heat Transfer analysis (as the 1st Order method base prediction) will be implemented in the analysis studies and the MATLAB parameter optimization procedure.

3.4 Proposed Studies

3.4.1 Motion Studies

The first studies deal with the evaluation of arbitrary functions that deviate from the sinusoidal net piston motion that occurs in the expansion and compression spaces. It is intended to assess cycle optimization based on the modification of piston motion. Also, the concept of Ideal motion (developed from the Ideal cycle) will be tested using the 2nd Order method. In this manner, the effect of losses can be explored on the performance of the idealized linear function concept. First, the function based on the elliptical drive motion described by Fang et al. [41] (which approximates the Ideal linear motion) will be evaluated. The thermal results presented in Fang et al. are for the 1st Order Adiabatic model, thus, no losses were considered. In addition, the comparison to the sinusoidal function is vague. The thermal analysis and comparison executed here provides more detail. The second function developed here, is an arbitrary step function that dwells in the minimum and maximum values of V_c and V_e . For the third function, the damp or dwell produced in the compression piston by the slider/bar mechanism proposed by Dehelean et al. [38-40] will be studied. The idea behind Dehelean's work is that if the compression piston dwells during the expansion phase of the Stirling cycle more net work should be generated. However, Dehelean's studies did not include thermal results; instead the focus was on the

mechanical design and motion analysis. The sinusoidal volume variations from the Ford-Philips 4-215 engine will serve as the baseline comparison in this study. The Finite Heat Transfer (FHT) model along with the 2nd Order method will be used in the procedure of acquiring the thermal results. Both Fang and Dehelean functions were recreated from their data and scaled to match the parameters for the Ford-Philips 4-215 engine. The three functions considered, have the same maximum and minimum values in the expansion and compression volumes to have a fair comparison. A visual comparison between the functions for the volume variation is shown in Figure 3–46. The arbitrary functions were constructed using the Fourier series approximation. The Fang et al. function was created using 6 terms, while the Step and Dehelean functions used 10 and five terms, respectively. The use of the Fourier series was shown to provide the same results, when approximating the sinusoidal function.

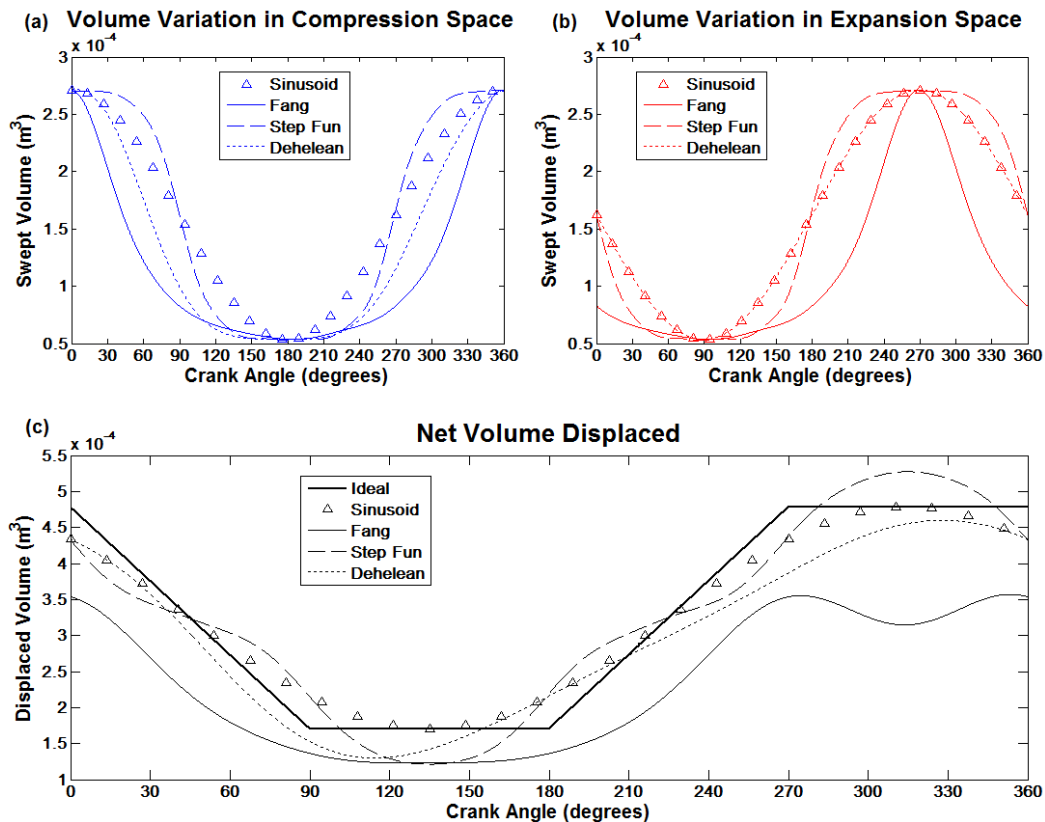


Figure 3–46: (a) Compression Space Volume Variation (b) Expansion Space Volume Variation (c) Net Volume Displaced

3.4.2 Parametric Studies

Based on the motion studies performed, it was concluded that cylinder size and phase angle (α) also influence the net piston motion. Therefore, it is important to investigate whether the baseline sinusoidal function can be optimized by changing the relative size of V_c and V_e . There are only three parameters that determine the value of the volume variation in V_c and V_e , these are:

- (1) Swept Volume
- (2) Clearance Volume
- (3) Phase Angle

Based on parameter (1) Equation 3.50 was used in order to relate the compression cylinder size with that of the expansion cylinder.

$$SVR = V_{clc}/V_{cle} \quad (3.50)$$

For parameter (2) it was decided to maintain the same clearance volume for V_e and V_c , since it can be argued that a minimum clearance volume is desired in both spaces, because both contribute to dead space volume. Therefore, the dimensionless relation for clearance length to piston stroke length was explored (Eq. 3.51) for a more practical approach. In this manner it can be determined if a feasible reduction of clearance length can positively influence the engine efficiency.

$$CLR = X_{cl}/L_s \quad (3.51)$$

For the final parameter (3), the phase angle will be revisited. The 2nd Order method provides the capability of determining the change in efficiency when varying the phase angle. It was not possible to determine the change in efficiency using the Isothermal analysis (is equal to the Ideal cycle analysis); however, it is expected that for the maximum power output the phase angle will remain close to 90° as it was found with the Isothermal analysis. The first step was to report the cycle efficiency and power output as a function of each individual parameter in order to establish the parameter range where improvement occurred relative to the baseline values. After establishing each range and obtaining a preliminary optimum value for each parameter separately, a simultaneous analysis was performed. A set of 10 CLR and 10 SVR values were chosen for the simultaneous parametric

studies as shown in Table 3–9. The analysis is repeated for 60°, 77°, 90°, and 105° phase angles. The parameters study concludes with the solution of the optimized parameters, using a MATLAB optimization subroutine.

Table 3–9: CLR and SVR Set Data in Parametric Studies for 60°, 90°, 77°, and 105° Phase Angles.

CLR: [0.5 0.6 0.7 0.8 0.9 1.0 1.1 1.3 1.5 2.0]
SVR: [0 0.025 0.05 0.1 0.15 0.2 0.246 0.3 0.35 0.4]

CHAPTER 4: DISCUSSION AND RESULTS

4.1 Preview of Analysis Studies

The purpose of this chapter is to evaluate the functions described in Section 3.4 and pursue cycle optimization of the Alpha Stirling engine by modifying the net piston motion that occurs in the expansion and compression spaces. The sinusoidal volume variations from the Ford-Philips 4-215 engine will serve as the baseline for the results in this study. As stated in Section 3.4, the Finite Heat Transfer (FHT) model along with the 2nd Order method will be used in the procedure. The volume motion concepts developed in the previous work of Fang et al. [41] and Dehelean [38-40] will be explored here. In the work presented by Fang et al., the thermal results were for a 1st Order Adiabatic model and no losses were considered. Dehelean's studies did not include thermal results; instead the focus was on the mechanical design and motion analysis. Both Fang and Dehelean functions were recreated in this study from their data and scaled to match the parameters for the Ford-Philips 4-215 engine. An arbitrary Step Function that dwells in the minimum and maximum values of V_c and V_e is also considered here. The 2nd Order analysis performed in this chapter will serve to validate the previous work and if in fact following an "idealized" motion will result in performance improvement. It will be shown that the pressure drops in the heat exchanger are significantly affected by the type of piston motion and the end results deviate from what is expected from the Ideal cycle analysis.

Based on the motion studies performed, it was determined that cylinder size and phase angle (α) also influence the net piston motion. Therefore it is important to investigate whether the Baseline sinusoidal function can be optimized by changing the relative size of V_c and V_e . The three parameters explored here are the swept volume ratio (SVR), clearance length ratio (CLR), and the phase angle. These parameters are related to the design of compression and expansion swept volume, cylinder clearance and compression ratio. The development of SVR, CLR and α is explained in detail in Section 3.4. In Section 4.4 the efficiency and power output of the Ford-Phillips 4-215 engine is used for the purpose of the parametric studies and an optimal configuration was found.

4.2 Ideal Motion from a 2nd Order Method Perspective

When representing the Ideal cycle for an Alpha type Stirling engine with the P- \forall diagram, the cycle pressures will be too large if the dead space volume is not considered. For this reason, the practical interpretation of the Ideal P- \forall diagram needs to consider the instant cycle pressure vs. the total gas volume in the engine. This ensures that the 1st Order models are enclosed within the Ideal cycle (implicating less amount of cycle work) as shown in Figure 3–37. However, if the P- \forall diagram for the 1st Order model does not need such comparison, the working space volume can be used. Note that the area remains the same. For example, such diagram is better suited for comparing the SE to IC engines, although, the dead space volume should be reported to keep track of actual engine size.

The Ideal piston motion for the Stirling engine has always been viewed from the Ideal cycle analysis perspective. More specifically, from the Ideal P- \forall diagram. As demonstrated in Section 3.1.1, the Stirling P- \forall diagram is deterministic, once the high and low operating temperatures and the minimum and maximum volumes are established. Following the convention for the Ideal cycle example in Section 3.1.1, the operating pressures for the isothermal processes are fixed as follows,

$$\begin{array}{l} \text{Isothermal} \\ \text{Compression} \end{array} \quad \frac{P_2}{P_1} = \frac{\forall_1}{\forall_2} = \frac{\forall_{max}}{\forall_{min}} \quad ; \quad T_2 = T_1 = T_L \quad (4.1)$$

$$\begin{array}{l} \text{Isothermal} \\ \text{Expansion} \end{array} \quad \frac{P_4}{P_3} = \frac{\forall_3}{\forall_4} = \frac{\forall_{min}}{\forall_{max}} \quad ; \quad T_4 = T_3 = T_H \quad (4.2)$$

The isochoric regeneration internal processes are also fixed,

$$\begin{array}{l} \text{Isochoric} \\ \text{Heat Addition} \end{array} \quad \frac{P_3}{P_2} = \frac{T_3}{T_2} = \frac{T_H}{T_L} \quad ; \quad \forall_3 = \forall_2 = \forall_{min} \quad (4.3)$$

$$\begin{array}{l} \text{Isochoric} \\ \text{Heat Extraction} \end{array} \quad \frac{P_1}{P_4} = \frac{T_1}{T_4} = \frac{T_L}{T_H} \quad ; \quad \forall_1 = \forall_4 = \forall_{min} \quad (4.4)$$

Note that equations 4.1 to 4.4 can be obtained from the ideal gas law. However, equations 4.1 to 4.2 are also a result of a polytropic process for a constant temperature condition.

It is observed from the equations describing the four Ideal Stirling processes, that the cycle volume at any given time is either linear or constant and is a function that can be

determined with the minimum or maximum volume. If each Ideal process is assumed to have the same duration during the cycle, the Ideal total volume displacement would appear as shown in Figure 3–19. Now the question is how the total Ideal volume displacement is transferred to the individual compression and expansion space volumes. Fang et al. arbitrarily defined this Ideal motion as a combination of linear functions in V_c and V_e (Fig. 2–14 (a)). Fang and the other investigators in this work intended to dwell the motion in V_e when V_c is in compression and dwell V_c when V_e is expanding, both dwell processes occur at min V_e or V_c . Finally, this “idealized” motion is to be approximated by an elliptical drive (Fig. 2–14 (b)). Although Fang et al. claim the arbitrary linear motion as Ideal for both the compression and expansion piston, this is not theoretically true. Note that the Ideal P - V diagram represents the total or net volume displacement and the individual working volumes in the Alpha Stirling Engine are not represented separately. For example if V_e is maintained sinusoidal, an “Ideal” function V_c could still be created by subtracting V_e to the total Ideal volume (Fig. 4–1). Furthermore, a larger area will result from the P - V diagram as shown in Figure 4–2.

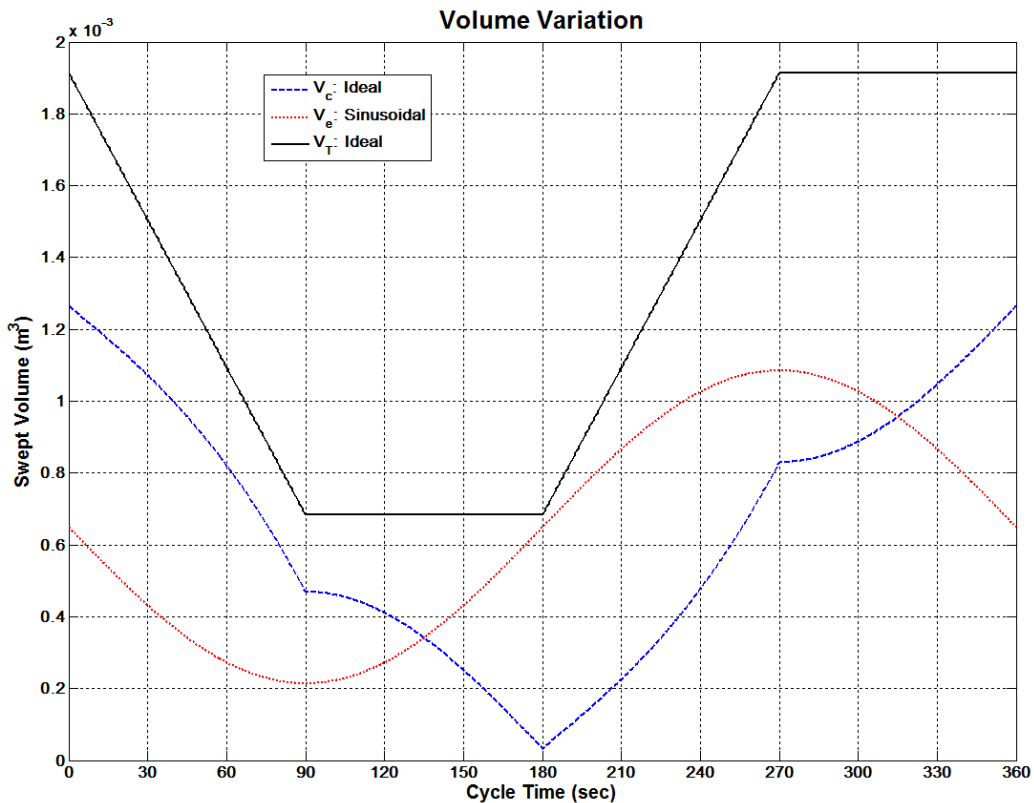


Figure 4– 1: Swept Volumes for an Arbitrary Ideal Function

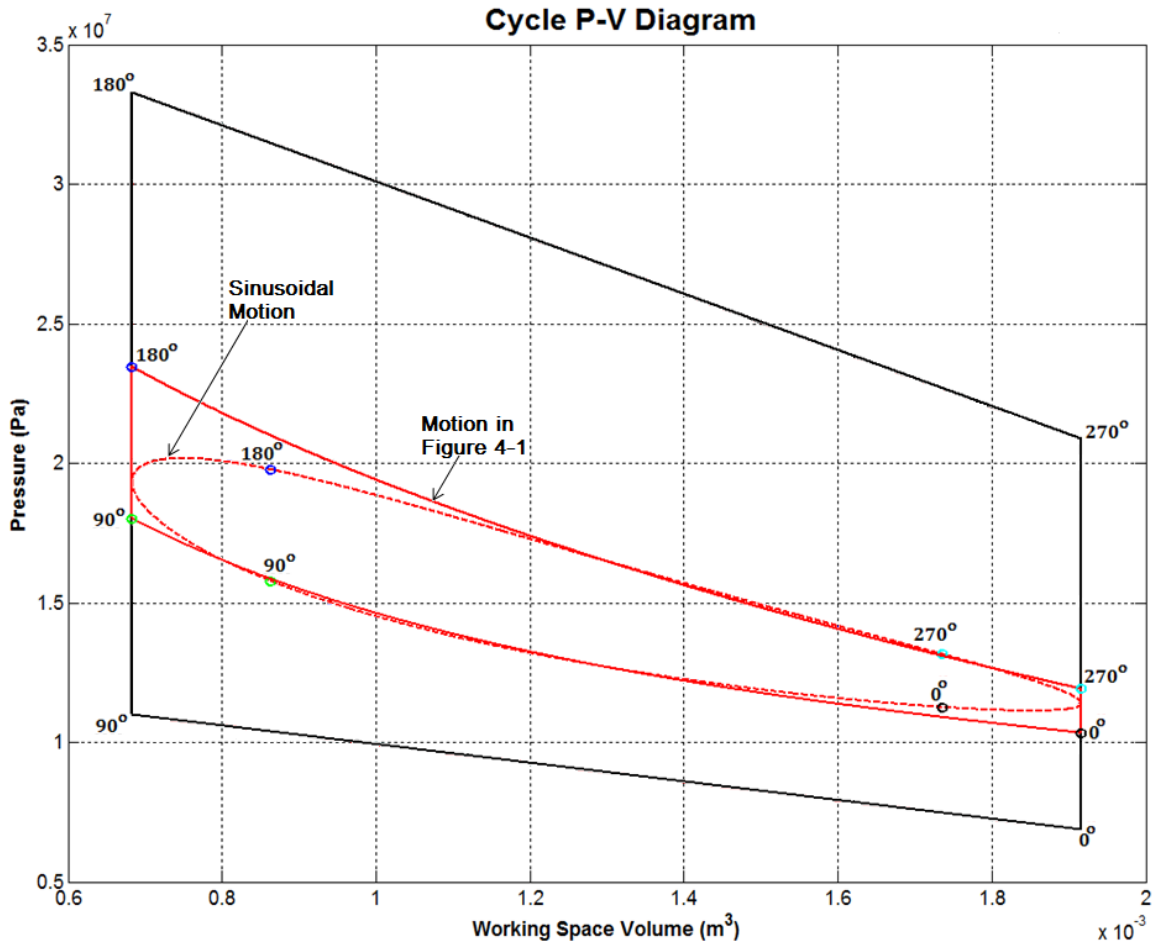


Figure 4– 2: Cycle P-V diagram for Ideal, Sinusoidal and Arbitrary motion in Figure 4-1

4.3 Motion Studies

The 2nd Order method performance (with FHT analysis) comparison for the motion study is given in Table 4–1. Two major observations come across from these results. The first is that the sinusoidal function actually outperforms the other three functions. And the second is that the function proposed by Fang et al., which intends to approximate the “idealized” motion, results in the lowest thermal efficiency and its value is almost a third of the sinusoidal motion thermal efficiency. This difference will be later explained to be a result of higher velocity flows in the heat exchangers that consecutively increase the pressure loss (or pumping power loss). The Step Function degraded the efficiency by 24.4%. Dehelean function produces almost the same efficiency relative to the sinusoidal. The engine power output and net cycle work follow the same trend as the efficiency. The reason for the trend is that the pumping power loss was found to be the loss most significantly

affected in changing the motion. In terms of heat transfer there is a highly measurable improvement from Fang et al. as the value of heat input is reduced by 22.4% relative to the sinusoidal. This improvement in heat transfer is largely due to the fact that in the crank angle range of 90° to 180°, Fang et al. approximate the actual isochoric process, and the flow remains almost constant providing a more steady heat transfer. The Step Function is actually the worst in terms of the heat input required, and although the efficiency is not as low as Fang it is not desirable either due to its implication input energy at the given engine speed. The final observation from Table 4–1 is for the operating pressure. Usually in IC engines, higher operating pressures will result in higher efficiencies. However, Table 4–1 shows that this is not necessarily true for the SE. Due to the presence of heat exchangers, drastic changes in pressures are not recommended. Thus, if the higher operating pressure is a result of the large peaks in the pressures through the cycle and not a smooth and steady higher pressure the cycle efficiency is most likely to be reduced. This is what occurs in using the Fang et al. function. The large peaks in V_c and V_e cause large cycle pressure variations that are not desirable because these will also cause and increase in the gas flow (or velocity) through the heat exchangers.

Table 4–1: 2nd Order Performance Results for Sinusoidal, Fang and Step Functions at 4500 RPM

Performance Parameter	Motion			
	Sinusoidal	Fang	Step Function	Dehelean
Cycle Mean Pressure (bar)	147.55	168.45	151.18	160.25
Heat Input (J)	6606.2	5127.4	8415.4	7093.0
Net Cycle Work (J)	2290.8	620.6	2205.3	2414.7
Engine Power (kW)	171.7	46.5	165.3	181.1
Cycle Efficiency (%)	34.68	12.10	26.21	34.03

Table 4–2 summarizes the 2nd Order losses for the motion study. As explained earlier, the losses due to pressure drops occurring in the heat exchangers were found to have the largest impact on decreasing the efficiency. Fang et al. and the Step Function resulted in the largest total pumping power loss (~3 times the loss from the sinusoidal motion) and the function described by Dehelean increased the losses by 22.3%. Note that the Step Function resulted in slightly larger pumping losses, although, it has a significantly larger cycle efficiency. This is explained by the fact that the Step Function produces a higher 1st Order

power output relative to Fang, and proportionally the decrease to 2nd Order is less than what occurs for the motion described by Fang et al.. Under the current analysis, the mechanical friction loss is the same, since it was considered only as a function of engine frequency (Appendix D.3). The implementation of a model that can more accurately capture the power loss from friction occurring in the piston and cylinder wall is recommended in a future analysis. The formulas used to estimate the mechanical friction losses in this analysis represent an overall view of the friction losses, since the 2nd Order method results were verified against actual data. However, it was found that the implicit effects of external losses are not valuable for the purpose of this study. In the case of heat losses, the regenerator heat loss is less sensitive to motion types. The regenerator heat loss is for the most part determined by the regenerator effectiveness. The effectiveness depends on the design characteristics such as overall heat transfer coefficient (UA_s) and the heat capacity flowing through the boundaries. Thus, the change in flow is less significant to regenerator heat loss than to pressure drops. To further investigate the large pumping power loss, the Sinusoidal, Fang and Step functions were studied in terms of swept volume, volume rate of change and the volume difference (or delta) occurring from compression to the expansion space. Consequently, changes on these from the sinusoidal motion were found to drastically affect the cooler, regenerator and heater gas velocities and produce higher pressure losses.

Table 4-2: 2nd Order Performance Results for Sinusoidal, Fang and Step Functions at 4500 RPM

Loss Terms	Motion			
	Sinusoidal	Fang	Step Function	Dehelean
Total Pumping Loss (kW)	36.27	98.64	103.78	44.40
Mechanical Fiction (kW)	48.54	48.54	48.54	48.54
Regenerator Heat Loss (J)	214.47	234.91	316.63	211.0

Figure 4-3 is a motion comparison of the Sinusoidal, Fang and Step Function proposed for the study. In figures 4-3 (a) and 4-3 (b) the volume variation and volume rate of change (function derivative) are plotted, respectively. The volume rate of change is higher for the Fang and Step Function when compared to the sinusoidal motion. Volume rate in the compression and expansion cylinders is directly proportional to the volumetric rate of air passing through the boundaries of the heat exchangers. Figure 4-3 (c) illustrates this more specifically with delta ($V_c - V_e$) in volume variation. The behavior of this delta impacts

directly the behavior and magnitude of the net flow through the heat exchangers. Therefore, steep slopes in delta volume rate of change (Fig. 4–3 (d)) will cause higher through flow. If the new motion has slopes that are significantly steeper than the sinusoidal function, the expected end result is that the resulting peaks in volume rate for the new function will be of a higher magnitude.

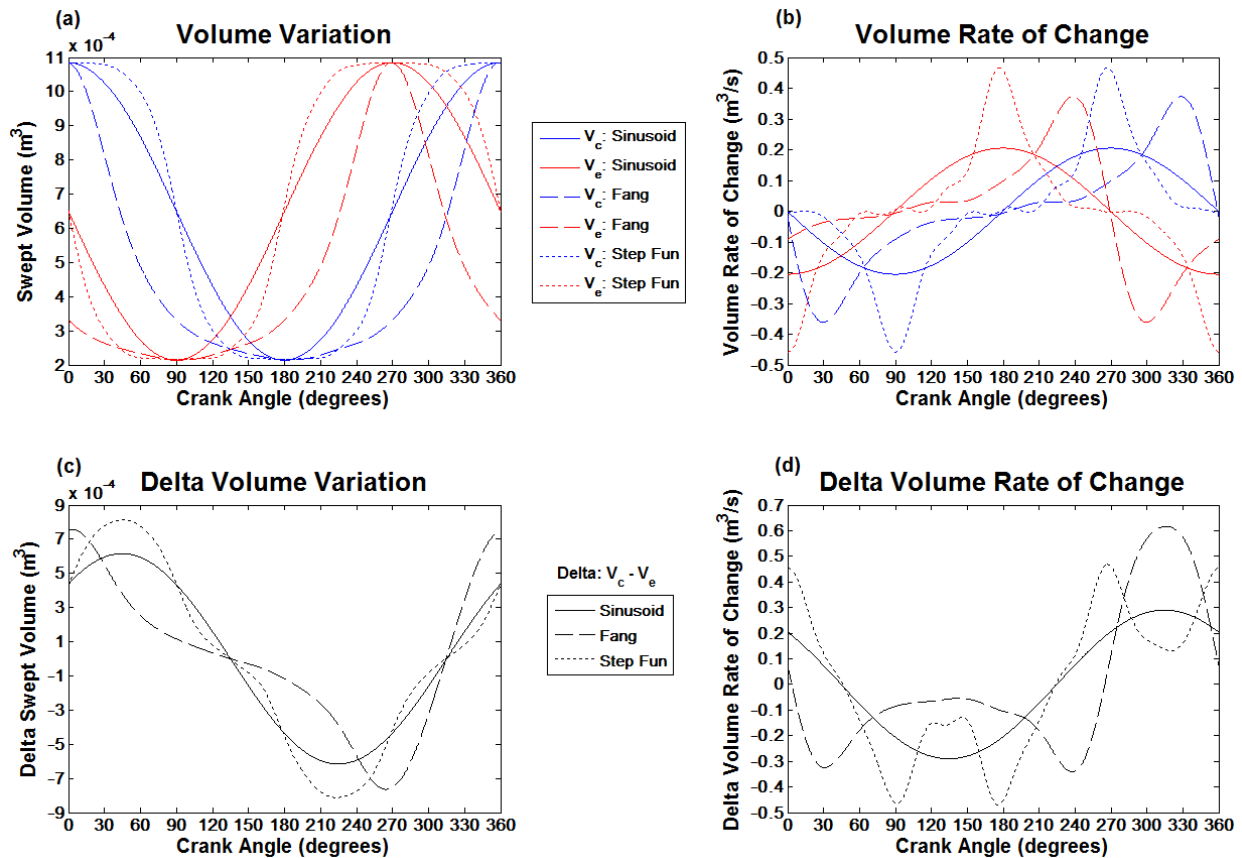


Figure 4– 3: (a) Volume Variation in V_c and V_e (b) Volume Rate of Change (c) Difference in Volume Variation (d) Difference in Volume Rate of Change

To further explain the impact the higher volume rates observed in the Fang and Step Function will have on the 2nd Order losses, the heater volumetric flow rate and heater gas velocity is plotted in figures 4–4 (a) and 4–4 (b), respectively. In Figure 3–39 it was shown that the major pressure drop and pumping power loss occur in the heater component. Thus, following the flow behavior in the heater should be sufficient to determine if the new functions will yield lower or higher losses. The heater volumetric flow rate is calculated from Eq. D.5 (Appendix D), and is basically proportional to heater size and the average

mass flow rate at the boundaries. The average heater gas velocity, used in the pressure drop estimation, is simply the volumetric flow rate divided by the flow area.

$$Vel_h = \dot{V}_h / A_{fh} \quad (4.5)$$

The significance of Figure 4–4 (b) is that both the Fang and Step Functions have considerably larger heater velocity magnitudes. And any increase in velocity is not trivial, since the losses due to pressure drop are proportional to the cubic of the velocity. The heater pumping power loss is,

$$\dot{W}_{pl,h} = F_h \frac{1}{2} \rho_h A_{fh} Vel_h^3 \quad (4.6)$$

In Equation 4.6, F_h is the total friction coefficient in the heater and ρ_h is the heater density. From all the terms in Eq. 4.7 only the velocity is expected to change significantly according to the motion under consideration for the swept volumes.

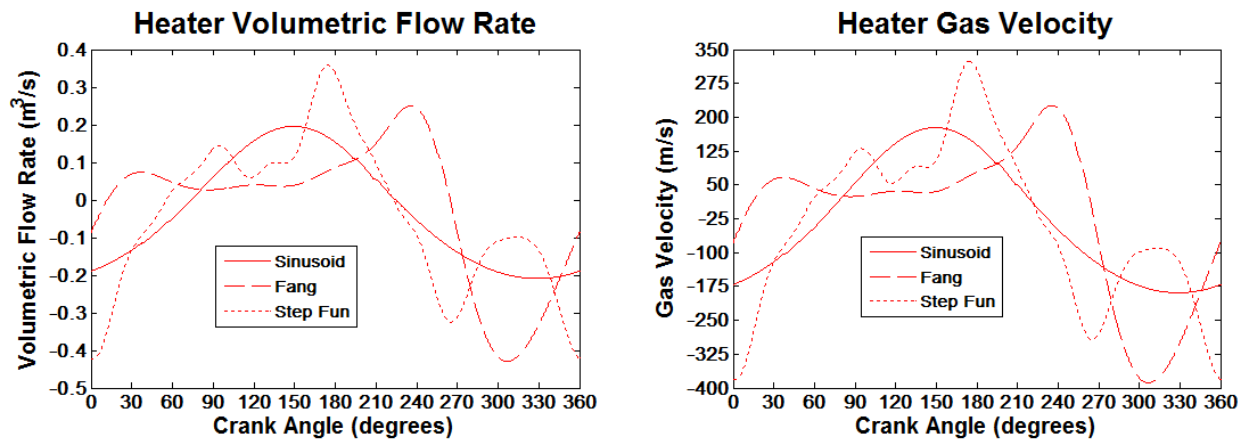


Figure 4– 4: (a) Heater Volumetric Flow Rate Comparison (b) Heater Gas Velocity Comparison

4.4 Parametric Studies for the Cylinder Compartments

4.4.1 Individual Parametric Analysis

The first step in the cylinder size and phase angle parametric studies was to verify the performance effect individually for each parameter while the other parameters remain fixed. The cycle efficiency and power output are reported in order to evaluate the engine performance as a function of swept volume ratio (SVR), clearance ratio (CLR) and phase angle (α). All of the aforementioned parameters directly determine the magnitude of V_c and V_e , and therefore impact the total displaced volume (or net displaced volume).

The swept volume ratio is the ratio of the swept volume in the compression space to that of the expansion space. For a SVR < 1, the swept volume in the expansion space remains at Ford-Phillips 4-215 engine specified value while the swept volume in compression space is reduced. Inversely if SVR > 1, the compression space is kept at the original swept volume and the swept volume at the expansion space is decreased. The 2nd order efficiency and 2nd Order power output is plotted in figures 4–5 (a) and 4–5 (b), respectively, for a SVR ranging from 0.5 to 2. At a 0.5 SVR, the compression space is half of the volume of the expansion space, and at a 2.0 SVR it is twice the size. The optimum values for SVR were found to be 0.89 for maximum efficiency and 1.0 for maximum power output.

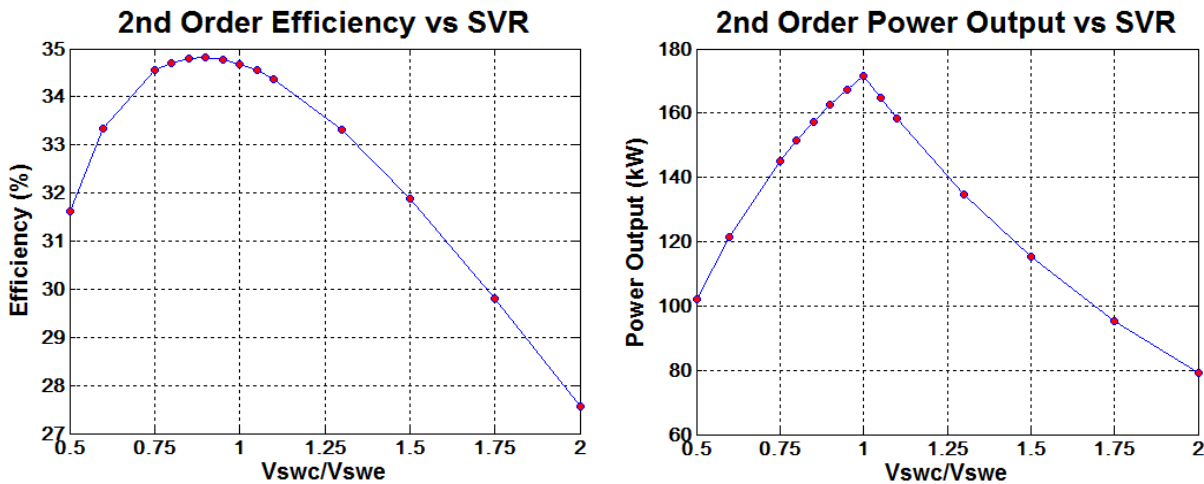


Figure 4– 5: 2nd Order Cycle Efficiency and Power Output vs. Swept Volume Ratio

Contrary to the SVR, the clearance length ratio (CLR) is not a relative size comparison of the compression and expansion cylinders, rather a convenient way to express the amount of clearance in the cylinder volume. The piston stroke length (53 mm) is used to normalize the ratio (Eq. 4.2) and the clearance volume is obtained by multiplying the clearance length by cylinder area, which is given by the bore diameter (73 mm). The CLR for the current Ford-Phillips 4-215 engine configuration is 0.246 (for a 12.8 mm clearance). As shown in Figure 4–6 (a) and (b), there is much room for improvement as theoretically the engine efficiency and power output can increase to 36.8% and 255 kW, respectively, at a CLR equal to zero. However, it is impractical to consider eliminating the clearance in the design for structural reasons. Nevertheless, the results in Figure 4–6 should motivate design efforts of minimizing the clearance as much as structurally possible.

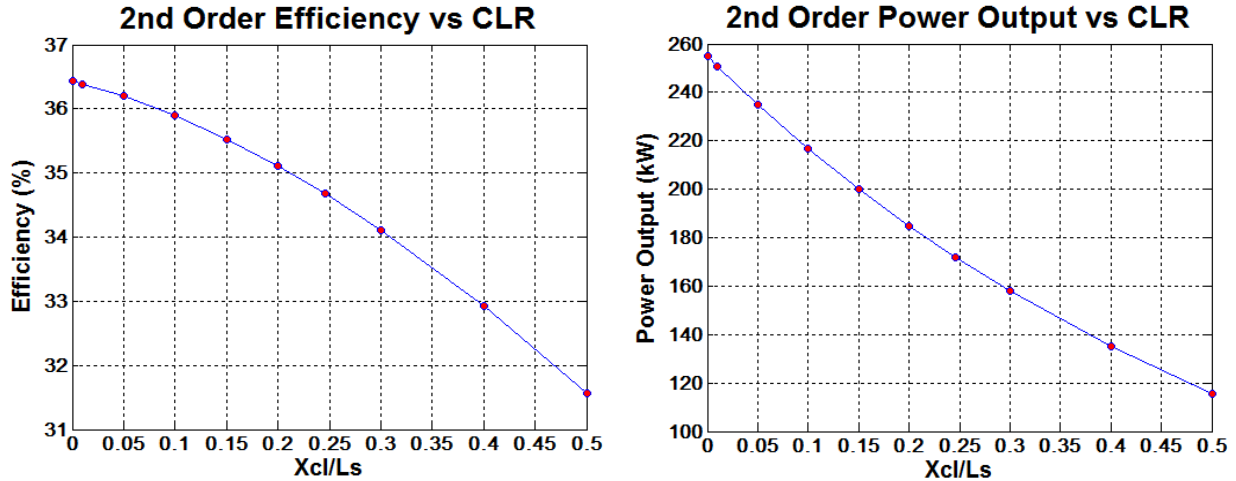


Figure 4- 6: 2nd Order Cycle Efficiency and Power Output vs. Clearance Length Ratio

The phase angle is now revisited from a 2nd Order method point of view. In Section 3.2.1 it was shown that the maximum power output was approximately 90°. The efficiency could not be investigated since Isothermal efficiency is determined by the operating temperature limits (same as the Ideal efficiency). The 2nd Order efficiency varies significantly for the 35° to 120° phase angle range as seen in Figure 4-7 (a). It is interesting to note that the maximum efficiency of 35.2% occurs at a 77° phase angle and not 90°. As was determined for the motions studies, power losses and heat loss play a considerable role and are minimized at the 77° phase angle. In the case of maximum output power (171.9 kW) the phase angle occurs at 88.3°, which is close to what is found using the Isothermal analysis and is not much different than the power produced at a phase angle of 90°.

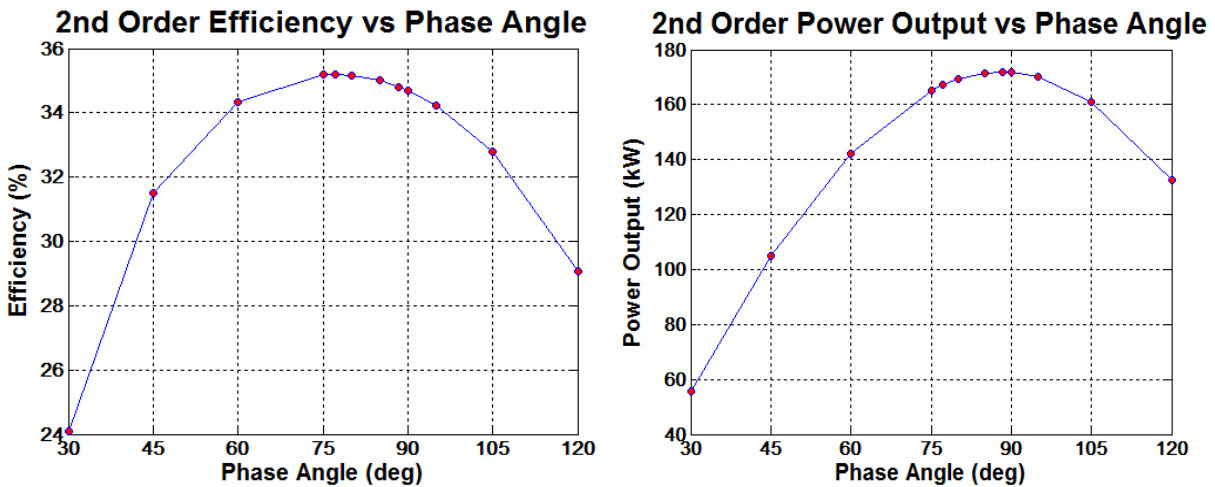


Figure 4- 7: 2nd Order Cycle Efficiency and Power Output vs. Phase Angle

4.4.2 Simultaneous Parametric Analysis

Based on the individual parametric studies in Section 4.4.1 the matrix set of data shown in Table 3-9 was used to further investigate the simultaneous effect of SVR, CLR and α on the cycle efficiency and the net power output. Contours of cycle efficiency vs. CLR and SVR are plotted for phase angles of 60° , 77° , 90° , and 120° in Figure 4-8. The non dimensional SVR and CLR ratios provided a convenient 2D Matrix (or plane) in which to visualize the contours. The effect of the phase angle can be evaluated separately in the different contours by using the same plotting scale. Figure 4-8 is an important aid as it can be used to point toward an optimal configuration. The 77° phase angle contour plot encloses larger areas with higher efficiency values, and the optimum values of SVR are shown to be close to 0.75. As stated above the optimum CLR is zero but is impractical for structural reasons. Depending on the design requirements the clearance length may have to be a constraint in the optimization effort. For example the large clearance for the Ford-Phillips 4-215 engine could be due to the fact that power control was achieved by varying the piston stroke length through the swashplate angle. In this matter, the use of similar plots to that of Figure 4-9 become useful, since the optimum SVR can be obtained for any clearance constraint.

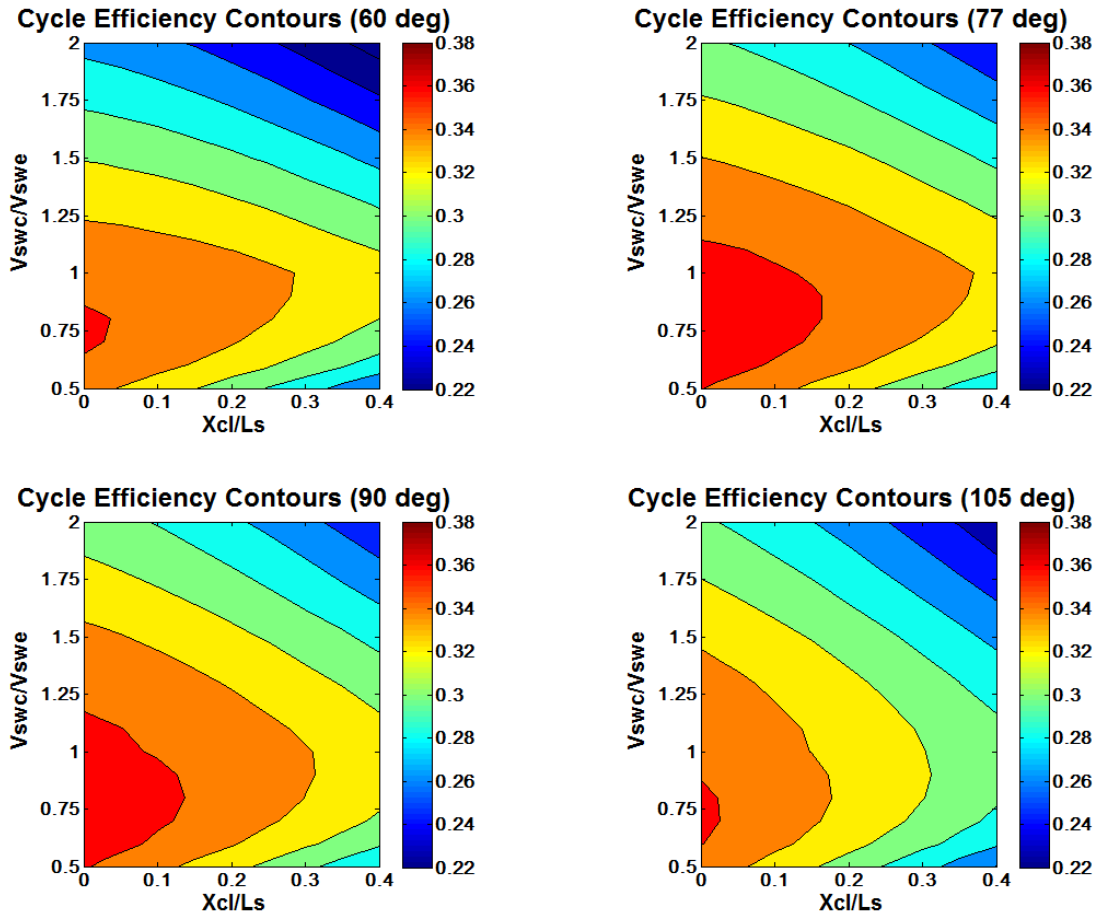


Figure 4– 8: Cycle Efficiency Contours vs CLR and SVR for 60°, 90°, 77°, and 105° phase angles.

The same approach that was used for the cycle efficiency contours was followed for the power output contours Figure 4–9. The trend observed for the power output is different than that of the cycle efficiency. Thus, the pursuit of maximum power will not necessarily result in higher efficiency. Furthermore, Figure 4–9 shows that in terms of power the Double Acting Swashplate is an excellent configuration to consider in a SE (note that the maximum power occurs at a 90° α and a SVR equal to 1, design parameters in a DA Swashplate configuration).

To conclude our parametric analysis, an optimization scheme was performed using the MATLAB fmincon tool. The CLR was fixed at 0.05, or 2.6 mm (1/10 of an inch) which can be argued to be an achievable clearance. Then, the optimization was run in both the SVR and α variables using 0.89 and 77° as the initial guess, respectively. The optimum configuration was found to be at a SVR of 0.763 and a phase angle of 82.6°. The improvement at 4500

RPM in terms of cycle efficiency is 7% (34.6% to 37%) and 19.5% (171 kW to 205 kW) in terms of power output. The resulting design parameters and performance results are summarized in Table 4-3. It is concluded that the optimization procedure brought about a higher compression ratio. To finalize the study, the Baseline and Optimized configuration performance is plotted against RPM. It is observed that the improvement increases for the higher RPM engine operation.

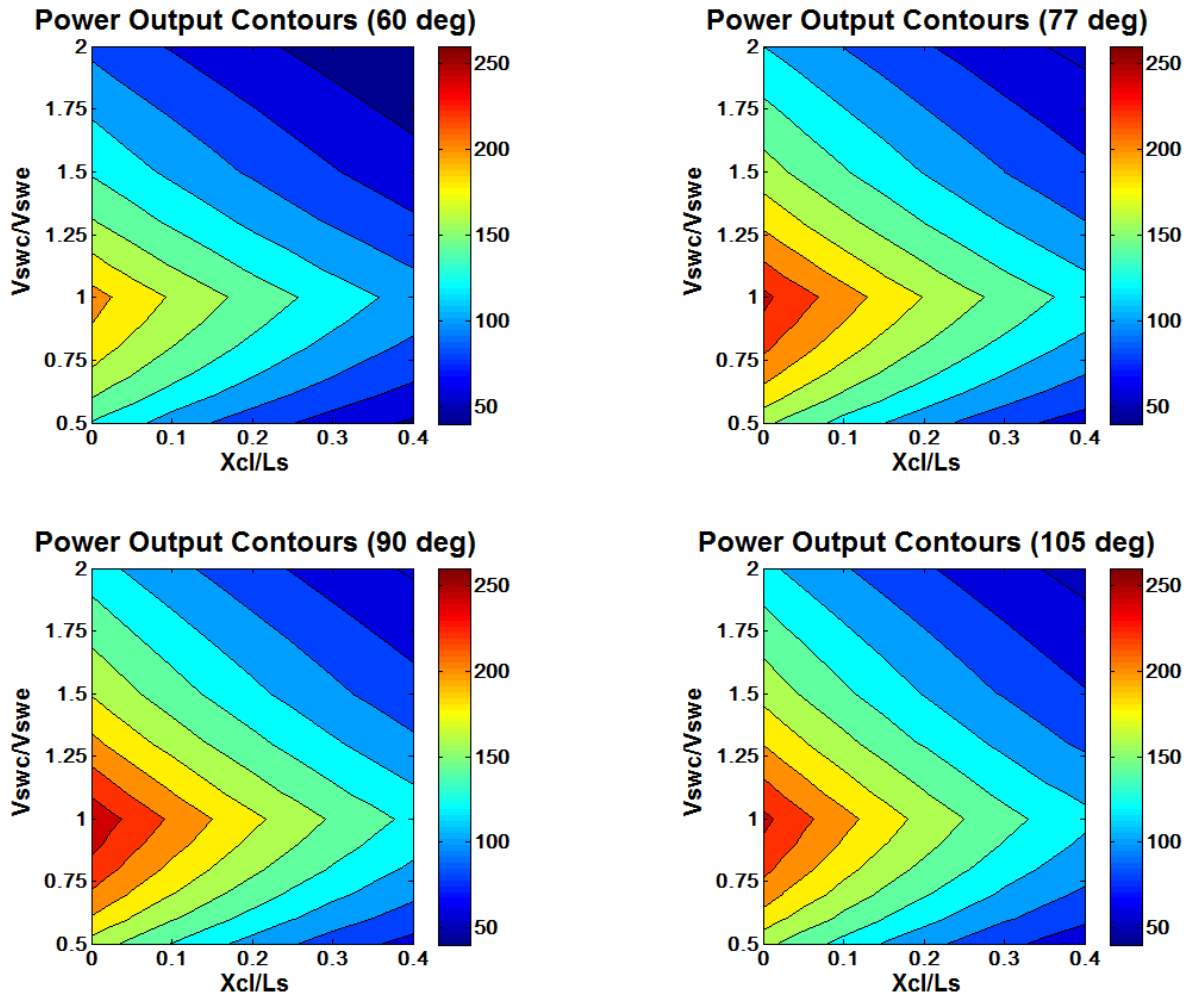


Figure 4- 9: Power Output Contours vs CLR and SVR for 60°, 90°, 77°, and 120° phase angles.

Table 4–3: Design and Performance data for Baseline and Optimized Ford-Phillips Engine

Parameter	Baseline	Optimum
Clearance (X_{cl})	12.6 mm	2.6 mm
Clearance Volume (V_{cl})	214.2 cc	43.53 cc
Compression Swept Volume (V_{swc})	870.6 cc	664 cc
Expansion Swept Volume (V_{swe})	870.6 cc	870.6 cc
Phase Angle (α)	90°	82.6°
Compression Ratio (r_c)	2.8	4.57
Power Output (\dot{W})	171 kW	205 kW
Efficiency (η)	34.6%	37%

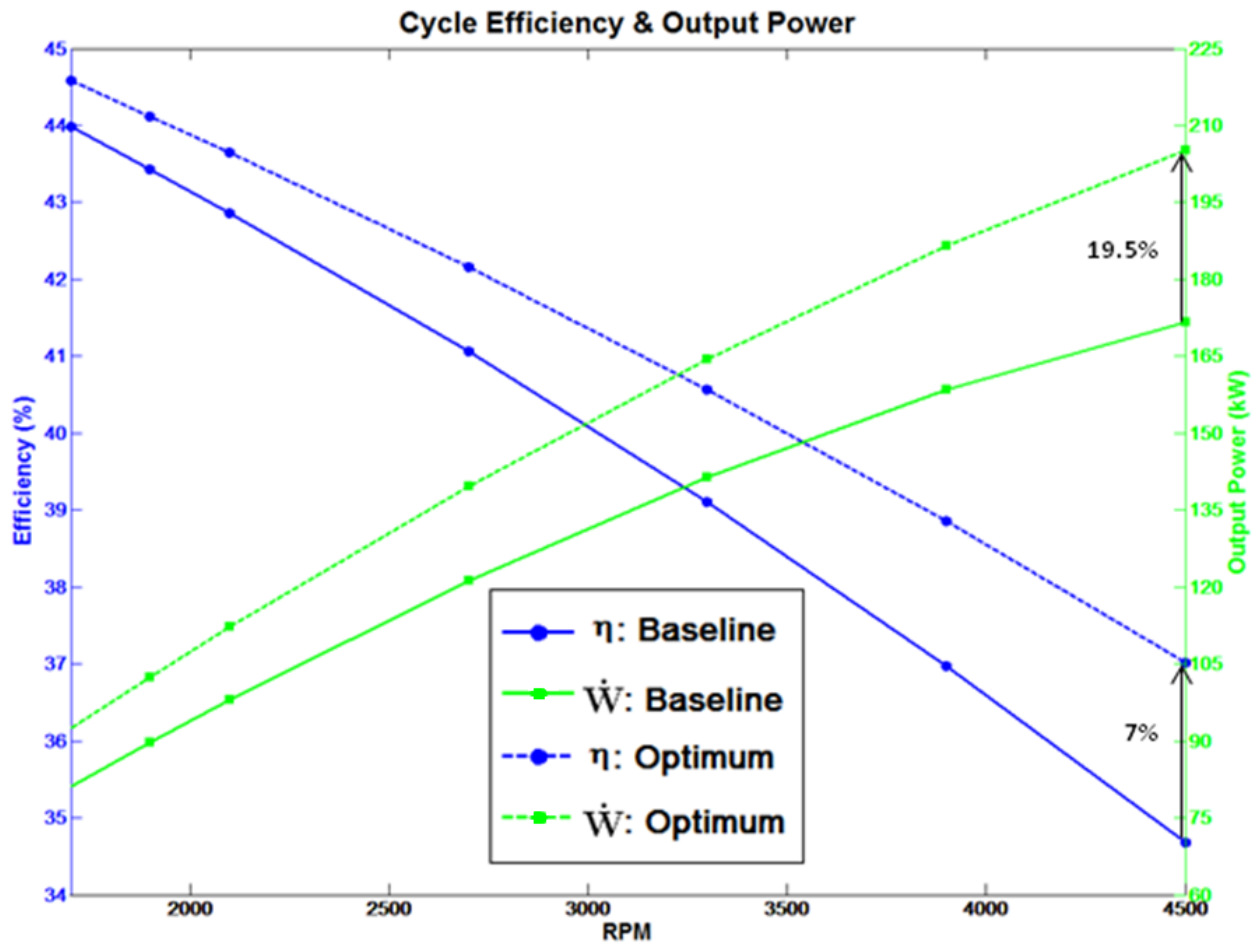


Figure 4– 10: Cycle Efficiency and Power Output for Baseline and Optimize Ford-Phillips Engine

CHAPTER 5: CONCLUSION AND FUTURE WORK

5.1 Conclusion

A Second Order method was developed in order to study the volume variations in the expansion and compression spaces of an Alpha Stirling engine. The analysis model considers, adiabatic working spaces, internal finite heat transfer, and losses from pressure drops, mechanical friction and imperfect regeneration heat transfer. The discretization approach is based on the five space component model, where the cooler, regenerator, heater and expansion spaces are considered as individual homogenous cells. However, the regenerator is subdivided in two cells so that the linear temperature distribution can be obtained from the regenerator (gas) cell temperatures. The cell subdivision, leads to a precise temperature representation at the regenerator boundaries. The current analysis model predicts a power output relative to the Ford Philips 4-125 engine data with less than 10% difference at 4500 RPM. However, the calculated cycle efficiency (34.6%) deviates from the engine data (24%). Since the brake power is closely approximated, the difference in the cycle efficiency can be attributed to parasitic or external heat losses not considered in the analysis. Nevertheless, it is realized that the proposed model considers the most significant internal losses and external losses are not important for the scope of this work.

The sinusoidal function was found to outperform the other functions considered in this study. With the current data it is not possible to conclude if the sinusoidal variation produces the optimum thermal efficiency. However, it is possible to conclude, that motions such as the one proposed by Fang et al. will not result in favorable engine performance if the piston motion produces higher gas velocities compared to the baseline sinusoidal motion. The pumping power loss through the heat exchangers is proportional to the cubic of the gas velocity, and increases in velocity magnitude are not trivial due to the transient nature of the processes. This is the fundamental challenge in heat exchanger design since for increased heat rate transfer rate, higher fluid velocities are desired at the expense of increased pressure losses. The results from the motion studies encourages further studies in this area, since the Stirling engine efficiency is sensitive to the function that describes the

motion of the pistons. This is a very important finding which validates the principal motivation of this study.

The function that describes the net volume variation for the expansion and compression spaces is determined by the swept volume, the clearance volume and the phase angle. It was decided to investigate whether the Ford Philips 4-125 engine could be optimized by modifying the three parameters. The swept volume was explored by using the swept volume ratio (SVR), ratio of compression to expansion volumes. The clearance volume was expressed in terms of the clearance length ratio (CLR); CLR is defined as the ratio of clearance length to stroke length. The parametric analysis was finalized by performing an optimization scheme in MATLAB. An optimum configuration was found with a SVR of 0.763, a CLR of 0.05 (2.6 mm or 1/10 of an inch) and a phase angle of 82.6° . The improvement of the configuration at 4500 RPM is an increase of 7% (from 34.6% to 37%) in terms of cycle efficiency and an increase of 19.5% (from 171 kW to 205 kW) in terms of power output. The resulting design parameters and performance results are summarized in Table 4-3. It is concluded that the optimization procedure brought about a higher compression ratio due to a higher net displaced volume. It is observed that the performance improvement increases for higher RPM engine operation. In a practical sense, the new configuration would require the design to move from the swashplate double acting Alpha Stirling to the V-rocker type engine. The obvious reasons are that the swashplate design cannot accommodate for the 82.6° phase angle and that double acting pistons cannot accommodate different swept volumes.

Three major contributions to the field of Stirling engines are provided in the scope of this work. In the first contribution it was explicitly shown that the finite heat transfer in the cooler, regenerator and heater significantly affects the performance calculation (both power and efficiency). The second contribution is related to decoupling the mechanism from the thermal analysis and using Fourier series to evaluate arbitrary piston motion. The simplification is proven useful since the thermal efficiency is sensitive to the piston motion. The third contribution was demonstrating the importance of parameterizing the compression and expansion cylinders in the design. An optimum configuration can be

found using SVR, CLR and phase angle (is not 90°) since these determine the net displaced volume.

5.2 Future Work

Future improvement of the Second Order method developed in this work can be achieved in multiple areas. For example, the current analysis model uses the average of the mass flow at the boundaries to characterize the mass flow at the heat exchanger control volumes. Instead, it is recommended, that the heater and cooler components are divided in two cells (as it is done for the regenerator), the mass flow for the heat exchangers could then be characterized with the flow at the center boundary. This approach would be more precise as the resulting flow is from the equation coupling at the center boundary and not by arbitrarily assuming an average. Another aspect that needs revising is the mechanical friction estimation. The correlation used in this work considers the overall mechanical losses of the system. However, in Stirling engine studies such as the one presented here, the internal losses are more pertinent than losses due to external factors. It is recommended that in future analysis only the piston head-cylinder friction is considered as a function of piston motion and velocity. Finally, the Second Order method develop here can become more robust if it is tested against higher order methods (e. g. Third Order methods, CFD) and experimental engine data that accounts for internal losses. The availability of such data could be used to refine the analysis, by either accounting for other losses or by implementing correction factors to loss estimations in the current Second Order method.

An evaluation of the heater design is recommended, since the pressure drops are more than twice that of the regenerator and cooler components. The external heat transfer configuration does not seem favorable either. The single burner serving all four cylinders in the symmetrical heater head arrangement produces high heat losses as estimated from the engine data (Table 3–8). A more isolated heat addition for the cylinders should improve the heat transfer and decrease the heat input required in the Ford Philips 4-125 engine.

Further analysis in the study of volume variations in the Alpha Stirling engine is suggested, in view of the fact that the efficiency is sensitive to piston motion. Ideally, an optimization scheme of the function that describes the motion in terms of the cycle

efficiency is preferred. This requires the function of the volume variation to be expressed parametrically. One way to achieved this is by optimizing the coefficients for a Fourier function approximation. However, the proper amount of coefficients and the stability of the Fourier function approximation should be verified. Also, higher computing power is needed to decrease the processing time of each iteration done in the optimization for the current MATLAB code. To solve each case it takes around 4 to 5 minutes to solve in a dual core CPU with 8 GB of RAM. This is due to the large gradients and stiffness of the numerical system of the Finite Heat Transfer (FHT) analysis, in addition to the Second Order calculations.

APPENDIX A

Appendix A.1

Appendix A.1 presents important derivations of the mathematical expressions used for the Isothermal analysis. The derivations were obtained from Urieli's approach in solving the sinusoidal volume variations for a sinusoidal Alpha Stirling engine [4]. This appendix also includes some of the theory behind Schmidt's original Isothermal formulation. It is not intended in Appendix A to give too much detail in the mathematical derivation of the Isothermal analysis (Urieli and many authors have already done this), rather present a point of reference for equations 3.16 to 3.21.

The net compression work is found from the closed cycle integration of instantaneous cycle pressure times the volume differential (volume change) in the compression space. The instantaneous pressure is obtained from equation 3.16 and the volume rate of change is the derivative of the sinusoidal motion of the compression piston. Before solving the integral the following constants are defined,

$$c = \frac{1}{2} \left[\left(\frac{V_{swe}}{T_h} \right)^2 + 2 \left(\frac{V_{swe} V_{swc}}{T_h T_k} \right) \cos \alpha + \left(\frac{V_{swc}}{T_k} \right)^2 \right]^{1/2} \quad (\text{A. 1})$$

$$s = \left[\frac{V_{swe}}{2T_h} + DSR + \frac{V_{swc}}{2T_k} \right] \quad (\text{A. 2})$$

$$DSR = \frac{V_{cle}}{T_h} + \frac{V_h}{T_h} + \frac{V_r \ln(T_h/T_k)}{T_h - T_k} + \frac{V_k}{T_k} + \frac{V_{clc}}{T_k} \quad (\text{A. 3})$$

$$b = c/s \quad (\text{A. 4})$$

$$\beta = \tan^{-1} \left(\frac{V_{swe} \sin \alpha / T_h}{V_{swe} \cos \alpha / T_h + V_{swc} / T_k} \right) \quad (\text{A. 5})$$

Now the work integral can be conveniently defined as,

$$W_c = \int_0^{2\pi} p \left(\frac{dV_c}{d\theta} \right) d\theta = \frac{-V_{swc} m R}{2s} \int_0^{2\pi} \frac{\sin \theta}{1 + b \cos(\theta + \beta)} d\theta \quad (\text{A. 6})$$

For the net expansion work the same analogy follows and a similar expression for a

work integral is obtained.

$$W_e = \int_0^{2\pi} p \left(\frac{dV_e}{d\theta} \right) d\theta = \frac{-V_{swe} mR}{2s} \int_0^{2\pi} \frac{\sin(\theta + \alpha)}{1 + b \cos(\theta + \beta)} d\theta \quad (\text{A. 7})$$

The only difference between A.6 and A.7 is the phase angle term of the expansion piston. After integrating A.6 and A.7 from 0 to 2π the analytical expressions for net compression work and net expansion work are obtained.

$$W_c = \frac{\pi V_{swc} mR \sin \beta}{c\sqrt{1-b^2}} (\sqrt{1-b^2} - 1) \quad (\text{A. 8})$$

$$W_e = \frac{\pi V_{swe} mR \sin(\beta - \alpha)}{c\sqrt{1-b^2}} (\sqrt{1-b^2} - 1) \quad (\text{A. 9})$$

The net work output for the cycle is simply the addition of net compression work and net expansion work.

$$W_{net} = W_c + W_e$$

And thus the analytical equation for net cycle work results in,

$$W_{net} = \frac{\pi mR}{c\sqrt{1-b^2}} (\sqrt{1-b^2} - 1) [V_{swc} \sin \beta + V_{swe} \sin(\beta - \alpha)] \quad (\text{A. 10})$$

Solution A.9 can be further simplified by grouping the following terms,

$$p_m = \frac{mR}{s\sqrt{1-b^2}} \quad (\text{A. 11})$$

$$\Pi = \frac{\pi}{b} (\sqrt{1-b^2} - 1) \quad (\text{A. 12})$$

Finally, the same expression presented in Chapter 3 for the Isothermal net work output is obtained.

$$W_{net} = p_m \Pi [V_{swc} \sin \beta + V_{swe} \sin(\beta - \alpha)] \quad (\text{A. 13})$$

Appendix A.2

Appendix A.2 properly defines the Schmidt number making use of parameters defined in Appendix A.1. The Schmidt number is given by Urieli [4] basically as,

$$Sc = \Pi[\kappa_{swc} \sin \beta + \kappa_{swe} \sin(\beta - \alpha)] \quad (\text{A. 14})$$

Where the swept volume constants are,

$$\kappa_{swc} = \frac{V_{swc}}{V_{sw}} ; \kappa_{swe} = \frac{V_{swe}}{V_{sw}}$$

The value V_{sw} is an arbitrary value that for Alpha Stirling engines may be convenient to define either as the compression space swept volume of the total swept volume ($V_{swc} + V_{swe}$). Using $V_{sw} = V_{swc}$ is found to be more convenient, since it establishes only one constant in Eq. A.14.

$$Sc = \Pi[\sin \beta + \kappa \cdot \sin(\beta - \alpha)]; \kappa = \frac{V_{swe}}{V_{swc}} \quad (\text{A. 15})$$

Other manipulations are done to Eq. A.15 and the related parameters for the purpose of parametrically studying Equation 3.11.

APPENDIX B

Appendix B contains information on various aspects of the formulation, implementation and validation of the Adiabatic 1st Order method of analysis. The set of equations, algorithm flow charts, convergence monitoring, along with a comparison of different numerical integrations techniques are presented. The system of 23 equations in the Adiabatic analysis is given in Table B-1. The equations required to be integrated numerically are B.1 (pressure), B.6 (compression space mass), and B.19 to B.23 (energy terms). The algorithm implemented in the numeric iterative process is shown in Fig. B-1 and the numerical algorithm of the 4th Order Runge Kutta method is illustrated in Fig. B-2.

Table B-1: Set of Thermal Cycle Equations for Adiabatic Analysis (Urieli, [2011])

Pressure Change	$\frac{dp}{dt} = \frac{-\gamma p \left(\frac{dV_c/dt}{T_{ck}} + \frac{dV_e/dt}{T_{he}} \right)}{\left(\frac{V_c}{T_c} + \frac{V_k}{T_k} + \frac{V_r}{T_r} + \frac{V_h}{T_h} + \frac{V_e}{T_e} \right)}$	(B. 1)
Mass Terms	$m_k = pV_k/RT_k$	(B. 2)
	$m_r = pV_r/RT_r$	(B. 3)
	$m_h = pV_h/RT_h$	(B. 4)
	$m_e = m - m_c - m_k - m_r - m_h$	(B. 5)
Mass Accumulation Rates	$\frac{dm_c}{dt} = \frac{\left(p dV_c/dt + \frac{1}{\gamma} V_c dp/dt \right)}{RT_{ck}}$	(B. 6)
	$\frac{dm_e}{dt} = \frac{\left(p dV_e/dt + \frac{1}{\gamma} V_e dp/dt \right)}{RT_{he}}$	(B. 7)
	$\frac{dm_k}{dt} = m_k \frac{dp/dt}{p}$	(B. 8)
	$\frac{dm_r}{dt} = m_r \frac{dp/dt}{p}$	(B. 9)
	$\frac{dm_h}{dt} = m_h \frac{dp/dt}{p}$	(B. 10)

	$\dot{m}_{ck} = -\frac{dm_c}{dt}$	(B. 11)
Mass Flow Rates	$\dot{m}_{kr} = \dot{m}_{ck} - \frac{dm_k}{dt}$	(B. 12)
	$\dot{m}_{rh} = \dot{m}_{kr} - \frac{dm_r}{dt}$	(B. 13)
	$\dot{m}_{he} = \dot{m}_{rh} - \frac{dm_h}{dt}$	(B. 14)
Interface Temperatures	$\text{if } \dot{m}_{ck} > 0 \Rightarrow T_{ck} = T_c; \quad \text{else} \Rightarrow T_{ck} = T_k$	(B. 15)
	$\text{if } \dot{m}_{he} > 0 \Rightarrow T_{he} = T_h; \quad \text{else} \Rightarrow T_{he} = T_e$	(B. 16)
Compression Gas Temperature	$T_c = \frac{pV_c}{Rm_c}$	(B. 17)
Expansion Gas Temperature	$T_e = \frac{pV_e}{Rm_e}$	(B. 18)
Work Rates	$\dot{W}_c = p \frac{dV_c}{dt}$	(B. 19)
	$\dot{W}_e = p \frac{dV_e}{dt}$	(B. 20)
Heat Rates	$\dot{Q}_k = C_p(T_{ck} - T_k) \frac{dm_c}{dt} - RT_k \frac{dm_k}{dt}$	(B. 21)
	$\dot{Q}_r = C_v T_r \frac{dm_r}{dt} - C_p \left[T_k \left(\frac{dm_c}{dt} + \frac{dm_k}{dt} \right) + T_h \left(\frac{dm_e}{dt} + \frac{dm_h}{dt} \right) \right]$	(B. 22)
	$\dot{Q}_h = C_p(T_{he} - T_h) \frac{dm_e}{dt} - RT_h \frac{dm_h}{dt}$	(B. 23)

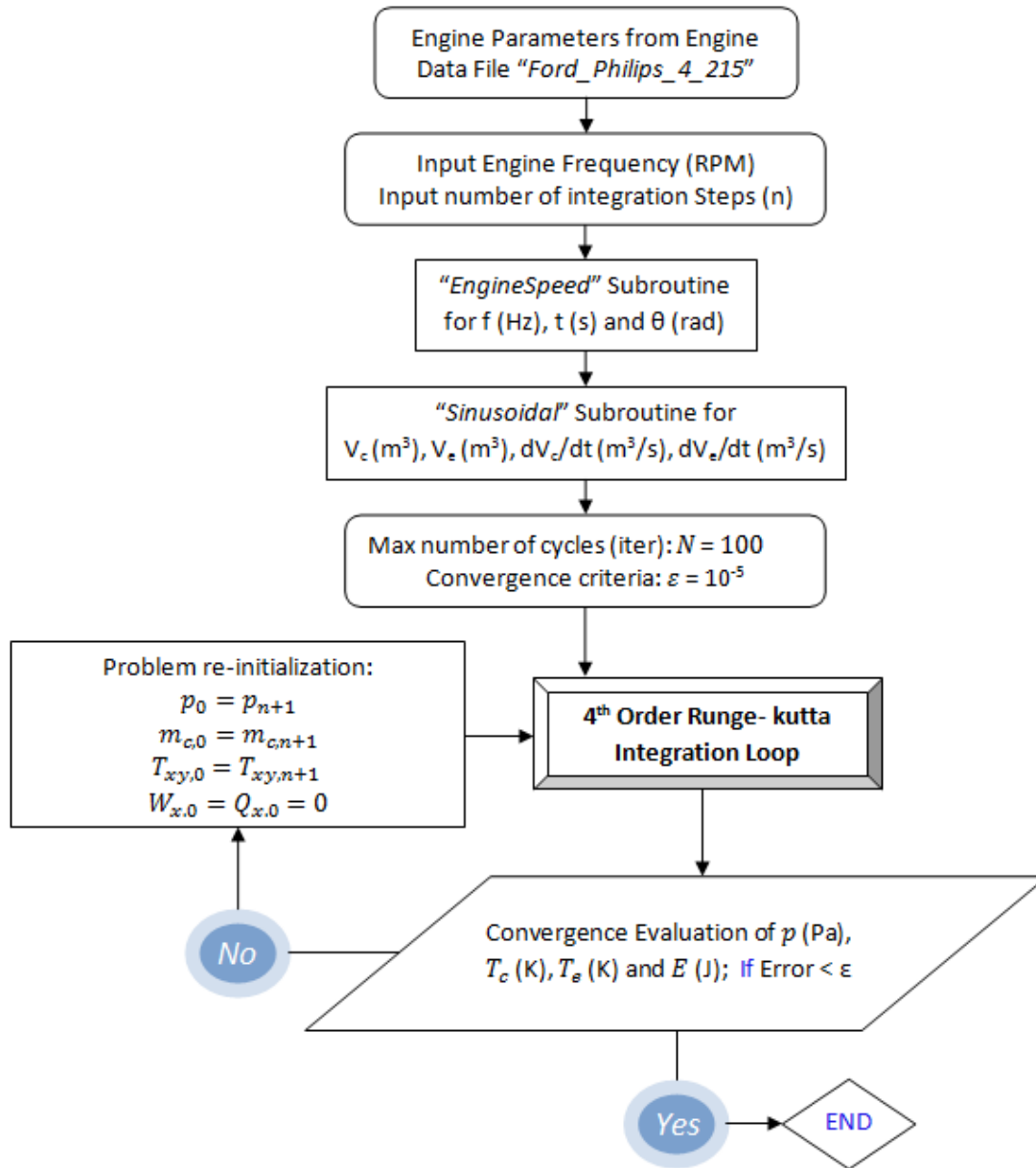


Figure B-1: Flow Chart for Adiabatic Analysis Program

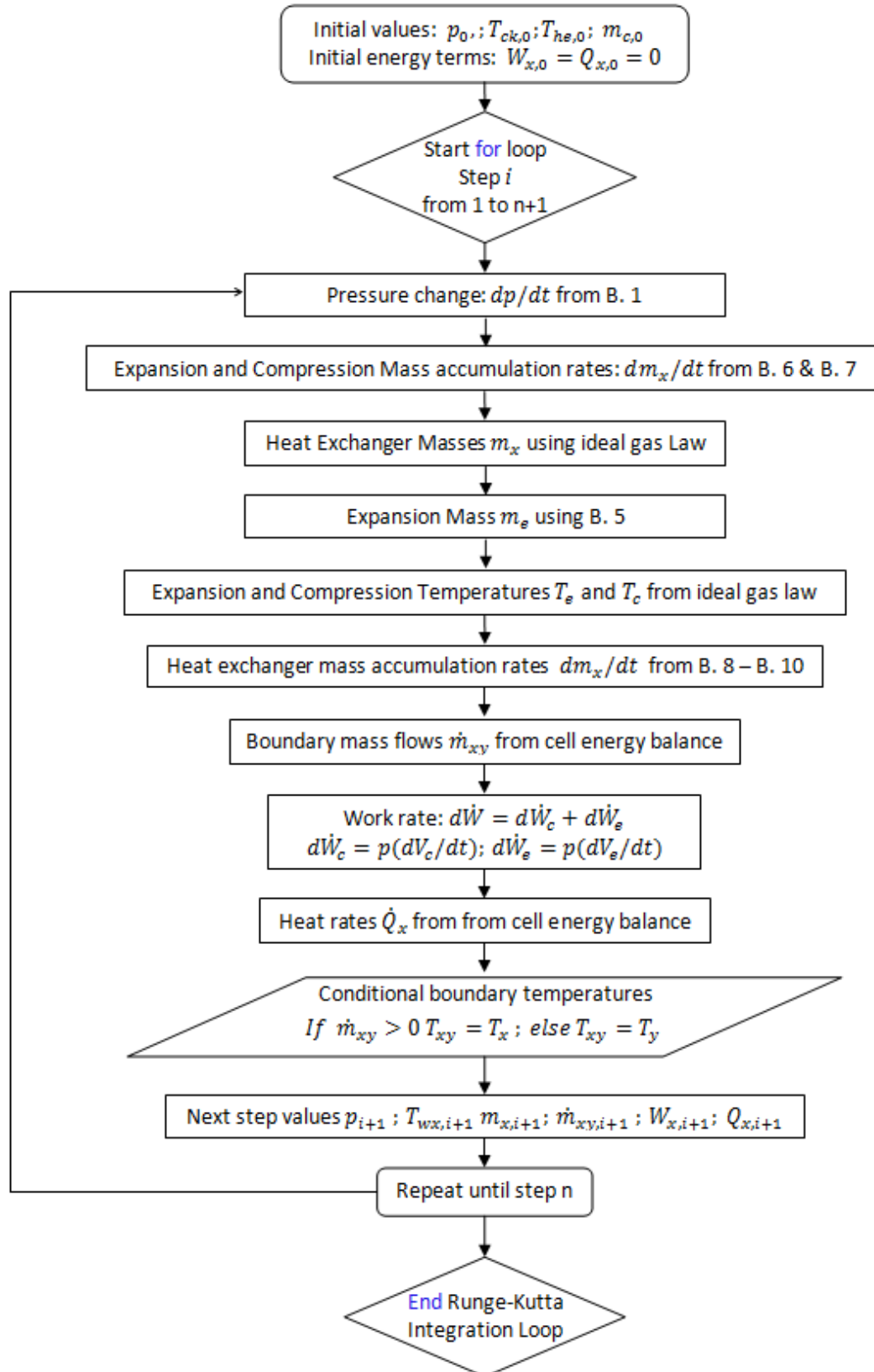


Figure B-2: Flow Chart for 4TH Order Runge-Kutta Integration Loop in Adiabatic Analysis Program

Figure B-3 was plotted to have a visual representation of the conservation of energy through the cycle for the total engine. At the start of the cycle there is no accumulated work or heat from the cycle, so both Q_{net} and W_{net} are zero. The first law of thermodynamics requires that at the end of the cycle the net work output is equal to the net heat transfer to the system. Figure B-3 confirms that energy is conserved in the Adiabatic analysis, not only from this perspective of heat and work, but as well in terms of the internal energy of the engine (U), which is equal at the start and at the end of the cycle.

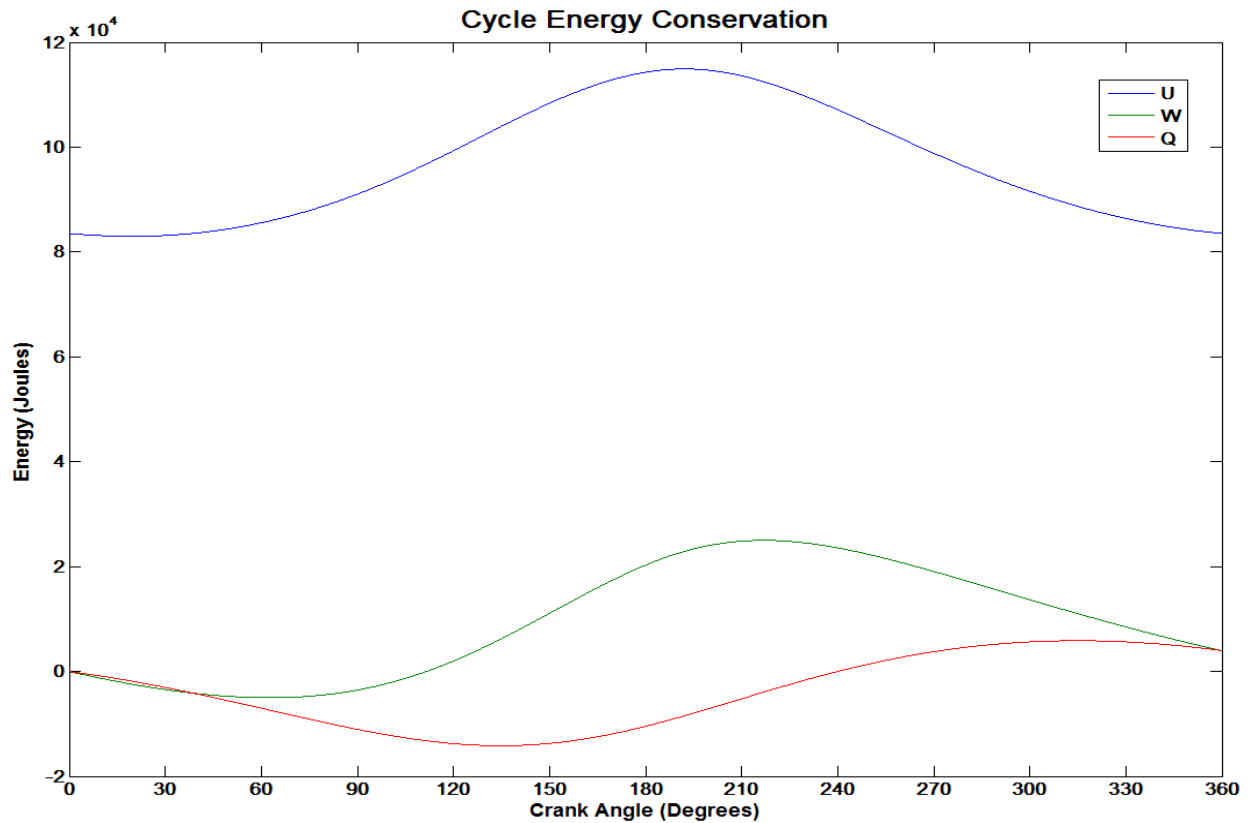


Figure B-3: Energy Conservation for Adiabatic Analysis

For the purpose of plotting Fig. B-3, the internal energy was assumed as:

$$U = C_v[m_c T_c + m_k T_k + m_r T_r + m_h T_h + m_e T_e] \quad (\text{B. 24})$$

To test the numerical stability, convergence and consistency in the results of the 4th Order Runge Kutta other integration methods were compared (Table B-2). Both the modified Euler (2nd order) and the Runge Kutta (4th Order) method yielded almost identical results, and both converged at 19 iterations (or cycles). The explicit Euler (1st Order) numeric solution did not meet the convergence criteria for the error in energy conservation.

However, this error is still relatively small compared to the energy terms and the final results are in close agreement with both the modified Euler and the 4th Order Runge Kutta integration methods. The lesson learned from this comparison was that the Order of the numerical method has a considerable impact on the number of iterations it will take to converge the solution. It was also found that to guarantee stability, convergence and consistency the minimum number of integration steps (or subintervals in which the cycle time period is divided) should be around 1000 for 4th Order Runge Kutta and around 5,500 for both modified Euler and explicit Euler. For this comparison 15,000 integration steps and a rotational speed of 4500 RPMs were used.

Table B-2: Comparison of numerical result for n=15,000 (number of steps) and 4500 RPMs

Numerical Method	Explicit Euler	Modified Euler	Runge Kutta 4th Order
Convergence Iteration (j)	n/a	19	19
Error in T_c (e₁)	5.6843×10 ⁻¹³	4.6646×10 ⁻¹⁰	4.6356×10 ⁻¹⁰
Error in T_e (e₂)	2.2737×10 ⁻¹²	5.4115×10 ⁻¹⁰	5.4013×10 ⁻¹⁰
Error in p (e₃)	5.5879×10 ⁻⁹	7.6741×10 ⁻⁶	7.6219×10 ⁻⁶
Error in Q_{net} - W_{net} (e₄)	4.7259	3.4913×10 ⁻⁷	6.2601×10 ⁻⁸
Cycle Efficiency (η)	0.6177	0.6176	0.6176
Net Cycle Work (W_{net})	3.9818×10 ³ J	3.9795×10 ³ J	3.9795×10 ³ J

The approach used in order to determine the errors for the convergence evaluation is shown in Table B-3. Mass conservation is not evaluated since the expansion space mass is calculate from Eq. B.5. This forces the mass balance in the individual cells, because the summation of the each cell mass always equals the total mass in the engine.

Table B-3: Set of equations for error and convergence evaluation in the Adiabatic Analysis

Error in T _c	$e_1 = T_c(0^\circ) - T_c(360^\circ) $	(B. 25)
Error in T _e	$e_2 = T_e(0^\circ) - T_e(360^\circ) $	(B. 26)
Error in p	$e_3 = p(0^\circ) - p(360^\circ) $	(B. 27)
Error From Energy Conservation	$e_4 = Q_{net} - W_{net} $	(B. 28)

Figure B-4 to B-7, were done to monitor the residual error as iterations progress. The normalized error ($\xi = e/e_{max}$) is shown in Fig. B-4; this is simply the normalization of the

error monitor in terms of the maximum calculated error. Figure B-5 displays the error from the expansion and compression space temperature calculation. In Figure B-6 the pressure numerical error is plotted. Finally, the energy conservation is monitored (Fig. B-7). The error plots suggest that for less strict convergence criteria, convergence should be achieved in around 6 or 7 iterations.

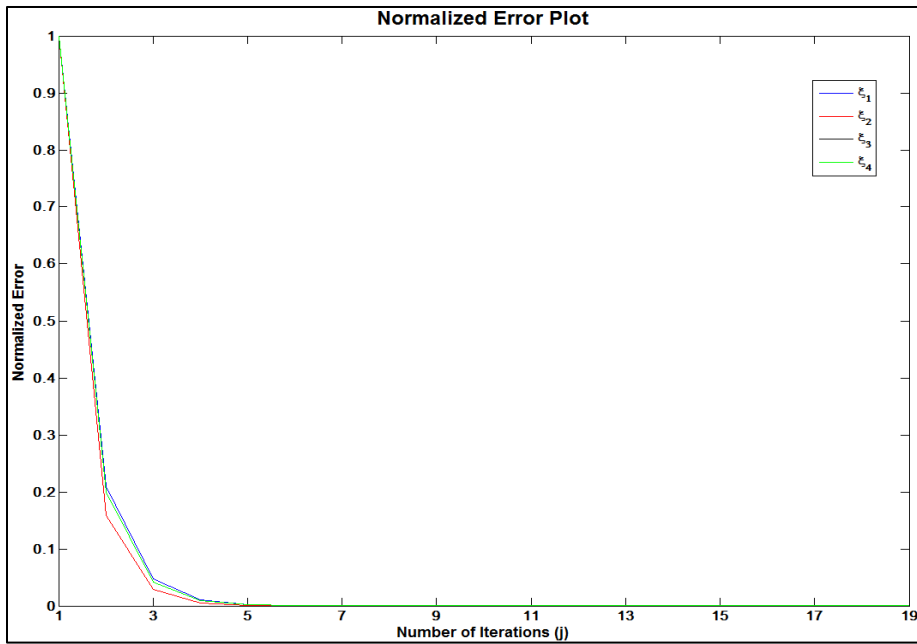


Figure B-4: Normalized Error (using max error) for Adiabatic Analysis

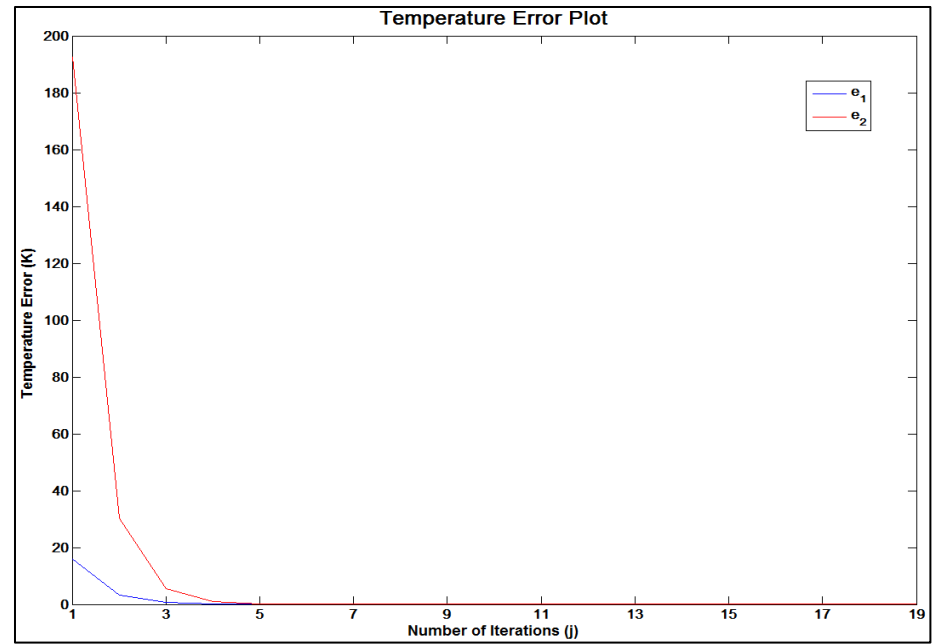


Figure B-5: Error in Expansion and Compression Space Temperature for Adiabatic Analysis

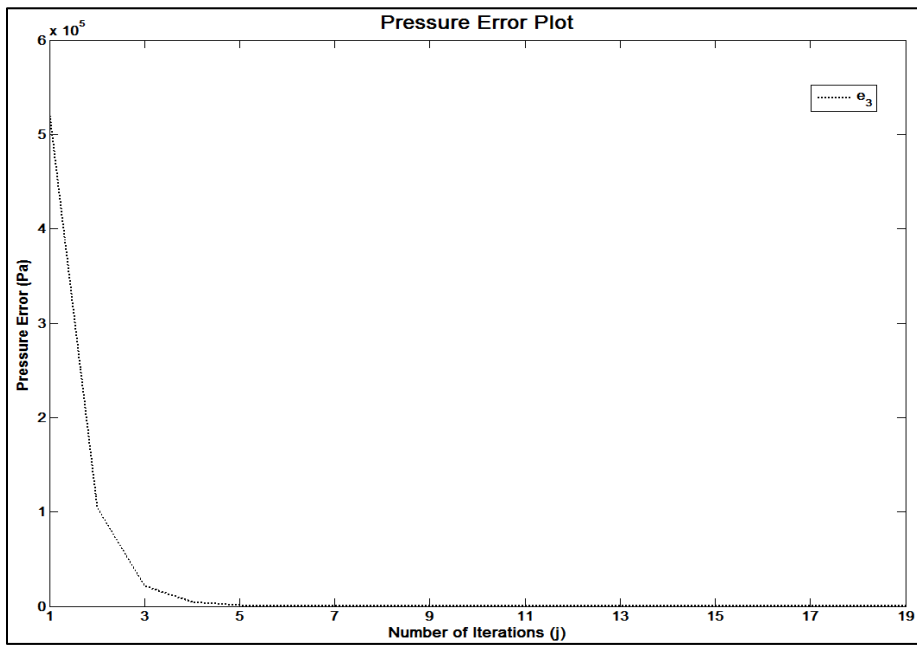


Figure B-6: Error in Pressure for Adiabatic Analysis

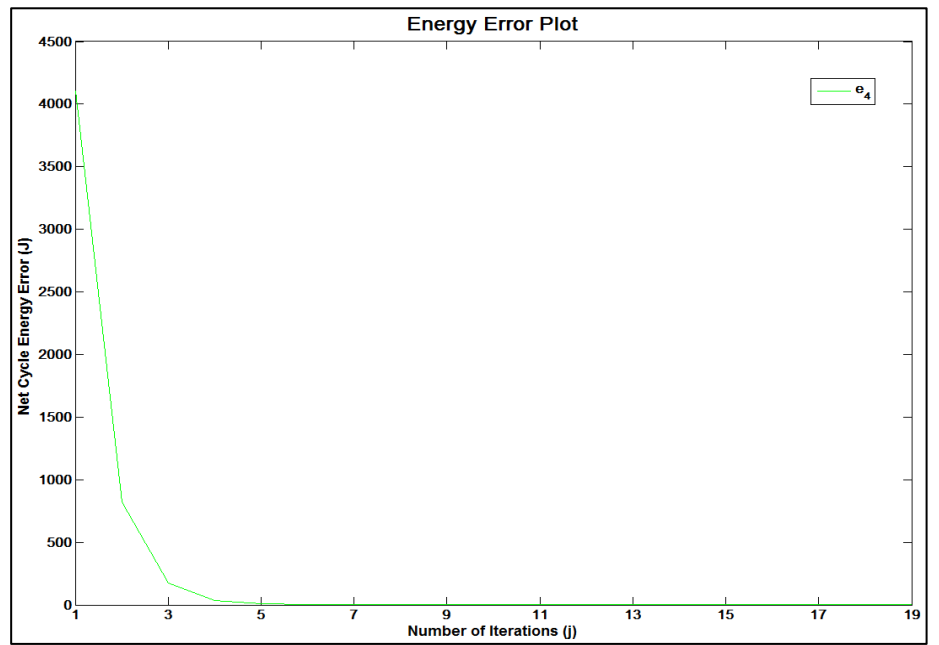


Figure B-7: Error in Energy Conservation for Adiabatic Analysis

APPENDIX C

Appendix C.1

Appendix C.1 contains information on various important aspects of the formulation, implementation and validation of the Finite Heat Transfer (FHT) analysis. The set of equations, algorithm flow charts, convergence monitoring, along with a comparison of different numerical integrations techniques are presented. The system of 37 equations in the FHT analysis is given in Table C-1. The equations required to be integrated numerically are C.14, C.15 (work terms), C.17 to C.21 (heat terms), C.23 (pressure), C.24, C.25 (regenerator wire matrix temperatures), C.31 (compression space mass), and C.33 to C.36 (mass terms). The algorithm used to implement the numeric iterative process is shown in Figure B-1 and the numerical implementation of the 4th Order Runge Kutta method is illustrated in Figure B-2. The flow chart contained in Fig. B-1 is almost identical to the one for the Adiabatic analysis (Fig. C-1). However, the convergence evaluation and the problem re-initialization differ from what is used in the Adiabatic analysis. This is associated in the difference of the numerical implementation of the 4th order integration which is not the same for both analyses.

Table C-1: Set of Thermal Cycle Equations for Finite Heat Transfer Analysis (Urieli, [1984])

	$T_c = pV_c/(Rm_c)$	(C.1)
	$T_k = pV_k/(Rm_k)$	(C.2)
Gas	$T_{r1} = pV_{r1}/(Rm_{r1})$	(C.3)
Temperatures	$T_{r2} = pV_{r2}/(Rm_{r2})$	(C.4)
	$T_h = pV_h/(Rm_h)$	(C.5)
	$T_e = pV_e/(Rm_e)$	(C.6)
Regenerator	$T_{rk} = 1.5T_{r1} - 0.5T_{r2}$	(C.7)
Linear Tem-	$T_{rr} = 0.5(T_{r1} + T_{r2})$	(C.8)
peratures	$T_{hr} = 1.5T_{r2} - 0.5T_{r1}$	(C.9)
	$if \dot{m}_{ck} > 0 \Rightarrow T_{ck} = T_c ; \quad else \Rightarrow T_{ck} = T_k$	(C.10)
Interface	$if \dot{m}_{kr} > 0 \Rightarrow T_{kr} = T_k ; \quad else \Rightarrow T_{kr} = T_{rk}$	(C.11)
Temperatures	$if \dot{m}_{rh} > 0 \Rightarrow T_{rh} = T_{rh} ; \quad else \Rightarrow T_{rh} = T_{hr}$	(C.12)
	$if \dot{m}_{he} > 0 \Rightarrow T_{he} = T_h ; \quad else \Rightarrow T_{he} = T_e$	(C.13)
	$\dot{W}_c = p \frac{dV_c}{dt}$	(C.14)
Work Rates	$\dot{W}_e = p \frac{dV_e}{dt}$	(C.15)
Total Work	$\dot{W} = \dot{W}_c + \dot{W}_e$	(C.16)
Rate	$\dot{Q}_k = h_k A_{wk} (T_{wk} - T_k)$	(C.17)
	$\dot{Q}_{r1} = h_{r1} A_{wr1} (T_{wr1} - T_{r1})$	(C.18)
Heat Rates	$\dot{Q}_{r2} = h_{r2} A_{wr2} (T_{wr2} - T_{r2})$	(C.19)
	$\dot{Q}_r = \dot{Q}_{r1} + \dot{Q}_{r2}$	(C.20)
	$\dot{Q}_h = h_h A_{wh} (T_{wh} - T_h)$	(C.21)
Total Heat	$\dot{Q} = \dot{Q}_k + \dot{Q}_r + \dot{Q}_h$	(C.22)
Rate		

Pressure Change	$\frac{dp}{dt} = \frac{\left(\frac{R}{C_v}\dot{Q} - \gamma\dot{W}\right)}{(V_c + V_k + V_r + V_h + V_e)}$	(C.23)
Regenerator Matrix Temperatures	$\frac{dT_{wr1}}{dt} = -\frac{\dot{Q}_{r1}}{V_{mr1}\rho_{mr1}c_{mr1}}$	(C.24)
	$\frac{dT_{wr2}}{dt} = -\frac{\dot{Q}_{r2}}{V_{mr2}\rho_{mr2}c_{mr2}}$	(C.25)
	$\dot{m}_{ck} = -\frac{dm_c}{dt}$	(C.26)
	$\dot{m}_{kr} = \frac{\dot{Q}_k + \dot{m}_{ck}C_pT_{ck} - \frac{C_v}{R}V_k(dp/dt)}{C_pT_{kr}}$	(C.27)
Mass Flow Rates	$\dot{m}_{rr} = \frac{\dot{Q}_{r1} + \dot{m}_{kr}C_pT_{kr} - \frac{C_v}{R}V_{r1}(dp/dt)}{C_pT_{rr}}$	(C.28)
	$\dot{m}_{rh} = \frac{\dot{Q}_{r2} + \dot{m}_{rr}C_pT_{rr} - \frac{C_v}{R}V_{r2}(dp/dt)}{C_pT_{rh}}$	(C.29)
	$\dot{m}_{he} = \frac{\dot{Q}_h + \dot{m}_{rh}C_pT_{rh} - \frac{C_v}{R}V_h(dp/dt)}{C_pT_{he}}$	(C.30)
	$\frac{dm_c}{dt} = \frac{\left(p dV_c/dt + \frac{1}{\gamma}V_c dp/dt\right)}{RT_{ck}}$	(C.31)
Mass Accumulation Rates	$\frac{dm_e}{dt} = \frac{\left(p dV_e/dt + \frac{1}{\gamma}V_e dp/dt\right)}{RT_{he}}$	(C.32)
	$dm_k/dt = \dot{m}_{ck} - \dot{m}_{kr}$	(C.33)
	$dm_{r1}/dt = \dot{m}_{kr} - \dot{m}_{rr}$	(C.34)
	$dm_{r2}/dt = \dot{m}_{rr} - \dot{m}_{rh}$	(C.35)
	$dm_h/dt = \dot{m}_{rh} - \dot{m}_{he}$	(C.36)
Expansion Space Mass	$m_e = m - m_c - m_k - m_r - m_h$	(C.37)

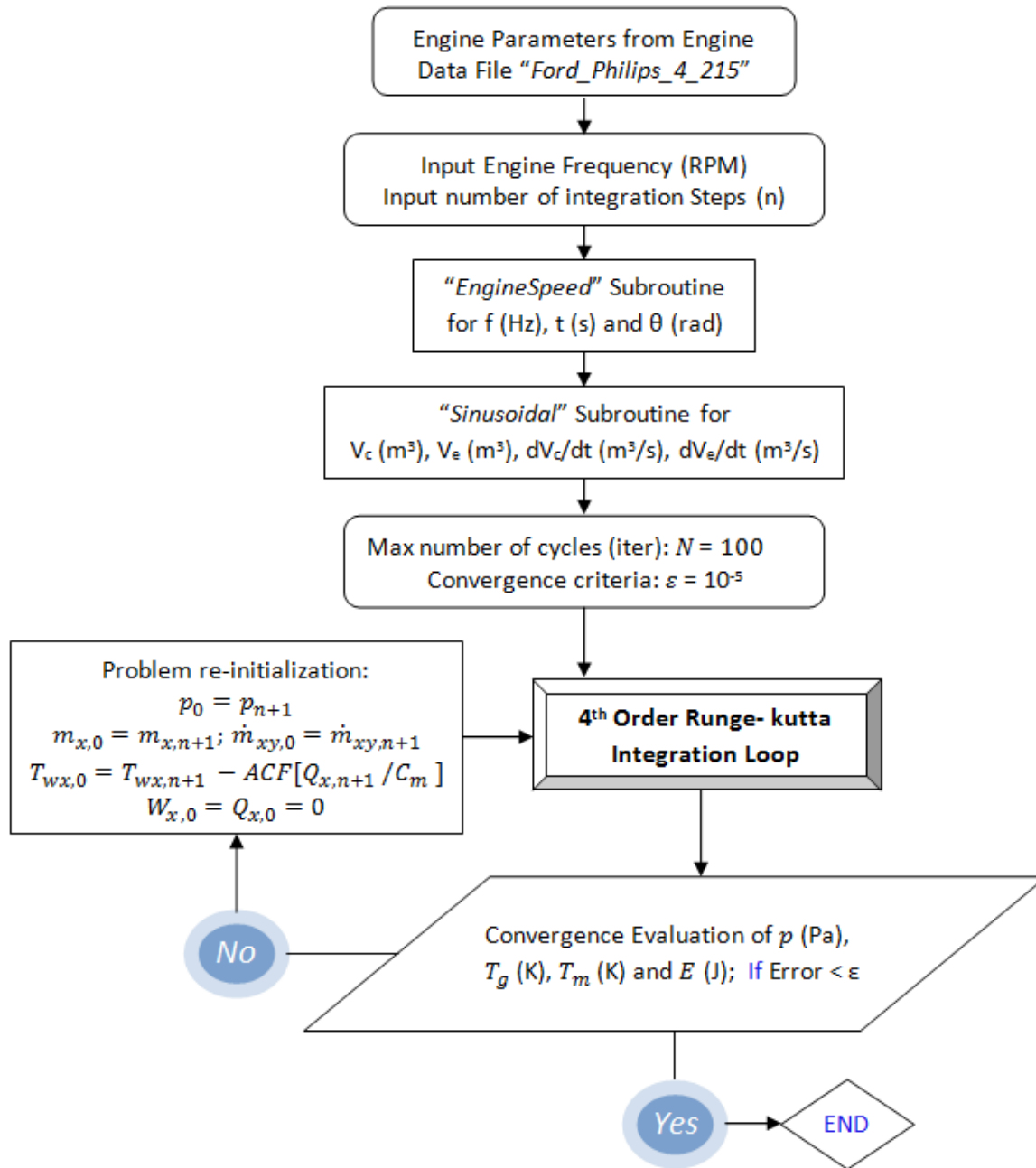


Figure C-1: Flow Chart for Finite Heat Transfer (FHT) Analysis Program

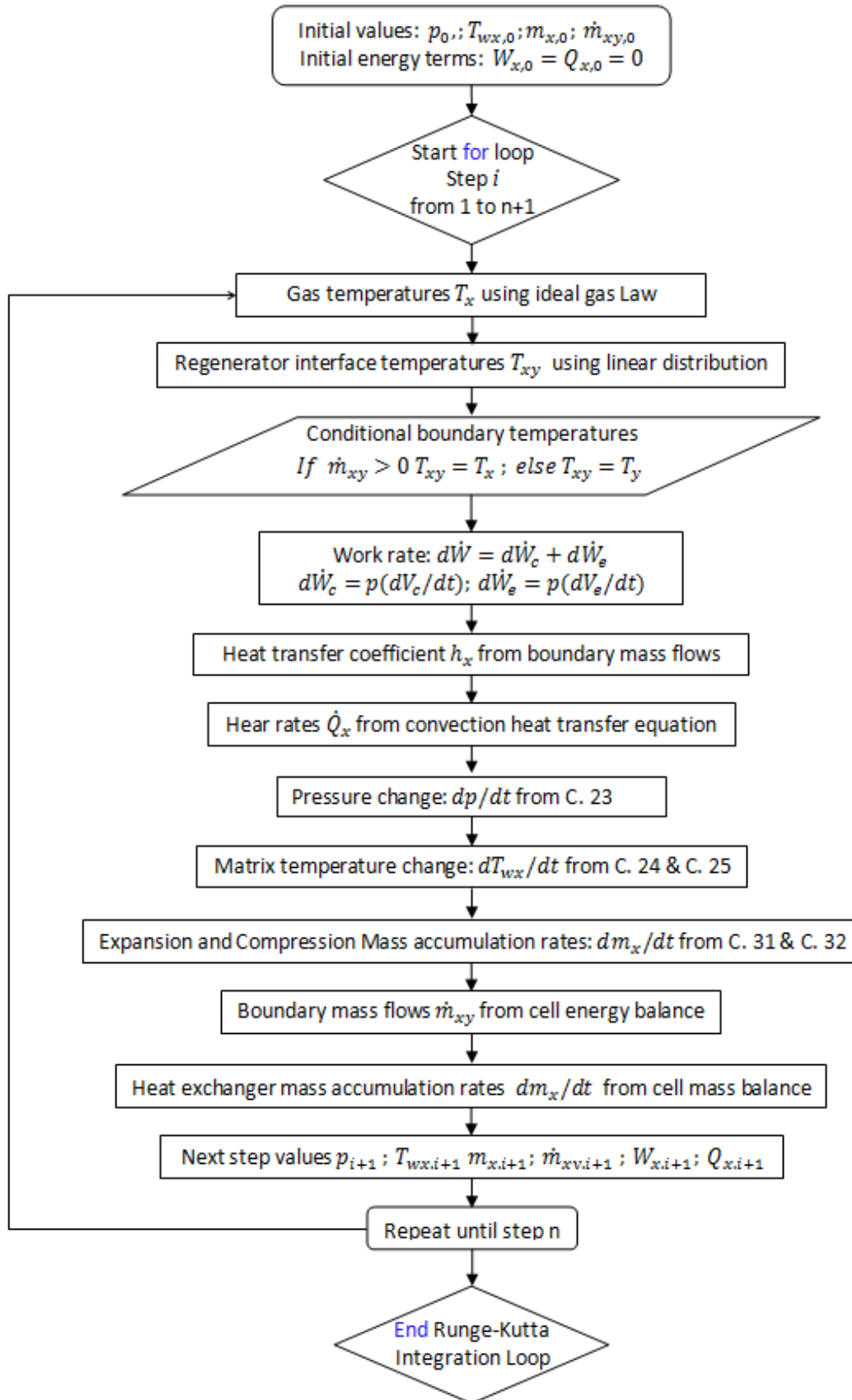


Figure C-2: Flow Chart for 4TH Order Runge-Kutta Integration Loop in FHT Analysis Program

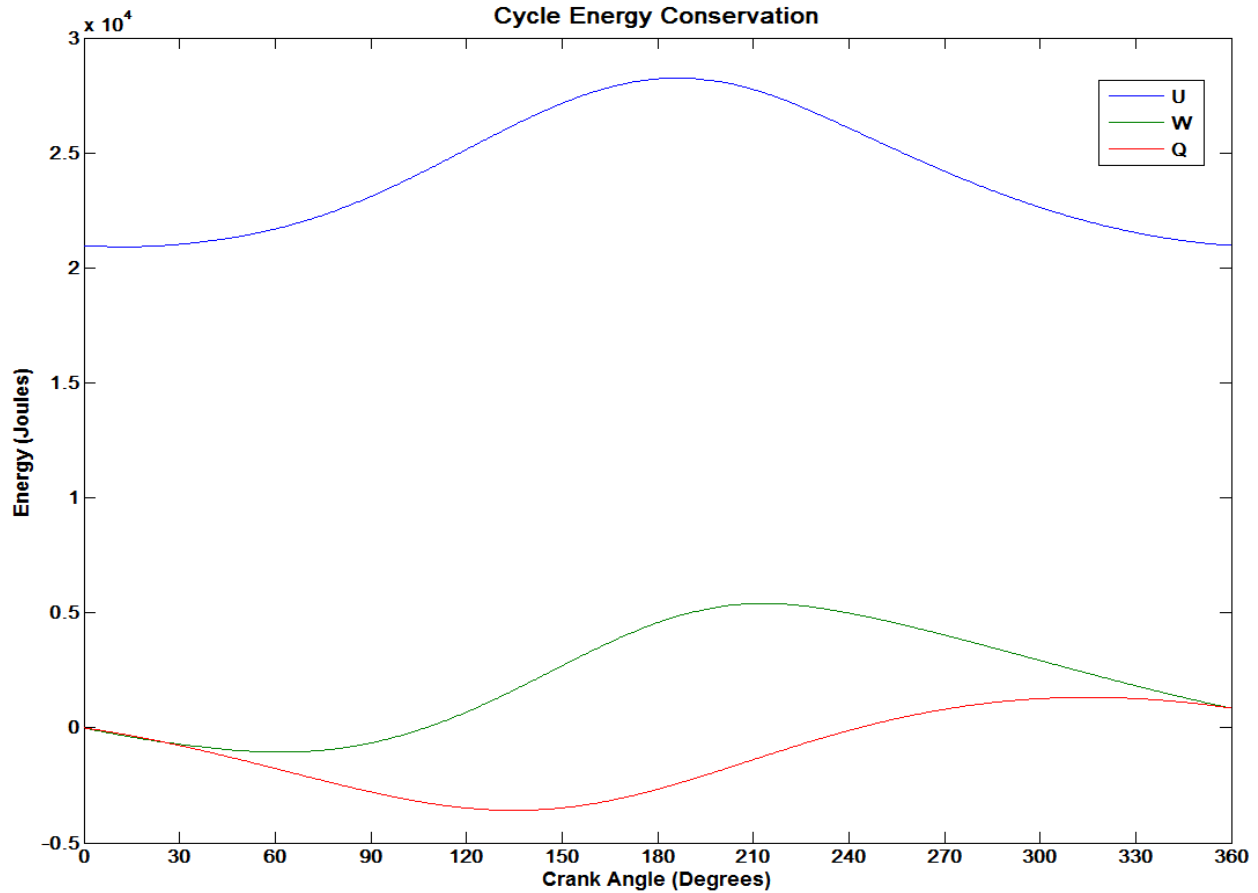


Figure C-3: Energy Conservation for Finite Heat Transfer Analysis

Following the approach in the Adiabatic analysis, the conservation of the total energy through the cycle for the Finite Heat Transfer analysis is plotted in Figure C-3. Again, it is assumed that the cycle is starting with no accumulated work or heat from the cycle, so both Q_{net} and W_{net} are zero. At the end of the cycle the first law of thermodynamics requires that the net work output equals the net heat transfer to the system, and it also requires that the same internal energy at start and at the end of the cycle. Figure C-3 confirms that both energy conservation requirements are met in the Finite Heat Transfer analysis. For the purpose of plotting Fig. C-3, the internal energy was assumed as:

$$U = C_v[m_c T_c + m_k T_k + m_{r1} T_{r1} + m_{r2} T_{r2} + m_h T_h + m_e T_e] \quad (C.38)$$

As demonstrated in Appendix B the numerical stability, convergence and consistency of the solution will depend on the order of the numerical technique used in the analysis. In the Adiabatic problem both the 4th order Runge Kutta and the modified Euler methods showed

favorable results in this aspect, compared to the explicit Euler method. It is assumed that for the Finite Heat Transfer (FHT) problem, the difference between one numerical method or the other stays relatively the same, and the effort is rather focused on accelerating the convergence of the stiffer and larger system of equation contained in the FHT analysis. It was found that the high values of matrix wire thermal capacitance, causes a considerably small change in the matrix temperatures at each iteration. Therefore, the relative large values (in comparison to hydrogen) for the heat capacity of regenerator matrix wire will affect the overall convergence rate of the solution. The technique suggested by Urieli [4] is used in order to accelerate convergence. The approach consist of using the net residual heat of the regenerator along with an arbitrary accelerating convergence factor (ACF) to modify the regenerator temperatures at the end of the cycle (Eq. 3.32 and 3.33), when the cycle is not converged. The optimum value for ACF was around 7 when solving for the sinusoidal motion variations of the compression and expansion spaces. However, for other types of motion (as well for other engine parameters) the optimum value for ACF will change. The results of the 4th order Runge Kutta integration method when using ACF=7 and not using ACF are compared in Table C-2. As shown, both approaches yielded almost identical results. However, using the ACF=7 reduced the number of iterations required significantly. For the comparison a rotational speed of 4500 RPMs was used, and the cycle time period was divided in to 1,000 integration steps (or subintervals).

Table C-2: Comparison of numerical results of Finite Heat Transfer Analysis, when using ACF=7 and ACF=0

Numerical Method	Runge Kutta 4th Order (No ACF)	Runge Kutta 4th Order (Using ACF=7)
Convergence Iteration (j)	427	63
Error in Gas Temperatures (e₁)	1.667×10 ⁻⁹	1.777×10 ⁻⁹
Error in Matrix Temperatures (e₂)	1.4852×10 ⁻⁹	1.435×10 ⁻⁹
Error in Pressure (e₃)	9.5647×10 ⁻⁶	7.782×10 ⁻⁶
Error in Energy Conservation (e₄)	8.5134×10 ⁻⁶	8.506×10 ⁻⁶
Cycle Efficiency (η)	0.5353	0.5353
Net Cycle Work (W_{net})	3.4215×10 ³ J	3.4215×10 ³ J

The approach used in order to determine the errors for the convergence evaluation is shown in Table C-3. Since for the FHT analysis, several cell temperatures vary along the cycle, the root sums square (RSS) error value for the gas temperatures (C.39) and the

regenerator matrix wire temperatures (C.40) are monitored instead of the individual error value. As for the Adiabatic analysis, mass conservation is not evaluated since the expansion space mass is calculated from Eq. C.37. This forces the mass balance in the individual cells, because the summation of the mass at each cell always equals the total mass in the engine. It should be noted, that at first, the regenerator net residual heat was monitored for convergence. This follows from the assumption in the thermodynamic equations, that do not account for any net heat accumulated in the regenerator. However, the author believes that monitoring the energy conservation (through or at the end of the cycle) is more convenient for several reasons. One is that if the accumulated heat is accounted for, $Q_{r,net}$ will be unknown (not zero at the end of the cycle) when imperfect regeneration is considered. And the other reason is to avoid double book keeping in the convergence of the energy terms.

Table C-3: Set of equations for error determination and convergence evaluation in FHT analysis

Error in T_g	$e_1 = \sqrt{\epsilon_{g1}^2 + \epsilon_{g2}^2 + \dots + \epsilon_n^2}$	(C.39)
Error in T_m	$e_2 = \sqrt{\epsilon_{m1}^2 + \epsilon_{m2}^2}$	(C.40)
Error in p	$e_3 = p(0^\circ) - p(360^\circ) $	(C.41)
Error From Energy Conservation	$e_5 = Q_{net} - W_{net} $	(C.42)

The cell gas temperature individual error is evaluated as follows,

$$\epsilon_g = |T_x(0^\circ) - T_x(360^\circ)| \quad (C.43)$$

Similarly the regenerator matrix wire temperature is,

$$\epsilon_m = |T_{wx}(0^\circ) - T_{wx}(360^\circ)| \quad (C.44)$$

Figures C-4 to C-7, were generated to monitor the residual error as iterations progress. Note that these figures are for when the ACF is zero. The normalized error ($\xi = e/e_{max}$) shown in Fig. C-4 is simply the normalization of the error monitors in terms of the maximum calculated error. Figure C-5 displays the RSS error in the gas temperatures and

the RSS error in the matrix wire temperatures. In Figure C-6 the pressure numerical error is plotted. Finally, the energy conservation is monitored (Fig. C-7). The error plots shown, were produced for the case having no ACF. The monitor curves have the same trend when a value of 7 is used for ACF; however, the convergence is achieved in less iterations. In contrast to the Adiabatic analysis the error in temperature, pressure and energy do not follow a similar trend, which can be attributed to the higher non linearity of the FHT system of equation in comparison to the Adiabatic analysis.

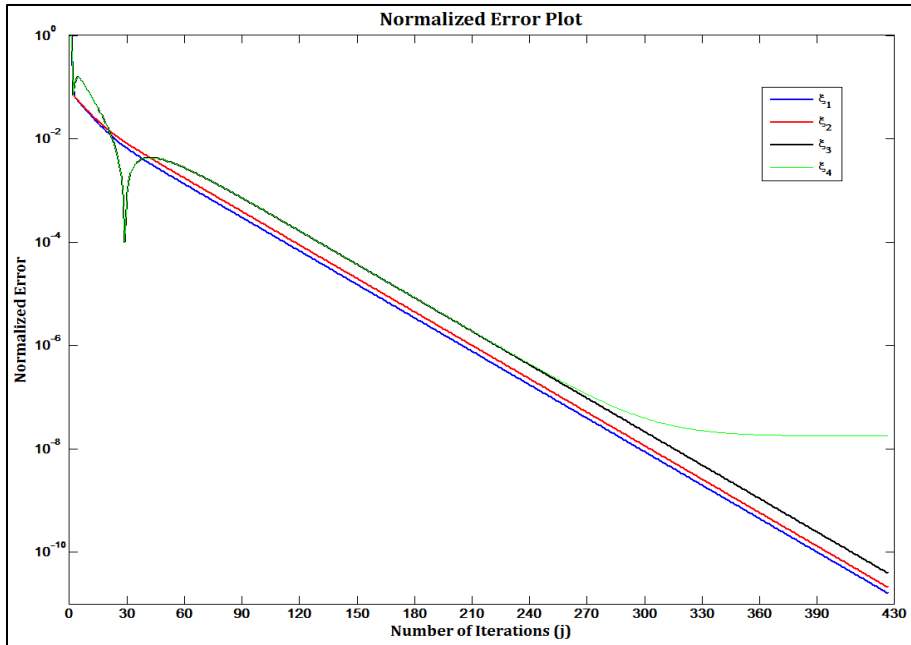


Figure C-4: Normalized Error (using max error) for FHT Analysis

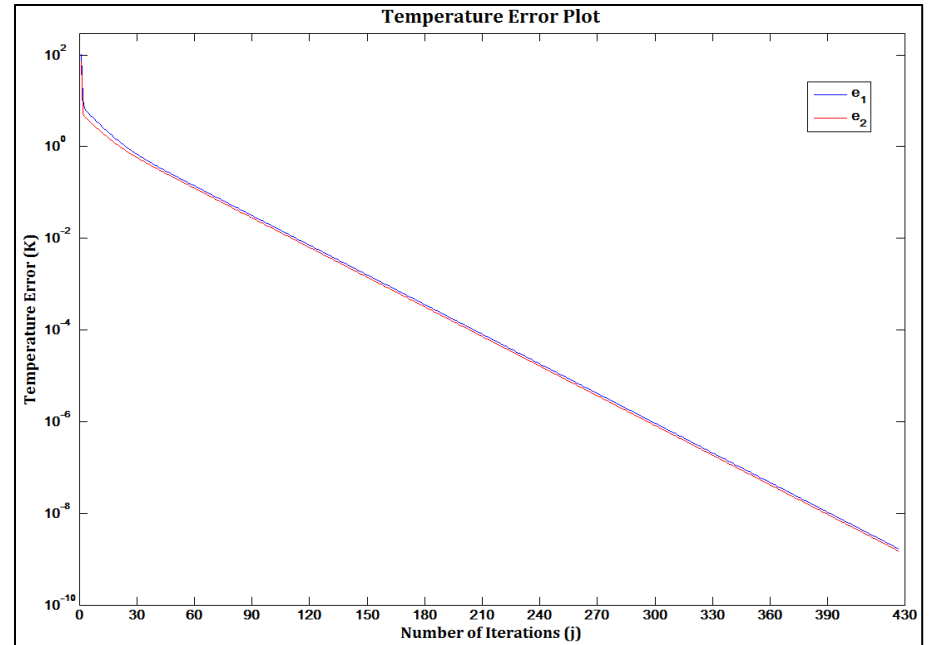


Figure C-5: Error in Gas and Matrix Wire Temperatures for FHT Analysis

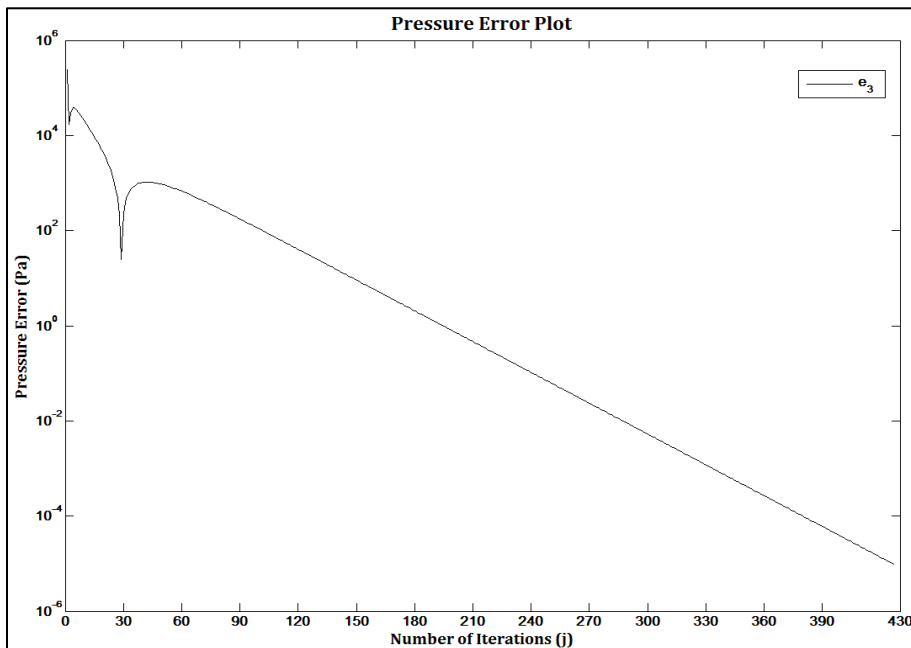


Figure C-6: Error in Pressure for FHT Analysis

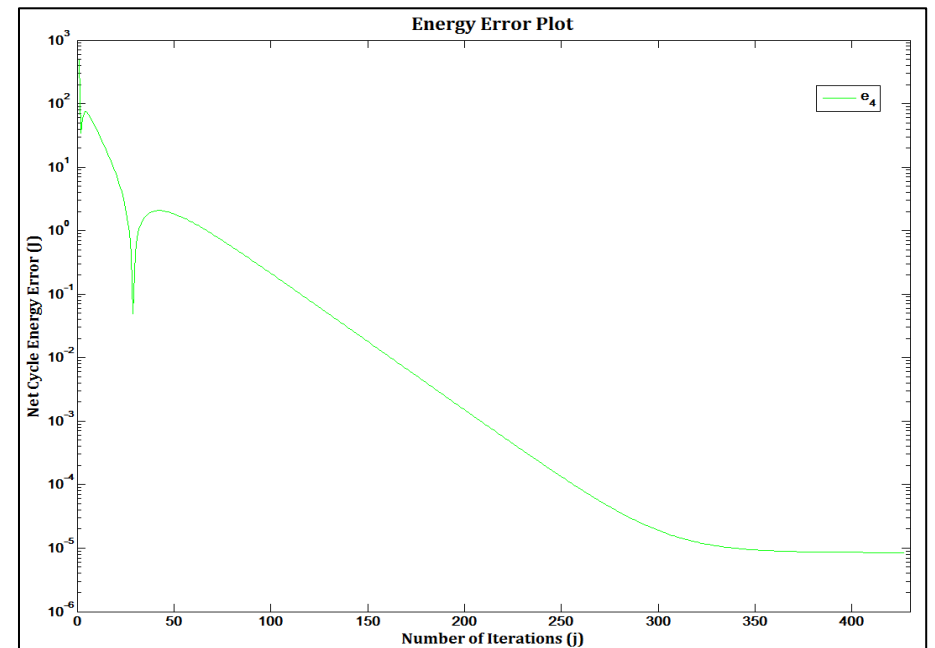


Figure C-7: Error in Energy Conservation for FHT Analysis

Appendix C.2

The purpose of Appendix C.2 is to show the mathematical equations used for modeling the heat transfer in the cooler, regenerator, and heater. The set of equations used to determine the heat transfer coefficient (h) is summarized in Table C-4. First the mass flux for the particular control volume is calculated using the average mass flow rates at the boundaries and the free flow area (C.45). Then, Re is obtained from the mass flux as in C.46 and the Fanning friction factor (from Martini [29]) is determined (C.47). The Gnielinski correlation [46] is used to estimate the Nu of the heater and cooler (C.48). However, if the flow is laminar ($Re < 2,300$), a value of 3.66 is used for Nu [46]. For the regenerator a different Nu formulation is used, since flow behavior is characteristic of porous media. The Nu relationship to wire matrix porosity and Re is describe using Gedeon-Wood correlation as stated in Pittman [47] was found to be applicable in this study. Equation C.49 is valid for wire matrix porosities of 0.62 to 0.78 (Ford-Phillips 4-215 regenerator has a porosity of 0.62), and covers Re data for actual Stirling engine regenerators. For validation purposes, the Gedeon-Wood correlation was plotted against Martini's correlation for matrix porosity of 0.717 in Figure C-8. As seen in Figure C-8, both correlations are in good agreement. The other curve shown in Fig. C-8 is for the actual Ford-Phillips 4-215 regenerator matrix porosity. Finally, the value of h is found from the theoretical definition of Nu (C.50).

Table C-4: Set of Equations for HTC Calculation in Finite Heat Transfer Analysis.

Mass flux	$G_x = \frac{\dot{m}_{x,avg}}{A_{fx}}$	(C.45)
Reynolds Number	$Re_x = \frac{G_x D_{hx}}{\mu_x}$	(C.46)
Turbulent Fanning Friction Factor	$\log(f_{f,x}) = -1.34 - 0.2 \cdot \log(Re_x)$	(C.47)
Nusselt Number for Heater and Cooler	$Nu_x = \frac{\frac{1}{2}f_{f,x}(Re_x - 1000)Pr_x}{1 + 12.7 \cdot (\frac{1}{2}f_{f,x})^{0.5} (Pr_x^{2/3} - 1)}$	(C.48)
Nusselt Number for Regenerator	$Nu_r = [1 + 0.99 \cdot (Re_r \cdot Pr_r)^{0.66}] \cdot \phi^{1.79}$	(C.49)

Heat Transfer Coef-
ficient

$$h_x = \frac{Nu_x D_{hx}}{k_{fx}} \quad (C.50)$$

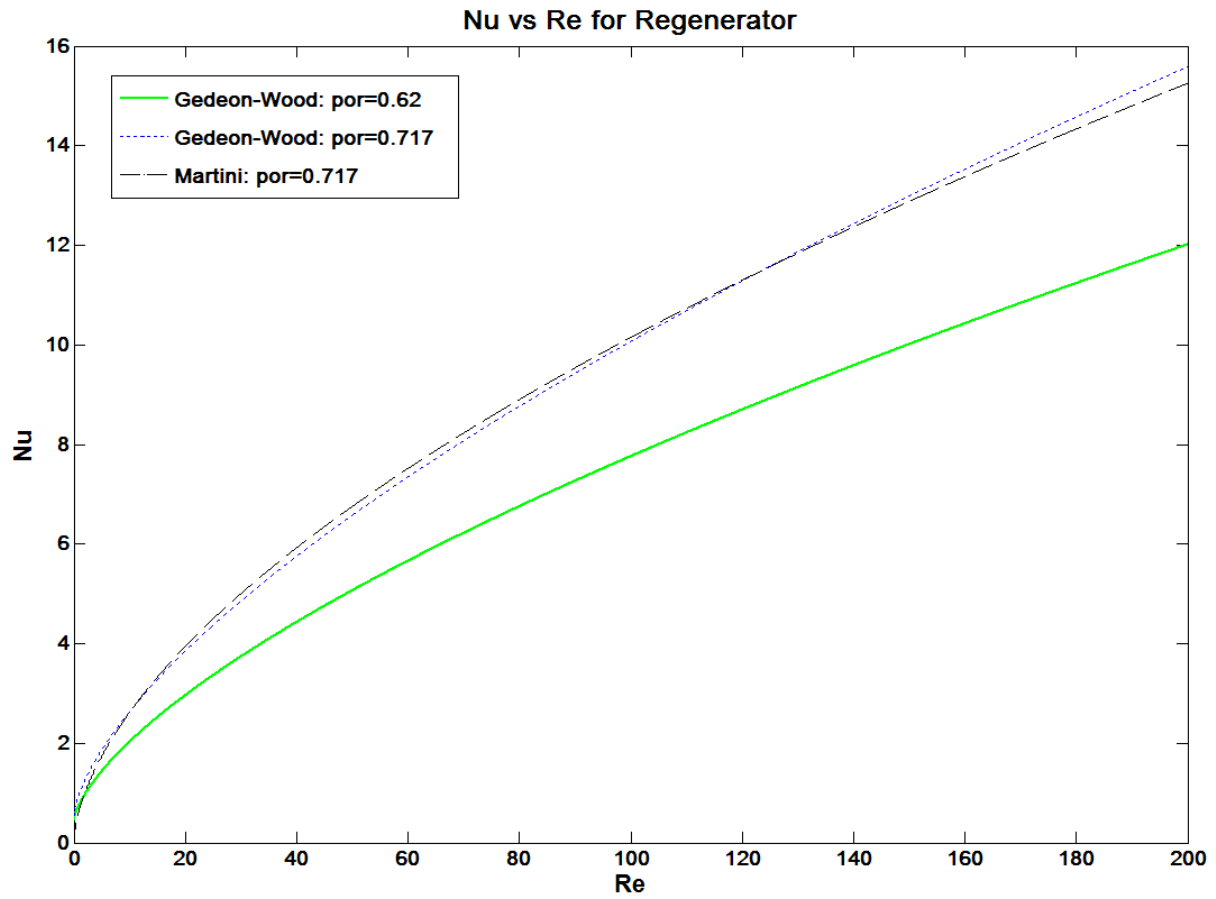


Figure C-8: Comparison of Gedeon-Wood and Martini's Correlation for Regenerator Nu Correlation

APPENDIX D

Appendix D.1

Appendix D.1 explains the reasoning and formulation behind the 2nd Order method used in the presented Stirling engine analysis. First, the Isothermal, Adiabatic, or Finite Heat Transfer (FHT) analyses are solved to serve as the 1st Order method analysis baseline calculation. The current 2nd Order method routine was developed in MATLAB to be adaptable for any of the previous 1st Order analysis methods mentioned (Appendix A to C).

The cycle pressure, mass flows, and other output parameters from the 1st Order method are used as inputs for the 2nd Order loss calculations. Then, the flow characteristics and the power loss from the pressure drop in the heat exchanger are estimated. To account for the total value of power loss, the average pressure drop in the cooler, regenerator, and heater are used. Afterwards the power loss from mechanical friction is correlated from Costea et al. correlation [52] (Eq. D.10 to D.12). The final loss considered in the engine is the regeneration heat loss due to the imperfect heat transfer. This MATLAB subroutine is capable of using (user specified) Organ-Finkelstein, Urieli or Martini approaches to evaluate the regenerator heat loss. Finally, equations 3.49 to 3.51 are used to obtain the 2nd Order net performance prediction for the engine. A general overview of the determination of 2nd Order losses is shown in Figure D-1. More details for the pressure loss, mechanical loss, and heat loss are given in the subsequent sections in this appendix.

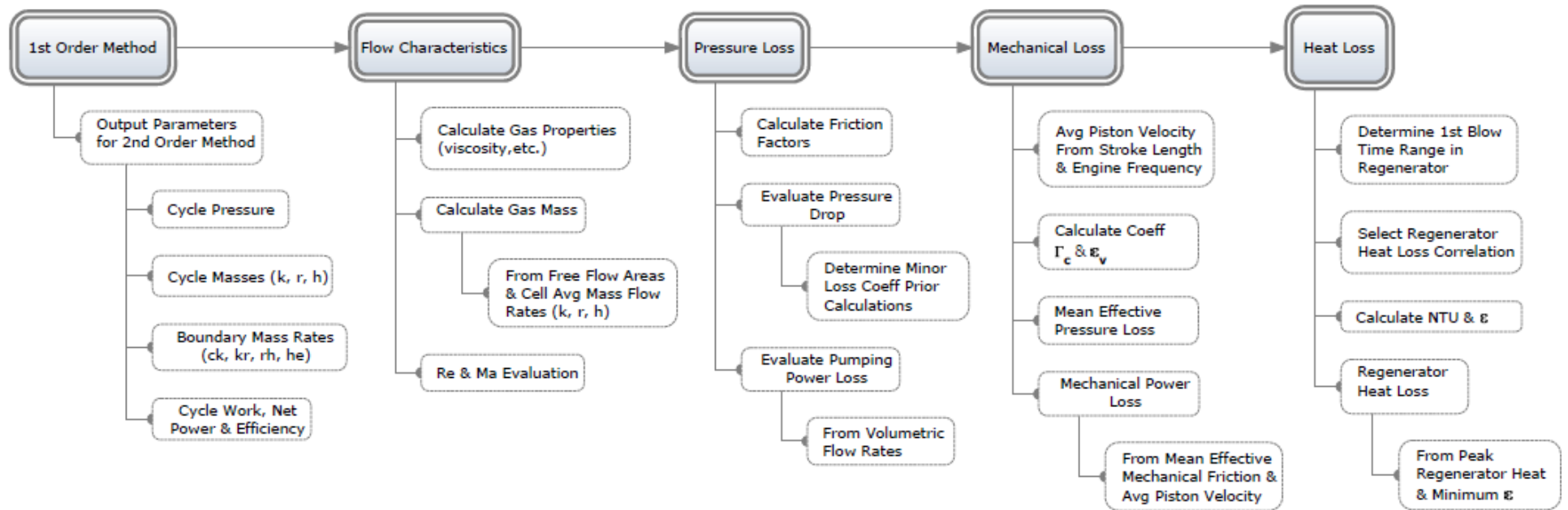


Figure D-1: 2nd Order Method Calculation Flow Chart

Appendix D.2

For the analysis, it is assumed that the flow field compressible effects are negligible, and that the flow characteristics are determined by whether the flow is laminar or turbulent. In Figure D-2, the first flow assumption is shown to be satisfied as the maximum Mach number (Ma) is less than 0.1. Since the plotted values in Fig. D-2 are for 4,500 RPM, which is the maximum engine speed, it is expected that for other lower speed conditions the maximum Ma value will be lower. Note that for the regenerator Ma, the values are scaled by a factor of 10 for visualization purposes. Although Ma values calculated in the regenerator are an order of magnitude less than the heater and cooler, it should be realized that the regenerator is governed by porous media phenomena. This implies that compressible effects can be significant for flow through the regenerator even for small Ma flow condition. However, compressible effects are typically studied when using a Method of Characteristic approach which falls out of the scope of this work. Therefore, the fluid in the regenerator is modeled as an ideal gas law without flow induced compressibility effects.

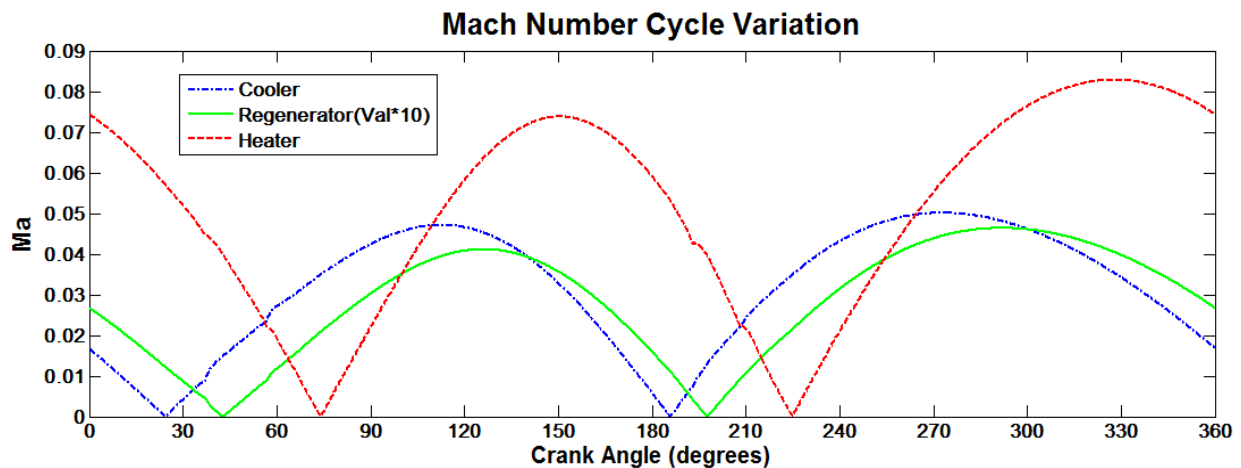


Figure D-2: Cooler, Regenerator and Heater Mach Numbers for 4500 RPM

As stated above, the flow behavior is assumed to depend only on the Reynolds Number (Re). From Figure D-3 it is seen that the higher Re occurs in the heater ($\max Re > 10^5$). Also, for the heater and cooler, the flow is predominantly turbulent except when close to the flow reversals, where the laminar flow condition ($Re < 2000$) exists. Note that for the flow reversals the flow at one of the boundaries approaches zero. The Re for the regenerator is scaled by a factor of 100; this value is arbitrary and is used only for visualization purposes.

Similar to the regenerator Ma values, regenerator Re values are orders of magnitude smaller than the cooler and heater. Nevertheless, it is highlighted again that flow through the regenerator matrix is governed by the physics of flow through porous media. For this reason even for such low Re, the flow in the regenerator can be extremely turbulent based on conventional porous media understanding.

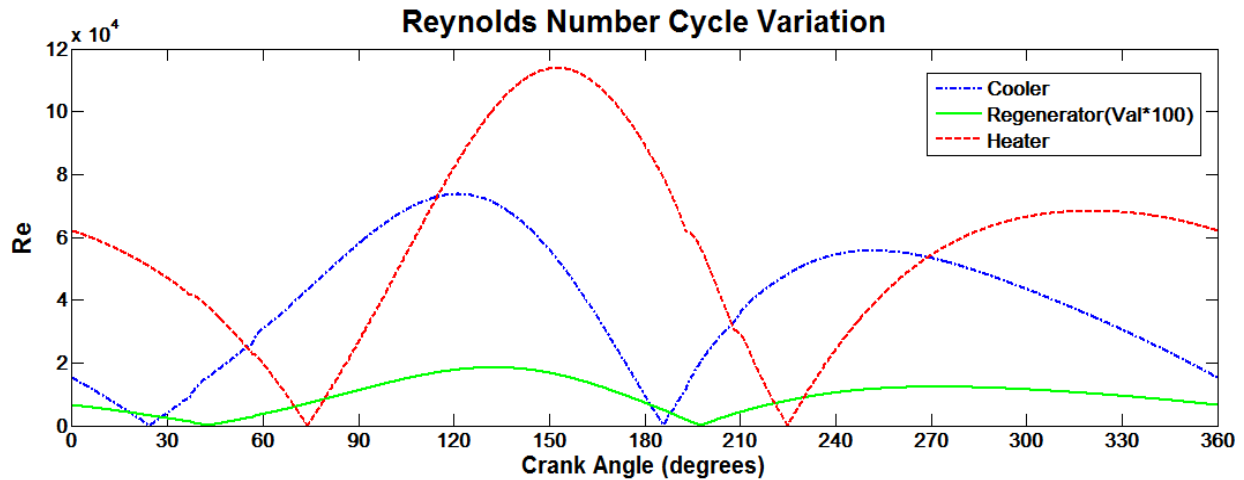


Figure D-3: Cooler, Regenerator and Heater Reynolds Numbers for 4500 RPM

The Fanning friction factor for the cooler and heater were determined using Eq. C.47. This correlation is suggested by Martini [29] as the pipe flow model for the Stirling engine heater and cooler. To calculate the pipe losses, the Fanning friction factor is multiplied by a factor of 4 (equivalent to Darcy-Weisbach). The Fanning friction factor from Martini is compared to the equivalent Darcy-Weisbach friction factor using Haaland's [55] correlation in Figures D-4. In the Haaland's correlation, a pipe relative roughness of 10⁻⁵ and 10⁻⁶ was used. Although, Haaland recommends his equations for relative roughness higher than 10⁻⁴, the error that might arise for the lower values used should not be significant enough to affect the comparison. For both the cooler and the heater, Darcy-Weisbach friction factor (from Haaland's) approaches the Fanning friction factor for small relative roughness values. Smooth pipes, with such roughness values, are expected for Stirling engines using high performance heat exchangers. Thus it appears that Martini's correlation [29] gives a good approximation for the Fanning friction factor in the cooler and heater.

Pressure drop estimated across the regenerator is a very complicated subject. The complex and sometimes irregular geometry of the porous medium makes it difficult to

capture the flow behavior with enough resolution. Therefore, the associated pressure drop predictions tend to become inaccurate. For Stirling engine regenerators, three major factors come to play when determining the pressure drop across the regenerator porous medium:

1. Type of Matrix used (Stack –Wire Screens, Metal Felts, etc.)
2. Porosity of the Matrix
3. Reynolds Number

The pressure drop correlation considered in this study is from the one devised by Martini [29]. Martini proposed a correlation based on the data of the Kays and London chart. The data of the Kays and London experiments was obtained from pressed stack wire screens matrices, corresponding to porosities of 0.602, 0.725, 0.766 and 0.832 (Figure 3–38). Martini’s correlation was compared to the Pinker-Hebert correlation (as Described by R. Remsburg [50]) and was validated using the Darcy’s Law and the Darcy-Forchheimer equation for unidirectional flow in porous media [56-58]. The equivalent loss coefficient for Pinker-Hebert is calculated from a parameter β (dependent on Re), the screen porosity, and the number of screens. Subsequently the pressure drop is obtained from the equivalent loss coefficient and the velocity head. The form of this pressure loss prediction does not depend on the length and hydraulic radius of the regenerator, and therefore is different to how the pressure drops are expressed in most Stirling engine literature. The comparison of regenerator pressure drop correlations is shown in Figure D–5, for a constant engine speed of 4500 RPM. It is shown that Pinker and Herbert’s correlation deviates from Darcy’s Law and the Darcy-Forchheimer equation, since it does capture the downstream effects as the flow goes from screen to screen. However, the approach presented by Martini [29] is fairly close to Darcy’s Law and the Darcy-Forchheimer equation [56-58].

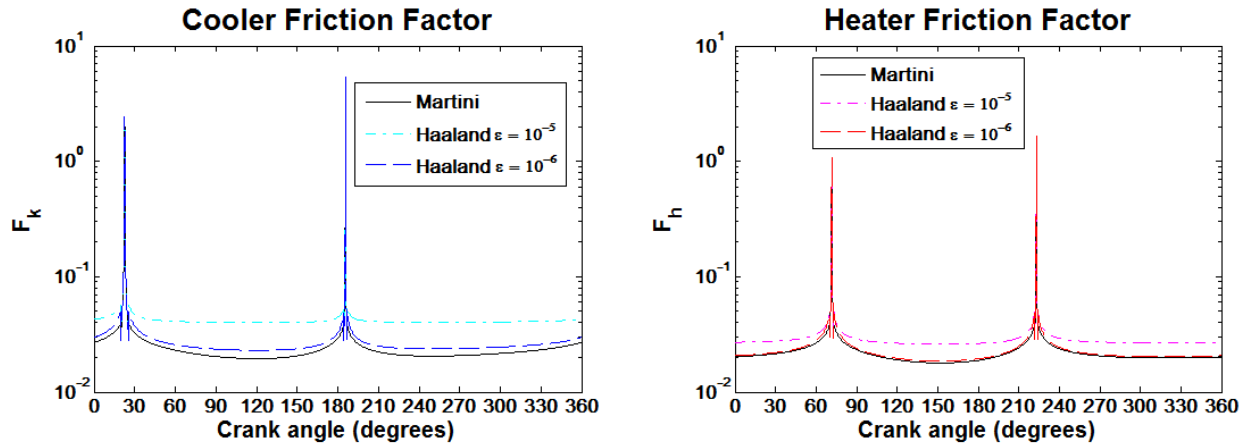


Figure D-4: (a) Cooler Friction Factor Correlation Comparison (b) Heater Friction Factor Correlation Comparison

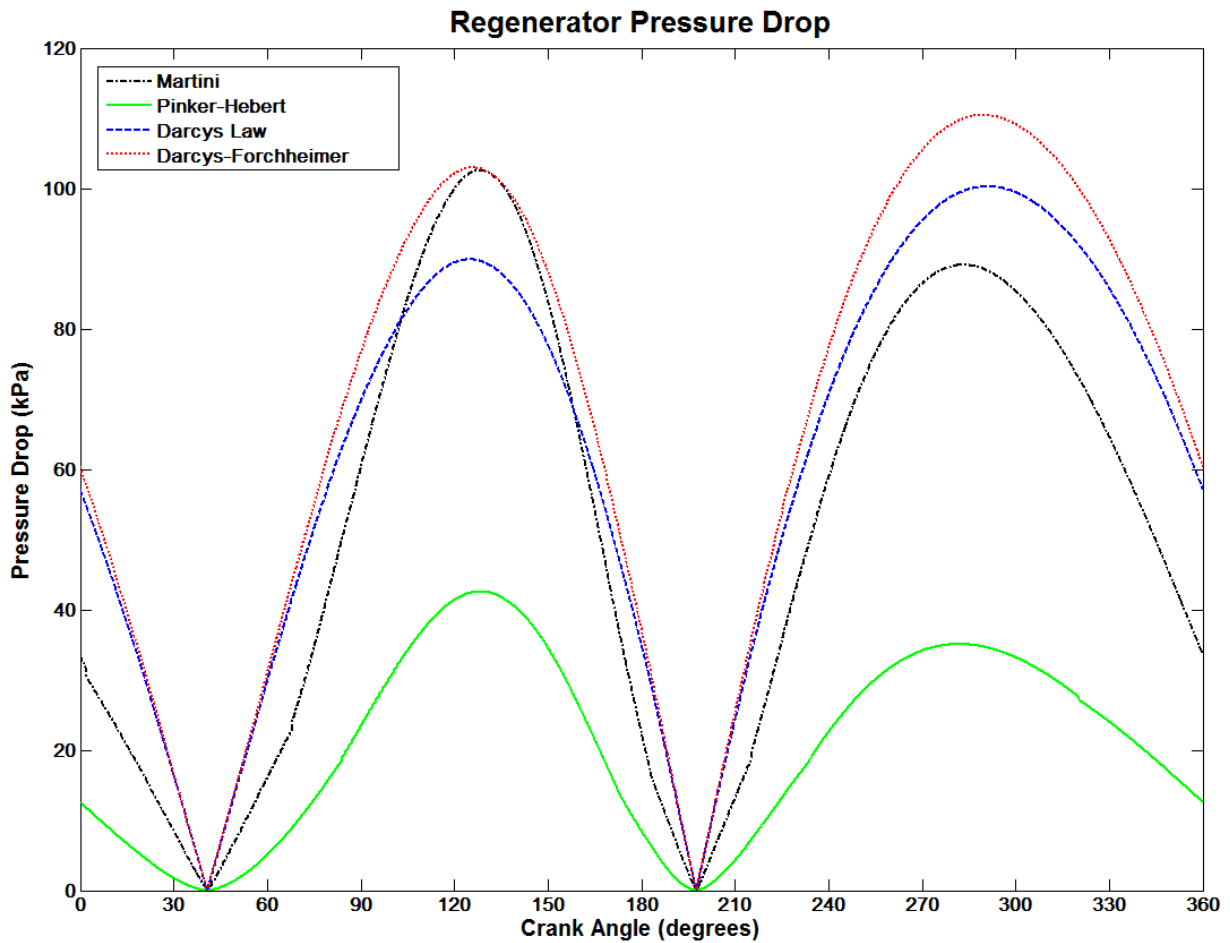


Figure D-5: Regenerator Pressure Drop Comparison and Validation

Table D-1 summarizes the set of equations used for the pressure (or pumping) power loss calculation. For the cooler and heater equations D.1 and D.3 are obtained from the Fanning friction factor and the minor losses, fluid properties and gas flow through the tubes.

In the case of the regenerator, the pressure drop depends on the equivalent friction factor developed for stack wire screen matrices [29]. Using the definition of pumping power loss (D.4) and realizing that Equation D.5 can express the volume flow rate, Equation D.6 is used to calculate the pumping power loss (in the cooler, regenerator and heater).

Table D-1: Summary of Equations for Pumping Power Loss Calculation

Cooler Pressure Drop	$\Delta p_k = \left[4f_{f,k} \frac{L_k}{D_k} + K_k \right] \cdot \frac{1}{2} G_k^2 \cdot \left(\frac{RT_k}{p} \right)$	(D. 51)
Regenerator Pressure Drop	$\Delta p_r = F_r \frac{L_r}{D_r} \cdot \frac{1}{2} G_r^2 \cdot \left(\frac{RT_r}{p} \right)$	(D. 52)
Heater Pressure Drop	$\Delta p_h = \left[4f_{f,h} \frac{L_h}{D_h} + K_h \right] \cdot \frac{1}{2} G_h^2 \cdot \left(\frac{RT_h}{p} \right)$	(D. 53)
Definition of Pumping Loss	$\dot{W}_{pl} = \Delta p \cdot \dot{V}$	(D. 54)
Volume Flow Rate	$\dot{V}_x = V_x \frac{\dot{m}_x}{m_x}$	(D. 55)
Individual Pumping Power Loss	$\dot{W}_{pl,x} = \Delta p_x \cdot \left(V_x \frac{\dot{m}_x}{m_x} \right)$	(D. 56)

Appendix D.3

A brief description of the procedure undertaken in order to establish the calculation for mechanical friction power loss is describe here. The complete set of equations used is summarized in Table D-2. References [52] (D. 7 to D.10) and [51] (D. 11 and D.12) are used to derive the equation for power loss due to mechanical friction. The average piston velocity is determined from the total displacement of the piston in one cycle times the engine frequency ($\Delta x/\Delta t$), basically this reduces to Equation D.7. After the average piston velocity is obtained, sizing parameters of Eq. D.8 to Eq. D.10 are calculated to later estimate the mean affective pressure loss from Costea et al. correlation (Eq. D.10). Finally, Eq. D.11 and Eq. D.12 are derived from Heywood [51] in order to estimate the power loss from mechanical friction.

Table D-2: Summary of Equations for Mechanical Power Loss Calculation

Avg. Piston Velocity	$V_p = 2L_s f$	(D. 57)
Swept to Clearance Volume Ratio	$\Gamma_c = \frac{V_{sw}}{V_{cl}}$	(D. 58)
Scaling Factor	$\lambda_v = \frac{(1 - \Gamma_c)}{(3 - \Gamma_c)}$	(D. 59)
Costea, et al. Mean Effective Pressure Loss Correlation	$\Delta p_{mf} = \lambda_v(0.94 + 0.045 \cdot V_p) \times 10^5$	(D. 60)
Mean Effective Mechanical Friction	$F_{mf} = \Delta p_{mf} \frac{V_{sw}}{L_s}$	(D. 61)
Mechanical Friction Power Loss	$\dot{W}_{ml} = NC \cdot [F_{mf} \cdot V_p]$	(D. 62)

The compression ratio here was determined as the ratio of swept to clearance volume (D.8). With this ratio, the scaling factor coefficient (D.9) is determined for the mean effective pressure loss correlation by Costea, et al. [52]. Now the mechanical friction power loss is related to the friction based mean effective pressure using the general definition of mean effective pressure [51],

$$\text{mep} = \frac{W}{V_d}$$

where W is the net work per cycle and V_d is the displaced volume. This definition can also be used to define the friction mean effective pressure (fmep) for the piston. By recognizing that the power per rate over volume rate of change is equal to work per volume displaced, the friction mean effective pressure is defined as,

$$\Delta p_{mf} = \frac{\dot{W}_{ml}}{\dot{V}_d} = \frac{\dot{W}_{ml}}{\left(\frac{V_d}{L_s}\right) V_p}$$

With $F_{mf} = \text{mep}(V_d/L_s)$ and $V_d = V_{sw}$ Equation D.12 can be derived. Note that NC represents the number of cylinders which need to be accounted for, since D.10 is derived for only one cylinder configuration (this is the case for a solar Stirling engine).

Appendix D.4

In Appendix D.4 the approach for the regenerator heat loss is reviewed. As discussed in sect. 3.3.3, the regenerator heat loss imposes an additional heat load on the heater. This additional heat load requirement lowers the efficiency of the cycle. The heat loss in the regenerator is associated with the fact that not all the energy from convection can be effectively transferred from the regenerator to the gas and vice versa. Regenerator effectiveness (ϵ) is a parameter that measures the capacity of the heat transfer in the regenerator. The effectiveness is a function of the number of transfer units (NTU) in the regenerator. Table D-3 contains the NTU and ϵ correlations given by different authors. The code developed in this study is setup so the user can choose which correlation to use, and plots all 3 curves for NTU and ϵ so the difference may be visualized. Table D-4 summarizes the equations used for the regenerator loss calculations. A conservative approach should use the maximum regenerator heat and minimum regenerator effectiveness to arrive at the Q_{rl} solution.

Table D-3: Expressions for ϵ and NTU Found in SE Literature (Organ & Finkelstein, [2001], Urieli, [1984], Martini, [1979])

Author	Organ-Finkelstein	Urieli	Martini	
NTU	$\frac{hA_s}{fmC_p}$ (a)	$\frac{hA_s}{\rho VA_f C_p}$ (b)	$\frac{hA_s}{\dot{m}C_v}$ (c)	(D. 63)
ϵ	$1 - \frac{2}{1 + NTU}$ (a)	$\frac{NTU}{1 + NTU}$ (b)	$1 - \frac{2}{NTU + 2}$ (c)	(D. 64)

Table D-4: Summary of Equations for Regenerator Heat Loss Calculation

Regenerator Unit Heat Loss by Organ or Urieli	$Q'_{rl} = Q_{r,max}(1 - \epsilon_{r,min})$	(D. 65)
Regenerator Unit Heat Loss by Organ or Urieli	$Q'_{rl} = \dot{m}_{r,eff} \cdot FCT \cdot C_v(T_h - T_k)(1 - \epsilon_{r,min})$	(D. 66)
Time Fraction for Regenerator First Blow	$FCT = t_2 - t_1$	(D. 67)
Total Regeneration Heat Loss	$Q_{rl} = Q'_{rl} \cdot NR \cdot NC$	(D. 68)

REFERENCES

- [1] Finkelstein, T. and Organ. A. J. *Air Engines: The History, Science, and Reality of the Perfect Engine*. New York: ASME, 2001.
- [2] Christoph, M., Arnaud, G., Rafael, A., Li, S., & Xue, Y. (2007). *Stirling Engine*. University of Gävle.
- [3] Organ, A. J. *The Air Engine: Stirling cycle power for a sustainable future*. Boca Raton: CRC Press, 2007.
- [4] Urieli, I. and Berchowitz, D.M. *Stirling Cycle Engine Analysis*. Bristol: A.Hilger, 1984.
- [5] Stirling Energy Systems, Inc. *Sun Catcher (Pure Power : Made Simple)*. 2011. 3 August 2011. <<http://www.stirlingenergy.com>>
- [6] Sunpower Inc. *Stirling Engines*. 2006. 3 August 2011. < <http://www.sunpowerinc.net>>
- [7] Sandia National Laboratories. *Concentrating Solar Power Technologies Overview*. 2012. 13 April 2012. <http://energy.sandia.gov/?page_id=907 >
- [8] Renewable Energy Focus. *Global CSP market to reach 25 GW by 2020*. 2009. 16 May 2011. <<http://www.renewableenergyfocus.com/view/1747/global-csp-market-to-reach-25-gw-by-2020/>>
- [9] Stirling Cryogenics. *Home: 60 years of cryogenic expertise*. 2012. 5 May 2012. <<http://www.stirlingcryogenics.com/>>
- [10] Twinbird Corporation. *Welcome to the Dr. Cool's FAQ Room*. 2007. 16 May 2011. <<http://fpssc.twinbird.jp/legacy/en/index.html>>
- [11] Kockums. *Kockums Stirling AIP System*. 2009. 14 May 2012. <<http://www.kockums.se/en/>>
- [12] Nightingale, N. P. *Automotive Stirling Engine: MOD II Design Report*. DOE NASA Technical Report NASA CR-175106. New York: Mechanical Technology Inc., 1983.
- [13] Hargreaves, C. M. *The Philips Stirling engine*. Elsevier, 1991.
- [14] Harrison, Jeremy. *Micro Combined Heat & Power: Introduction*. 2012. 16 May 2012. <<http://www.microchap.info>>
- [15] Inspirit Energy. *The Product: mCHP*. 2009. 16 May 2011. <<http://www.inspiritenergy.com/productmchp.html>>
- [16] Sunpower Inc. *Cryocoolers*. 2006. 3 August 2011. <<http://www.sunpowerinc.net/cryocoolers/index.php>>
- [17] Thombare, D.G., & Verma, S. K. "Technological development in the Stirling cycle engines". *Renewable and Sustainable Energy Reviews* (2008), 12.1: 1-38.

- [18] Stine, W. B. *“Stirling Engines”*. Energy Conversion. Ed. D. Yogi Goswami & Frank Kreith. Boca Raton: CRC Press, 2007.
- [19] Fraser, P. R. *Stirling Dish System Performance Prediction Model*. Diss. University of Wisconsin, 2008.
- [20] Snyman, H., & Harms, T. “Design analysis methods for Stirling engines”. *Journal of Energy in Southern Africa* (2008), 19.3: 4-19.
- [21] Karabulut, H., Yücesu, H. S., et al. “An experimental study on the development of a β -type Stirling engine for low and moderate temperature heat sources”. *Applied Energy* (2009), 86.1: 68-73.
- [22] Karabulut, H., Aksoy, F., & Ozturk, E. “Thermodynamic analysis of a β type Stirling engine with a displacer driving mechanism by means of a lever”. *Renewable Energy* (2009), 34.1: 202-208.
- [23] Karabulut, H., Yucesu, H., & Cinar, C. “Nodal analysis of a Stirling engine with concentric piston and displacer”. *Renewable Energy* (2006), 31.13: 2188-2197
- [24] Urieli, I. *Gamma Type Stirling Engines*. 2011. 5 February 2011. <<http://www.ohio.edu/people/urieli/stirling/engines/gamma.html>>
- [25] Abdullah, S., Yousif, B., & Sopian, K. “Design consideration of low temperature differential double-acting Stirling engine for solar application”. *Renewable Energy* (2005), 30.12: 1923-1941.
- [26] Kongtragool, B., & Wongwises, S. “A four power-piston low-temperature differential Stirling engine using simulated solar energy as a heat source”. *Solar Energy* (2008), 8.6: 493-500.
- [27] Kongtragool, B., & Wongwises, S. “A review of solar-powered Stirling engines and low temperature differential Stirling engines”. *Renewable and Sustainable Energy Reviews* (2003), 7.2: 131-154.
- [28] Reader, G. T., Potter, I. J., Clavelle, E. J., & Fauvel, O. R. “Low power Stirling engine for underwater vehicle applications”. *Proceedings of 1998 International Symposium on Underwater Technology* (1998), 411-416.
- [29] Collie, M.J., Ed. *Stirling Engine Design and Feasibility for Automotive Use*. New Jersey: Noyes Data Corp, 1979.
- [30] Martini, W. R. *Stirling engine design manual*. DOE NASA Technical Report NASA CR-168088. Richland: Martini Engineering, 1983.
- [31] Chen, N. C. J., Griffin, F. P. *A REVIEW OF STIRLING ENGINE MATHEMATICAL MODELS*. DOE EERE Research Report ORNL/CON-135. Oak Ridge: Oak Ridge National Laboratory (ORNL), 1983.

- [32] Dyson, R. W., Wilson, S. D., & Tew, R. C. "On the Need for Multidimensional Stirling Simulations". NASA, Glenn Research Center. *Third International Energy Conversion Engineering Conference*, San Francisco, CA, August, 2005.
- [33] Dyson, R. W., Wilson, S. D., & Tew, R. C. "Review of Computational Stirling Analysis Methods". *Proceedings of the 2nd International Energy Conversion Engineering Conference*, Paper No. AIAA-2004-5582, Providence, RI, 2004.
- [34] Malroy, E. T. *Solution of the Ideal adiabatic Stirling model with coupled first order differential equations by the Pasic method*. Diss. Ohio University, 1998.
- [35] Larson, V. A study of dynamic energy equations for Stirling cycle analysis. Final Report Cleveland State Univ., OH. (Vol. 1), 1983.
- [36] Sahu, A. *CFD Simulation of a Small Stirling Cryocooler*. Diss. National Institute Technology at Rourkela, 2010.
- [37] Van Giessel, R. and Reinink, F. "Design of the 4-215 D.A. Automotive Stirling Engine". SAE Technical Paper, 1977.
- [38] Dehelean, N., et al. "A Theoretical Improvement of a Stirling Engine PV Diagram". *New Trends in Mechanism Science* (2010), 5.11: 613-623.
- [39] Dehelean, N., et al. "A Digital Model of a Dwell Mechanism for Alpha-Stirling Engine". *SYROM* (2009), 521-527.
- [40] Dehelean, N., and Cuipe, V. "The Analysis of a Dwell Mechanism for Alpha -Stirling Engine". *SYROM* (2009), 511-519.
- [41] Fang, H., Herold, K. "A novel Stirling engine with an elliptic drive". *Energy Conversion Engineering Conference, 1996. IECEC 96., Proceedings of the 31st Intersociety*. Washington, DC, August 11-16, 1996.
- [42] Beach, E. H. *Efficient energy conversion apparatus and method especially arranged to employ a stirling engine or alternately arranged to employ an internal combustion engine*. United States patent US 4,969,591. 1990 Nov 13. 994502, March 6, 1999.
- [43] Bejan, A.. *Advanced Engineering Thermodynamics*. 3rd Ed. New Jersey: Wiley, 2006.
- [44] Hoffman, J. D. *Numerical Methods for Engineers & Scientists*. 2nd Ed. New York: McGraw-Hill Inc., 1992.
- [45] Herzog, Z. *Ideal Adiabatic Simulation of Stirling Engines*. 2005. 15 April 2011. <<http://mac6.ma.psu.edu/stirling/simulations/IdealAdiabatic>>
- [46] Incropera, F., et al. *Introduction to Heat Transfer*. 5th Ed. New Jersey: Wiley, 2007.
- [47] Thomas, B., Pittman, D. "Update on the evaluation of different correlations for the flow friction factor and heat transfer of Stirling engine regenerators". *Intersociety Energy Conversion Engineering Conference, Las Vegas, NV, 2000*.

- [48] Shock, A. "Stirling Engine Nodal Analysis Program". *Journal of Energy* (1978), 6.2: 354-362.
- [49] Shock, A. "Nodal Analysis of Stirling Cycle Devices". *Intersociety Energy Conversion Engineering Conference, San Diego, CA, August, 1978*.
- [50] Remsburg, R. *Thermal Design of Electronic Equipment*. (pp. 85-182) Boca Raton: CRC Press, 2001.
- [51] Heywood, J. B. *Internal Combustion Engines Fundamentals*. New York: McGraw-Hill, 1988.
- [52] Costea, M., et al. "The Effect of Irreversibilities on Solar Stirling Engine Cycle Performance". *Energy conversion and management* (1999), 15.40: 1723-1731.
- [53] Kagawa, N., et al. "Mechanical analysis and durability for a 3 kW Stirling engine". *Intersociety Energy Conversion Engineering Conference, Washington, DC, 1989*.
- [54] Urieli, I. *Regenerator Simple Analysis*. 2011. 5 February 2011. <http://www.ohio.edu/mechanical/stirling/simple/regen_simple.html>
- [55] Hodge, B.K. and Taylor, R. *Analysis & Design of Energy Systems*. 3rd Ed. New Jersey: Prentice Hall, 1999.
- [56] Ibrahim, M. B., Tew, R .C.Jr. *Stirling Convertor Regenerators*. Boca Raton: CRC Press, 2012.
- [57] Bejan, A., Ed. *Porous and Complex Flow Structures in Modern Technologies*. New York: Springer Verlag LLC, 1979.
- [58] Andrade, J. S., Costa U.M.S., et al. "Physical Review Letters". *Physical Review Letters* (1978), 82:5249-5252.